On the rheology of shear-thickening and magnetorheological fluids under strong confinement

TESIS DOCTORAL

Programa de Doctorado en Física y Ciencias del Espacio

Elisa María Ortigosa Moya

Directores

Juan de Vicente Álvarez-Manzaneda
Roque Isidro Hidalgo Álvarez

UNIVERSIDAD
DE GRANADA

Grupo de Física de Fluidos y Biocoloides
Departamento de Física Aplicada
2020

Editor: Universidad de Granada. Tesis Doctorales
Autor: Elisa María Ortigosa Moya
ISBN: 978-84-1306-706-3
URI: http://hdl.handle.net/10481/65310

A mis padres y mi hermana.

A los hijos de la tierra
y los peces de ciudad.

Agradecimientos

Llega el momento de dedicar unas líneas de agradecimiento sincero a todos aquellos que de una u otra manera han estado a mi lado en días de sol, nubes y lluvia, ofreciéndome su ayuda, apoyo y tiempo para llevar a buen término esta tesis.

En primer lugar quiero comenzar por dar las gracias a mis directores de tesis. A Juan, por ofrecerme la posibilidad de trabajar junto a él, un excepcional investigador con capacidad para guiar el trabajo de cada vez más gente y hacerlo bien, además. Y a Roque, un insaciable aprendiz que contagia su ilusión por la ciencia. Gracias por lo aprendido y por vuestra confianza, consejos y paciencia durante estos años.

Gracias también a los miembros del Departamento de Física Aplicada, en especial al Grupo de Física de Fluidos y Biocoloides, por dejarme aprender de vosotros en cada seminario y ayudarme en lo que he necesitado: Ana Belén, Julia, Alberto, Arturo, Teresa, Wagner, Curro y Miguel Ángel. A María, por su disposición y su sonrisa imborrable; a Pepe, compañero en el sótano con quien habría disfrutado en clase como alumna; a Delfi por sus firmas y cariño; a Miguel Cabrerizo, por acercar la ciencia a la gente; y especialmente a María José, Fernando y Stefania, por su constante ayuda en las prácticas de Biofísica cada curso. Del mismo modo, también ha sido un placer compartir las prácticas de Fundamentos físicos aplicados a las estructuras con Artur, Javier, Enri-

que, Matilde, José Antonio y Jorge, que tantas veces ha bajado las escaleras para asegurarse de que todo funcionaba bien en la sala. También quiero agradecer la labor de los administrativos Conrado, Belén y Raquel, y la de Ángel y María Jesús como coordinadores del programa de doctorado, por su amable trato y facilitarnos la burocracia. Así mismo también me acuerdo de Felisa y su preciosa Ángela, de Marisa y esa coreografía tan ensayada y de María del Mar, que no dejó de repartir abrazos, alegría y sororidad.

Este tiempo habría sido muy distinto de no ser por mis compañeros de la sala π^f, gracias a todos ellos por compartir tantos momentos juntos. A aquellos que estuvieron poco tiempo al principio pero que sembraron un ambiente estupendo: Juan Pablo, Azahara, Germán y Diego. A José Antonio, por su simpatía e inestimable ayuda en mis innumerables tropiezos con las simulaciones. Al hijo adoptivo de Nerja, Keshvad, por enseñarme tribología y encontrar los dulces más ricos en cada aeropuerto. A José Rafael, un ejemplo de eficiencia que ha superado cada rasguño del rugby. Al fascinante y aventurero Guille, que nos llevó en chanclas hasta el techo peninsular y no dejó de alentarnos por aquellos preciosos parajes. A Tamara, por traer orden al laboratorio y una nueva sonrisa a la sala. A los que estuvieron de paso menos tiempo, como María Laura con sus palabras de ánimo, antiguas y recientes, para "meterle pila" a la tesis; la encantadora Camila, Ester, Mónica, Ángel, Blanca, Alan, Jianjian, Martin y Dorota. Gracias también a Pablo Ibáñez, Yan, Alicia, Matthew, Pablo Graván y Sara por reavivar la sala, espero que sigáis cuidando de ella.

Quiero dar las gracias a Paloma, Pablo y Samuel por luchar por todos, y a Milagros por su cercanía y apoyo. A Jose y Santiago, por solucionar problemillas en los clusters Proteus y Alhambra y su disposición a ayudarme cuando lo he necesitado. A los compis de la peña, con los que recargué las pilas cada miércoles. A Aurora, por su fiel compañía carrera tras carrera y hacerse un hueco entre nosotros. A Matt y David, por acompañarnos siempre que han podido. Y también a Maxwell, del que cada vez me asusto menos aunque salte más, y a Pablo Pamplona, Oviedo, Zamora…, por las divertidas confusiones.

Recorrer el largo y pedregoso camino que emprendí ha sido mucho más fácil dentro de una burbuja rebosante de calidad humana, comprensión, compañía, entretenimiento, comida (mucha) y, en definitiva, amistad. Gracias por dejarme crecer y aprender a vuestro lado. A la divertida y organizada Irene, que tanto me ha hecho reír y enseñado sobre la idiosincrasia granaína. Es imposible no echarla de menos a mi espalda, en el fútbol o bailando con lenguaje de signos. Menos mal que aun sin estar sigue estando y deleitándonos con sus

peripecias y virtuosismo eligiendo GIFs. A la pizpireta Aixa, por esas recetas tan ricas que nos ha preparado durante este tiempo y contagiarnos su alegría. A Luis, por estar pendiente de mí en los momentos delicados, ser un buen senpai y entretenernos con sus aventuras. Gracias Leo, por ser el pegamento más antiguo y duradero del grupo, cuidar de todos nosotros y enseñarnos a compartir. A Migue, que casi no tuvo cascarón y de quien tanto se puede aprender. A Pablo con su desparpajo malagueño y su faceta actoral, porque todo es más divertido si está cerca. A Nico, por su energía desbordante y su memoria infinita para el quesito rosa, lleno de ideas para hacer regalos de tesis y sobre dónde ir a comer, y por presentarme a los dragones. A Ana, que no puede ser más "apañá", por los ratos de recetas, costura, deporte y los cursillos exprés de sevillanas. A Javi con sus apuestas siempre ganadoras, por enseñarme algo de fonética y por qué el 28 es un número perfecto, aunque nunca viéramos su tesis. A su particular Zipi, Alvaro, por sus acertadas recomendaciones tecnológicas. El brillante Adri consiguió que muchos nos leyéramos su tesis para encontrar dónde estaba la gracia, al mismo tiempo que nos recordaba que somos una ohana en la que nadie se deja atrás. Gracias al polifacético José Alberto, por aguantarme estos años y cuidar de mí, por enseñarnos a protegernos para ser un poquito más libres, por las clases de armonía y mostrarme unos anillos muy lejanos, por tantas risas y complicidad. Soy muy consciente de que difícilmente volveré a toparme con tanta gente tan capaz, divertida y cariñosa como vosotros. Sois especiales.

También quiero dar las gracias a mis ingenieros repartidos por el mundo, por su memoria, con la que completamos nuestros puzles de anécdotas pasadas para acabar llorando de risa: Nuria, Susana, Blanco, Juanjo, Antonio, Abraham, Candela y mis queridos tomatitos. También quiero agradecer su continuo interés y apoyo a Amabel, Lorena, Dani y Alfonso.

A Pedro, que me peina el alma y me la enreda, y cuyo aliento y sustento no me dejan caer. Gracias por seguir estando a mi lado por lejos que me encuentre, por hacerme reír y mimarme, por quererme. A mi familia, que siempre está ahí aunque todo cambie, y a la dulce Rocío. A mi hermana, Jose y sus dos tesoros, que consiguen sacarme una sonrisa a la mínima. Y, finalmente, gracias a mis padres, los cimientos firmes que siempre me ofrecen su ejemplo de lucha, unión y amor, y que me enseñaron que ante un gran salto como este hay que coger un gran impulso. Os quiero.

Financiación

La investigación que ha conducido a la realización de esta tesis doctoral ha sido financiada por el Ministerio de Economía y Competitividad (MINECO), mediante los proyectos MAT 2013-44429-R y MAT 2016-78778-R, el Fondo Europeo de Desarrollo Regional (FEDER) y por la Junta de Andalucía mediante el proyecto P11-FQM-7074. La doctoranda agradece la ayuda predoctoral para la formación de doctores FPI 2014/069341.

Contents

Abstract

Suspension rheology is capturing a great interest in recent years due to the importance of complex suspensions in multitude of industrial applications. Among them, shear-thickening (ST) and magnetorheological (MR) fluids are very valuable materials for their ability of readily tuning their rheological behaviour, well passively by shear or actively in presence of external fields, respectively. Both complex fluids are used in energy dissipating systems: ST fluids are mainly used as impact-resistant materials or shock absorbers in protective applications, while MR fluids are extensively employed in torque transfer applications.

The counter-intuitive phenomenon of shear thickening displays a reversible increase in viscosity (continuous or discontinuous) under applied shear rates or stresses. For this non-Newtonian behaviour to occur it is necessary to reach a critical volume fraction and shear rate, in systems where attraction is negligible. These shear-thickening features can be controlled by means of several strategies, such us changing some particle or fluid properties during the formulation of these complex fluids, or introducing net attractive forces. Nowadays scientific community broadly agrees that ST is due to a transition from a hydrodynamically lubricated regime to a friction dominated situation, especially in dense systems. It is in close contact conditions where the fields of rheology and tribology are connected, as the local friction deter-

mines the microstructure that give rise to certain macroscopic rheological response.

On the other hand, as it happens in the case of ST fluids, the rheological properties of MR fluids can also be varied, but by the action of an external magnetic field. They are suspensions of magnetic micronsized particles suspended in a non-magnetic Newtonian fluid. When subjected to an external magnetic field these particles become polarized and aggregate in chains or columnar structures that orientate along magnetic field lines. As a result of this field-induced assembly, the suspension experiences a reversible liquid-to-solid transition, as the viscosity of MR fluids rapidly increases several orders of magnitude, what is known as magnetorheological effect, and it is occasionally accompanied by a yield stress. Magnetorheological applications have to deal with some drawbacks due to particle sedimentation, which is generally improved by the incorporation of additives into the carrier in order to reduce the density mismatch between particles and carrier.

The meeting point between ST and MR systems are magnetorheological shear-thickening (MRST) suspensions, i.e., concentrated hybrid systems whose rheological behaviour can be easily tuned, well passively with a given flow deformation or actively through an applied magnetic field strength. These suspensions are still scarcely studied and, apart from controlling the appearance and intensity of the shear thickening behaviour, it has been shown that the partial substitution of magnetic particles by non-magnetic ones in MR fluids produces an increase in yield stress.

Besides, the operational mode also affects the MR fluid performance. In this sense, it has been demonstrated a yield stress enhancement when the MR fluid with certain concentration is subjected to slow compression prior to a shear flow mode under the application of an external field, the so-called squeeze strengthening effect.

Having said that, the research works presented in this dissertation can be classified in three main topics: rheology of concentrated suspensions that show shear-thickening and/or magnetic response, tribology of non-Newtonian fluids, and squeeze-strengthening effect under constant-volume and constant-area conditions. These three matters were studied experimentally and by simulations. Regarding the first topic, we investigated shear-thickening in dense suspensions formulated with one and two types of particles, magnetic and non-magnetic ones, and explore the effect of the type of

particle, concentration, carrier fluid and magnetic field. Particle-level dynamic simulations were performed in both monodisperse and polydisperse mixtures of particles in order to reproduce shear-thickening behaviour and the enhancement in yield stress due to partial substitution of magnetic particles in MR fluids. With respect to the second topic we studied tribological behaviour of non-Newtonian fluids, both shear-thinning and shear-thickening fluids, in the elastohydrodynamic regime. Numerical simulations try to reproduce the pressure distribution, film thickness and frictional properties of these fluids within this regime, and a master curved is proposed and evaluated with experimental results. Concerning the last topic, we investigated the slow compression of diluted MR fluids subjected to an external magnetic field, under constant-volume and constant-area conditions. We highlight that higher yield stresses found in constant-area compared to constant-volume conditions, are due to the effect of the densification occurring during the compression of the fluid in the constant-area case. Particle-level simulations mimicked the compression and shear processes and also showed higher yield stresses in constant-area compression.

Resumen

En los últimos años, la reología de suspensiones está captando un gran interés por su importancia en multitud de aplicaciones industriales. Entre ellas, los fluidos espesantes y magnetorreológicos son materiales muy apreciados por su capacidad de modificar su comportamiento reológico fácilmente, bien sea de pasivamente al someterlos a cizalla o de forma activa en presencia de campos externos, respectivamente. Ambos fluidos complejos se utilizan en sistemas de disipación de energía: los fluidos espesantes su usan principalmente en aplicaciones de absorción de impactos, mientras que los fluidos MR se emplean ampliamente en aplicaciones que requieren transferencia de par.

El comportamiento espesante en condiciones de cizalla es un fenómeno contrario a la intuición, ya que muestra un aumento reversible de la viscosidad (continuo o discontinuo) con la velocidad de deformación o el esfuerzo aplicados. Para que este comportamiento no newtoniano tenga lugar es necesario alcanzar valores críticos de fracción de volumen y velocidad de deformación, en sistemas en los que la atracción es insignificante. Las características del perfil de espesamiento pueden controlarse mediante varias estrategias, como la modificación en las propiedades de las partículas o los fluidos portadores durante la formulación de estas suspensiones complejas, o la introducción de fuerzas atractivas. Hoy en día la comunidad científica coincide ampliamente en que el origen del comportamiento espesante en sistemas

concentrados se debe a la transición desde un régimen lubricado hidrodinámicamente hasta una situación dominada por la fricción. En condiciones de estrecho contacto confluyen los campos de la reología y la tribología, ya que la fricción local entre partículas determina la microestructura que da lugar a una determinada respuesta reológica macroscópica.

Por otro lado, las propiedades reológicas de los fluidos MR también pueden modificarse, como sucede con los fluidos espesantes, pero por la acción de un campo magnético externo. Estos fluidos son suspensiones de partículas magnéticas de tamaño micrométrico suspendidas en un fluido newtoniano no magnético. Cuando se someten a un campo magnético externo, estas partículas se polarizan y se agregan en cadenas o estructuras columnares que se orientan a lo largo de las líneas de campo magnético. Como resultado de este ensamblaje inducido por el campo, la suspensión experimenta una transición reversible de líquido a sólido, como consecuencia de un aumento muy rápido en la viscosidad del fluido, de varios órdenes de magnitud. Esto se conoce como efecto magnetorreológico, y ocasionalmente va acompañado de un esfuerzo umbral. Las aplicaciones de estos fluidos requieren acciones que mitiguen la sedimentación de partículas, generalmente ésta se mejora mediante la incorporación de aditivos en el fluido portador y así reducir el desequilibrio entre partículas y líquido.

El punto de encuentro entre los sistemas espesantes y los fluidos MR son las suspensiones espesantes magnetorreológicas (MRST). Se trata de sistemas híbridos concentrados cuyo comportamiento reológico se puede ajustar fácilmente, bien de forma pasiva con una determinada deformación de flujo o de forma activa a mediante la aplicación de un campo magnético. Estas suspensiones que combinan tanto el comportamiento espesante como el magnético han sido foco de algunas investigaciones, pero han sido poco estudiadas. Aparte de controlar la aparición e intensidad del espesamiento debido a la cizalla, se ha demostrado que la sustitución parcial de las partículas magnéticas por otras no magnéticas en los fluidos MR produce un aumento del esfuerzo umbral.

Además, el tipo de flujo al que se someten los fluidos MR afecta a su comportamiento reológico. En este sentido, se ha demostrado un aumento del esfuerzo umbral cuando el fluido MR con una cierta concentración se somete a una compresión lenta previa al flujo de cizalla, en condiciones de campo aplicado. Este efecto se debe a una recolocación de las partículas magnéticas que

forman las cadenas, como consecuencia de la compresión, y que da lugar al refuerzo de estas estructuras.

Dicho esto, los trabajos de investigación presentados en esta tesis pueden clasificarse en torno a tres temas principales: reología de suspensiones concentradas que muestran un espesamiento en flujo de cizalla y/o respuesta magnética, tribología de los fluidos no newtonianos y comportamiento de fluidos MR sometidos a compresión lenta en condiciones de volumen y área constantes. Estas tres materias se han abordado tanto experimentalmente como mediante simulaciones. En cuanto al primer tema, investigamos el espesamiento en suspensiones concentradas formuladas con uno y dos tipos de partículas, tanto magnéticas y como no magnéticas, y exploramos el efecto del tipo de partícula, la concentración, el fluido portador y el campo magnético. Se realizaron simulaciones dinámicas a nivel de partícula en mezclas de partículas monodispersas y polidispersas, con el fin de reproducir el comportamiento espesante y el aumento del esfuerzo umbral provocado por la sustitución parcial de las partículas magnéticas en los fluidos MR. Con respecto al segundo tema, se estudió el comportamiento tribológico de fluidos no newtonianos, tanto fluidos espesantes como fluidificantes, en el régimen de lubricación elastohidrodinámica. Las simulaciones numéricas realizadas pretenden reproducir la distribución de la presión, el espesor de la película y las propiedades de fricción de estos fluidos dentro de este régimen, y se ha propuesto una expresión para la curva maestra, que ha sido validada con los. En cuanto al último tema, investigamos la compresión lenta de los fluidos diluidos de MR sometidos a un campo magnético externo, bajo condiciones de volumen y área constantes. Destacamos la obtención de mayores esfuerzos umbrales en compresiones a área constante con respecto a los experimentos realizados a volumen constante, y que son consecuencia del aumento de la fracción de volumen entre los platos a medida que la compresión avanza. Se han usado nuevamente simulaciones a nivel de partícula que replican los flujos de compresión y cizalla experimentales, y también mostraron mayores esfuerzos umbrales en compresión en área constante.

I

Introduction

1. Background

1.1. Complex fluids

The mechanical behaviour of matter can be classified basically in two categories: solid and fluid. However most materials belong to a grayscale between these two cases and present intermediate characteristics between these limits, so that this binary classification is insufficient [1]. It is the case of soft matter and complex fluids [2]. This kind of materials self-organizes in mesoscopic structures that provide a partial order. Interactions between these entities are generally weak and comparable with thermal energy, what contribute to some of their features, as an easy deformability and sensitivity to thermal fluctuations and other external actions [3,4]. Soft matter is ubiquitous both in nature and in industrial applications. Examples of soft materials include, among others, polymers, colloids, liquid crystals, biological matter or granular materials, and are applied in fields like food, personal care products, paints and cements.

These systems may occasionally display a particularly complex and counter-intuitive behaviour, even at room temperature. The subset of soft matter that can flow but exhibit non-Newtonian rheology is called complex fluids. These structured multicomponent systems are known by some of their defining adjectives as smart, tuneable or responsive materials, because of their

ease in changing some properties under a given external stimuli, such as stress, temperature, light or magnetic field.

In relation to the supramolecular assembling characterizing soft matter, Pierre Gilles de Gennes received the Nobel Prize in Physics (1991) "for discovering that methods developed for studying order phenomena in simple systems can be generalized to more complex forms of matter, in particular to liquid crystals and polymers". He is considered the father of this broad discipline that covers from the vulcanisation of rubber to the lather of a shampoo [5]. He compared this fragile and deformable matter with the clay of a sculptor, as its malleability allows for a delicate adjustment upon the subtle action of the artist's hand.

1.1.1. Colloids

Colloids are dispersed systems composed by mixtures of one or more dispersed phases homogeneously distributed in a continuous medium. The particle size of the colloidal range goes from 1 nm to 1 μm. Systems with particles in this range are known as dispersions (average diameter being 100 nm), while in the case of having larger particles, the colloidal system is called suspension. In colloidal science the suspending medium is considered a continuum, and the lower limit of the colloidal range guarantee that particles are larger than the carrier molecules. Below this limit both particles and molecules of the suspended fluid are indistinguishable, so that we would be talking about solutions, with a unique phase. On the other hand, the upper limit seeks to ensure negligible sedimentation and still significant thermal forces in the motion of colloidal particles. Sedimentation can occur when particles are above 1 μm (Brownian motion becomes negligible) or have high density.

These composed systems are mainly characterized by high particle diffusion coefficient, slow sedimentation under normal gravity, showing weak light scattering, and suspension structuring. Due to the fineness of particles (i.e., large specific surface area), surface area properties of the dispersed phase and their physico-chemical interaction with the solvent are properties of great importance in colloidal science. Other interesting features comprise the particle morphology, concentration and suspension properties (such as turbidity, viscosity and stability), among others [6].

Colloidal particles are not necessarily solids neither the carrier fluid a liquid. Depending on the state of the matter of both dispersed phase and dispersion medium, several types of colloids are found: foams, aerosols, emul-

sions, gels, sols. Typical examples of colloids in daily life are inks, milk, blood, gelatine, whipped cream, fog and atmospheric particulate matter [7].

The kinetic stability or colloidal stability of these systems depends on the forces the particles are subjected to. In this sense, the macroscopic behaviour of the whole suspension relies on the nature of microscopic interactions between colloidal particles.

A single colloidal particle suspended within the carrier fluid is subjected do three forces: Brownian, hydrodynamic and gravitational forces. In general, the order of magnitude of these forces ($O(10^{15}$ N)) is similar for colloidal-sized particles.

- Small particles dispersed in a medium are always subjected to Brownian motion, which randomly moves the particles due to the thermal fluctuations and collisions with the fluid molecules.
- Hydrodynamic force is due to the particle drag (Stokes) because of being immersed within the carrier fluid.
- Gravitational forces give rise to particle sedimentation, which can be avoided by equalizing the densities of each phase.

Colloidal interactions [6] refer to particle-particle interactions through the fluid, and three types can be distinguished: dispersion, surface, and hydrodynamic forces. These interactions depend on the chemical and material properties of the particles and can be attractive or repulsive.

- Surface forces are short-range forces that arise when particles are close enough: electrostatic interaction is generally repulsive and is due to electrical charge often carried by colloidal particles on their surfaces and properties of the continuous phase; repulsive steric forces (or excluded volume), usually generated when particles are covered with grafted polymers or surfactants; and attractive depletion forces that exclude smaller solutes (non-adsorbed polymers) from the vicinity of large colloidal particles.
- Dispersion forces, such as the attractive and short-range van der Waals forces, appear when atoms in a given colloid induce polarization in other colloid nearby.
- The last comes from the disturbance in the flow produced by the presence of other particles.

The linear addition of the attractive diffusion potential and the electrostatic repulsive potential is known as Derjaguin-Landau-Verwey-Overbeek (DLVO) theory [8–11] and is used satisfactorily to explain stabilization. Generally, the total interaction energy as a function of the distance between particle surfaces presents two local minima and one local maximum. Van der Waals attraction give rise to the first primary minimum at small surface distances, as adhesion of particles is an energetically favourable process. At larger surface distances, if van der Waals interactions are strong and repulsion from the double layer interactions play a significant role, the second minimum appears as well as the local energy maximum. This means that coagulation is produced when decreasing the electrostatic repulsive forces and when particles are forced to be in close proximity. At great distances there will not be any interactions between identical colloidal particles.

Besides previous interactions, other short-range repulsive interaction may be observed, particularly for hydrophilic surfaces in polar solvents, the so-called solvation or hydration interaction.

Particles will aggregate if attractive forces dominate, while when repulsive forces prevail, the colloidal system remains stable. For the sake of clarity, in this case we refer to microscopic stability (absence of particle aggregation) and not to the less used macroscopic stability (constant and homogeneous distribution of the dispersed phase). Aggregation and sedimentation are the main phenomena involved in the destabilization of the colloidal system. Therefore, the minimization of particle aggregation requires the enhancement of repulsive interaction forces, through electrostatic and steric stabilization. Regarding particle sedimentation it can be improved by reducing the density mismatch between the carrier fluid and the dispersed phase. Polymers are broadly used for this function as they are able to form a gel matrix that complicates the normal particle motion. Moreover, polymeric chains also hinder particle aggregation as impede them to be closer.

Colloidal stability can be enhanced through changes in the viscosity, acidity, ionic concentration or addition of some component, such a surfactants or polymers to the suspending fluid. It is interesting that the use of additives to improve the stability was already employed by ancient Egyptians, when they added Arabic gum to impede flocculation of carbon black particles in the preparation of inks [5]. In this case, the explanation of the stabilization of the colloidal suspension of carbon black comes from the fact that grains of carbon black were coated by hydrophilic polymers whose bonds with water mole-

cules were stronger than van der Waals attractions between the macromolecules.

1.1.2. Field-responsive materials

Field-responsive fluids have attracted much attention during last century due to the ease in changing and controlling material properties upon the application of an external stimulus, namely electric or magnetic fields. Electrorheological (ER) fluids and magnetorheological (MR) suspensions [12] belong to this subclass of smart materials, as well as magnetic colloids and other magnetic hybrid systems with solid matrices.

The discovery of ER and MR fluids occurred almost simultaneously. On the one hand, in 1948 Jacob Rabinow [13] designed several devices at the US National Bureau of Standards in which an iron-oil mixture became almost solid when subjected to a magnetic field; it was the origin of a new type of magnetic fluids, i.e., MR fluids. For its part, Willis M. Winslow reported the ER effect also in the 1940s [14]. ER fluids are the electric analogous of MR fluids, and consist of electrical polarizable particles (silica, titania, zeolites) dispersed in a carrier fluid (silicone oil, mineral oil). Similarly to MR fluids, under the influence of an electric field they dramatically modify their rheological properties. Both field-responsive fluids respond to an external field exhibiting a reversible and fast transition from liquid to solid state as a consequence of the dipole-dipole interactions between the constituent particles. The apparent viscosity can show an increase of several orders of magnitude from the off-state to the on-state, which can be easily tuned by controlling the external field. Other difference is the maximum yield strength obtained in ER fluids, which is much lower than that found in MR fluid. This affects the mechanical applicability of each type of fluid as well as the size of the required device. Because of the stronger field-induced interactions in MR fluids, they are usually preferred over ER fluids. One of the focuses during this thesis is the study of magnetorheological fluids under certain flow conditions.

Apart from MR fluids, other types of magnetic fluids structure under the action of a magnetic field giving rise to changes in their properties [15]. They can be classified according to their magnetizable phase. If the solid phase is magnetic we can talk about ferrofluids (FF) [16] and magnetorheological fluids (MRF) [17,18]. In inverse ferrofluids (IFF) instead it is the carrier fluid that provides the magnetic response [19,20]. Some of the main characteristics of these magnetic fluids are exposed below.

- **Magnetorheological fluids**

A typical MR fluid is generally formulated with magnetic soft particles (e.g., carbonyl iron) suspended at high concentration in mineral oils, aqueous solutions, etc. In this case particle size ranges from tens of nanometers to tens of micrometers. Above a critical value in particle size they possess magnetic multidomains. In the absence of magnetic field this fluid acts as a conventional suspension as the net dipole is very small. When subjected to magnetic field, Bloch walls gradually shift in the sense of increasing the magnitude of the magnetic moments oriented in the field direction and so the interparticle interactions. Attractive interactions between particles result in columnar aggregates that enhance the mechanical characteristics of the fluid. As a consequence, the apparent viscosity of the fluid increases several orders of magnitude, what is known as magnetorheological effect, and it is occasionally accompanied by a yield stress. This increase produces a rapid and reversible transition from liquid-like to solid-like state at sufficiently high fields, and can be easily controlled by varying the magnetic field intensity. The maximum effect depends on the saturation magnetization of the magnetic phase which often shows magnetic remanence. In this sense, particles with a larger saturation magnetization provide larger magnetic moments and thus larger MR effect.

Unlike the following magnetic fluid, particles in MR fluids may settle easily, due to the big particle size that hinders the occurrence of Brownian motion and to the density difference between particles and fluid.

- **Ferrofluids**

Ferrofluids were first formulated in the early 1960s by Steve Papell, an engineer at Lewis Research Center (NASA), with the primary purpose of moving the rocket fuel in no gravity conditions thanks to the magnetization of this kind of magnetic liquid [21]. After that, Rosenzweig's work improved the fabrication process, magnetization and stability of these fluids, and gave rise to their industrial synthesis and commercialization. The fluid mechanics of these magnetic fluids constitutes a branch of science is known a Ferrohydrodynamics [22].

This stable colloidal magnetic fluid is composed of ferro- or ferrimagnetic nanoparticles less than 10 nm in size (which is the typical size of monodomains), usually magnetite, dispersed in polar or non-polar carriers. These nanoparticles are frequently covered by some surfactant, in order to

inhibit spontaneous coagulation. Due to the small particle size the particles form individual magnetic domains, and Brownian motion due to thermal energy prevails over magnetic interaction, so that in absence of field the net magnetization is null. Once the field is active particles orient in the direction of the magnetic field. A remarkable difference with respect to MR fluids is that FF always remains in fluid state in the presence of the field, and field-induced structures that may develop a yield stress are not observed in this magnetic fluid. Moreover, the small particle size provides a weaker magnetic response compared to MR fluids. Therefore, unlike in MR fluids, their applications are dictated for the fact of being magnetic fluids more than for the enhancement in viscosity under an applied field.

- **Inverse ferrofluids**

As previously commented, in IFF the magnetic response comes from the carrier fluid and not from the particles. The carrier is a ferrofluid with micrometric and nonmagnetic particles dispersed in it. It can be seen somewhat as the combination of MR fluids and FF. In IFF (or magnetic holes) interactions appear between particles even being non-magnetic, but as opposed to MR fluids, the use of a FF as carrier provides a weak magnetic response. The major advantage compared to conventional MR fluids comes from the possibility of selecting specific characteristics for the non-magnetic particles, as a given morphology or a certain and controlled size.

- **Magnetorheological elastomers**

Magnetorheological elastomers are obtained by dispersing micrometric-sized magnetizable particles in a viscoelastic solid-like polymer gel or an elastomer. Magnetic structures are formed if a uniform magnetic field is applied during the cross-linking process, and these structures result retained within the matrix. These materials are solid under all circumstances, their modulus or stiffness can be varied by an applied field. The MR elastomers may find use in vibration-control applications.

Apart from a particulate phase and a carrier, magnetic liquids may carry certain additives, such as polymers and surfactants, that improve the formulation as contribute to enhance the colloidal stability, reduce particle sedimentation or prevent oxidation, which are the main drawbacks affecting their durability and response in some applications. Unlike ER fluids where such additives may decrease the ER effect, they have no influence on the polarization mechanism of MR fluids.

Among the broad range of applications of magnetic fluids in everyday life we will pay attention to those of ferrofluids and magnetorheological fluids as they are the most widely used nowadays in industrial and biomedical applications.

Magnetic nanoparticles are receiving considerable attention due to their potential application in drug delivery or hyperthermia treatment, and thus ferrofluids formulated with them due to their magnetic control. For example, in magnetic hyperthermia, a supplementary therapy in cancer treatments, a combination of alternating magnetic fields and magnetic nanoparticles (a ferrofluid is injected) are used to heat specific tumour regions without damaging other surrounding tissues. Magnetic nanoparticles are also employed in environmental applications, such as in the removal of contaminants in water treatment. These contaminants have high affinity for the specific functionalization of particles, and the magnetic core allows for an easy recovery. Besides, ferrofluids are employed in sealing and damping applications, with a remarkable use as energy dissipating system in loudspeakers dampers.

Regarding MR fluids, an ideal magnetorheological device should enable certain magnetic field with the least electrical power consumption and weight. Moreover it should provide a significant response to the field (strong MR effect), for which the selection of the involved phases and their interaction become crucial. Some of the most common applications [15,23] are exposed below.

- MR dampers are used to reduce vibrations by means of the dissipation of kinetic energy through the fluid. Those dampers are found in shock absorbers, mounts, car and suspension, seismic protection in buildings, cable stayed bridges or washing machines, among others.
- Torque-transfer applications such as in clutches, rotary brakes or hydraulic valves.
- Magnetic-circuits in which it is important to achieve an efficient production and transmission of magnetic field.
- Manufacturing and process applications, such as the polishing and finishing of optical components. In this application non-magnetic abrasive particles are added to a MRF, and driven to the MR-component interface under by applying a magnetic field.

1.1.3. Concentrated suspensions

Suspensions of non-colloidal particles are found in numerous applications in industrial processes such in food processing or concrete, and in natural phenomena such as slurries or lava. Due to the large particle size Brownian motion is neglected in these suspensions while the main interactions to be considered are hydrodynamic. However, interparticle forces depending on surface interactions have to be taken into account only in the case of near contact, it is, in concentrated suspensions.

Even if the carrier fluid is Newtonian (and without the influence of any external field), the rheological behaviour of dense suspensions is nonlinear, especially at high concentrations. Multi-body interactions in the system are inevitable at large volume fractions so that apart of hydrodynamic interactions through the liquid, frictional contacts become important due to the close proximity the particles are subjected to. Therefore, the flow regime of dense suspensions is intermediate between that of pure suspensions and granular flow [24]. The description of the macroscopic behaviour of these complex suspensions clearly depends on the microstructure formed as a consequence of such interactions.

The addition of particles to a suspending Newtonian fluid with viscosity η_s leads to an increase in its viscous dissipation and thus the deviation from the Newtonian response. For example, at high particle concentration the suspension may display an apparent yield stress, i.e., the fluid would only flow if the applied stress overcomes this critical value. The increase in energy dissipation comes from the friction of the particle surface with the fluid and from the disturbance of the flow caused by the presence of particles. In this sense, the increase in viscosity with particle concentration is higher when their sphericity is decreased.

Among nonlinear and often unwanted effects that these concentrated suspension can develop we usually encounter normal forces, shear-induced migration, shear banding, sedimentation, thixotropy, aging, shear thickening or jamming. For example, shear-induced migration appears when there are spatial variations in shear rate so that particles migrate from high to low shear regions, with the consequent concentration gradient and thus viscosity gradient. Normal stresses for its part emerge as a consequence of the anisotropy generated in the microstructure during shear. This variety of rheological

behaviours depends on the shape, size and particle volume fractions and the features of the applied deformation.

The dependence of the suspension viscosity η as a function of the applied shear rates or stresses gives rise to different rheological behaviours, explained in detail in the Subsection 1.3.2.

1.1.4. Shear thickening

Shear thickening is a counter-intuitive phenomenon occurring in highly concentrated dispersions and suspensions, and it is characterized by a reversible increase in the viscosity η with the applied shear rate $\dot{\gamma}$ or shear stress τ [25–27]. The rise in viscosity and the critical shear rate $\dot{\gamma}_c$ above which it is observed depend on the particle volume fraction ϕ (see Figure 1.1). The shear-thickening region can be modelled with a power-law function (see Table 1.1), while a recent work tackles the fitting of the whole viscosity function with a very good agreement [28]. While at low and moderate concentrations the increase is gradual, i.e., continuous shear thickening (CST) is found, at higher volume fractions a sudden jump in viscosity is observed, i.e., discontinuous shear thickening (DST) is developed. This non-Newtonian behaviour is due to lubrication hydrodynamic forces and frictional forces appearing when the fluid is subjected to shear flow [29,30]. The macroscopic rheology is coupled to the microstructure formed by the particles in close contact. Shear thickening is observed in stable colloidal suspensions while it is obscured in samples showing high interparticle attractions or with an apparent yield stress [26,31].

This striking behaviour of shear-thickening fluids (STF) can be used in a wide assortment of forms: the STF itself, combined with a flexible porous material, coated, impregnated or held between plates in a sandwich structure [32–34].

It is worth distinguishing shear thickening from other two terms that also involve an increase in viscosity, and which are frequently misled with shear thickening: dilatancy and rheopexy [25]. The former is the expansion in volume as a consequence of frictional interactions between the particles; it entails positive normal stress differences and is mainly found in granular systems. The second term refers to a time-dependent behaviour in which the viscosity increases with time upon the application of a constant shear rate.

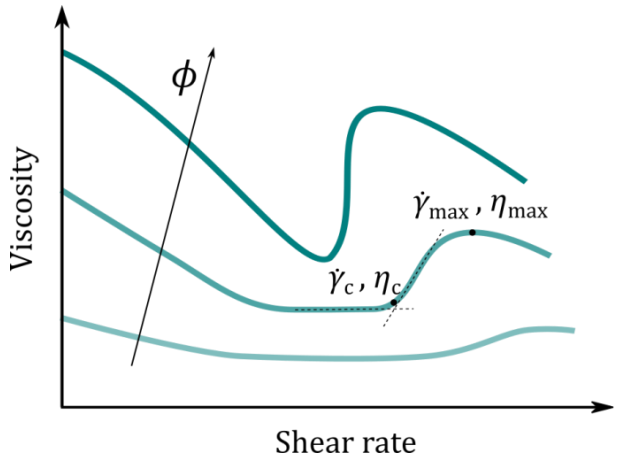

Figure 1.1: Schematics of the rheological behaviour of a concentrated suspension as a function of the volume fraction. The shear-thickening region appears at high shear rates, after shear-thinning and Newtonian regions. Significant shear-thickening parameters are shown in the flow curve.

Different mechanisms have been proposed over the last decades to describe this unusual response to applied stresses occurring in densely packed suspensions. In early works [35] shear thickening (mainly DST) was observed together with dilatancy, and both concepts were used as synonyms. However, dilatancy is just one of the necessary conditions to find the DST response. Other mechanism developed by Hoffman [36,37] associated the DTS transition with an order-disorder transition. later, other scientists proposed the formation of transient aggregates [38] as a consequence of the shear, labelled hydroclusters, which are responsible for the viscosity increase. Hydrocluster theory quantitatively agrees with the moderate increase in viscosity with the shear rate (i.e., CST), but is insufficient to reproduce the large stresses found during DST. In recent years, simulations have demonstrated that the use of frictional forces along with hydrodynamic interactions adequately reproduce DST curves as well as the transition from CST to DST when volume fraction increases [29,39]. This demonstrates the intimate connection between rheological and tribological properties in densely-packed systems.

Systems developing this astonishing increase in the flow resistance and energy dissipation are by far less known that shear-thinning materials, for which the viscosity decreases with the shear rate. In spite of this peculiar response to shear stresses or shear rates, it is interesting that one of the most representative suspensions showing this behaviour is based on a widely-used household product: cornstarch [40–43]. Dense suspensions of starch in water

are perhaps the best known shear-thickening fluid exhibiting a dramatic increase in viscosity when sheared or subjected to. It is fascinating how this behaviour arises from such a simple system and the fact that the main features of shear thickening can be exhibited also by non-attractive hard spheres suspended in a Newtonian liquid. This support the suggestion that shear thickening could be observed in all suspensions if the right conditions exist.

This thesis is primarily devoted to the study of dense cornstarch-based suspensions and their rheological and tribological behaviour, as well as the effect of adding magnetic particles to the systems to become thus in field controlled suspensions.

1.2. Basis on magnetism

Natural iron minerals found in the proximities of the ancient city of Magnesia were the first mysterious stones in which magnetic phenomena were observed, and their magnetic properties gave rise to the term magnetism.

Nowadays it is known that magnetic phenomena appears not only in permanent magnets but also arises from forces between electric charges in movement. During electron motion around the atomic nucleus each electron has an additional moment (spin magnetic moment) apart of the orbital magnetic moment, which is induced from the electron rotation around its own axis. Both contribute to the magnetic atomic moment, and influence the type of magnetism. Àmpere proposed that the magnetic properties of a material come from a great number of tiny and closed circuit within the material. In this sense, the total magnetic induction $\boldsymbol{B}$ in a material is the sum of the external field intensity $\boldsymbol{H}$ and an additional field caused from these microscopic currents, i.e., due to the intrinsic magnetization of the material. The general relationship between them is given by:

$$\boldsymbol{B} = \mu_0(\boldsymbol{H} + \boldsymbol{M}) \,, \tag{1.1}$$

where $\mu_0 = 4\pi \cdot 10^{-7}$ N/A^2 is the magnetic permeability of the free space and $\boldsymbol{M}$ is a vector field called magnetization, that quantifies the density of magnetic moments $\boldsymbol{m_i}$, $\boldsymbol{M} = \frac{\sum_i^n \boldsymbol{m_i}}{V}$, and is related to the extent to which a given material is influenced by a magnetic field. Null magnetization is obtained in the case of having randomly oriented magnetic moments or if they do not exist.

Magnetic materials can exhibit a linear behaviour under certain conditions as at constant temperature and low values of magnetic field, i.e., the

three vector fields $\boldsymbol{H}$, $\boldsymbol{M}$ and $\boldsymbol{B}$ are proportional. The coefficients of proportionality are the magnetic susceptibility $\chi = \boldsymbol{M}/\boldsymbol{H}$ and the magnetic permeability $\mu = \boldsymbol{B}/\boldsymbol{H}$ of the material. The former coefficient is dimensionless while the other has the same units as μ_0, and the ratio between magnetic permeabilities of the material and the free space is called relative magnetic permeability $\mu_r = 1 + \chi$. With this, Equation 1.1 can also be written as:

$$\boldsymbol{B} = \mu_0(1 + \chi)\boldsymbol{H} = \mu_0\mu_r\boldsymbol{H} = \mu\boldsymbol{H}\,. \tag{1.2}$$

Both the magnetic induction (also called magnetic flux density) and the magnetic field intensity (or strength) can be represented through field lines. In the free space, both sets of lines have the same form as the magnetization is zero and so the magnetic susceptibility.

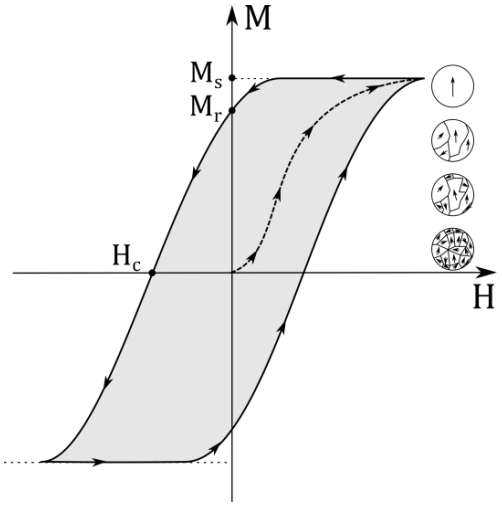

Figure 1.2: Non-linear magnetization for ferro- and ferromagnetic materials. Typical hysteresis curve and domain growth.

However, some materials have field dependent magnetic permeability $\mu = \mu(\boldsymbol{H})$ so that the ratio between $\boldsymbol{B}$ and $\boldsymbol{H}$ is no longer a constant, i.e., these vector fields are no proportional. In these cases, the process of magnetization provides a magnetization curve that show hysteresis (see Figure 1.2). The Frohlich-Kennely equation [44] is an example of empirical relationship that correlates the magnetic field strength $\boldsymbol{H}$ and the material permeability $\mu(\boldsymbol{H})$ for ferromagnetic materials. Therefore it provides information about how magnetization $\boldsymbol{M}$ changes with the field:

$$\frac{\mu(\boldsymbol{H})}{\mu_0} = 1 + \frac{(\mu^0 - 1)\frac{\boldsymbol{M_s}}{\boldsymbol{H}}}{(\mu^0 - 1) + \frac{\boldsymbol{M_s}}{\boldsymbol{H}}}. \tag{1.3}$$

This expression can be rewritten as:

$$\boldsymbol{M} = \frac{(\mu^0 - 1)\boldsymbol{H}}{1 + (\mu^0 - 1)\frac{\boldsymbol{H}}{\boldsymbol{M_s}}}, \tag{1.4}$$

where μ^0 is the relative initial permeability, i.e., the value of magnetic permeability at low magnetic fields, at the beginning of the magnetization.

1.2.1. Types of magnetic materials

Magnetic properties are present to a greater or lesser extent in all materials. They can be categorized according to their response upon the application of an external magnetic field. The orientation of their magnetic moments will result in a net value with implications in the final response of the material.

As it has been previously said, some materials show proportionality between the vector fields. It is the case of diamagnetic and paramagnetic materials. In the formers a small and negative magnetic susceptibility is observed, and a very weak magnetization opposes to the field. In contrast, in paramagnetic materials, magnetization reinforces the external field as they aligned parallel to the field direction but the magnetic susceptibility is positive. Both behaviours are induced by an applied magnetic field so that the magnetization disappears with the field.

Ferromagnetic solids are the most identifiable magnetic materials. They show magnetic remanence in the absence of a magnetic field and their magnetic susceptibility is larger than 1. It is the case of permanent magnets. In absence of magnetic field dipolar moments align parallel within their magnetic domains, randomly aligned in turn, so that there is no net magnetization. In presence of a magnetic field those domains favourably oriented in the field direction rotate and grow and a net magnetic moment emerges. These materials present hysteresis (see Figure 1.2) in their magnetization curves. At very high field they show saturation magnetization and when the field is reduced to zero, a remnant magnetization remains (lower than in saturation, due to the tendency of magnetic domains to rotate to their original alignment). In order to completely demagnetize a ferromagnetic material it is necessary to apply an opposed field (coercitive). If this field is high enough saturation

again reappears. As a function of the value of the coercitive field and the area of the hysteresis loop, ferromagnetic materials can be soft or hard. For low values of coercivity, tipically less than 1000 A/m, the material is magnetically soft, and for values above 10000 A/m it is considered a hard material [44]. Besides, soft magnetic materials have low anisotropy and wide domain walls while hard magnetic materials present opposite features. Ferromagnetic systems become paramagnetic, i.e., their hysteresis loops vanish as both coercivity and remanence go to zero, above the Curie temperature of the materials as the parallel alignment of magnetic moments becomes disordered because of thermal energy. In magnetorheological fluids it is desirable to have particles with small coercivity and remnant magnetization (i.e., magnetically soft materials) so that the magnetizing/demagnetizing process to be carried out at lower field strengths (easy process), as well as large saturation magnetization for the applied field.

Other types of magnetic materials include antiferromagnet, ferrimagnets, and superparamagnet. They share the magnetic order with ferromagnets. In presence of a magnetic field antiferromagnetic dipoles display antiparallel (aligned in opposite directions) resulting in zero net moment. A particular case of antiferromagnetism appears in ferrimagnetic materials. They have similar macroscopic trends to ferromagnets in response to a magnetic field as a net magnetic moment is obtained during the antiparallel alignment, due to different magnitude of magnetic moments, but show lower electric conductivity. They also exhibit hysteresis and saturation. Ferrimagnetic materials are called ferrites, like magnetite Fe_3O_4. Finally, superparamagnetism occurs in sufficiently small (single-domain) ferromagnetic or ferrimagnetic nanoparticles with no long-range order between particles. In this form of magnetism temperature randomly affect the direction of the magnetization. This behaviour is found in colloidal magnetic fluids, i.e., ferrofluids.

1.3. Rheology

Rheology is the study of the deformation and flow of matter. This term was coined in 1928 by Eugene C. Bingham, from the Greek words ρέω and λόγοσ (meaning flow and study, respectively). This concept was investigated by Robert Hook and Isaac Newton, who stablished concepts and laws related to plasticity and body deformations. The Hookean elastic solid just like the Newtonian viscous fluid are ideal substances that constitute the true limits of the

rheological behaviour. However, most materials exhibit both elastic and viscous features, they are viscoelastic.

1.3.1. Types of materials and their rheological response

Hooke's law (1678) of elasticity is a constitutive equation describing the behaviour of a perfect elastic solid. This empirical law states that in an elastic body the deformation is proportional to the applied force (or stress) that produces this deformation:

$$\sigma = G\gamma \,, \tag{1.5}$$

where σ is the stress, G is the elastic modulus and γ the strain. The rheological behaviour is independent of time and there is no lag between the application of the load and the deformation. It implies that deformation completely disappears when the load is retired and the body recovers its initial shape. Although it is referred to a theoretical solid, in practice, many substances can be considered as ideally elastic.

Newton's law, for its part, is the constitutive law applying to viscous fluids. The dynamic viscosity η is defined as the ratio between the tangential tension $\tau = F/A$ (shear stress, i.e., the shear force per surface area) and the velocity gradient $\dot{\gamma} = v/h$ (shear rate), which is in turn the ratio between fluid velocity and the height of the volume element, so that

$$\tau = \eta\, \dot{\gamma} \,. \tag{1.6}$$

A fluid obeying this linear relation is called Newtonian, it is, η is independent of $\dot{\gamma}$. Newtonian behaviour is then characterized by a constant viscosity, which is also independent of the time of shearing and a permanent deformation. Analogously to the elastic solid, the Newtonian liquid is irreal but many liquids are considered to be Newtonian in a broad range of shear stresses. Water, honey and silicone oils are typical examples of Newtonian liquids.

With this, most fluids exhibit non-Newtonian behaviours, i.e., the relationship between shear stress and shear rate is not linear. Thus viscosity may depend on shear rate, time or present partial recovery. Non-linear fluids can be classified as time-independent, time-dependent and viscoelastic fluids. In Figure 1.3 the rheological behaviour of different types of fluids subjected to shear flow are schematically shown.

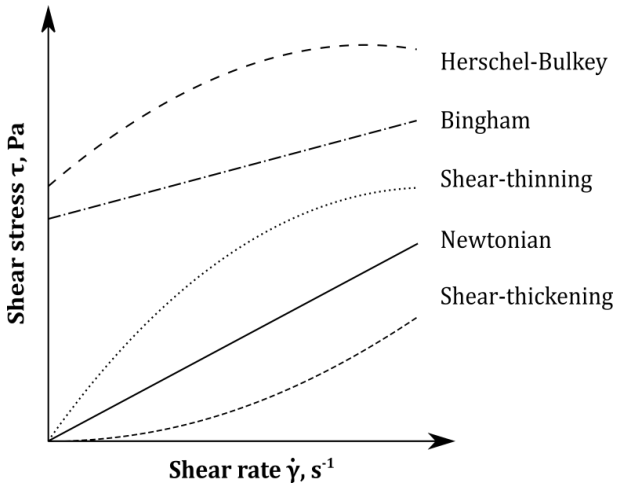

Figure 1.3: Flow curves for time-independent fluids.

Time-independent fluids are those for which the viscosity is dependent on the shear rate. Within this category three flow behaviours can be distinguished:

- Pseudoplastic or shear-thinning fluids such as paints, shampoo or ketchup, where the viscosity falls progressively with increased shear rate.
- Dilatant or shear-thickening fluids such as wet sand or concentrated starch suspensions, in which the viscosity increases with the shear rate.
- Bingham or ideal plastics as tooth paste or hand cream, characterized by a yield stress.

The flow behaviour of time-dependent fluids depends not only on the shear rate but also on the time during which the fluid has been sheared (at constant shear rate). Thus predictions of the flow behaviour of these types of fluids have to consider the flow history of the material. This category can be subdivided into:

- Thixotropic fluids, related to a breakdown of the structure by shear and as a consequence their viscosity decreases with the time of shearing, as in yogurts. Once the stress is removed, the material shows a gradual recovery.
- Rheopectic fluids, much less common than thixotropic ones are those for which the viscosity increases with time, like gypsum.

Most materials are viscoelastic, it is, they show both fluid-like or solid-like properties on different timescales, so that the solid and fluid parts are not pure elastic nor pure viscous, respectively. Moreover they exhibit partial recovery after deformation. Viscoelasticity is then related to the materials' ability to store (elastic) or dissipate (visco) energy. One well-known example of viscoelastic material is the classic Silly Putty, whose main ingredient is polydimethylsiloxane (a silicone-based polymer) mixed with boric acid. This paste, which has no practical application other than as a toy, was discovered in 1943 by the engineer James Wright while searching for inexpensive substitutes for synthetic rubber. At rest it spread like a viscous liquid because the material has time to adapt to the change in the applied stresses or deformations, compared to the time scale of the process, but it bounces when throw against the soil.

The response of the viscoelastic materials to an applied load is then a matter of characteristic time scales, as Reiner pointed out. The well-known Déborah number [45] was defined to quantify the ratio between the relaxation time of the material t_r and the observation time t_o(for linear viscoelasticity):

$$De = t_r/t_o \ . \tag{1.7}$$

This number highlights the relative importance of elastic phenomena. In this sense, for values of this dimensionless number well below the unity the system behaves like more viscous, whereas it show elastic solid-like features at higher Deborah numbers and the material behaviour changes to a non-Newtonian regime.

1.3.2. Constitutive equations and material functions

Constitutive equations are relationships that describe the response of a material to stress or to deformation. Mass and momentum balance equations [46] enables us, together with the constitutive equation, to solve flow problems.

- Continuity equation:

$$0 = \frac{\partial \rho}{\partial t} + \nabla \cdot (\rho \bar{v}) \, . \tag{1.8}$$

- Equation of motion:

$$\rho \frac{D\bar{v}}{Dt} = \rho \left(\frac{\partial \bar{v}}{\partial t} + \bar{v} \cdot \nabla \bar{v} \right) = -\nabla \cdot \bar{\bar{\Pi}} + \rho \bar{g} \, . \tag{1.9}$$

The total stress tensor $\bar{\bar{\Pi}} = \mathrm{p}\,\bar{\bar{\mathrm{I}}} + \bar{\bar{\tau}}$ has two main contributions: the thermodynamic pressure, which is isotropic, and the contribution depending on the flow field, originated from the fluid deformation. The equation that expresses the so-called extra stress tensor $\bar{\bar{\tau}}$ as a function of the flow field is the stress constitutive equation. This equation must be valid for any kind of flow. Once this expression is known, the total stress tensor is inserted in the equation of motion and, considering the continuity equation and the boundary conditions of the systems, the solution of the velocity field can be obtained.

As shown in previous subsection, Newton's law of viscosity relates the shear stress to the shear rate for an incompressible and Newtonian fluid in shear flow. In particular, the tangential shear component τ_{21} is proportional to the variation of the velocity in the flow direction with the position in the gap dv_x/dy. The coefficient of proportionality is the shear viscosity η, which describes the resistance to flow. However this expression cannot be used for other types of flows, and a general expression is needed.

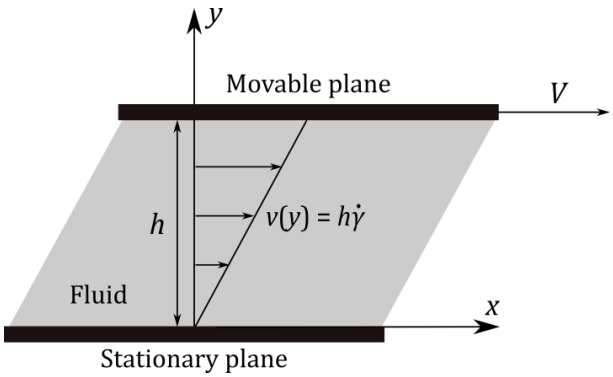

Figure 1.4: Simple shear flow.

The constitutive equation for Newtonian and compressible fluids takes this form:

$$\bar{\bar{\tau}} = -\eta[\nabla\bar{v} + (\nabla\bar{v})^T] + \left(\frac{2}{3}\eta - \kappa\right)(\nabla\cdot\bar{v})\,\bar{\bar{\mathrm{I}}}\,, \qquad (1.10)$$

where κ is a coefficient related to the changes in the density fluid upon deformation, called bulk viscosity. The sum of the velocity gradient $\nabla\bar{v}$ and its transpose is a symmetric tensor known as the rate-of-strain or rate-of-deformation tensor $\bar{\bar{\dot{\gamma}}}$.

In the case of incompressible (i.e., fluid density is constant) Newtonian fluids, the constitutive equation simplifies as

$$\bar{\bar{\tau}} = -\eta\,\bar{\bar{\dot{\gamma}}}\,, \tag{1.11}$$

and substituting Equation 1.11 into the equation of motion the well-known Navier-Stokes equation for incompressible Newtonian fluid results:

$$\rho\frac{D\bar{v}}{Dt} = -\nabla p + \eta\nabla^2\bar{v} + \rho\bar{g}\,. \tag{1.12}$$

However, the description of the flow of non-Newtonian fluids, i.e., its changes with position and time, is more complex. Equation 1.11 and 1.12 do not apply for these materials and other non-linear constitutive equations have to be developed to model their behaviour. A constitutive equation that predict some experimentally observed non-Newtonian behaviours is the generalized Newtonian fluid (GNF) model [47]. It stands out for being a first and simple approach that matches steady shearing data very well (although it is unclear its validity in non-shear flows) and that is useful for predicting pressure-drop relationships and flow-rate information. This stress-deformation law is alike to that for incompressible Newtonian fluids, but instead the fluid viscosity is taken as a shear rate dependent viscosity:

$$\bar{\bar{\tau}} = -\eta(\dot{\gamma})\bar{\bar{\dot{\gamma}}}\,, \tag{1.13}$$

where $\dot{\gamma} = |\bar{\bar{\dot{\gamma}}}|$.

This expression comply the physical and mathematical constrains that guarantee the mathematical sense of the tensorial equation. The viscosity dependence $\eta(\dot{\gamma})$ can take multiple forms [47,48]. Among them, we can highlight power-law models, Carreau-Yasuda or Cross model, and yield stress models. Their expressions are shown in Table 1.1.

The power-law (or Ostwald-de Waele) model provides an empirical and simple relationship between viscosity and shear rate with two parameters that can fit reasonably well for shear thinning or shear thickening fluids in limited ranges of shear rates.

The Carreau-Yasuda model accounts better the shape of viscosity curves as it considers five parameters. Specifically, constant viscosity values (plateaus) at zero η_0 and infinite shear rate η_∞ are predicted, a critical shear rate $\dot{\gamma}_c$ determines the transition from one value to another, and the curvature and slope of the transition is modelled with a and n, respectively.

Model	Mathematical expression
Newtonian	$\tau = \eta(\dot{\gamma})\dot{\gamma} = K\dot{\gamma}$
Power law	$\tau = K\dot{\gamma}^n,\ 0 < n < 1$ Shear-Thinning Fluid $\tau = K\dot{\gamma}^n,\ 1 < n < \infty$ Shear-Thickening Fluid
Carreau-Yasuda	$\eta(\dot{\gamma}) = \eta_\infty + (\eta_0 - \eta_\infty)\left[1 + \left(\frac{\dot{\gamma}}{\dot{\gamma}_c}\right)^a\right]^{\frac{n-1}{a}}$
Bingham	$\tau = \tau_y + K\dot{\gamma}$
Herschel-Bulkey	$\tau = \tau_y + K\dot{\gamma}^n$
Casson	$\tau^{0.5} = \tau_y^{0.5} + K\dot{\gamma}^{0.5}$

Table 1.1: Rheological models for the description of time-independent fluids.

Regarding to yield stress models, Bingham plastic model is commonly used to describe this complex rheological behaviour. It combines the behaviour of a Newtonian fluid with a yield condition. Yield stress reflects the tendency of a material to flow. Below a certain shear stress value the material behaves as solid and does not flow; however, once this threshold is overcome the material starts to flow. Other yield stress models include the Herschel-Bulkey, which generalises the former, and Casson model that does not contain Bingham model.

The usefulness and reliability of a constitutive equation is related to the success of the predictions with respect to the experimental observations. In spite of the ease of flow calculations with these GNF models, as they are empirical extensions of the Newtonian fluid model, the elastic effects of complex fluids are not properly accounted for, such as predictions of shear normal stresses. Moreover, these models rely on the instantaneous shear rate tensor and the dependence with history effects or fluid memory is missing.

The past deformation experienced by the fluid is called memory, and it quantitatively affects the steady shear viscosity, while in unsteady flows a qualitative effect is also found. In this sense, the flow history of a material should be taken into account to estimate its flow behaviour. In the elastically dominated regime, such as in slow or time-dependent flows, other constitutive equations that consider both current and previous deformation of the material are required.

An example of constitutive equation for shear flows that incorporates some elastic effects was proposed by James Clerk Maxwell in 1867. In its scalar form Maxwell equation is given by:

$$\tau_{21} + \frac{\eta}{G}\frac{\partial \tau_{21}}{\partial t} = -\eta\dot{\gamma}_{21}\,, \tag{1.14}$$

which converts into Newton's law when temporal effects are insignificant and into Hook's law for rapid motions at short times, as the derivative term greatly exceed the stress.

In steady simple shear flow (see Figure 1.4), the flow is generated as a consequence of the relative motion of one flat plate relative to another. These plates are parallel and the gap between them is constant. Due to the symmetry of the stress tensor, only four components are nonzero in this type of flow: normal stress components (i.e., diagonal elements: $\tau_{11}, \tau_{22}, \tau_{33}$) and the shear stress $\tau_{21} = \tau_{12}$. The differences between normal components can generate deformation and they have more rheological interest than the magnitude of these components. This lead to the definition of two stress-related quantities, the first and second normal stress differences, as follows:

$$N_1(\dot{\gamma}) = \tau_{11} - \tau_{22};\;\; N_2(\dot{\gamma}) = \tau_{22} - \tau_{33}\,. \tag{1.15}$$

In the case of Newtonian fluids, the shear stress is proportional to the shear rate $\tau(\dot{\gamma}) = \tau_{21} = \eta\dot{\gamma}$, and normal stress differences are zero. The state of stress of a fluid in viscometric flow is fully described with three shear-rate-dependent material functions, which are related to τ, N_1, and N_2. They are called viscosity, first normal stress coefficient and second normal stress coefficient, respectively:

$$\eta(\dot{\gamma}) = \frac{\tau}{\dot{\gamma}};\; \psi_1(\dot{\gamma}) = \frac{N_1}{\dot{\gamma}^2};\; \psi_2(\dot{\gamma}) = \frac{N_2}{\dot{\gamma}^2}. \tag{1.16}$$

Material functions have the same values whatever the viscometric flow used, and can be predicted once the constitutive equations are known and the stress responses are measured.

1.3.3. Effect of volume fraction in viscosity

In the ideal case of hard spheres, one of the simplest cases of non-interacting systems, the apparent viscosity η_{app} in the case of dilute systems (below a concentration of 5 %) can be calculated through the well-known Einstein equation [49,50]. It is a linear function of the particle volume fraction

$\phi = \frac{V_p}{V_p+V_f}$, i.e., the ratio between the particle V_p and total system volume $V = V_p + V_f$ (for a suspension containing N spheres with radius a, $\phi = \frac{4}{3}\pi a^3 \frac{N}{V}$), as follows:

$$\eta_r = \frac{\eta_{app}}{\eta_s} = (1 + 2.5\phi)\,. \tag{1.17}$$

This expression is valid when there is no internal dissipation but only that from the fluid, so that this relation is useful for emulsions as particles in these systems are liquid. The linearity with the concentration appears as a consequence of particles not interacting each other and so the deformation of the flow due to each particle is additive. Moreover, as can be observed, this expression is independent of the size, shape, polydispersity, and density of the particles. So that for two different systems the suspension viscosity would be the same if the carrier fluid and the particle concentration coincide.

In the semi-dilute regime ($0.05<\phi<0.15$) the distance between particles is comparable to the particle size and interactions of nearby particles provoke a higher energy dissipation. Again, the suspension viscosity depends on the volume fraction and viscosity of the medium. Both the effects of hydrodynamic interactions in the suspension viscosity and the Brownian motion were considered by Batchelor [51] by including a term of order ϕ^2:

$$\eta_r = 1 + 2.5\phi + 6.2\phi^2\,. \tag{1.18}$$

Polydispersity comes into play in this regime because hydrodynamic forces are affected by the distance between particles compared to their size. A higher polydispersity reduces the system viscosity as for a given volume fraction polydispersity results in more free space to flow (better packing), but this effect competes with the increase in viscosity caused by the increase in particle-particle interactions when the particle size decreases.

In concentrated systems, the viscosity rapidly increases due to the fact that multi-particle interactions become decisive, and near the maximum packing fraction it diverges. This is a problem in theoretical methods, and although a determining method is lacking particle level simulations can be helpful in the determination of the suspension viscosity if the employed time steps are low enough.

In practice, viscosity models for more concentrated suspensions often use semi-empirical expressions with an adjustable parameter, the maximum vol-

ume fraction ϕ_m, before which the viscosity would become infinite in the equation relating the relative viscosity and the particle concentration. This parameter depends on the shape and size distribution of suspended particles. A great number of viscosity relations take the form of $\eta_r = \eta_r(\phi, \phi_m)$. In the case of monodisperse hard spheres the maximum packing fraction capable to flow is $\phi_{rcp} = 0.64$, that corresponds with a random close packing. Quemada [52] included this parameter within his model as follows:

$$\eta_r = \left(1 - \frac{\phi}{\phi_m}\right)^{-2}. \tag{1.19}$$

Suspensions with higher polydispersity can better densify the packing, as smaller particles occupy holes between big particles. As it has been previously said this provokes a decrease in viscosity for a given volume fraction. The maximum packing depends on the size distribution and particle shape but not on particle size.

The model developed by Irvin Krieger and Thomas Dougherty [53] considers a different exponent:

$$\eta_r = \left(1 - \frac{\phi}{\phi_m}\right)^{-\eta_1 \phi_m}, \tag{1.20}$$

where η_1 is an intrinsic viscosity dependent on the particle shape, that takes the value of 2.5 for spheres. If the suspension show non-Newtonian behaviour (see Subsection 1.3.1), the predictive models of the suspension viscosity should include a shear-rate dependent term. If not included in the model, the viscosity could be estimated only in tight regions (low or high shear rate Newtonian regions).

1.4. Tribology

1.4.1. Generalities

Tribology is defined as the science that deals with the design, friction, wear, and lubrication of interacting surfaces in relative motion. This word also derives from the Greek and the literal translation would be the "science of rubbing". The term tribology was coined by Hans Peter Jost**,** who in 1966 published a landmark report on the costs of friction, wear and corrosion to the UK economy, titled "*Lubrication (Tribology), Education and Research: A Report on the Present Position and Industry's Needs*" [54]. In fact, the analysis of tribo-

logical behaviour in technical equipment tackles remarkable economic problems, ranging from spacecraft to household applications. In this sense, the successful in machine elements design (and durability), and the minimization of losses (i.e., energy efficiency) from friction and wear greatly depends on the understanding of tribological principles. However, tribology not only affects industrial applications but also our daily life, like in the process of writing (pencil/paper contact), walking (shoes/ground contact) or in many joints in the human body.

The relative motion between two surfaces entails the appearance of dissipative phenomena that produces heat and resists to this movement, i.e., friction. Indeed, the origin of friction comes from the deformation of the contacting surface roughness or asperities, as a consequence of the relative movement and the load. Two types of friction are distinguished: static friction occurring between quiet surfaces in contact and dynamic friction which concerns the resistance to relative motion between the surfaces after the movement starts. This distinction was made by Coulomb, and each type of friction can be quantified with dimensionless parameters called static μ and dynamic k friction coefficients. They are given by the ratio of the frictional force F to the applied load W.

Observations of the physicist Guillaume Amontons (1699) and years later by Charles-Augustin Coulomb (1785) resulted in three laws governing friction:

- First law (Amontons): the friction force is directly proportional to the normal load, so that $F = \mu W$.
- Second law (Amontons): the friction force is independent of the apparent area of contact.
- Third law (Coulomb): the dynamic friction is independent of velocity once motion starts.

Wear is the progressive removal of material from a surface in relative motion with other surface or with a fluid. It plays a fundamental role in tribology as it causes damage or changes in the shape of the components. These changes are comparable to elastic deformation and have to be considered in the distribution of stresses or in the dimensions of contacting areas. However, wear is not always seen as an unwanted consequence of friction since it is often used to reduce the roughness or eliminate asperities in some materials. There are distinct types of wear such as adhesive, abrasive, fatigue, or corro-

sive wear. Contrarily to what could be thought a larger friction may not entail a larger wear. The true is that the relationship between these phenomena is not necessarily proportional but rather the frictional energy distribution varies in different tribosystems.

In order to control friction and wear a proper lubrication between the components is required and with this purpose some materials, coatings or surface treatments are used. In this sense, lubricants are materials (liquids, solids or gases) characterized by their viscosity that contributes to reduce friction between surfaces, as they avoid the direct contact between surfaces and thus restrict the wear.

The lubrication behaviour is measured with a tribometer and can be understood with the Stribeck curve. It is a plot that relates the coefficient of friction and a parameter that combines the fluid viscosity, the relative speed of surface movement and the applied load. The unit of this combined parameter has unit of a length and is somehow seen as the lubricant film thickness between the surfaces in movement. Stribeck curve tipically contains three lubrication regimes as can be observed in Figure 1.5. The lubrication conditions are affected by the applied load, speed, and properties of the fluid lubricant and the contacting surfaces:

- At small relative motion between surfaces the lubricant hardly enters the contact, so that the separation is small, the surface asperities are in direct contact and they are the main responsible for supporting the applied load. This is called boundary lubrication regime and reflects a scenario where the friction force is highly related to the surface roughness. This region is characterized by a high value of the friction coefficient, which is governed by the physicochemical properties of both the fluid film and surfaces.
- A higher lubricant entrainment is induced at moderate speeds, where the surface separation increases. This produces a decreasing trend in friction coefficient with increasing the speed in the Stribeck curve. This regime, known as mixed lubrication regime, is driven by the bulk properties of the lubricant and the surface topography, where only large asperities contribute to friction.
- The last part in the Stribeck curve is the hydrodynamic lubrication or full-film regime. Higher entrainment speeds permit the lubricant fully enters the contact and this thick film completely separates the solid surfaces. In this regime, the load is fully supported by the lubricant so

that the friction between surfaces is mainly determined by the lubricant's bulk properties, such as viscosity and structure. When the shape of the surfaces and the thickness of the lubricating film are considerably modified due to significant elastic deformation of the surfaces, this lubrication regime is called elastohydrodynamic (EHL) lubrication. This mode of hydrodynamic lubrication is usually employed in non-conformal contacts.

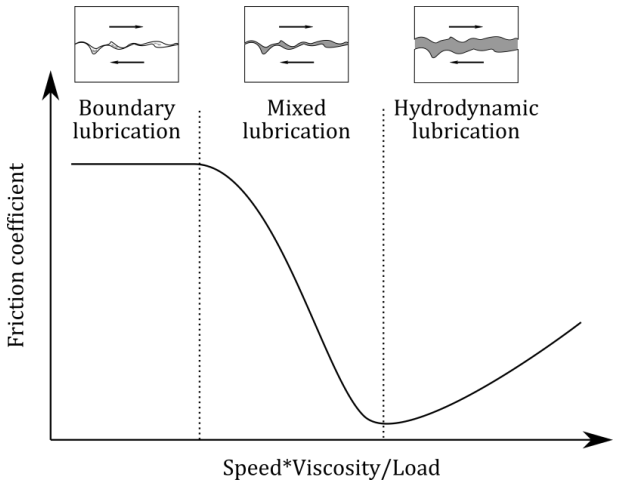

Figure 1.5: Schematic of Stribeck curve.

According to the geometric conformity between surfaces we can distinguish between conformal and non-conformal surfaces, which characterize hydrodynamic lubrication and elastohydrodynamic lubrication, respectively. In the former case the load is supported by a relatively large area due to a tight fit. However, non-conformal surfaces poorly conform so that they present small lubrication areas. On the contrary to compliant surfaces, where the area practically remains constant with increasing the load, in non-conformal surfaces the initial small area enlarges with the load.

Moreover, four types of fluid lubrication can occur in non-conformal conjunctions, depending on two effects: the elastic deformation of the solid subjected to the applied load and the contact pressure with the subsequent change in fluid viscosity:

- Isoviscous-rigid: both the elastic deformation and the contact pressure are insignificant to cause an appreciable increase in fluid viscosity.

- Piezoviscous-rigid: the pressure within the conjuction is quite high and affects the fluid viscosity, while the elastic deformation can be neglected.
- Isoviscous-elastic (Soft EHL): the contact pressure is low so that its effect on the viscosity throughout the conjunction, and the elastic deformation of solids is high compared to the film thickness.
- Piezoviscous-elastic (Hard EHL): In this regime both the elastic deformation and the variation of viscosity with the pressure must be taken into account.

Symbol	Meaning
a, b	Elements involved in the contact
a_H, b_H	Hertzian contact radius in x and y direction, m
D_x, D_y	Minor (direction of entraining motion) and major (transverse direction) axes of the elliptical contact
E	Elastic modulus, Pa
E'	Effective modulus of elasticity, $2\left(\frac{1-\nu_a^2}{E_a}+\frac{1-\nu_b^2}{E_b}\right)$, Pa
G	Dimensionless material parameter, $\xi E'$
g_E	Dimensional elasticity parameter, $W^{8/3}/U^2$
g_V	Dimensionless viscosity parameter, GW^3/U^2
$\widehat{H}$	Dimensionless film thickness parameter, $H_e(W/U)^2$
H_e	Dimensionless film thickness for elliptical contacts, h/R_x
k	Ellipticity parameter, D_y/D_x
R_x	Effective radius in x direction, $\left(\frac{1}{r_{ax}}+\frac{1}{r_{bx}}\right)^{-1}$, m
U	Dimensionless speed parameter, $\eta_0 u_m/E'R_x$
u_m	Mean surface velocity in x direction, $u_m=(u_a+u_b)/2$, m/s
W	Dimensionless load parameter $w_z'/E'R_x$
w_z'	Normal load per unit width, N/m
η_0	Absolute viscosity at p =0 and constant temperature, Pa·s
ν	Poisson's ratio
ξ	Pressure-viscosity coefficient, m^2/N

Table 1.2: Notation used in elastohydrodynamic regime equations in accordance with nomenclature appearing in *Fundamentals of fluid film lubrication*[55].

These lubrication regimes can be mapped [55] as a function of a dimensionless viscosity g_V and elasticity parameters g_E [56]. The notation is given in Table 1.2.

In compliant contacts both rolling and sliding frictions have to be taken into account, while in non-conformal ones, rolling friction can be neglected in comparison with sliding friction. The ratio between sliding speed (the relative velocity difference between the contacting surfaces) and entraining speeds (the mean of rolling speeds of two surfaces relative to the contact) is expressed by the slide-to-roll ratio S, which will be further developed. In this sense, in pure rolling conditions $S = 0$.

When two elastic bodies approach, a contact area appears whose form depends on the type of surfaces and the applied load involved in the contact. Among them, point (sphere-sphere) and line contacts (cylinder-plane) are the most commonly encountered. However, elliptical contacts [57] cover a wider range of deformations occurring in practice, according to the radius ratio, from the circular point contact to near line contact

1.4.2. Reynolds equation

In fluid film lubrication problems the predominant terms of Navier-Stokes equations belong to pressure and viscous terms so that they are indeed slow viscous motion problems. The pressure distribution in fluid film lubrication, assumed to behave as a Newtonian fluid, was determined by a differential equation derived from the Navier-Stokes equations by Osborne Reynolds in 1886 [58]. In its general form it becomes:

$$\frac{\partial}{\partial x}\left(\frac{\rho h^3}{12\eta}\frac{\partial p}{\partial x}\right)+\frac{\partial}{\partial y}\left(\frac{\rho h^3}{12\eta}\frac{\partial p}{\partial y}\right)= \\ =\frac{u_a+u_b}{2}\frac{\partial}{\partial x}(\rho h)+\frac{v_a+v_b}{2}\frac{\partial}{\partial y}(\rho h)+ \\ +\rho(w_a-w_b)-\rho u_a\frac{\partial h}{\partial x}-\rho v_a\frac{\partial h}{\partial y}+\frac{\partial}{\partial t}(\rho h)\,, \tag{1.21}$$

where p, h, ρ, and η are the pressure, film thickness, density and viscosity of the lubricant, and u_i, v_i, and w_i denote the components of the velocity surfaces of an i-body in x, y and z directions, respectively.

The Reynolds equation cover four terms, whose physical meaning [55] are exposed below:

- Poiseuille terms, in the left side of the equation, describe the net flow rates due to pressure gradients within the lubricated area.

- Couette terms, the first and second terms in the right side, accounts for the net entraining flow rates due to surfaces velocities. Each Couette term, in turn, leads to three actions: density wedge, stretch and physical wedge.
- Squeeze terms, from the third to the fifth term in the right side, describe the net flow rates due to a squeezing motion.
- Local expansion term, the time partial derivative, describes the net flow rate due to local expansion.

1.4.3. Film thickness

The film thickness describes the separation of the surfaces and the lubricant film protection from wear and high friction. The minimum and central film thickness relies on the speed and load conditions, the lubricant and material properties, and the geometry. An accurate determination of the film thickness requires full numerical solutions of pressure, viscosity and deformation equations. The Hertz theory [59] provides an acceptable approximation of the pressure distribution and film thickness. This theory predicts an ellipsoidal pressure distribution $p(x, y)$ for a dry elastic point contact, in the form:

$$p(x,y) = p_H \left[1 - \left(\frac{x}{R_x}\right)^2 - \left(\frac{y}{R_y}\right)^2\right]^{1/2}, \qquad (1.22)$$

where $p_H = \frac{3w_z}{2\pi a_H b_H}$ is the maximum Hertzian pressure, and D_x and D_y are the diameters of the ellipsoidal contact in x and y direction, respectively, as can be seen in the Figure 1.6.

In elastohydrodynamic regime the pressure distribution across the contact leads to the deformation of the surfaces in the contact. The general form of the pressure distribution and the developed film thickness profile are shown in Figure 1.7. In the inlet zone the lubricant is entrained into the contact and a film thickness is formed, which maintain an almost constant film thickness within the central region. It can be seen that in the elastohydrodynamic lubricated case the pressure profile in the contact region is near the Hertzian parabolic profile, but slightly deformed near the outflow, where a pressure spike appears. The rise in pressure provokes such an increase in the flow rate that the film thickness must be diminished. This minimum in the film thickness usually occurs slightly shifted toward the outlet, with respect to the pressure spike in elastohydrodynamic lubrication.

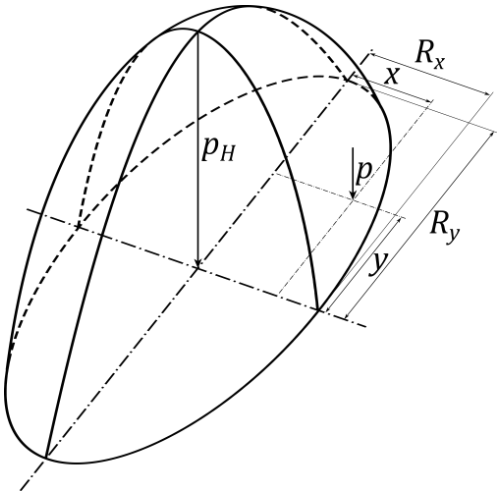

Figure 1.6: Pressure distribution in an ellipsoidal contact. The maximum pressure p_H occurs at the center of the contact and $p(x, y)$ approaches zero in the ellipsoidal perimeter, following Equation 1.22.

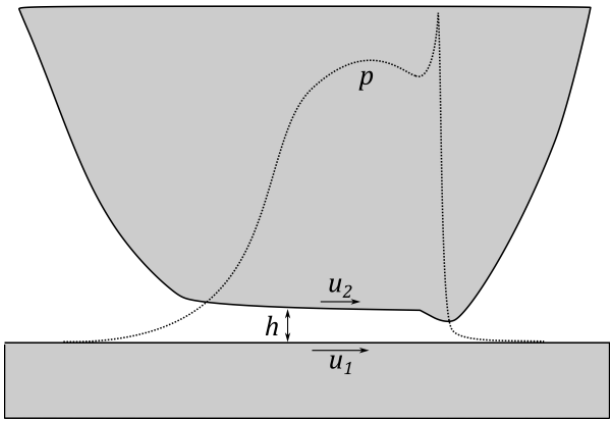

Figure 1.7: Typical elastohydrodynamic pressure and film thickness profile.

The film thickness equation valid for this regime is based in the Hertzian parabolic expression but also consider a term related to the elastic deformation $\delta(x, y)$ of the interacting surfaces, caused by the high pressure in the contact. In the case of point contact the expression for film thickness may be written as:

$$h(x,y) = h_0 + \frac{x^2}{2R_x} + \frac{y^2}{2R_y} + \frac{2}{\pi E'} \iint \frac{p(x',y')\,dx'dy'}{\sqrt{(x-x')^2 + (y-y')^2}}. \qquad (1.23)$$

A general expression for the dimensionless film thickness parameter $\widehat{H}$ appears below. The dimensionless central and minimum film thicknesses vary for different film lubrication regions, and this set of film thickness equations are based on two dimensionless parameter, U and W:

$$\widehat{H} = H_e \left(\frac{W}{U}\right)^2 . \tag{1.24}$$

The applied load must be balanced with the pressure generated in the fluid film. In this sense, the integral of the pressure distribution over the contact area must fit the value of the load:

$$w_z = \iint p(x,y)dxdy . \tag{1.25}$$

Although most lubricants are Newtonian others may present Non-Newtonian behaviour. They exhibit a nonlinear relationship between shear stress and shear rate, so that the expression of viscosity that has to be inserted in Reynolds equation becomes more complex. For example, the shear-thinning behaviour of polymer melts is accurately predicted with the Carreau-Yasuda model, where the fit at both low and high shear rates is better than with the power-law model. Carreau-Yasuda model predicts two Newtonian plateaus at low and high shear rates, and the transition between these states can be adjusted through variations in its parameters. In this sense this model would not be only restricted to shear thinning fluids, and could be applicable to shear-thickening fluids if the Newtonian plateau at low shear rates is lower than that at high shear rates, as it will be shown in Chapters 6 and 7.

Thus, in the elastohydrodynamic regime the change in the lubrication viscosity of a non-Newtonian fluid comes from its nonlinear behaviour but also from the effect of the high hydrodynamic pressure in non-conformal contacts, which also influences the elastic deformation of surfaces.

In this thesis predictions of the pressure distribution, film thickness and friction coefficient for non-Newtonian fluids are tackled with numerical modelling methods. The governing equations are first written in their nondimensional forms, and secondly discretized at each pressure point. The numerical solution for pressure and film thickness is then obtained after selecting an appropriate numerical method.

1.5. Simulation methods for colloidal suspensions

Numerical simulation is a powerful tool that allows for the modelling of processes in very distinct scientific areas. The development in computers' efficiency and computational methods offer the chance of replicating experiments and explore other scenarios by easily tuning the system features, thus saving time and money. The computational costs (in terms of simulation time) rely on the required level of detail and accuracy in the results. In this sense, approaches usually provide acceptable results that complement theory and experimental observations, even if some interaction in the system has been simplified or directly neglected. Although simulations are limited by computational requirements they enable the prediction of macroscopic information of the system such as the effective viscosity or the temporal evolution in the microstructure.

Of particular interest in this thesis is the motion of particles suspended in a fluid, their effect on the flow field and the resultant macroscopic behaviour. Suspension dynamics can be properly addressed with molecular simulations, which can be divided into four main categories [60]: Monte Carlo [61], Molecular Dynamics [62], Stokesian Dynamics [63] and Brownian Dynamics methods [64,65]. Monte Carlo simulations analyse the energy of microscopic states (particle configurations) randomly generated with a frequency proportional to the equilibrium probability distribution. This is a non-deterministic method that is used to simulate physical phenomena for systems in thermodynamic equilibrium. Molecular dynamics methods provide the temporal evolution of the particle position and velocity by solving Newton's motion equations. They are deterministic and applicable to dilute systems as hydrodynamic interactions among particles are neglected and so Brownian motion. Stokesian dynamics by its part tackle the suspension dynamics in non-dilute systems, where multi-body hydrodynamic interactions are relevant, while Brownian motion is not taken into account. Finally, Brownian dynamics methods consider Brownian motion through a random and stochastic force. Molecules of the carrier fluid are generally much smaller than Brownian particles in dispersions, so that these particles are regarded as a continuum in Brownian dynamics. They are based on the Langevin equation for the motion of particles in dilute dispersions, while other more complex Brownian dynamic methods are employed when hydrodynamic interactions between particles are taken into account (case of non-dilute systems).

In Section 3.3 a detailed description of simulations employed throughout this thesis is addressed. The rheological behaviour of suspensions of mixtures of particles as well as squeeze simulations under constant-volume and constant-area conditions will be studied through particle-level simulations. On the other hand, the solution of the fluid film lubrication of non-Newtonian fluids in elastohydrodynamic lubrication regime is tackled numerically.

1.6. References

[1] Vitelli V and Hecke M van 2011 Marginal matters *Nature* **480** 325–326

[2] Hołyst R 2005 Some features of soft matter systems *Soft Matter* **1** 329

[3] van der Gucht J 2018 Grand challenges in soft matter physics *Front. Phys.* **6**

[4] Nagel S R 2017 Experimental soft-matter science *Rev. Mod. Phys.* **89**

[5] Gennes P-G de and Badoz J 1997 Fragile objects: soft matter, hard science, and the thrill of discovery *Choice Rev. Online* **34** 34–3369–34–3369

[6] Babick F 2016 *Suspensions of colloidal particles and aggregates* (Springer International Publishing)

[7] Bajpai P 2018 Colloid and surface chemistry *Biermann's Handbook of Pulp and Paper* (Elsevier) pp 381–400

[8] Derjaguin B V and Landau L 1941 Theory of the stability of strongly charged lyophobic sols and of the adhesion of strongly charged particles in solutions of electrolytes *Acta Physicochim. URSS* **14** 633–622

[9] Verwey E J W and Overbeek J T G 1948 *Theory of the stability of lyophobic colloids* (Amsterdam: Elsevier)

[10] Derjaguin B V, Churaev N V and Muller V M 1987 The Derjaguin—Landau—Verwey—Overbeek (DLVO) Theory of Stability of Lyophobic Colloids *Surface Forces* (Boston, MA: Springer US) pp 293–310

[11] Israelachvili J N 2011 *Intermolecular and surface forces* (San Diego: Academic Press)

[12] Rankin P J, Ginder J M and Klingenberg D J 1998 Electro- and magneto-rheology *Curr. Opin. Colloid Interface Sci.* **3** 373–381

[13] Rabinow J 1948 The magnetic fluid clutch *Trans. Am. Inst. Electr. Eng.* **67** 1308–1315

[14] Winslow W M 1949 Induced fibration of suspensions *J. Appl. Phys.* **20** 1137–40

[15] Ginder J 2003 Rheology controlled by magnetic fields *Digit. Encycl. Appl. Phys.*

[16] Odenbach S 2002 *Ferrofluids* vol 594 (Berlin, Heidelberg: Springer Berlin Heidelberg)

[17] Bossis G, Volkova O, Lacis S and Meunier A 2002 Magnetorheology: fluids, structures and rheology *Ferrofluids* (Springer Berlin Heidelberg) pp 202–230

[18] Park B J, Fang F F and Choi H J 2010 Magnetorheology: materials and application *Soft Matter* **6** 5246

[19] Ramos J, Klingenberg D J, Hidalgo-Álvarez R and Vicente J de 2011 Steady shear magnetorheology of inverse ferrofluids *J. Rheol.* **55** 127–152

[20] Ramos J, Vicente J de and Hidalgo-Álvarez R 2010 Small-amplitude oscillatory shear magnetorheology of inverse ferrofluids *Langmuir* **26** 9334–9341

[21] Salomon Stephen Papell 1965 Low viscosity magnetic fluid obtained by the colloidal suspension of magnetic particles

[22] Rosensweig R E 1997 *Ferrohydrodynamics* (Mineola, N.Y: Dover Publications)

[23] Klingenberg D J 2001 Magnetorheology: Applications and challenges *AIChE J.* **47** 246–249

[24] Boyer F, Guazzelli É and Pouliquen O 2011 Unifying suspension and granular rheology *Phys. Rev. Lett.* **107**

[25] Barnes H A 1989 Shear-thickening ("Dilatancy") in suspensions of nonaggregating solid particles dispersed in Newtonian liquids *J. Rheol.* **33** 329–366

[26] Brown E, Forman N A, Orellana C S, Zhang H, Maynor B W, Betts D E, DeSimone J M and Jaeger H M 2010 Generality of shear thickening in dense suspensions *Nat. Mater.* **9** 220–224

[27] Brown E and Jaeger H M 2014 Shear thickening in concentrated suspensions: phenomenology, mechanisms and relations to jamming *Rep. Prog. Phys.* **77** 046602

[28] Galindo-Rosales F J, Rubio-Hernández F J and Sevilla A 2011 An apparent viscosity function for shear thickening fluids *J. Non-Newton. Fluid Mech.* **166** 321–325

[29] Seto R, Mari R, Morris J F and Denn M M 2013 Discontinuous shear thickening of frictional hard-sphere suspensions *Phys. Rev. Lett.* **111**

[30] Gurnon A K and Wagner N J 2015 Microstructure and rheology relationships for shear thickening colloidal dispersions *J. Fluid Mech.* **769** 242–276

[31] Gopalakrishnan V and Zukoski C F 2004 Effect of attractions on shear thickening in dense suspensions *J. Rheol.* **48** 1321–1344

[32] Lee Y S, Wetzel E D and Wagner N J 2003 The ballistic impact characteristics of Kevlar® woven fabrics impregnated with a colloidal shear thickening fluid *J. Mater. Sci.* **38** 2825–2833

[33] Dawson M A, McKinley G H and Gibson L J 2009 The dynamic compressive response of an open-cell foam impregnated with a non-Newtonian fluid *J. Appl. Mech.* **76** 061011

[34] Tan Z H, Zuo L, Li W H, Liu L S and Zhai P C 2016 Dynamic response of symmetrical and asymmetrical sandwich plates with shear thickening fluid core subjected to penetration loading *Mater. Des.* **94** 105–10

[35] Metzner A B and Whitlock M 1958 Flow behavior of concentrated (dilatant) suspensions *Trans. Soc. Rheol.* **2** 239–254

[36] Hoffman R L 1974 Discontinuous and dilatant viscosity behavior in concentrated suspensions. II. Theory and experimental tests *J. Colloid Interface Sci.* **46** 491–506

[37] Hoffman R L 1982 Discontinuous and dilatant viscosity behavior in concentrated suspensions III. Necessary conditions for their occurrence in viscometric flows *Adv. Colloid Interface Sci.* **17** 161–184

[38] Brady J F and Bossis G 1985 The rheology of concentrated suspensions of spheres in simple shear flow by numerical simulation *J. Fluid Mech.* **155** 105

[39] Fernandez N, Mani R, Rinaldi D, Kadau D, Mosquet M, Lombois-Burger H, Cayer-Barrioz J, Herrmann H J, Spencer N D and Isa L 2013 Microscopic mechanism for shear thickening of non-Brownian suspensions *Phys. Rev. Lett.* **111**

[40] Merkt F S, Deegan R D, Goldman D I, Rericha E C and Swinney H L 2004 Persistent holes in a fluid *Phys. Rev. Lett.* **92**

[41] Waitukaitis S R and Jaeger H M 2012 Impact-activated solidification of dense suspensions via dynamic jamming fronts *Nature* **487** 205–209

[42] Fall A, Bertrand F, Hautemayou D, Mezière C, Moucheront P, Lemaître A and Ovarlez G 2015 Macroscopic discontinuous shear thickening versus local shear jamming in cornstarch *Phys. Rev. Lett.* **114**

[43] Gálvez L O, Beer S de, Meer D van der and Pons A 2017 Dramatic effect of fluid chemistry on cornstarch suspensions: Linking particle interactions to macroscopic rheology *Phys. Rev. E* **95**

[44]Jiles D 1991 *Introduction to Magnetism and Magnetic Materials* (Boston, MA: Springer US)

[45] Reiner M 1964 The Deborah Number *Phys. Today* **17** 62–62

[46] Bird R B, Armstrong R C and Hassager O 1987 *Dynamics of polymeric liquids. Volume 1: Fluid mechanics*

[47] Morrison F 2001 *Understanding rheology* (New York: Oxford University Press)

[48] Steffe J F 1996 *Rheological methods in food process engineering* (East Lansing, MI: Freeman Press)

[49] Einstein A 1905 Über die von der molekularkinetischen. Theorie der Wärme geforderte Bewegung von in ruhenden Flüssigkeiten suspendierten Teilchen. *Ann. Phys.* **322** 549–560

[50] Oliver D R and Ward S G 1954 The Einstein relation between relative viscosity and volume concentration of suspensions of spheres *Nature* **173** 1090–1090

[51] Batchelor G K 1977 The effect of Brownian motion on the bulk stress in a suspension of spherical particles *J. Fluid Mech.* **83** 97–117

[52] Quemada D 1977 Rheology of concentrated disperse systems and minimum energy dissipation principle *Rheol. Acta* **16** 82–94

[53] Krieger I M and Dougherty T J 1959 A mechanism for non-Newtonian flow in suspensions of rigid spheres *Trans. Soc. Rheol.* **3** 137–152

[54] Jost H P 1966 *Lubrication (Tribology) - A report on the present position and industry's needs* (London, UK: Department of Education and Science, H. M Stationary Office)

[55] Hamrock B, Schmid S and Jacobson B 2004 *Fundamentals of fluid film lubrication* (CRC Press)

[56] Johnson K L 1970 Regimes of elastohydrodynamic lubrication *J. Mech. Eng. Sci.* **12** 9–16

[57] Hamrock B J and Brewe D 1983 Simplified solution for stresses and deformations *J. Lubr. Technol.* **105** 171

[58] Reynolds O 1886 On the theory of lubrication and its application to Mr. Beauchamp Tower's experiments, including an experimental determination of the viscosity of olive oil *Philos. Trans. R. Soc. Lond.* **177** 157–234

[59] Heinrich Hertz 1881 Ueber die Berührung fester elastischer Körper. *J. Für Reine Angew. Math. Crelles J.* 156–71

[60] Satoh A 2003 *Introduction to molecular-microsimulation of colloidal dispersions* (Amsterdam ; Boston: Elsevier)

[61] Metropolis N and Ulam S 1949 The Monte Carlo method *J. Am. Stat. Assoc.* **44** 335–41

[62] Alder B J and Wainwright T E 1959 Studies in molecular dynamics. I. General method *J. Chem. Phys.* **31** 459–66

[63] Brady J F and Bossis G 1988 Stokesian dynamics *Annu. Rev. Fluid Mech.* **20** 111–157

[64] Deutch J M and Oppenheim I 1971 Molecular theory of Brownian motion for several particles *J. Chem. Phys.* **54** 3547–55

[65] Ermak D L and McCammon J A 1978 Brownian dynamics with hydrodynamic interactions *J. Chem. Phys.* **69** 1352–60

2. Justification

Colloidal systems have a great importance in our daily life. They are present in foodstuffs as milk, in personal care products as toothpaste, in paints, foams or fog, for example. These systems are basically constituted by a particulate phase that is dispersed in a continuous phase. The rheological behaviour of these systems, i.e., their ease to flow upon certain shear stress, is not only dependent on the way the stress is applied, but also on the physical and chemical features of the components of the colloidal system (the disperse phase and the dispersion medium).

In this sense, a colloidal system may display a Newtonian behaviour, may flow from a given yield stress onwards, or exhibit shear-thinning or shear-thickening phenomena, depending on the shear rate or stress the fluid is subjected to or on the time during which they are applied (in the case of time-dependent fluids). Their rheological performance is described successfully in model systems, but most suspensions present a combination of these behaviours, and their theoretical analysis is much more complex.

The increase in the viscosity of a system subjected to stress is a fascinating and counter-intuitive phenomenon. Far from what it could be thought, we can have this behaviour at home, in a rapid and cheap way, if we prepare a concentrated suspension of cornstarch in water. Starch is one of the most

abundant, easy to obtain and thus cheap, natural polymers. It is so simple, and, at the same time, so complex.

Apart from this model suspension, the shear-thickening behaviour can be found in other combinations of particles and dispersing mediums. In fact, "*under the right circumstances, all suspensions of solid particles will show the phenomenon*", according to H. A. Barnes (1989). With right circumstances, we refer, for instance, to the level of attraction between particles suspended in a given fluid, roughness, concentration, shear rate range in which the system is observed or the time of observation, among others. Keeping in mind these aspects it is possible to tune and control the rheological response of these complex fluids to our liking, thus offering new opportunities to the progress in colloidal science.

Moreover, in systems with high particle concentration, the role of lubrication and friction is essential. Hence, a thorough insight of this behaviour requires both the understanding of the macroscopic bulk rheology and the close linking with the tribological properties of dense suspensions.

On the other hand, other type of complex fluids which is receiving a great interest are field-responsive materials, as their properties can be controlled in presence of an external field. Within this category we focus on magnetorheological (MR) fluids, which are characterized by a reversible and quick transition from liquid-like to solid-like state at high magnetic fields, due to the anisotropic particle structuration in the field direction that provokes a strong increase in the apparent viscosity. At sufficiently large values of field strength and particle concentration, a stress threshold may be required for the suspension to flow, known as yield stress.

It is desired in commercial applications of MR fluids a remarkable response to the field, i.e., a strong MR effect with a high yield stress. Furthermore, in order to reduce the cost and weight of the device, if the required particle concentration for reaching a given value of yield stress is lower, so much the better. Besides, the operational mode also affects the fluid performance. In this sense the study of the rheological properties of MR fluids under compression is a topic of current interest in the field, as higher yield stresses in MR fluids under field have been found when they are subjected to slow compression prior to imposing a shear flow mode. This reinforcement in comparison with the shearing without previous compression for a given particle concentration is the so-called squeeze-strengthening effect.

2.1. Objectives

The former considerations prompted us to study the rheological and tribological behaviour of concentrated suspensions of very different nature, as well as the rheological performance of diluted MR fluids under constant-volume and constant-area compression. These three matters are carried out by means of experiments and simulations. In more detail, the main goals of this thesis may be summarized as follows:

- Evaluate the effect of particle and suspending medium features in the rheological response of unimodal and bimodal concentrated suspensions displaying shear thickening, as well as flow conditions or external field.
- Understand the main forces involved in the motion of particles suspended in a Newtonian fluid when subjected to both absence and presence of flow and magnetic field.
- Incorporate local field theory and hydrodynamic lubrication in particle-level simulations, in order to develop a rigorous simulation code that faithfully may reproduce experimental results in mixtures of magnetic and non-magnetic particles.
- Study the thin film and frictional properties of inelastic non-Newtonian fluids in the elastohydrodynamic lubrication regime by means of numerical simulations, and intend to provide a master curve where film thickness and friction coefficient of these fluids collapse.
- Investigate the influence of the concentration of particles, polarity and carrier viscosity in the tribological response of cornstarch-based shear-thickening suspensions.
- Check the tribological simulation results by comparison with experiments of model shear-thinning and shear-thickening suspensions.
- Study, in terms of micromechanical models, the rheological behaviour of diluted MR fluids in squeeze flow and in presence of a magnetic field, as a function of compressive deformations, initial gap and carrier fluid.

- Compare constant-volume and constant-area conditions, and determine the significance of the densification effect occurring during constant-area experiments regarding the yield stress.
- Perform particle-level simulations in both squeeze conditions and compare the tendencies with experiments.

2.2. Outline of the thesis

This thesis is structured in three parts. As approach, the first one is devoted to the rheology of dense suspensions, the second one to the tribological behaviour of inelastic non-Newtonian fluids, and the last part corresponds to the rheology of diluted MR fluids under squeeze flow.

2.2.1. Rheology in dense suspensions

This contents block, composed of **Chapter 4** and **Chapter 5**, is intended for the rheological characterization of non-Brownian concentrated suspensions.

Chapter 4 is dedicated to dense unimodal suspensions, i.e., those in which only one type of particle constitutes the particulate phase of the system. The starting point was the investigation of model shear-thickening suspensions based on cornstarch and fumed silica in steady shear flow conditions. We identified critical parameters from shear viscosity in the shear-thickening region and also from normal stress generated as a consequence of the shear-induced anisotropy and dilation. Then, we investigated this non-Newtonian behaviour in field responsive fluids by exploring the effect of suspending fluid, magnetic field and, in general, attractions in the appearance of shear thickening.

The two-way response of the previous magnetorheological fluids displaying shear-thickening behaviour under certain conditions awakened our interest and encouraged us to formulate other types of hybrid suspensions. These bimodal systems could open the possibility of controlling their rheological behaviour, well passively, by doing changes in the formulation, or actively, by regulating the magnetic field. In **Chapter 5** we addressed the study of dense bimodal suspensions, where both magnetic and non-magnetic particles are part of the dispersed phase. Two routes of preparing these hybrid suspensions were followed. On the one hand, we prepared suspensions of mixtures of particles, and determined the effect of the addition of magnetic particles and the field intensity in the shear-thickening response at high shear rates.

On the other hand, several methods were employed to coat carbonyl iron particles with starch. These core-shell particles were used in the formulation of the second type of hybrid suspension, and were rheologically characterized. Finally, we performed particle-level simulations on mixtures of monodisperse and polydisperse particles with distinct magnetic response, and analysed the effect of the partial substitution of magnetic particles by non-magnetic ones in the yield stress of the systems.

2.2.2. Tribology in inelastic non-Newtonian fluids

Recent progress in the understanding of the counter-intuitive shear-thickening phenomenon highlights the critical role of friction in dense systems, where particles are very near to others, mainly in the development of discontinuous shear thickening. It is in close contact conditions where the fields of rheology and tribology are connected, as the local friction determines the microstructure that give rise to certain rheological response. This part, that comprises **Chapter 6** and **Chapter 7,** accounts for experiments and numerical simulations of non-Newtonian fluids, both shear-thinning and shear thickening, in the elastohydrodynamic regime.

Chapter 6 is dedicated to the development of numerical simulations that could reproduce the pressure distribution, film thickness and frictional properties of flow-dependent systems in the isoviscous elastohydrodynamic lubrication regime. In this sense, in the so-called full solution approach, regression formulas for friction coefficient and film thickness are provided for both shear-thinning and shear-thickening fluids. Moreover, an effective lubricant viscosity is also defined and a master curve is proposed and tested with some experimental tribological results of these kinds of fluids.

Chapter 7, with an eminently experimental nature, tackles the rheological and tribological characterization of starch-based concentrated suspensions. In particular, the effect of particle concentration, type of suspending fluid and its wettability in relation with the tribopairs' material was analysed in the three parts of Stribeck curves. Finally, experimental results in the isoviscous elastohydrodynamic regime were compared to numerical simulations developed in the previous chapter.

2.2.3. Rheology of diluted MR fluids under squeeze flow

The last chapter of results is **Chapter 8**, focused on the squeeze-strengthening effect of diluted MR fluids. The slow compression was carried out in constant-volume and constant-area experiments, and measurements of normal force acting on the plate surface as a function of compressive strains are compared with a micromechanical model. We identified yield stresses within the shearing step for both cases and analysed the effect of the densification in constant-area measurements, as a consequence of the retention of particles between the parallel plates due to the presence of magnetic field during the compression. Regarding constant-volume measurements, the influence of the continuum medium and the field gradient is evaluated. Finally, particle-level simulations for both types of squeeze are carried out in an attempt to compare them with the experimental findings on normal and yield stress.

3. Methodology

3.1. Materials

3.1.1. Starch

Starch is the major energy store in plants, mainly found in stems, roots or tubers. It is the most important carbohydrate in human diet and can be found in different foodstuff such as potato, corn, wheat, rice and other cereals. Its main applications reside in food industry due to its nutritional value, its use as thickener, stabiliser, additive to improve food textures, and as a raw material for other products. For instance, sugars as glucose syrup, dextrose, fructose or caramel are produced from the starch industry. However starches are also employed in the production of paper, in pharmaceutical products as filler or in coatings, in construction industry, as well as in textile finishing and sizing, among others. Starch is thus a versatile product and, together with their numerous by-products, their use and utility are widely expanded around the world.

This natural polymer basically consists in a mixture of two polysaccharides, amylose and amylopectin, that arrange in semi-crystalline granular morphology. Amylose is a linear or slightly branched polysaccharide that usually represents between 15 and 30% [1,2] by weight in naturally occur-

ring starches, while amylopectin is an extensively branched molecule, much larger than amylose.

The basic building blocks in both molecules are α-D-glucose units as can be appreciated in Figure 3.1. Glucose units are joined in amylose by α-(1,4) glycosidic bonds that produce a natural right-handed helix, while in amylopectin both α-(1,4) and α-(1,6) bonds appear in linear and branched parts, respectively.

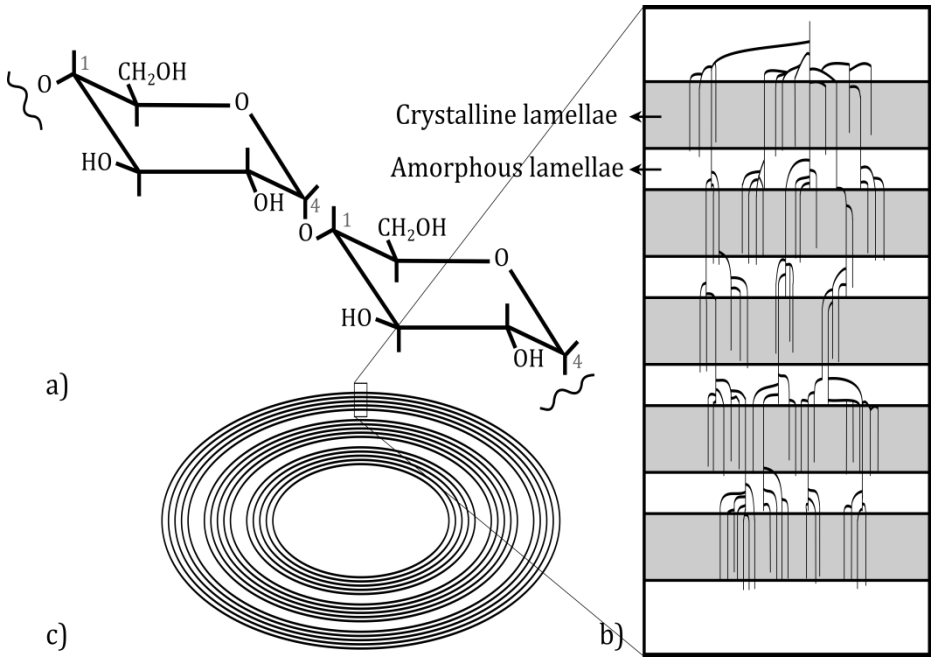

Figure 3.1: Different levels of structural organization in starch granules. a) Linkage between two glucose units through α-(1,4) glycosidic bond in amylose; b) Schematics of amylopectin molecular structure and arrangement of amorphous and crystalline regions, and c) Representation of growth rings in granule structure.

The vegetal source affects the polysaccharides proportion within the granule, its size and shape, and properties such as solubility or swelling capacity, among others [3].

Starch granules have diameters ranging from less than 1 μm to 100 μm possess long-range and short-range molecular order. The origin of growth of each granule is called hilum. This nucleus is surrounded by alternating semi-crystalline and amorphous rings. Amylopectin is assumed to form the crystalline phase while amylose is thought to be located in amorphous zones, though it remains unsure and depends on the type of starch.

The granule structure provides information on its swelling capacity. When granules are heated in excess of water, they expand their volume as a consequence of water absorption. This swelling process mainly takes place in the amorphous zones of the granule, so that a part of the amylose molecules is released into the medium increasing the viscosity. This irreversible loss in the granular/molecular order is called gelatinization, which is marked by the disappearance of birefringence and in native starches occurs at a range of temperature between 55 and 80 ˚C depending on the botanical source [1]. Moreover, if the sample is subjected to shear the swollen starch granules disintegrate forming a paste. When this paste is cooled retrogradation takes place, i.e., amylose molecules associate again and a three-dimensional network is formed.

Physically or chemically modified starches appeared in order to improve their native performance in diverse applications. Their functionalization enables for example a better stability or change the solubility in cold water. The first modified starches of which there is evidence were produced by Kirchoff in 1811 when performed the hydrolysis of potato starch with acid, transforming starch into a sweet substance [4]. An extensive description of modified starches can be found elsewhere [1,4].

Although most applications of starches involve their heating in presence of water, where the granular structure is destroyed, it is very conspicuous their behaviour in water at room temperature and at high concentrations. These concentrated suspensions are one common example of the counter-intuitive shear-thickening phenomenon, basically characterized by an increase in viscosity under shear stress or shear rate.

Cornstarch particles have been used along this thesis within several types of suspensions:

- Concentrated suspensions in water (Chapter 4): the study of the rheological behaviour is carried out in several geometries as well as the evolution of normal forces during the shear-thickening range.

- As part of the carrier fluid in the formulation of magnetorheological shear-thickening fluids (Chapter 5): the addition of starch particles to the MR fluid permits a considerable reduction in weight for a given volume fraction, and under the application of a magnetic field the appearance of the shear-thickening behaviour can be easily tuned.

- Cornstarch was also used as organic coating for carbonyl iron particles (Chapter 5). The effect of the coating in the rheological behaviour of suspensions formulated with these core-shell particles was studied.

- Suspensions in several carrier fluids (Chapters 6 and 7), to study their effect in the shear-thickening response and their tribological behaviour. In these sense, the physical and chemical interactions among particles and carrier fluid play an important role in the appearance or inhibition of the shear-thickening phenomenon.

3.1.2. Fumed silica

Fumed silica (FS) is a white powder with a very high fineness that is obtained through continuous flame hydrolysis [5,6]. In this synthesis process evaporated silicon tetrachloride $SiCl_4$ reacts with hydrogen H_2 and oxygen O_2 to be converted into amorphous silicon dioxide SiO_2, and the only by-product being hydrogen chloride HCl.

Silica, especially fumed silica, is well known for its ability to increase the viscosity of suspensions in organic media [7–10]. When this material is dispersed in the carrier fluid their silanol groups (Si-OH) interact with other silanol groups through hydrogen bonding, both directly and by means of the solvent molecules. It causes the formation of a three-dimensional network that upon certain conditions gives rise to the appearance of shear thickening.

This material was used in the formulation of ethylene glycol-based concentrated suspensions, and their rheological behaviour will be studied in Chapter 4 as complement to unimodal suspensions showing shear-thickening response under certain circumstances. Moreover, dispersions of FS were prepared as model shear-thickening fluids and tribologically characterized in Chapter 6.

3.1.3. Carbonyl iron

Carbonyl iron (CI) is produced by thermal decomposition of iron pentacarbonyl ($Fe(CO)_5$). The synthesis conditions employed during this process control the particle properties and so determine the type of powder grade. A broad spectrum of carbonyl iron grades are commercialized; they are characterized by a given particle size distribution, a particular coating or not, and different properties according to the requirements of each final application.

Throughout this thesis, several types of carbonyl iron were used, all of them brought from BASF. They are summarized in Table 3.1.

CI grade	d_{50} (μm)	Coating	Chapter
CC	3.8-5.3	No	4, 5
EW/EW-I	3.0-4.0	Yes	5
OM	3.9-5.2	No	5
HS	2.0	No	4
HQ	2.0	No	8

Table 3.1: Characteristics of several types of carbonyl iron grades used in next chapters.

Carbonyl iron is widely utilized as suspended particle in the formulation of MR fluids [11–13]. It is the preferred magnetic phase in these fluids for being a soft magnetic material with a high purity, and provides higher yield stresses. Its high saturation magnetization and low coercivity convert these micrometric particles in excellent candidates for MR suspensions.

Notwithstanding, its main drawback as component of MR fluids comes from its high density, which at the end leads to severe sedimentation and heavy MR devices. Several strategies may be followed in order to reduce the weight of the final device and improve their suspension stability [14], such as the use of viscoplastic fluids [15,16] or the coating of these magnetic particles with substances as polymer or inorganic materials [17,18]. The coating, apart from opening the possibility of functionalizing the particles, decreases the density mismatch with the carrier fluid, as it provides a shell with lower density compared to the magnetic core. Subsequently, the overall particle density is lower, but this improvement occurs at the expense of the net magnetic moment of each particle and so the system, due to the imposed steric separation between the magnetic bulks of the particles.

In Chapter 5 we used starch as coating for carbonyl iron particles and prepared suspensions of these hybrid particles in water. A thin layer was deposited onto the magnetic particle surface through several methods, and rheological experiments were performed and compared with other water-based suspensions at the same volume fraction, both in off-state and on-state magnetic field conditions.

As alternative to these hybrid particles in water-based suspensions, we proposed the formulation of magnetorheological fluids composed of both

magnetic and non-magnetic particles. The idea of this hybrid system is based on recent works [19–21] where it has been shown that the partial substitution of magnetic particles by non-magnetic ones results in an improved magnetic response, i.e., a higher yield stress for the same volume fraction compared to the unimodal case of a conventional MR fluid.

If these non-magnetic particles form part of the carrier fluid, its viscosity would be a function of the particle concentration. Moreover, a higher viscosity would inhibit particle sedimentation and magnetic aggregation in no-field conditions. In this manner, a required yield stress for a specific application could be obtained in a suspension with a lower concentration of carbonyl iron, with the subsequent reduction in weight and cost, and improved particle stability.

We selected starch as non-magnetic particle so that the carrier fluid may show shear-thickening response under adequate circumstances. In this sense, the addition of carbonyl iron particles to a shear-thickening suspension results in a fluid with both shear-thickening and magnetic characteristics. Thus, the appearance of shear-thickening behaviour will depend on the applied magnetic field, particle concentration, range of shear rates and the interactions between starch and the fluid. These types of suspensions are called magnetorheological shear-thickening (MRST) fluids.

3.1.4. Sample preparation

- **Starch suspensions**

In these experiments starch from corn (S4126, containing a 27% of amylose and a 73% of amylopectin) from Sigma Aldrich was used, and suspended at the required volume fractions in distinct carrier fluids, whose properties are shown in Table 3.2. Native starch granules have irregular faceted shape as can be observed onwards in the ESEM micrographs (see Subsection 3.2.3). The mean particle diameter was 10.7 μm.

Suspensions were prepared in plastic containers by weighting the required amount of cornstarch and carrier fluid. Then, both components were carefully and manually mixed with a spatula to ensure a homogeneous distribution of particles within the sample. This procedure was of special importance when working at high particle concentrations, for which rapid movements (high stresses) would entail the thickening of the sample and the development of normal stresses, so that some time would be needed for their

relaxation before settling them in the rheometer geometry. The deposition of a given volume of sample was carefully carried out with a small spoon and the samples were well closed in order to avoid water evaporation and the subsequent change in volume fraction. Each measurement was carried out at least three times to guarantee the reproducibility of the results. In the case of highly concentrated suspensions fresh samples were prepared for each measurement, as the duration of the imposed protocol (between 10 and 15 minutes) was enough for encountering significant changes in viscosity (see Figure 3.2), even if the conservation of the sample was adequate. This is thought to be due to granule swelling.

Carrier fluid	**Shear viscosity,** $\boldsymbol{\eta}$ (mPa·s)	**Density,** $\boldsymbol{\rho}$ ($g \cdot ml^{-1}$)	**Supplier**
Deionized water	0.89 ± 0.01	1	-
Ethylene glycol	16.66 ±0.14	1.113	Sigma-Aldrich
Glycerol 87 % w/w	119 ± 5	1.23	Scharlau
Glycerol 99 % w/w	834 ± 16	1.261	Sigma-Aldrich
Silicone oil 20 cSt	18.88 ±0.13	0.95	Sigma Aldrich
Silicone oil 100 cSt	90 ± 19	0.968	Fluka

Table 3.2: Physical properties of the carrier fluids employed in the formulation of suspensions characterized within this thesis. Shear viscosity were measured in the Anton Paar MCR 302 rheometer. Values for densities are given by the supplier.

It is worth noting that the density of starch particles was considered as $1.68\ g \cdot cm^{-3}$ in every calculation of volume fractions, in accordance with Fall's work [22]. In comparison with the densities of Table 3.2, it can be observed certain mismatch. Some authors employ cesium chloride CsCl as additive in water suspensions to match particles and carrier fluid densities and so avoid particle sedimentation [23]. We performed some proofs with and without this additive and no clear differences were observed within the measuring time. If a small deposit of particles was formed in the bottom of the container during a test, the use of the spatula in the sample just before performing the next test was sufficient to redisperse the system. This fact, together with the elevated cost of this product, contributed to the rejection of the use of this additive.

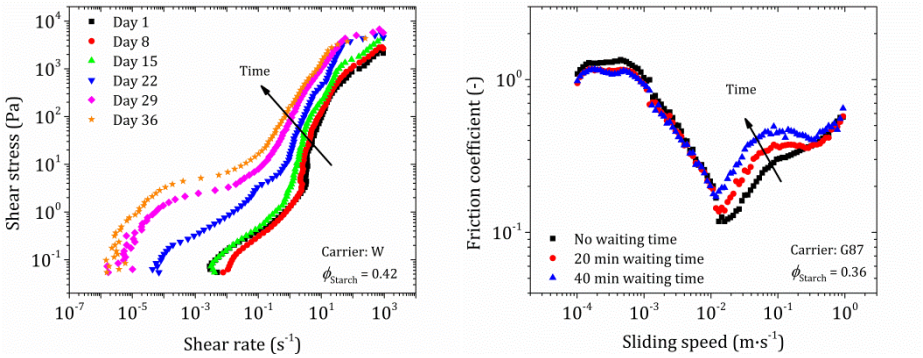

Figure 3.2: Examples of temporal evolution of the rheological (left) and tribological behaviour (right) of two concentrated suspensions of starch in several carrier fluids. The sample in the rheological case was measured each weak, and in the tribological case the time between curves was the duration of the experimental test and posterior cleaning of the tribological elements.

Moreover, it is interesting to know that starch suspensions suffer from degradation with time. For this reason, small amounts of sodium azide NaN_3 are usually employed [24,25] to conserve this type of samples by preventing bacterial growth during long times. In our case, in order to avoid this problem we opted for preparing fresh samples for each type of experiment, what was also convenient due to the tendency of starch granules to absorb water and so change their rheological properties.

- **Fumed silica suspensions**

In this work hydrophilic fumed silica was purchased from Sigma Aldrich (S5130). Individual and spherical SiO_2 particles with diameter of 7 nm are initially formed, but subsequently they collide and arrange in branched aggregates of about 200 nm in an irreversible fusion process [6]. As a result, the final fumed silica particles possess an open internal structure, with a surface area of 395 $m^2 \cdot g^{-1}$ and a tamped density of 2.3 $lb \cdot ft^3$ according to the product specifications. Due to the great fineness, and the difficulty in finding an apparent density for calculations of volume fractions, the results of fumed silica samples will be given by their mass fractions, as other authors do when working with this substance.

Concentrated dispersions of fumed silica were prepared by dispersing these fluffy particles in ethylene glycol (Sigma Aldrich, ≥99 %). The mixing process is quite laborious as the incorporation of dry particles into the suspending medium has to be done very delicately to avoid the loss of material.

The shear-thickening behaviour of these samples was studied in wide range of concentrations.

On the other hand, fumed silica was employed in dispersions with different mixtures of water and glycerol in order to study the effect of the carrier fluid in their shear-thickening and tribological response.

- **MR suspensions**

In Chapter 4 concentrated MR suspensions were investigated. They were prepared by dispersing carbonyl iron (EW grade, from BASF SE, Germany) in four carrier fluids, namely ethylene glycol, glycerol 87 %w/w, and silicone oil with viscosities of 20 cSt and 100 cSt (see Table 3.2). These suspensions combine a magnetic response upon the application of a given magnetic field strength and certain shear-thickening character, due to their high particle concentration, which depends on the physicochemical properties of the carrier fluid.

However, in squeeze experiments conventional MR suspensions of carbonyl iron (grade HQ, from BASF SE, Germany) in silicone oil were studied (Chapter 8). The concentration was a 5 % in order to compare with previous squeeze results on diluted samples [26].

The preparation of these types of samples involved the simple mixing of both components with the spatula, the use of ultrasounds in order to disrupt magnetic aggregates as well as the planetary mixer, where the particles become homogeneously distributed within the suspension. These two steps were carried out before each measurement due to particle sedimentation.

- **MRST suspensions**

In Chapter 5 we studied the rheological behaviour of hybrid suspensions with magnetic and shear-thickening character. Two approaches were performed: by means of suspending a mixture of magnetic (carbonyl iron, CC grade) and non-magnetic particles (starch) in water, and on the other hand by using starch-coated carbonyl iron particles (EW and HS grades) suspended in water.

These MRST suspensions were easily prepared as for MR suspensions.

3.2. Experimental methods

3.2.1. Rheometry

The measurement of the rheological material functions is called rheometry. Rheological experiments provide the relationship between applied stresses and deformations in a material and can be performed in shear or extensional rheometers [27]. Most rheological measurements are carried out in shear geometries where experimentation is easier. However, the generation and measurement of homogeneous extensional flows have many practical difficulties and thus extensional rheometers are less developed. Shear flow is typically used when the viscosity is the main material property. Other classification of flows is by the use of small or large strains, as well as by transient or steady flows.

The stress responses of a given material under study depend both on the nature of the material and the type of flow imposed to it. Shear rheometers can be divided into two groups: drag flows and driven flows. In drag flow the shear is generated between a moving and a fixed solid surface. Sliding plates, concentric cylinders (Couette flow), cone and plate, and parallel disks are geometries belonging to drag flows. Rotational instruments may be operated in the steady shear (constant angular velocity) or oscillatory (dynamic) mode. On the other hand, capillary geometry (Poiseuille flow), slit flow and axial annular flow are types of pressure flows, where a pressure difference over a close channel, through which the material flows, is responsible for generating the shear. Other popular pressure-driven flow can also be produced by means of the squeezing flow between parallel plates.

Extensional flows by their part, exhibit very sensitive variations in structure and this type of deformation play a significant role in some industrial processes as fibre spinning flows. When a given material is subjected to extensional flows the material is stretched along streamlines. In fact, stretching occurs with all deformations but stretching in shear is only observed between particles in different streamlines.

The choice of a measuring system depends on the nature of the studied sample and determines the shear stress and shear rate ranges. The most commonly used devices within this thesis are cone-plate and plate-plate geometries. The main characteristics of each geometry are shown below:

- In cone-plate geometry the shear rate and stress are homogeneous in the whole gap, so that the viscosity is independent of the measuring point. For this assertion to be valid the angle of the cone has to be very small as it will be explained later in conversion of data. It requires small volumes of samples and is used in normal force measurements. The cone is truncated and the gap is fixed at a distance from the plate, and this fact restricts the type of sample that can be used within this geometry. In this sense, the particle diameter has to be below a tenth of the gap.
- Parallel plates enable the variation of the gap size and so the attainable shear rates the sample is subjected to. In the same manner the larger the plate radius, the larger the feasible shear rates. Moreover serrated plates can be used to avoid slippage.

In next sections, the rheological characterization of our complex fluids, which were carried out in torsional and squeeze modes in an Anton Paar magnetorheometer (MCR 501, MRD70-SN81112937), is described. Then the equations relating the raw data from the rheometer and shear stresses and strains are exposed. After that attention will also be paid to the quantification of normal stresses that may appear in our systems during the rheological measurements. At the end of this subsection we will take into account some considerations in the determination of yield stresses and the correction of a very important experimental artefact as wall slip.

- **Torsional experiments**

Small-angle cone-plate and plate-plate geometries have been employed in torsional experiments. Both geometries are traditionally used in rheological measurements of complex fluids.

The rheological characterization of concentrated starch (or silica) suspensions was principally performed with parallel plates, except for the determination of the normal force, for which the cone-plate measuring system was used. In the case of mixtures of magnetic and non-magnetic particles as well as for concentrated MR suspensions of carbonyl iron, the rheological measurements were carried out in parallel plates, as they allow for the application of an external magnetic field and a uniform distribution within the gap.

- **Squeeze experiments**

Squeeze experiments were used in Chapter 8 to study the squeeze strengthening effect in MR suspensions of carbonyl iron in silicone oil. Squeeze con-

stant-volume and constant-area tests (see Figure 3.3) were performed and compared. In this type of experiments, plate-plate geometry was used. Samples are subjected to a constant magnetic field during the whole test and were compressed in the direction of the magnetic field. Finally, the samples were subjected to shear and the yield stress was evaluated.

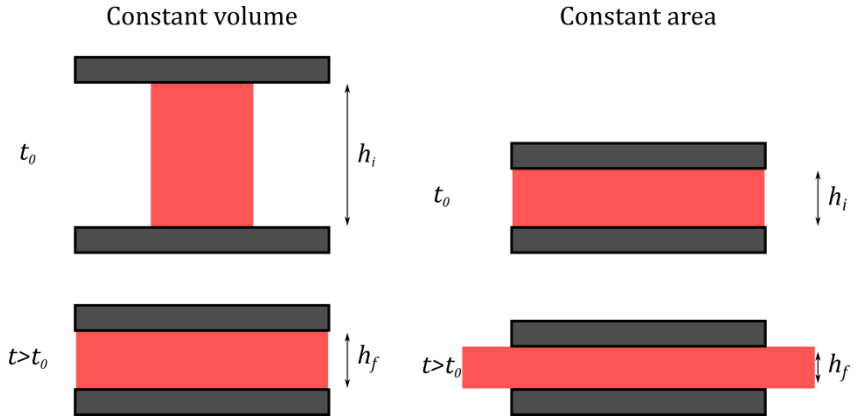

Figure 3.3: Schematic of both modes of operation during the squeeze step. In constant-volume tests the sample volume between the plates does not change and at the end of this step it occupies the whole area of the plates. In contrast, for constant-area tests what remains without variation is the area of the plate in contact with the sample. At the beginning of the compression the sample volume completely fulfil the space between plates while after squeezing, part of the sample is out of the plates and can be carefully removed.

In the slow-compression tests, the deformation at a given gap h was determined by the compression strain $\varepsilon(h) = (h_i - h)/h_i$, where h_i is the "initial" gap separation. Therefore, the total deformation was quantified as follows $\varepsilon_T = \left(h_i - h_f\right)/h_i$, where h_f is the final gap separation.

- **Conversion of data**

Rheometers supply torque and angular velocity data and they can work in stress or strain-controlled conditions. In the first case torque is applied and the strain or rotation is measured, in the other case values of torque are provided upon the application of given values of strain. The available rheometers in the research laboratory belong to the first type so that they possess better torque sensitivity, which is very useful in the determination of the yield stress of a system or in the study of the shear-thickening transition, where small changes in shear rates rapidly modify the value of stress with the consequent loss of stress data.

However, rheometers' macroscopic raw data in steady state measurements (i.e., torques and angular velocities), have to be converted into local data (i.e., shear stresses and shear strains), which are more interesting data for the rheologists' purposes. The torque-stress and angular velocity-shear rate relationships [27,28] for the geometries used within this thesis are described below, namely vane, plate-plate and cone-plate.

The use of the vane in cylinder geometry in stress-controlled rheometers is a simple and reliable method for determining the yield stress of a complex fluid [29,30]. Its main advantage resides in the possibility of avoiding undesirable wall slip effects. Other benefit is that little disturbance is provoked to the structure when the vane is inserted into the sample. This apparatus has to be completely immersed in the sample and have a pair number of blades, which are considered to be equivalent to an inner cylindrical surface, and somewhat analogous to a Couette device. The yield stress can be calculated from the total torque M_0 needed to overcome the yield stress of the sample and the vane dimensions, as

$$M_0 = (\pi dh)\left(\frac{d}{2}\right)\tau_0 + 2\int_0^{d/2} 2\pi r^2 \tau_e \, dr \, . \tag{3.1}$$

The first and second terms in this expression refer to the torque due to the shearing on the lateral surface of the cylinder, and on the end surfaces (bottom and top), respectively. If τ_e is assumed to vary with the radial position according to a power relationship, and considering that σ_0 is constant, the stress-torque relationship at the yielding point is calculated as follows:

$$\tau_0 = \frac{2M_0}{\pi d^3}\left(\frac{h}{d} + \frac{1}{m+3}\right)^{-1}, \tag{3.2}$$

where h and d are the height and diameter of the vane, and m the power-law coefficient in the expression of τ_e as a function of the vane radius.

The velocity profile can be assumed to follow the expression $u(r) = ar + b/r$, with the boundary conditions being $u(R_1) = \omega R_1$, and $u(R_2) = 0$. The radius at the end of the vane and at the inner radius of the cap is R_1 and R_2, respectively. With this, the shear rate is obtained by:

$$\dot{\gamma}(r) = -\frac{du}{dr} = \frac{\omega R_1^2}{R_2^2 - R_1^2}\left(\frac{R_2^2 + r^2}{r^2}\right), \tag{3.3}$$

which evaluated at the end of the vane is $\dot{\gamma}(R_1) = \omega\frac{(R_2^2+R_1^2)}{R_2^2-R_1^2}$.

In parallel plates geometry, the shear rate is again proportional to the angular velocity ω at which the upper plate moves as a consequence of the applied torque, and a function of the radius:

$$\dot{\gamma} = f(r) = \frac{\omega r}{h}, \quad \dot{\gamma}_R = \frac{\omega R}{h}, \tag{3.4}$$

where R is the radius of the plate and h the gap between plates.

Shear stress in parallel plates, in contrast to the cone-plate geometry, is a function of the radius ($\tau = f(\dot{\gamma})$) and has to be determined by integrating a force balance equation over the radius:

$$\int_0^M dM = 2\pi \int_0^R (r^2 \tau)\, dr\,. \tag{3.5}$$

Changing the limits of integration, substituting the radius by the expression of shear rate, and since the shear stress is function of shear rate, the equation can be written as

$$\frac{M(\dot{\gamma}_R)^3}{2\pi R^3} = \int_0^{\dot{\gamma}_R} (\dot{\gamma})^2 f\,(\dot{\gamma}) d\dot{\gamma}\,. \tag{3.6}$$

If the equation is differentiated with respect to the shear rate at the rim the Leibnitz' rule may be applied. It allows the integral in the right term (with the form of $\frac{d}{dz'}[\int_0^{z'} z^2 f\,(z) dz]$) to be written as $\dot{\gamma}_R^2 f(\dot{\gamma}_R)$. The expression for the shear stress at the rim of the plate is thus obtained as follows:

$$\tau_R = f(\dot{\gamma}) = \frac{M}{2\pi R^3}\left(3 + \frac{d \ln M}{d \ln \dot{\gamma}}\right). \tag{3.7}$$

This equation is similar to Rabinowitsch-Mooney equation, where the shear rate is expressed as a function of the shear stress, $\dot{\gamma} = f(\tau)$. If the law relating shear rate and stress is known, which depends on the type of fluid behaviour, the relationship between torque and the angular velocity can be easily obtained. The derivative in the right side of the equation can be calculated by data analysis software and the calculation of shear stress at the rim is thus straightforward.

When cone-plate geometry is used the transformation of raw data from the rheometer into shear stress and rate in the sample is simple:

$$\tau = \frac{3M}{2\pi R^3}\,. \tag{3.8}$$

The expression for the shear rate in cone-plate geometry is similar to(3.4, the analogous in plate-plate geometry:

$$\frac{h}{R} = \tan \alpha_{rad} \approx \alpha_{rad} \rightarrow \dot{\gamma}_R \approx \frac{\omega}{\alpha_{rad}}. \qquad (3.9)$$

The angle of the cone tool α_{rad} is usually very small, and from trigonometry, the ratio between the gap h and the radius of the cone R coincides with the tangent of this angle. For angles tending to zero this tangent can be approximated, with an acceptable accuracy, to the angle expressed in radians.

- **Normal stress differences**

Differences between normal components (τ_{xx}, τ_{yy}, τ_{zz}) are consequences of microstructure anisotropy, and result in deformation when they are distinct from zero. The first normal stress difference ($N_1 = \tau_{xx} - \tau_{yy}$) can be directly obtained in rheological measurements when the test is performed with a cone-plate geometry. The total thrust F_N in cone-plate geometry (a normal force acting on the upper tool, the cone) can be easily transformed in this parameter $\left(N_1 = \frac{2F_N}{\pi R^2}\right)$. Once the value of N_1 is known the second normal stress difference ($N_2 = \tau_{yy} - \tau_{zz}$) can be calculated from plate-plate measurements. The thrust measured in this geometry can be related with the difference between both quantities in this form [31]:

$$N_1(\dot{\gamma}_R) - N_2(\dot{\gamma}_R) = \frac{F_N}{\pi R^2}\left(2 + \frac{d \ln F_N}{d \ln \dot{\gamma}_R}\right). \qquad (3.10)$$

The normal stress determined from parallel plates data is generally a good approximation of the first normal stress difference, as the second one is usually very small compared to the former.

Thus, changes in normal stress differences during a rheological test involve changes in the sample microstructure and provide useful information about the sample behaviour. For instance, Royer et al. [10] studied concentrated non-colloidal suspensions formulated with silica particles under shear and observed a clear transition of N_1 from negative to positive values developed by the sample, as the particle concentration increase. For diluted samples the first normal stress difference remains negative as a consequence of the prevalence of hydrodynamic forces due to shear compared to Brownian ones. However, for higher concentrations at low values of shear stress hydrodynamic forces again dominate over other forces, while at higher shear stresses contact forces and frictional interactions prevail over hydrodynamic

ones, resulting in positive first normal stress differences. From the macroscopic point of view, these positive values reflect dilatancy, a volume expansion that in a confined system give rise to the appearance of shear-thickening behaviour.

- **Yield stress measurements**

Many complex fluids are characterized by an apparent yield stress, a rheological property by which a material flows when the applied stress exceeds a particular value, and below this stress the material elastically deforms. Concentrated suspensions with strong interparticle interactions often exhibit this yielding behaviour. These fluids have a structural skeleton which breaks in the yield stress. It is the case of many shear thinning fluids as daily products (toothpaste and ketchup), and of relevance within this thesis in MR fluids, where field induced yield stress is found [32–34].

In the classical description given by Bingham the critical value separates a region in the rheogram with infinite viscosity from other where the stress monotonically increases with the shear rate, so that the transition from solid to liquid state would occur at a unique value of stress. Years later Barnes and Walters [35] asserted that the yield stress was an artefact and that fluids capable of flowing at high stresses would also flow at all lower values, for which viscosity would be very high but not infinite. This work brought many reactions from other colleges and nowadays there is still controversy about the existence of a true yield stress [36–38]. Despite this, it is undeniable the usefulness of the concept of yield stress and yield-stress equations in numerous applications.

In practice, there is no a reliable method for determining the yield stress, which often results affected by the technique employed and thixotropic effects of the sample. Experimentalists observe small shear rates variations upon the application of small values of stress, instead of a completely static situation below the apparent yield stress. For many fluids there is a competition between aging and rejuvenation processes, two phenomena describing the spontaneous build-up occurring in the microstructure at rest and the breakage in flow conditions, respectively.

Yield stress fluids can be categorized into simple yield stress fluids and thixotropic yield stress fluids [39,40]. The former type corresponds to fluids for which the shear stress is only dependent on the shear rate and not on the shear history of the sample. Nevertheless, in thixotropic yield stress fluids the

flow history is very important: if an up-and-down stress ramp is performed with these fluids, the static and dynamic yield stresses will differ as the viscosity of the sample is reduced with time. Static yield stress is defined then as the stress above which the material starts to flow when starting from rest and the dynamic one is the stress at which the transition from liquid to solid takes place, so that the sample is subjected to a diminishing stress ramp up to it completely ceases its flow. However, for simple yield stress fluids the determination of the yield stress is easier as both static and dynamic yield stresses coincide. As an example of the rheological behaviour of these two types of yielding fluids subjected to consecutive up and down stress ramps, the work of Ovarlez et al. [41] can be consulted, namely in their Figure 2.

Although the determination of yield stress [42] is usually accompanied by experimental difficulties, it can be performed through several approaches. In order to obtain reliable yield stress measurements the test type has to be carefully selected. Among them stress ramp, stress growth, oscillation amplitude sweep and multiple creep are the easiest methods to perform the yield stress measurements. The choice of the measurement system is also important as wall slip effects should be avoided. In this sense, the use of roughened surfaces is recommended. When working with a cone-plate geometry with small cone angle the shear stress can be considered to be homogenously distributed, so that if the material exhibits yielding flow behaviour, this yielding would be homogeneous whatever the sample radius. Thus, in this case the cone measuring system would be preferable to parallel plates. However, although roughened cones are also available, the last geometry is used if the suspension is formed by large particles (remember the limitation that the particle diameter should not be above a tenth of the gap) and when the slippage is significant, and serrated plates are used in order to minimize it. Moreover, the vane geometry is a common tool for measuring the yield stress of structured systems, as this apparatus slightly disturbs the initial structure when it is inserted into the sample.

Once the rheological measurement has been carried out the value of the yield stress can be obtained by fitting the data to traditional yield models such as Bingham, Herschel-Bulkey or Casson equations, and extrapolating the data to zero shear rate. If the fit is not good enough, a tangent analysis can be used to extract the yield stress value from the data.

It will be seen in Chapter 8 that the yield stress determination may result greatly affected by the wall slip phenomenon. Corrections described below

were performed throughout this thesis when needed to obtain the true rheograms.

Furthermore, similarly to the shear yield stress in shear flow tests, in squeeze experiments a compressive yield stress is defined as the normal force in the low-strain region divided by the area of sample subjected to squeeze. A deeper explanation of the compressive yield stress appears in Chapter 8.

- **Wall slip correction**

Wall slip is an undesirable and widespread phenomenon that may occur when a suspension is subjected to shear flow. It is frequently encountered in polymer melts with high molecular weight and concentrated dispersed systems as suspensions or emulsions with large particles and droplets, respectively. Barnes [43] attributed wall slip to a depletion of particles near the solid boundaries, so that the local concentration of particles in the wall proximities would be lower than in the bulk. This fact provokes much greater local shear rates in a very thin layer adjacent to the shearing surfaces and the appearance of this apparent slippage (see Figure 3.4). An extensive review on flow heterogeneities occurring in high solid dispersions, especially focused in wall slip, has been recently published by Cloitre and Bonnecaze [44].

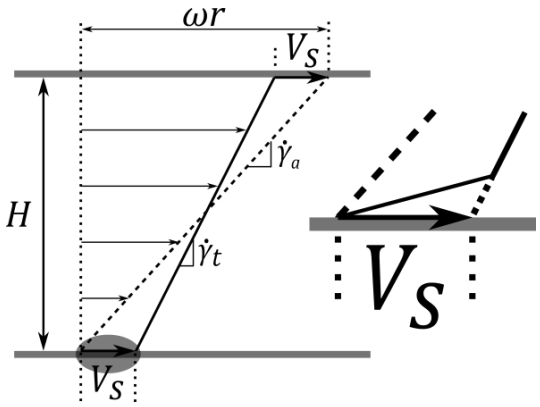

Figure 3.4: Schematic representation of wall slip.

A clear signal of the presence of wall slip is obtaining different rheological responses of a given sample from different-sized geometries. Wall slip is promoted under certain conditions as: the existence of large particles and the tendency to sediment or cream, a large dependence between viscosity and concentration, the presence of smooth walls, and low shear rates. The last condition can be observed in Figure 3.5, where for a given gap, the difference

between the experimental curve and the true flow curve is more conspicuous at low shear rates. This fact can be easily understood if we take into account the first condition: a sample with large particles would be more vulnerable and would cause a great slip. At low shear rates these particles are prone to be part of larger flocs that get destroyed as shear rates increase.

The parallel-plate measuring system allows for the detection and correction of wall slip effects, by performing measurements at multiple gap heights. Wall slip is commonly more prevalent at small gaps (see Figure 3.5). In this sense, the measured torques at different gap sizes would provide increasing viscosities with the gap distance, while in samples that do not slip the results are independent of the gap.

If the wall slip is assumed to be the same in both plates, the apparent shear rate $\dot{\gamma}_a(\tau_R)$ is the result of the true shear rate $\dot{\gamma}_t(\tau_R)$ experienced by the fluid at the rim and the contribution from the slip velocity V_s [45,46]:

$$\dot{\gamma}_a(\tau_R) = \dot{\gamma}_t(\tau_R) + \frac{2V_s(\tau_R)}{H}. \tag{3.11}$$

If apparent shear rates (obtained from Equation 3.4) are plotted against the inverse of the final gap H for several shear stresses the slip velocity at each shear stress will be obtained from the slope of each curve.

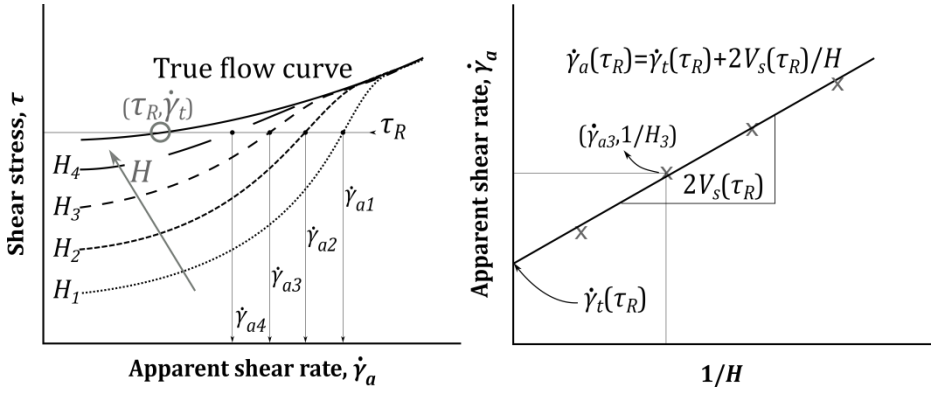

Figure 3.5: Process of correcting deviations in flow curves due to the presence of wall slip. On the left side, a schematic rheogram for several experimental gaps is shown. Non-continuous lines refer to experimental data for which wall slip exists (it can be seen that the shear rate for a given shear stress depends on the gap H), while continuous line corresponds to the slip-corrected flow curve. On the right side, apparent shear rates are plotted against the inverse of the gap for a given shear stress. The linear fit of these points permits the determination of the true shear rate $\dot{\gamma}_t(\tau_R)$. Note that the calculated true shear rate is shown within the true flow curve line in a grey point $(\tau_R, \dot{\gamma}_t)$ in the left figure.

In more detail, it is worth noting that this expression is a function of the shear stress at the rim of the plate τ_R. This parameter has been calculated through this thesis using Equation 3.7, once an averaged torque (and speed) is obtained from at least three repetitions maintaining the same experimental conditions, which is the normal procedure to have statistics of our measured data. In this sense, for each gap $(H_1, H_2, \dots, H_n)$ we have an apparent flow curve $(\tau_R, \dot{\gamma}_a)$. So that at a given imposed torque (or averaged value of τ_R for different gaps) we will have n values of apparent shear rates to be plotted against the inverse of the gap. The fitting of each group of points provides values of the slip velocity and the true shear rate for each shear stress so that it is possible to construct the true rheogram. A schematic of the correction process is shown in Figure 3.5.

Moreover, a general form for the slip law $\tau(V_s)$ can be derived from the fitting slopes, as the one given by the following equation:

$$V_s = \beta(\tau - \tau_c)^n \,, \tag{3.12}$$

where β is the slip coefficient ($\beta = 0 \rightarrow$ no slip), and τ_c is the critical stress for onset of slip. If we plot the slip velocity against the stress, the critical stress can be determined for $V_s = 0$.

Figure 3.6 shows the wall slip correction carried out in Chapter 4 in rheological measurements of concentrated suspensions of carbonyl iron in ethylene glycol. It can be confirmed that the main deviation from the true flow curve occurs at low shear rates.

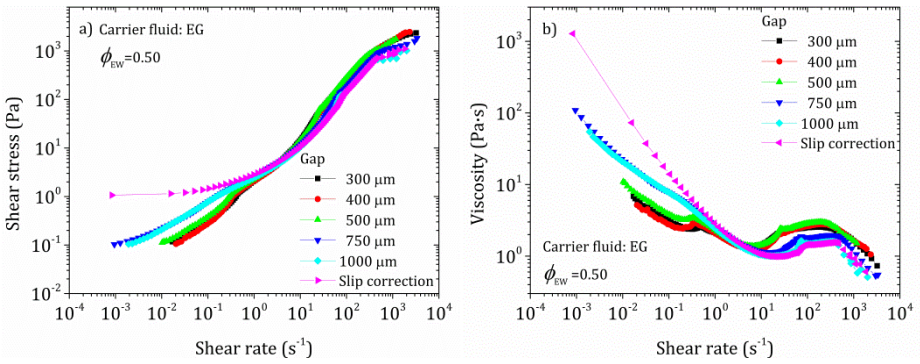

Figure 3.6: Wall slip correction for a suspension of carbonyl iron ($\phi_{EW} = 0.50$) in ethylene glycol.

3.2.2. Tribometry

The term tribometer was first used in writings of Goldsmith in the 1700s to refer an instrument for measuring the friction force developed between surfaces in relative motion. Nowadays, it is also extended to measurements of wear of the materials. These devices are intended to reproduce all the conditions around a given application (mainly in the field of engineering) entailing friction and wear.

A wide variety of commercial tribometers exists; however, the design and fabrication of specific tribometers still continues by manufacturers to account for particular situations. Some of the most common tribometers are: pin- or ball-on-disc, four ball tester, ball-on-three-plates, reciprocating pin, vacuum tribometer, and micro/nano tribometers, among others. In other cases specific friction attachments are coupled to rheometers to perform friction and lubrication measurements and capture the tribological properties of the system.

The choice among these tribometers will depend on the required environment to mimic. In this sense, several parameters can vary from one to other device, such as the range of speeds and loads to which the surface is subjected, the material of the surfaces in contact and its surface roughness and hydrophobicity.

- **Ball-on-three-plates geometry**

All tribological measurements of shear-thickening and shear-thinning fluids shown in Chapters 6 and 7 were carried out in a tribological device mounted in a MCR 302 Anton Paar rheometer. The set up consisted of a ball coupled in the rheometer shaft, and of three plates evenly distributed within the conical surface (with an inclination of 45 degrees with respect to the shaft) of a movable holder (see Figure 3.7). In this arrangement, the normal surface of the mounted plates is in tetrahedral coordination with the rotation axis, what ensures an equal distribution of the applied load.

The non-conformal tribopairs were made of polydimethylsiloxane (PDMS). They were fabricated with a two-component silicone elastomer kit (SilgardTM 184, from Dow). The liquid components are thoroughly mixed in a mass ratio of base and curing agent of 10:1. Then, PDMS is poured into moulds and cured during 8 h at 70 ºC, taking care of minimizing the trapped air in a vacuum chamber. This process results in a flexible and transparent

elastomer. The ball radius was 6.35 mm and the plates were rectangular parallelepipeds with dimensions of 3 mm × 6 mm × 16 mm.

Tribological tests were performed always following the next protocol, whatever the sample. Once the sample is put within the holder and the ball descends to the measurement position, the normal force is set at $F_N = 1$ N during 60 s. Then, while maintaining the commanded value of normal force, a logarithmic speed ramp is applied from 0.1 to 2000 rpm so that the ball rotates at an increasing sliding speed in the range of $V = 5 \cdot 10^{-5} - 1\ \mathrm{m \cdot s^{-1}}$. Due to the set up configuration, each plate is subjected to a normal load of $w = \sqrt{2}F_N/3$ during the test.

After each test the geometry is dismounted, the sample is retired from the holder and every element is carefully cleaned in successive rounds with water, and finally with ethanol.

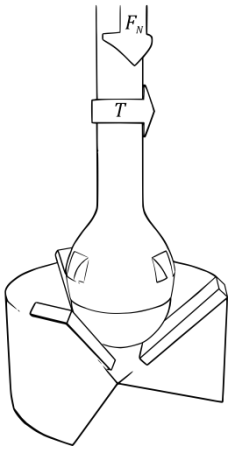

Figure 3.7: Ball-on-three-plates geometry used in tribological tests.

3.2.3. Microscopic characterization

- **Optical microscope**

An optical microscope (Leica DMI 3000) was used to study the change in size and shape of starch granules in water-based suspensions at different temperatures.

A diluted suspension was prepared to adequately appreciate the granules and avoid the overlap between them. After the addition of starch granules into distilled water, the suspension was heated under a gentle stirring. An ali-

quot was taken once the required temperature was reached and observed with the microscope. Some representative images at each measured temperature are shown in Figure 3.8.

When starch granules are heated in excess of water the granules begin to swell irreversibly, what causes the disruption of the granular structure. This progressive phenomenon is called gelatinization. During this process, occurring in a range of temperature, small amylose molecules are leached to the suspending fluid, leading to an increase in the fluid viscosity. From micrographs observations it can be appreciated the increase in granule size with temperature, which is more evident from the third to the fourth image. Thus, the gelatinization temperature range is found between 55 and 74 °C in this case. The analysis of the particle size distribution in these types of images was carried out using the Bool2k software in Subsection 3.2.4.

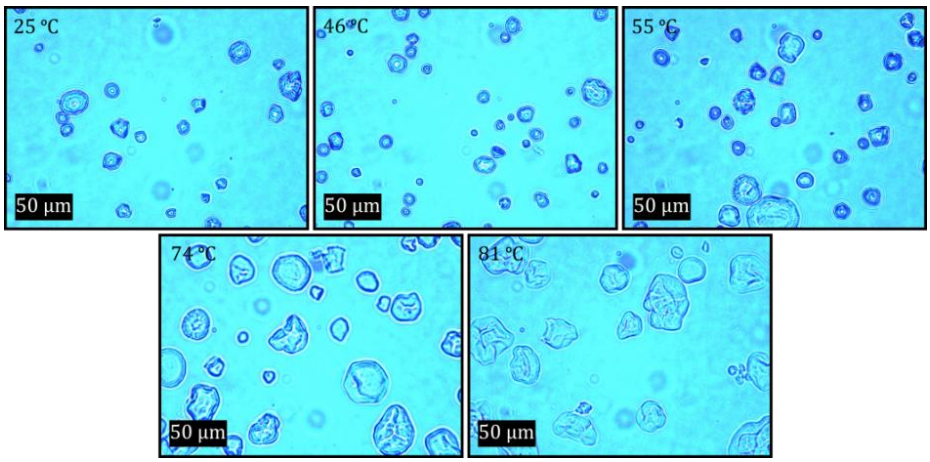

Figure 3.8: Micrographs of starch particles in water-based suspensions at different temperatures (25, 46, 55, 74, and 81 °C).

- **Electron microscopy**

Electron microscopy uses a beam of accelerated electrons as a source of illumination (instead of light). Several detectors collect the electrons generated during the interaction between the beam and the sample surface (secondary electrons, Auger electrons, backscattered electrons, X-ray, transmitted electrons…). As a result it is possible to construct a topographic image that is in fact a distribution map of the intensity of these signals. The image provides information about shapes, textures and chemical composition of their constituents. These microscopes usually work under vacuum conditions, so that

for studying insulator materials a thin layer of a conductive material (for example carbon) has to be deposited on the sample surface. This type of microscopy offers a high degree of magnification and resolution.

In scanning electron microscopy (SEM) the beam scans the sample and the emitted secondary electrons are collected, which are of low energy and must be near the surface to be ejected. For this reason they provide useful information about the sample topography in a 3-D black-and-white image. Two modes of operation were performed in SEM analyses: secondary electrons (SE) or circular backscattering mode (CBS). The former is used to study the topography of the surface, whilst in the CBS mode differences in concentration are reflected with different brightness. The use of these two modes of operation gains relevance in the analysis of composed particles, as those synthesized in Chapter 5. SEM micrographs of dry starch granules are shown in the left side of Figure 3.9, and they are later used to obtain the mean size diameter with the software Bool2k.

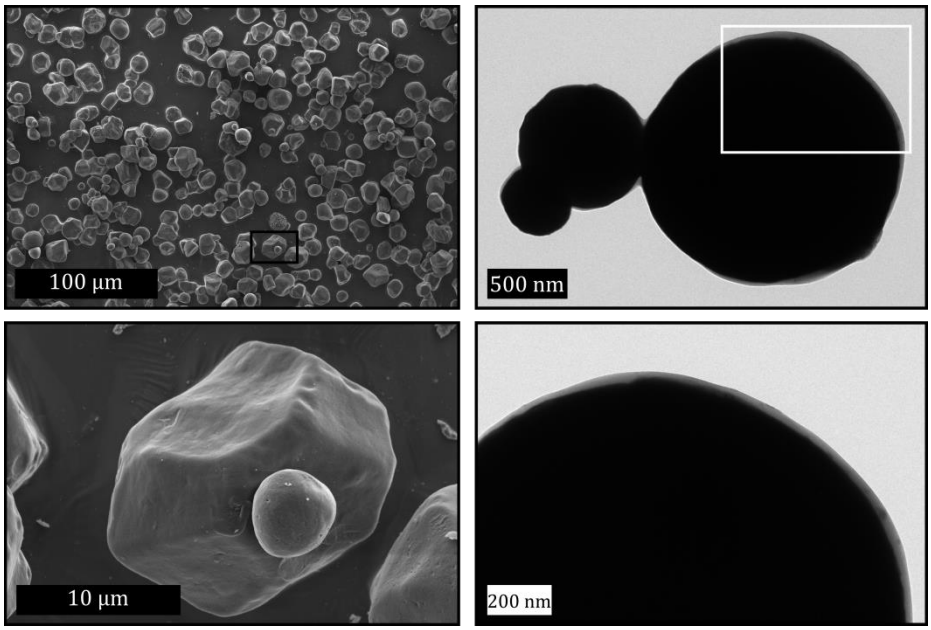

Figure 3.9: SEM micrographs (SE mode) of native cornstarch particles (left side) and TEM micrographs of hybrid particles formulated with a carbonyl iron core and a starch coating (right side).

In transmission electron microscopy (TEM) the electron beam transmitted through the sample is used to generate a 2-D image. The sample preparation in TEM requires the deposition of a small droplet of specimen over a

support grid. In Chapter 5 carbonyl iron particles were coated with starch and the success of the coverage was evaluated in TEM micrographs. In order to observe the core-shell structure (see right side in Figure 3.9) a diluted suspension of these particles was prepared and retained within the grid, so that each cell contains only a few of particles. Almost all the images were taken without a filter that diminishes the chromatic aberration (distortion in the image). Although the contrast of a given image increases with the use of this filter, in our case the difference between using it or not is quite insignificant.

- **Confocal microscopy**

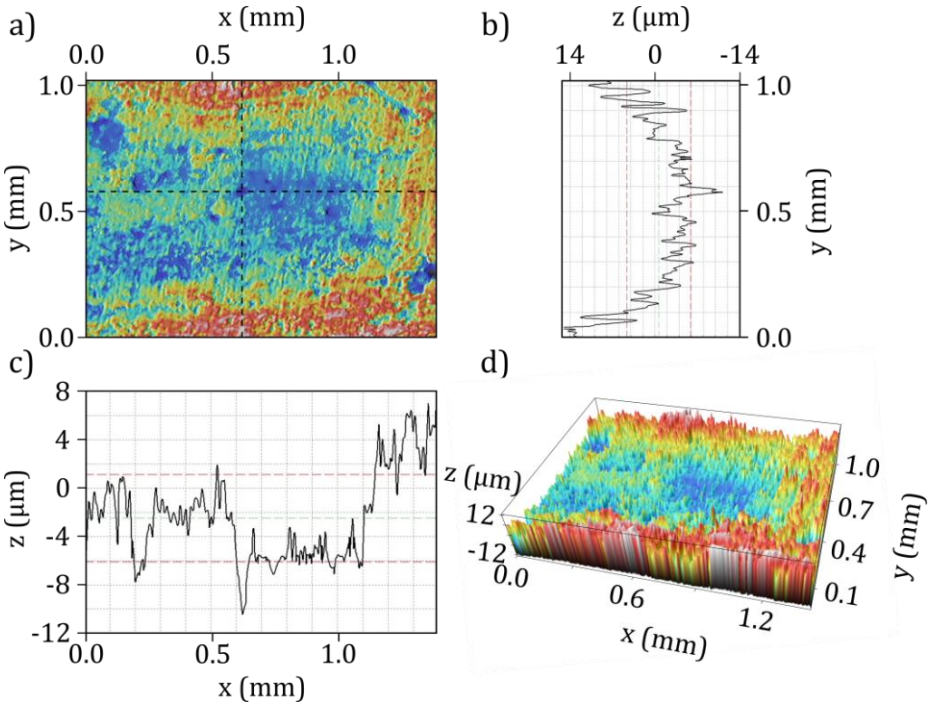

Figure 3.10: Wear in PDMS plate from confocal microscope measurements. Regarding the colour scale deep zones are depicted with blue while non-deformed zones show red colours. a) 2-D contour image, b) and c) are profiles of vertical and horizontal lines marked in a), d) 3-D contour image.

This type of microscopy uses one or several lasers as a lighting source and is based in fluorescence optics. This technique scans and illuminates the sample point by point and the emission of fluorescence light received by the detector corresponds just and exactly to the illuminated spot at each time and to a specific depth within the sample. The rest of out-of-focus fluorescence is blocked (and so not recorded) by means of some pinholes carefully allocated

(in confocal configuration) that act as a physical barrier. The optical sectioning of the sample enables the reconstruction of three-dimensional structures of the object under study.

The wear of PDMS plates used in tribological measurements was observed in a confocal microscope of white light PLμ 2300 (SENSOFAR). Figure 3.10 contains the depth profile corresponding to the contact point extracted from PLμ 2300 Non-Contact Optical Imaging Profiler software.

- **Dinolite camera**

In order to qualitatively observe the shear-thickening behaviour in concentrated starch suspensions, we recorded a rheological and a tribological experiment (Figure 3.11 and Figure 3.12, respectively) with a Dinolite camera.

It is a portable and compact camera that permits capturing high resolution photographs and videos. A concentrated suspension of starch $\phi = 0.36$ in glycerol 87 % w/w was prepared and subjected to the test. Parallel plates were used to perform an increasing ramp in torque. In Figure 3.11 we can see a white and dense starch suspension placed in the bottom plate before the measurement. Due to the small gap chosen and the shape of the bottom plate, it was no possible to appreciate the sample during the test. However, the expulsion of sample out of the plates at very high shear rates is noticeable in the border of the bottom plate once the test is finished. This occurs in the second shear-thinning regime, after the maximum viscosity is reached. Moreover, the same suspension was observed during the tribological measurement (see Figure 3.12), whose results are analysed in Chapter 7.

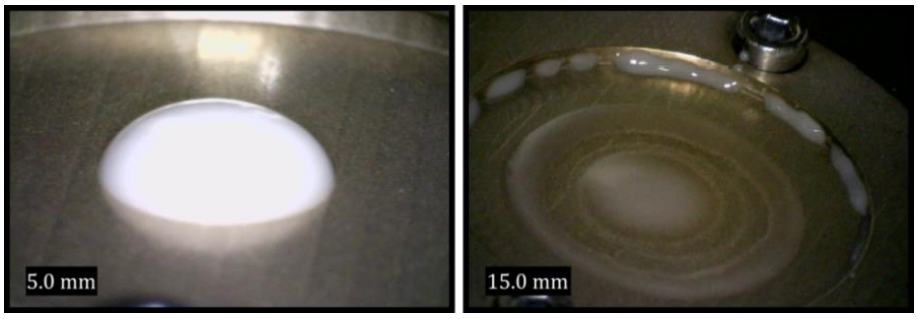

Figure 3.11: Snapshots of a starch suspension with $\phi = 0.36$ in glycerol 87 % w/w before (left) and after (right) carrying out the theological test. Note that as a consequence of high shear rates at the end of the experiment small droplets of the suspension are expelled out of the plate area (right image).

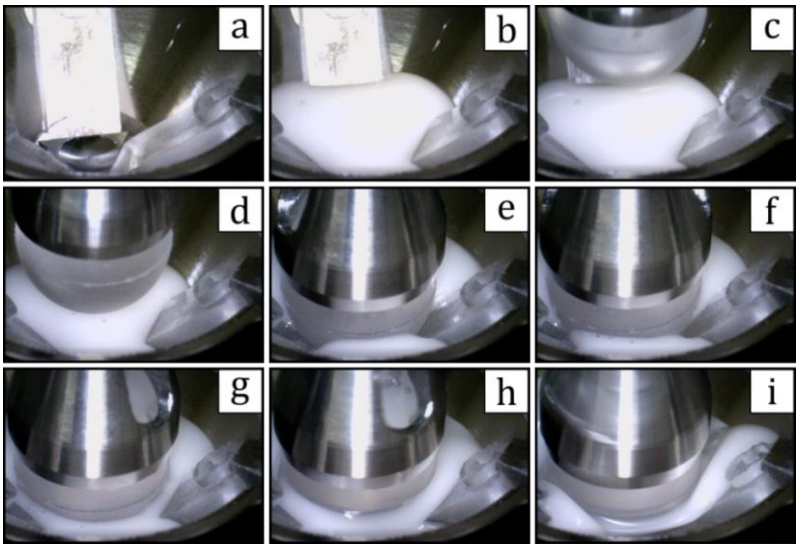

Figure 3.12: Snapshots of the evolution of the ball-on-three-plates tribological system during a test with a starch suspension with $\phi = 0.36$ in glycerol 87 % w/w. a) Clean movable holder with three PDMS plates. b) The suspension is placed in the holder. c) and d) PDMS ball approaching the measurement position. e) Beginning of the test, the ball is at rest. From f) to i) The ball rotates at increasing sliding speeds in Boundary lubrication regime, Mixed regime, region of minimum friction coefficient in Stribeck curve and Hydrodynamic regime, respectively.

3.2.4. Analysis of particle size distribution

Bool2k software was used for analysing the particle size distribution of starch granules. This software was specifically designed for automatically detecting spherical particles in images with bitmap format (8 bits, 256 colours). However starch granules have irregular shapes (see Figure 3.9) so that particles were manually identified. In order to evaluate the size of a representative sample, at least 300 particles were identified (distributed in several images) to have good statistical average.

On the one hand, we scanned a set of ESEM micrographs corresponding to dry granules, and the average size diameter was 10.7 μm with a standard deviation of 3.3 μm. On the other hand, the granule size in water-based suspensions in a wide range of temperatures was measured from optical microscope images, and the considerable increase in size with temperature as a consequence of the swelling of water is notable. In Figure 3.13 we show the particle size histogram of cornstarch as a function of temperature.

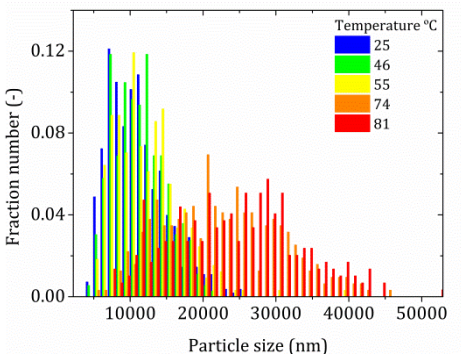

Figure 3.13: Particle size distribution of cornstarch in water suspensions at several temperatures obtained from the analysis of the respective micrographs in Subsection 3.2.3.

Moreover, the software provides several average diameters, statistical parameters as the standard deviation SD, and the polydispersity index PDI. Some of them, related to data in the histogram of Figure 3.13, are shown in Table 3.3. The average diameters by number d_n, weight d_w, volume d_v are defined as

$$d_n = \frac{\sum n_i d_i}{\sum n_i} \; ; \quad d_w = \frac{\sum n_i d_i^4}{\sum n_i d_i^3} \; ; \quad d_v = \left(\frac{\sum n_i d_i^3}{\sum n_i} \right)^{1/3} , \tag{3.13}$$

where n_i is the number of particles with a particular diameter d_i.

	Suspension temperature (°C)				
Parameter	**25**	**46**	**55**	**74**	**81**
$\boldsymbol{d_n}$ **(µm)**	11.14	11.42	12.39	22.41	24.25
$\boldsymbol{d_w}$ **(µm)**	15.46	14.46	18.24	29.84	32.09
$\boldsymbol{d_v}$ **(µm)**	12.52	12.47	14.03	24.03	27.06
$\boldsymbol{PDI}$	1.388	1.266	1.472	1.331	1.323
$\boldsymbol{SD}$ **(µm)**	3.98	3.56	4.50	7.98	8.64

Table 3.3: Summary of several parameters related to the size distribution analysis provided by Bool2k software.

3.2.5. Colloidal stability

- **Zetasizer Nano Z**

In Chapter 5 we prepared mixed suspensions of starch and carbonyl iron particles in water. Before the addition of carbonyl iron particles to the shear-thickening fluid, it is important to determine if both types of particles would interact due to their charges. For this reason we performed measurements of electrophoretic mobility of starch and carbonyl iron particles in a Zetasizer Nano Z device (Malvern Instruments). Size measurements of starch suspensions were also carried out in this apparatus.

This instrument is based on Dynamic Light Scattering (DLS) for size measurements. The scattering of light produced in all directions when a laser beam collides with suspended particles fluctuates with time due to the random Brownian motion of the particles. In this sense, reliable measurements depend on the sample concentration; if it is too low the light scattering may be insufficient, while if the sample is too concentrated multiple scattering phenomena may be produced and the free diffusion of the particles may complicate. Moreover, it is known that large particles move slowly than small ones. The Stokes-Einstein equation [47] relates the particle size and its speed, expressed in terms of the hydrodynamic diameter D_h and the diffusion coefficient D, respectively:

$$D = \frac{k_B T}{3\pi\eta D_h}, \tag{3.14}$$

where k_B is the Boltzmann's constant, T the absolute temperature and η the solvent viscosity.

When a charged particle is suspended in a liquid ions with an opposite charge become attracted to the particle surface forming a region of strongly bound ions called Stern layer. Then a diffuse layer of ions is distributed around this inner one. Both layers, Stern and diffuse, define the so-called electrical double layer and the potential existing at the end of the diffuse layer is called zeta potential ζ. It is worth noting that ζ cannot be directly measured in Zetasizer Nano Z system but instead the electrophoretic mobility. When an electric field E is applied to a suspension containing charged particles they then move with a constant velocity, called electrophoretic velocity U, towards the electrode of opposite charge. This velocity is the result of a balance between the applied electric field and the viscous resistance of the solvent to the

movement of the particles. If E is weak enough, $U = \mu_e E$, being the constant of proportionality the electrophoretic mobility μ_e. At this time the incident beams shot the sample and the scattered light undergoes a fluctuating intensity signal that is proportional to the speed of the particles. The calculation of μ_e is carried out by LDV (Laser Doppler Velocimetry) combined with a laser interferometric technique called M3-PALS (Phase analysis Light Scattering [48]. The application of Henry equation [49] permits relating the electrophoretic mobility to the zeta potential through this expression:

$$\mu_e = \frac{2\varepsilon\zeta f(\kappa a)}{3\eta}, \tag{3.15}$$

where ε is the dielectric constant of the medium, $f(\kappa a)$ is the Henry's function and depends on the particle shape, κ is the Debye length (somehow the inverse of the thickness of the double layer), and a is the particle radius.

The main factor influencing zeta potential is pH. The ζ-pH curve of a system of charged particles usually moves from positive values at low pH to negative values at high pH, and the transition point at which $\zeta = 0$ is called the isoelectric point. The value of ζ is related to the system stability; from $\zeta \in (-30, 30)$ mV the system is considered as unstable because there is no force preventing the particle attraction and flocculation, while outside this interval repulsion exists and there is no tendency to flocculate.

A model sample (AJ13) has to be prepared, inserted in the measuring cell, and measured in the device in order to evaluate the correct calibration of the apparatus and the well operation of the cell. After that, regular measurements can be performed. We used a folded capillary cell (DTS1070) to carry out both size and electrokinetic measurements. An important aspect to consider (mainly in electrophoretic measurements) is that the minimum volume of sample to be introduced in the cell for it to be in contact with the electrodes is 0.75 ml. Ultrasonication is frequently used during the sample preparation to remove air bubbles or to breakup particle aggregates, which can lead to erroneous results. In this sense, a careful filling with a syringe is desirable to avoid air bubbles in the cell.

In spite of the limitations in size (particle sizes above 6000 nm provide error messages) we performed size measurements at 25 °C of two diluted suspensions of starch in water, with volume fractions $\phi_{Starch} = 0.001$ and 0.01. Granule size reported in the former case was 5835 ± 2068 nm, and 4727 ± 833 nm for the suspension with $\phi_{Starch} = 0.01$. It is noticeable that in both

cases the results are far from the average diameter obtained in Subsection 3.2.4. However, although these values are not trustworthy, they qualitatively corroborate the process of sedimentation studied with Turbiscan. Consider that these suspensions have two populations of starch particles (small and big granules) and that the proportion between them is the same in both suspensions A and B, corresponding to less and more concentrated, respectively. At a given time (for example, the measuring time) the progress of sedimentation is higher for A so that, compared to the initial situation of well dispersed particles, a lower percentage of particles remain in the supernatant in the case of suspension A. As we know that small particles move quickly than big ones, thus the rate of small to big particles in the supernatant (i.e., where the laser beam shot the suspension) will be lower in suspension A than in suspension B and so the average mean size is higher for the less concentrated suspension.

In order to stablish the range of pH at which starch and carbonyl iron particles are more stable, electrophoretic measurements of both water-based suspensions were carried out in Zetasizer Nano Z device. Zeta potential was determined in a range of buffer solutions with different values of pH and the electric conductivity was adjusted to 400 μS/cm, in order to avoid the variability due to this parameter.

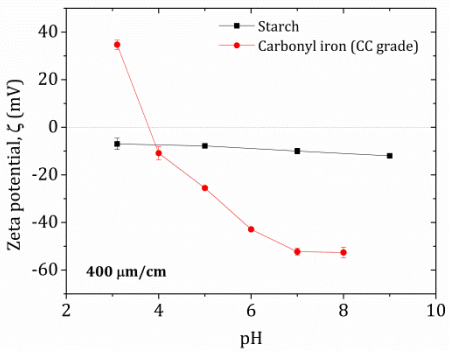

Figure 3.14: Calculated zeta potential ζ (from electrophoretic mobility measurements) as a function of pH for diluted starch and carbonyl iron (CC grade) suspensions in water, with an adjusted conductivity of 400 μm/cm.

Figure 3.14 contains results of ζ as a function of the pH. Starch particles are negatively charged during the whole range of pH, while carbonyl iron particles (CC grade) inverse it above a pH of 3. Therefore, the mixture of these types of particles is more favourable when their charges have the same sign, because of electrostatic repulsion. This circumstance occurs at pH above the

isoelectric point of carbonyl iron. In this sense, suspensions prepared in distilled water will have a good colloidal stability and low tendency to flocculate.

- **Turbiscan**

The analysis of the physical stability of starch suspensions was performed with Turbiscan. This optical technology uses multiple light scattering (i.e., it allows for the characterization of concentrated dispersed media) as well as transmission and backscattering detectors. The transmission detector receives the light, which goes through the sample, while the backscattering detector receives the light scattered backward by the sample. This tool is very useful in the determination of flocculation kinetics and the identification of phenomena such as sedimentation, coalescence or phase separation in emulsions and suspensions.

Two types of instabilities can be found in colloidal systems: particle migration and particle size increase. The former is due to local variations of the concentration, i.e., sedimentation or creaming. The increase in size of the particles can be produced by particle aggregation (flocculation) or fusion (coalescence). These instabilities provoke variations in the transmission and backscattering results.

A range of starch suspensions in water were prepared, with volume fractions being in the range from $\phi_{Starch} = 0.01$ to $\phi_{Starch} = 0.35$. The sample is placed in a transparent cylindrical tube and the detection head progressively scans the entire length of the sample vertically, from the bottom to the top. Transmission and backscattering data were acquired every 40 μm. The detection head is composed of a pulsed near-infrared light source (λ = 850 nm) and two synchronous detectors. In this case, the data acquisition was performed in the automatic mode, scanning the sample every minute. It allows us to study the evolution of the sample and its stability. The filling height was 38 mm.

As example we show in Figure 3.15 the transmission and backscattering profiles obtained for the sample with a cornstarch volume fraction of 0.25. The acquisition time varied between different samples with their concentration. In this case, the steady state was reached around 150 min (see Figure 3.16) and the acquisition time in Figure 3.15 was nearly 200 min. In starch suspensions the phenomenon of particle migration stands out, namely sedimentation, due to the density of starch particles is greater than that of the continuous phase. The sedimentation front due to particle accumulation can

be appreciated in both transmission and backscattering profiles. The peak in transmission separates the phases with different particle concentration formed during the measurement in the top and bottom part of the tube. Regarding to the scattering profile, it increases at the bottom (higher concentration) and decreases in the top (clarification).

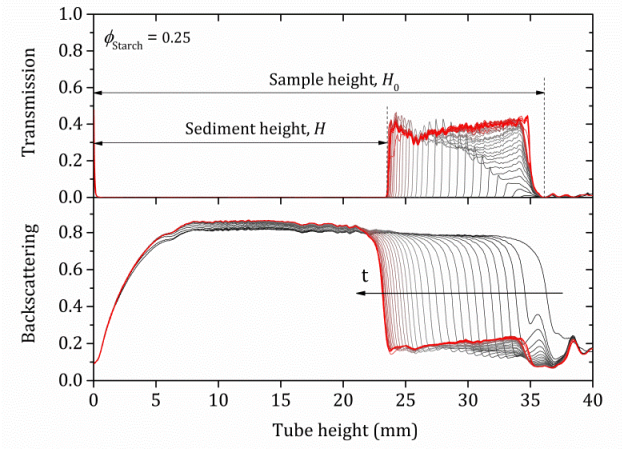

Figure 3.15: Example of transmission and backscattering profiles of a cornstarch suspension in water with $\phi_{Starch} = 0.25$.

The evolution of the absolute thickness in transmission ($H_0 - H$) during the data collection provides the migration rate (from the slope in the linear zone). In Figure 3.16 the temporal evolution of the ratio of sediment height H to the sample height H_0 is shown.

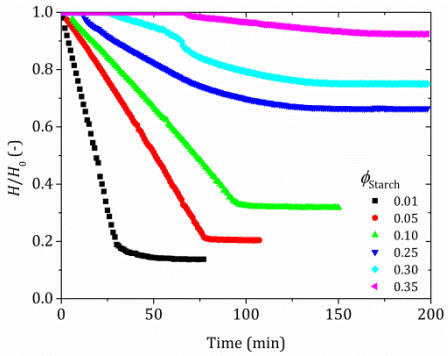

Figure 3.16: Evolution of the sediment height for all the starch suspensions.

The initial part of these curves represents the interval in which migration occurs, the thickness of the transmission profile and the sediment height in-

crease. The greater the slope in this linear section is, the greater the migration rate. In the second part of the curves, sedimentation is lower or even null, the packing fraction is constant.

3.2.6. Contact angle measurement

One of the effective methods to determine the affinity of a drop of liquid (exposed to air) toward the solid substrate where it is deposited is the contact angle θ measurement [50]. This angle is that formed by the intersection of the liquid-air and solid-liquid interfaces and its magnitude is used to calculate the surface tension of the solid material.

The interaction between the substrate and the liquid (i.e., affinity) influences its wetting characteristics and the analysis of the contact angle is associated to the surface energy of the material. If the liquid is water, lower contact angles stand out the hydrophilic nature of the substrate, while for higher values the material surface is considered to be hydrophobic. On the contrary, the interaction between a hydrophobic substrate and a non-polar liquid will provide lower values of contact angles. In summary, contact angles below 90 degrees correspond to high affinity between the drop and the substrate, and above this value the affinity is low.

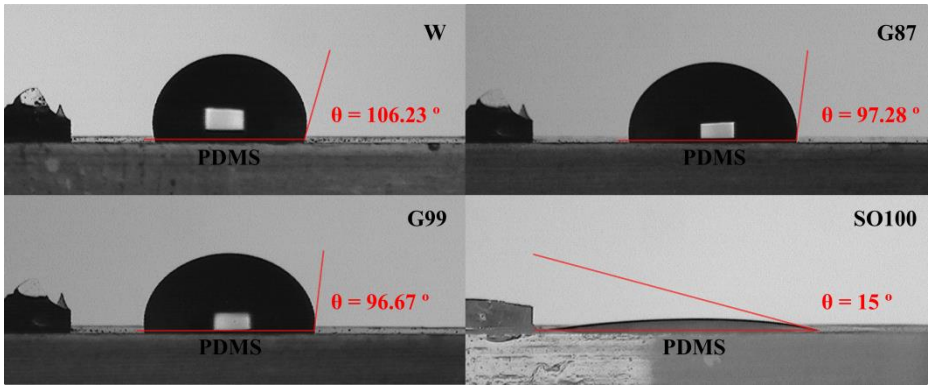

Figure 3.17: Contact angle between a solid surface of PDMS and some Newtonian fluids used as carrier fluids in suspensions of starch particles. From left to right and from top to bottom the liquid droplets are water, glycerol 87 % w/w, glycerol 99 % w/w and silicone oil with viscosity of 100 cSt. The errors in the provided values are shown in Table 7.1.

Contact angle measurements were carried out to account for the wettability of polydimethylsiloxane (PDMS) plates with several carrier fluids in tribological experiments appearing in Chapter 7. These measurements have

to be carried out under very controlled and clean conditions as contact angle is extremely sensitive to impurities.

We performed direct measurement of contact angles using the static sessile drop method at 25 °C. A contact angle goniometer is coupled with a camera that captures the profile of a drop placed over the horizontal surface, and the tangent angle to the drop at the three-phase equilibrium interfacial point is measured with an own software called Contacto. This method is characterized by its simplicity and the small amount of surface area of solid substrates and liquid volume needed to perform the measurement. The program is capable of providing information about the surface tension, drop volume and contact radius.

Figure 3.17 shows the droplet profiles captured during the static sessile drop method carried out with PDMS substrates and several fluids. The value of the measured contact angle appears in the images, and the hydrophobicity of the substrate is confirmed. It is worth noting the low contact angle in the case of the drop of silicone oil (SO100). This value is an approximation and was calculated geometrically, as for such low values the software is not able to measure it accurately. In this case no value was provided by Contacto due to the uncertainty of locating the tangent line in such a flat drop profile.

3.2.7. Calibration of the magnetic field applied by a solenoid

In most measurements in squeeze experiments the magnetic field is applied by the magnetorheological cell. However, in order to determine if a field gradient was affecting the strengthening effect in Subsection 8.5.5. we compared the results using a solenoid with those carried out within the magnetorheological cell, both at low magnetic field (15 mT).

The solenoid employed in these measurements had inner and outer radii of 9 cm and 15.6 cm, respectively, a ring thickness of 3 cm, and the height of turns was 4.5 cm. The use of this coil allows us to work at low magnetic inductions, from 0 to 20 mT. For the calibration of the solenoid a transverse probe has to be placed in the last loop of the magnetic coil, so that the measuring part (there is a mark in the correct position) to be in the centre of the solenoid, where the value of the magnetic field is maximum. First of all, the probe is introduced in a zero flux chamber. Then, the probe is fixed in the suitable position and we measure the magnetic induction as the voltage or intensity is tuned in the power supply.

Solenoid			MR cell		
I (A)	**B (mT)**	**H (kA/m)**	**I (A)**	**B (mT)**	**H (kA/m)**
0.09	0.05	40	0.1	15	11937
3.1	20.7	16473	5	767	610359

Table 3.4: Features of solenoid and magnetorheological cell.

An Instek GPS-1850D power supply was used in the calibration of the solenoid. This is a single output, 90 W, linear DC power supply. The output voltage and intensities range from 0∼18 V and 0∼5 A, respectively. The maximum intensity provided by the power supply is 3 A for this solenoid. In Table 3.4 we compare the magnetic field that can be reached using the solenoid and the magnetorheological cell.

3.3. Simulation methods

In this section, the two types of simulation methods applied during this thesis are carefully explained. Simulations of mixtures of particles (magnetic and non-magnetic) under shear were performed by means of particle-level dynamic simulations. In this case the simulation code was manually developed upon the basis of previous works [51,52] with some modifications. Concerning the second type of simulations, equations involved in EHL method were numerically solved instead.

3.3.1. Interactions in particle-level dynamic simulations

In this subsection we thoroughly describe the pairwise interactions that may be encountered in a concentrated and inertialess system of particles subjected to a constant magnetic field. The fluid is considered as a continuum compared to the particle size so that the solution of the system is indeed the solution of the second Newton's law. Specifically, when both Brownian movement and friction terms contribute to the total force acting on the particles Langevin motion equation is solved.

In the absence of external forces, particles move due to the random Brownian force. Under the application of the magnetic field magnetic particles orient in the direction of the magnetic field while accomplishing the system restrictions of avoiding the particle overlap and remain within the limits of the simulation box. In a later stage the system may be subjected to simple shear. Particles within the simulation box are subjected to an additional force

in x-direction that varies in z-direction (see Figure 1.4). In this sense, the additional velocity is null in the lower limit of the simulation box and maximum in the upper limit. In the case of squeeze, the height of the simulation box is diminished by applying a constant velocity to the system in z direction, so that particles have to reorganize in a changeable-size box. The volume of the simulation box does not change along the simulation time, neither in shear conditions nor in squeeze constant-volume simulations, so that the volume fraction is also maintained. In the last case the simulation box maintains its volume by increasing the other two sides; however, in squeeze constant-area simulations the height diminishes while the length and width remain fix.

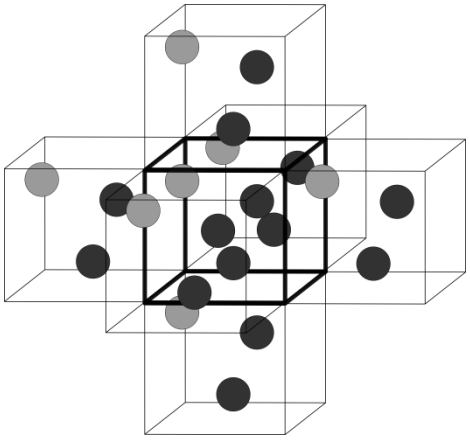

Figure 3.18: Schematic representation of periodic boundary conditions in three dimensions. The unit cell (i.e., the simulation box), with two dark spheres and a light one, is emphasized in the centre of the figure.

Other feature of the particle-level simulations carried out in this thesis is the use of periodic boundary conditions (see Figure 3.18), i.e., the simulation box is repeated in two (squeeze) or three directions (shear), depending on the specific case.

In summary, the simulation process starts by defining some parameters of the system such as the total and partial volume fractions, mean size of the particles and number of particles, viscosity of the carrier fluid, magnetic field vector or maximum simulation time. Then a collection of particles is randomly located within the simulation box. Particle interactions are evaluated and the sum of forces acting on each particle permits the resolution of the equation of motion. With this, particles move to their new positions, where the

forces acting on the system are again evaluated in the new time step. The process is iterated up to the energy of the system reaches a steady value.

- **Equation of motion**

The understanding of the interactions occurring between particles in close proximity is essential in the interpretation of the suspension behaviour. The equation of motion which better describes the interactions between Brownian particles is the Langevin equation. It incorporates the deterministic motion of the particles and additional stochastic forces:

$$m_i \frac{d^2 \boldsymbol{r_i}}{dt^2} = \sum \boldsymbol{F_i^e} + \boldsymbol{F_i^h} + \boldsymbol{F_i^b} \,, \tag{3.16}$$

where m_i is the mass of the particle and $\boldsymbol{r_i}$ the vector from the origin of coordinates to the position of the particle. $\boldsymbol{F_i^e}$ accounts for interparticle and external forces, namely three contributions are considered: magnetic force between magnetic particles $\boldsymbol{F_{ij}^m}$, Hertzian repulsive force $\boldsymbol{F_{ij}^r}$and an exponential wall normal force $\boldsymbol{F_i^w}$ that prevent particle overlap and particle motion beyond the walls, respectively. A cut-off radius is had into account to calculate $\boldsymbol{F_{ij}^m}$ and $\boldsymbol{F_i^w}$ in order to only consider interactions from particles that really contribute to the motion of a given particle i. In the case of the repulsive force, it is only activated when the particle overlap occurs. Hydrodynamic interactions $\boldsymbol{F^h}$ comprise the drag force $\boldsymbol{F_i^S}$, consequence of the relative motion of the particles in the surrounding fluid and approximated by the Stokes' law, and lubrication forces $\boldsymbol{F_i^l}$. The pairwise hydrodynamic lubrication interactions arise between two particles in close contact separated by a small film of fluid, such as it is found in concentrated suspensions, and can be calculated from resistance matrices. The random motion of particles within the fluid due to thermal fluctuations is considered in Brownian force $\boldsymbol{F^b}$.

If inertia is neglected, Equation 3.16 can be written as

$$\xi_i \frac{d\boldsymbol{r_i}}{dt} = \xi_i \boldsymbol{u_i^\infty} + \boldsymbol{F_i^l} + \boldsymbol{F_i^m} + \boldsymbol{F_i^r} + \boldsymbol{F_i^w} + \boldsymbol{F^b} \,, \tag{3.17}$$

where $\xi_i = 3\pi\eta\sigma_i$ is the friction coefficient of particle i, η is the fluid viscosity and σ_i is the particle diameter. In order to solve Equation 3.17 it is convenient to make it dimensionless by means of scaling parameters in Table 3.5:

$$\sigma_i^* \frac{d\boldsymbol{r_i^*}}{dt^*} = \sigma_i^* \boldsymbol{u_i^{\infty *}} + \boldsymbol{F_i^{l*}} + \boldsymbol{F_i^{m*}} + \boldsymbol{F_i^{r*}} + \boldsymbol{F_i^{w*}} + \boldsymbol{F^{b*}} \,. \tag{3.18}$$

Magnitude	Scale	Value
Length	$l_s = \sigma_m$	10^{-6} m
Force	$F_s = F_0 = \frac{3}{16}\,\mu_0\mu_{cr}\pi\sigma_m^2\beta^2H_0^2$	$1.16 \cdot 10^{-8}$ N
Time	$t_s = 3\pi\eta\sigma_m^2/F_0$	$8.15 \cdot 10^{-7}$ s
Pressure	$P_s = F_0/\sigma_m^2$	11559 Pa
Magnetic field	$H_s = H_0$	177000 A · m^{-1}
Magnetic moment	$m_s = \frac{\pi}{2}\beta H_0\sigma_m^3$	$1.96 \cdot 10^{-13}$ A · m^2

Table 3.5: Scaling parameters used in particle-level simulations.

The solution of the equation of motion provides the position of each particle at each moment. The orientation of the particles can be known by solving the rotational equation of motion, which relates the moment of inertia I_i of the particles with the sum of the torques $\boldsymbol{T}$ they are subjected to. In this sense, torque plays the same role in generating the angular momentum that force with linear (or translational) momentum:

$$I_i \frac{d\boldsymbol{\Omega_i}}{dt} = \sum \boldsymbol{T_i^e} + \boldsymbol{T_i^h} + \boldsymbol{T_i^b}\,, \tag{3.19}$$

where $\boldsymbol{\Omega_i}$ is the angular velocity of the particle, and superscripts have the same meaning than in the translational equation of motion.

- **Hydrodynamic interaction**

Hydrodynamic interactions comprise both Stokes' drag $\boldsymbol{F_i^S}$ and lubrication forces $\boldsymbol{F_{ij}^l}$:

$$\boldsymbol{F_i^h} = \boldsymbol{F_i^S} + \sum_{\boldsymbol{j \neq i}} \boldsymbol{F_{ij}^l}\,. \tag{3.20}$$

In a recent work [53], it was demonstrated that taking into account pairwise hydrodynamic interactions (i.e., lubrication) is only necessary if the related stress is the main contribution to the total stress. In the opposite case, there is no risk in ignoring hydrodynamic interactions.

Stokes' drag forces and torques can be expressed as

$$\begin{aligned} \boldsymbol{F_i^S} &= -3\pi\eta\sigma_i\left(\frac{d\boldsymbol{r_i}}{dt} - \boldsymbol{u_i^\infty}\right) = -3\pi\eta\sigma_i\boldsymbol{v_i}\,, \\ \boldsymbol{T_i^S} &= -\pi\eta\sigma_i^3(\boldsymbol{\Omega_i} - \boldsymbol{\Omega_i}^\infty) = -\pi\eta\sigma_i^3\boldsymbol{\omega_i}\,, \end{aligned} \tag{3.21}$$

with $\frac{d\boldsymbol{r_i}}{dt}$ being the velocity of the particle, $\boldsymbol{u_i^\infty}$ the velocity of the carrier fluid at the centre of the particle i in the absence of particles, and $\boldsymbol{v_i}$ is the vector of the difference. Analogously, $\boldsymbol{\omega_i}$ is the difference between the angular velocity of the particle $\boldsymbol{\Omega_i}$ and the vorticity of the fluid in the position of the particle $\boldsymbol{\Omega_i}^\infty$.

The description of the lubrication forces between two bodies is thoroughly explained by Kim and Karrila [55]. Lubrication forces are expressed as a linear combination of translational motion, rotational motion and shearing flow (first, second and third term, respectively), each contribution multiplied by its related resistance matrix:

$$\begin{pmatrix} \boldsymbol{F_{ij}^l} \\ \boldsymbol{F_{ji}^l} \end{pmatrix} = -\eta \begin{pmatrix} \boldsymbol{A_{ii}} & \boldsymbol{A_{ij}} \\ \boldsymbol{A_{ji}} & \boldsymbol{A_{jj}} \end{pmatrix} \begin{pmatrix} \boldsymbol{v_i} \\ \boldsymbol{v_j} \end{pmatrix} - \eta \begin{pmatrix} \widetilde{\boldsymbol{B}}_{\boldsymbol{ii}} & \widetilde{\boldsymbol{B}}_{\boldsymbol{ij}} \\ \widetilde{\boldsymbol{B}}_{\boldsymbol{ji}} & \widetilde{\boldsymbol{B}}_{\boldsymbol{jj}} \end{pmatrix} \begin{pmatrix} \boldsymbol{\omega_i} \\ \boldsymbol{\omega_j} \end{pmatrix} + \eta \begin{pmatrix} \widetilde{\boldsymbol{G}}_{\boldsymbol{ii}} & \widetilde{\boldsymbol{G}}_{\boldsymbol{ij}} \\ \widetilde{\boldsymbol{G}}_{\boldsymbol{ji}} & \widetilde{\boldsymbol{G}}_{\boldsymbol{jj}} \end{pmatrix} : \begin{pmatrix} \boldsymbol{E^\infty} \\ \boldsymbol{E^\infty} \end{pmatrix}. \tag{3.22}$$

In the last expression $\boldsymbol{E}^\infty$ is the rate-of strain tensor, and the components A and $\tilde{B}$ of the resistance matrices are tensors of rank 2, while $\tilde{G}$ has rank 3. For the case of particles with axisymmetric geometry, as spheres, the components of these tensors are defined [55] as

$$\begin{aligned} A_{\alpha\beta}^{ij} &= X_{ij}^A \hat{r}_\alpha \hat{r}_\beta + Y_{ij}^A \left(\delta_{\alpha\beta} - \hat{r}_\alpha \hat{r}_\beta\right), \\ B_{\alpha\beta}^{ij} &= -Y_{ij}^B \varepsilon_{\alpha\beta\gamma} \hat{r}_\gamma, \\ G_{\alpha\beta\gamma}^{ij} &= -X_{ij}^G \left(\hat{r}_\alpha \hat{r}_\beta - \frac{1}{3}\delta_{\alpha\beta}\right)\hat{r}_\gamma - Y_{ij}^G \left(\hat{r}_\alpha \delta_{\beta\gamma} + \hat{r}_\beta \delta_{\alpha\gamma} - 2\hat{r}_\alpha \hat{r}_\beta \hat{r}_\gamma\right). \end{aligned} \tag{3.23}$$

It is worth noting that indices i and j refer to particles, while α, β and γ refer to the component of the tensors. The unitary vector of the relative position of particle i with respect to particle j is $\hat{\boldsymbol{r}} = \frac{\boldsymbol{r_i} - \boldsymbol{r_j}}{|\boldsymbol{r_i} - \boldsymbol{r_j}|} = \frac{\boldsymbol{r_{ij}}}{|\boldsymbol{r_{ij}}|}$. Besides, the elements of the resistance matrix obey the following symmetric relationships: $A_{\alpha\beta}^{ij} = A_{\beta\alpha}^{ji}$, $B_{\alpha\beta}^{ij} = \tilde{B}_{\beta\alpha}^{ji}$, and $G_{\alpha\beta\gamma}^{ij} = \tilde{G}_{\gamma\alpha\beta}^{ji}$. The near field forms of the resistance functions for translation, rotation and shear are expressed as

Translation:

$$X_{ii}^A = 12\pi a_i \frac{\lambda^2}{(1+\lambda)^3}\frac{1}{\varepsilon}, \qquad X_{jj}^A = X_{ii}^A(\lambda^{-1}), \tag{3.24}$$

$$X_{ij}^{A} = -12\pi a_i \frac{\lambda^2}{(1+\lambda)^3}\frac{1}{\varepsilon}\,, \qquad X_{ji}^{A} = X_{ij}^{A}(\lambda^{-1})\,,$$
$$Y_{ii}^{A} = \frac{8}{5}\pi a_i \frac{\lambda(2+\lambda+2\lambda^2)}{(1+\lambda)^3}\ln\frac{1}{\varepsilon}\,, \qquad Y_{jj}^{A} = Y_{ii}^{A}(\lambda^{-1})\,, \tag{3.25}$$
$$Y_{ij}^{A} = -\frac{8}{5}\pi a_i \frac{\lambda(2+\lambda+2\lambda^2)}{(1+\lambda)^3}\ln\frac{1}{\varepsilon}\,, \qquad Y_{ji}^{A} = Y_{ij}^{A}(\lambda^{-1})\,;$$

Rotation:

$$Y_{ii}^{B} = -\frac{4}{5}\pi a_i^2 \frac{\lambda(4+\lambda)}{(1+\lambda)^2}\ln\frac{1}{\varepsilon}\,, \qquad Y_{jj}^{B} = -Y_{ii}^{B}(\lambda^{-1})\,,$$
$$Y_{ij}^{B} = \frac{4}{5}\pi a_i^2 \frac{\lambda(4+\lambda)}{(1+\lambda)^2}\ln\frac{1}{\varepsilon}\,, \qquad Y_{ji}^{B} = -Y_{ij}^{B}(\lambda^{-1})\,; \tag{3.26}$$

Shear:

$$X_{ii}^{G} = 12\pi a_i^2 \frac{\lambda^2}{(1+\lambda)^3}\frac{1}{\varepsilon}\,, \qquad X_{jj}^{G} = -X_{ii}^{G}(\lambda^{-1})\,,$$
$$X_{ij}^{G} = -12\pi a_i^2 \frac{\lambda^2}{(1+\lambda)^3}\frac{1}{\varepsilon}\,, \qquad X_{ji}^{G} = -X_{ij}^{G}(\lambda^{-1})\,,$$
$$Y_{ii}^{G} = \frac{2}{5}\pi a_i^2 \frac{\lambda(4-\lambda+7\lambda^2)}{(1+\lambda)^3}\ln\frac{1}{\varepsilon}\,, \qquad Y_{jj}^{G} = -Y_{ii}^{G}(\lambda^{-1})\,, \tag{3.27}$$
$$Y_{ij}^{G} = -\frac{2}{5}\pi a_i^2 \frac{\lambda(4-\lambda+7\lambda^2)}{(1+\lambda)^3}\ln\frac{1}{\varepsilon}\,, \qquad Y_{ji}^{G} = -Y_{ij}^{G}(\lambda^{-1})\,.$$

The distance between the surfaces of two interacting particles is given by a normalized parameter $\varepsilon = \frac{|\boldsymbol{r}_{ij}|-a_i-a_j}{(a_i-a_j)/2}$, a_i and a_j accounts for the particle radius, and $\lambda = \sigma_j/\sigma_i$ is the ratio between diameters of the involved particles. Note that only the leading terms in previous expressions were considered (i.e., ε^{-1} and $\ln\varepsilon^{-1}$), as in the case of concentrated suspensions ε will be very small.

From now on the lubrication force $\boldsymbol{F_{ij}^{l}}$ acting on particle i due to particle j is exposed, after combining Equations from 3.22 to 3.26. Translational $\boldsymbol{F_{ij}^{l,t}}$, rotational $\boldsymbol{F_{ij}^{l,r}}$ and shear $\boldsymbol{F_{ij}^{l,s}}$ terms are separately described below:

$$\boldsymbol{F_{ij}^{l,t}} = -\eta X_{ii}^{A}\boldsymbol{v}_{i\perp} - \eta X_{ij}^{A}\boldsymbol{v}_{j\perp} - \eta Y_{ii}^{A}\boldsymbol{v}_{i\parallel} - \eta Y_{ij}^{A}\boldsymbol{v}_{j\parallel} = \tag{3.28}$$

$$= 6\pi\eta\sigma_i \frac{\lambda^2}{(1+\lambda)^3}\frac{1}{\varepsilon}\left(\boldsymbol{v}_{j\perp} - \boldsymbol{v}_{i\perp}\right) +$$

$$+\frac{4}{5}\pi\eta\sigma_i \frac{\lambda(2+\lambda+2\lambda^2)}{(1+\lambda)^3}\ln\frac{1}{\varepsilon}\left(\boldsymbol{v}_{j\parallel} - \boldsymbol{v}_{i\parallel}\right);$$

$$\boldsymbol{F}_{\boldsymbol{ij}}^{\boldsymbol{l,r}} = -\eta Y_{ii}^{B}(\boldsymbol{\omega_i}\wedge\hat{\boldsymbol{r}}) - \eta Y_{ji}^{B}\left(\boldsymbol{\omega_j}\wedge\hat{\boldsymbol{r}}\right) =$$

$$= \frac{\pi}{5}\eta\sigma_i^2\frac{\lambda(4+\lambda)}{(1+\lambda)^2}\ln\frac{1}{\varepsilon}(\boldsymbol{\omega_i}\wedge\hat{\boldsymbol{r}}) + \frac{\pi}{5}\eta\sigma_i^2\frac{\lambda^2(4+\lambda)}{(1+\lambda)^2}\ln\frac{1}{\varepsilon}\left(\boldsymbol{\omega_j}\wedge\hat{\boldsymbol{r}}\right);$$

$$\boldsymbol{F}_{\boldsymbol{ij}}^{\boldsymbol{l,s}} = -\eta\dot{\gamma}\left(X_{ii}^{G} + X_{ji}^{G}\right)\boldsymbol{E_1} - \eta\dot{\gamma}\left(Y_{ii}^{G} + Y_{ji}^{G}\right)\boldsymbol{E_2} =$$

$$= -3\pi\eta\sigma_i^2\dot{\gamma}\frac{\lambda^2}{(1+\lambda)^2}\frac{1}{\varepsilon}\boldsymbol{E_1} - \frac{\pi}{5}\eta\sigma_i^2\dot{\gamma}\frac{\lambda(2+\lambda+2\lambda^2)}{(1+\lambda)^2}\ln\frac{1}{\varepsilon}\boldsymbol{E_2};$$

where $\boldsymbol{E_1} = \frac{\mathbf{1}}{\dot{\gamma}}(\hat{\boldsymbol{r}}\hat{\boldsymbol{r}}\colon \boldsymbol{E}^{\infty})\hat{\boldsymbol{r}} = \frac{\boldsymbol{x_{ij}z_{ij}}}{\boldsymbol{r_{ij}^2}}\hat{\boldsymbol{r}}$, and $\boldsymbol{E_2} = \frac{\mathbf{2}}{\dot{\gamma}}(\boldsymbol{E}^{\infty}\cdot\hat{\boldsymbol{r}} - (\hat{\boldsymbol{r}}\hat{\boldsymbol{r}}\colon \boldsymbol{E}^{\infty})\hat{\boldsymbol{r}})$.

These equations can be normalized by considering the scales of Table 3.5:

$$\boldsymbol{F}_{\boldsymbol{ij}}^{\boldsymbol{l,t*}} = -2\sigma_i^*\frac{\lambda^2}{(1+\lambda)^3}\frac{1}{\varepsilon}\boldsymbol{v}_{\boldsymbol{ij}\perp}^* - \frac{4}{15}\sigma_i^*\frac{\lambda(2+\lambda+2\lambda^2)}{(1+\lambda)^3}\ln\frac{1}{\varepsilon}\boldsymbol{v}_{\boldsymbol{ij}\parallel}^*;$$

$$\boldsymbol{F}_{\boldsymbol{ij}}^{\boldsymbol{l,r*}} = \frac{\sigma_i^{*2}}{15}\frac{\lambda(4+\lambda)}{(1+\lambda)^2}\ln\frac{1}{\varepsilon}(\boldsymbol{\omega}_{\boldsymbol{i}}^*\wedge\hat{\boldsymbol{r}}) +$$

$$+\frac{\sigma_i^{*2}}{15}\frac{\lambda^2(4+\lambda)}{(1+\lambda)^2}\ln\frac{1}{\varepsilon}\left(\boldsymbol{\omega}_{\boldsymbol{j}}^*\wedge\hat{\boldsymbol{r}}\right); \qquad (3.29)$$

$$\boldsymbol{F}_{\boldsymbol{ij}}^{\boldsymbol{l,s*}} = -\sigma_i^{*2}\dot{\gamma}^*\frac{\lambda^2}{(1+\lambda)^2}\frac{1}{\varepsilon}\boldsymbol{E_1} - \frac{\sigma_i^{*2}}{15}\dot{\gamma}^*\frac{\lambda(2+\lambda+2\lambda^2)}{(1+\lambda)^2}\ln\frac{1}{\varepsilon}\boldsymbol{E_2};$$

$$\boldsymbol{F}_{\boldsymbol{ij}}^{\boldsymbol{l*}} = \boldsymbol{F}_{\boldsymbol{ij}}^{\boldsymbol{l,t*}} + \boldsymbol{F}_{\boldsymbol{ij}}^{\boldsymbol{l,r*}} + \boldsymbol{F}_{\boldsymbol{ij}}^{\boldsymbol{l,s*}},$$

where $\boldsymbol{v_{ij\perp}} = \boldsymbol{v_{i\perp}} - \boldsymbol{v_{j\perp}}$.

It can be demonstrated that the lubrication force on particle j due to particle i is $\boldsymbol{F}_{\boldsymbol{ji}}^{\boldsymbol{l*}} = -\boldsymbol{F}_{\boldsymbol{ij}}^{\boldsymbol{l*}}$, and that lubrication forces diverge for particles in contact, i.e., for $\varepsilon = 0$.

Similarly to the development of the lubrication force, the torque on particles of the system can be obtained from the linear combination of analogous resistance matrices. After some algebra and using $F_0\sigma_m$ as the torque scale, the total torque that particle j exerts to the particle i, and vice versa are, is given by:

$$\boldsymbol{T}_{\boldsymbol{ij}}^{\boldsymbol{l}*} = \frac{\sigma_i^*}{15}\frac{\lambda(4+\lambda)}{1+\lambda}\left[\frac{1}{1+\lambda}\hat{\boldsymbol{r}} \wedge \boldsymbol{v}_{\boldsymbol{ij}}^* - \frac{2\sigma_i^*}{4+\lambda}\boldsymbol{\omega}_{\boldsymbol{i}\parallel}^* - \frac{\lambda\sigma_i^*}{2(4+\lambda)}\boldsymbol{\omega}_{\boldsymbol{j}\parallel}^* + \right.$$
$$\left. + \frac{\sigma_i^*\dot{\gamma}^*}{4}(2\hat{\boldsymbol{r}} \wedge \boldsymbol{E}_{\boldsymbol{2}})\right]\ln\frac{1}{\varepsilon}\,;$$
$$\boldsymbol{T}_{\boldsymbol{ji}}^{\boldsymbol{l}*} = \frac{\sigma_i^*}{15}\frac{\lambda^2(4+\lambda)}{1+\lambda}\left[\frac{1}{1+\lambda}\hat{\boldsymbol{r}} \wedge \boldsymbol{v}_{\boldsymbol{ij}}^* - \frac{\sigma_i^*}{2(4\lambda+1)}\boldsymbol{\omega}_{\boldsymbol{i}\parallel}^* - \right. \tag{3.30}$$
$$\left. - \frac{2\lambda\sigma_i^*}{4\lambda+1}\boldsymbol{\omega}_{\boldsymbol{j}\parallel}^* + \frac{\sigma_i^*\dot{\gamma}^*}{4}(2\hat{\boldsymbol{r}} \wedge \boldsymbol{E}_{\boldsymbol{2}})\right]\ln\frac{1}{\varepsilon}.$$

Now we focus on the translational equation of motion for the case of two particles and resolve the values of velocities of each particle. The interaction force $\boldsymbol{F}^{\boldsymbol{int}}$, due to the sum of magnetic, repulsive, wall and Brownian forces, is balanced to the negative sum of hydrodynamic forces:

$$\boldsymbol{F}_{\boldsymbol{12}}^{\boldsymbol{int}} = 3\pi\eta\sigma_1\boldsymbol{v}_{\boldsymbol{1}} + \eta X_{11}^A(\boldsymbol{v}_{\boldsymbol{1}\perp} - \boldsymbol{v}_{\boldsymbol{2}\perp}) + \eta Y_{11}^A(\boldsymbol{v}_{\boldsymbol{1}\parallel} - \boldsymbol{v}_{\boldsymbol{2}\parallel})\,,$$
$$\boldsymbol{F}_{\boldsymbol{21}}^{\boldsymbol{int}} = 3\pi\eta\sigma_2\boldsymbol{v}_{\boldsymbol{2}} + \eta X_{22}^A(\boldsymbol{v}_{\boldsymbol{2}\perp} - \boldsymbol{v}_{\boldsymbol{1}\perp}) + \eta Y_{22}^A(\boldsymbol{v}_{\boldsymbol{2}\parallel} - \boldsymbol{v}_{\boldsymbol{1}\parallel})\,, \tag{3.31}$$
$$\boldsymbol{F}_{\boldsymbol{21}}^{\boldsymbol{int}} = -\boldsymbol{F}_{\boldsymbol{12}}^{\boldsymbol{int}}\,.$$

The normal and tangential parts of these forces, divided by $3\pi\eta\sigma_1$, are given by:

$$\overline{\boldsymbol{F}_{\boldsymbol{12}}^{\boldsymbol{h}\perp}} = \boldsymbol{v}_{\boldsymbol{1}\perp}\left(1 + \overline{X_{11}^A}\right) - \boldsymbol{v}_{\boldsymbol{2}\perp}\overline{X_{11}^A}\,,$$
$$-\overline{\boldsymbol{F}_{\boldsymbol{12}}^{\boldsymbol{h}\perp}} = -\boldsymbol{v}_{\boldsymbol{1}\perp}\overline{X_{22}^A} + \boldsymbol{v}_{\boldsymbol{2}\perp}\left(\lambda + \overline{X_{22}^A}\right),$$
$$\overline{\boldsymbol{F}_{\boldsymbol{12}}^{\boldsymbol{h}\parallel}} = \boldsymbol{v}_{\boldsymbol{1}\parallel}\left(1 + \overline{Y_{11}^A}\right) - \boldsymbol{v}_{\boldsymbol{2}\parallel}\overline{Y_{11}^A}\,, \tag{3.32}$$
$$-\overline{\boldsymbol{F}_{\boldsymbol{12}}^{\boldsymbol{h}\parallel}} = \boldsymbol{v}_{\boldsymbol{1}\parallel}\overline{Y_{22}^A} - \boldsymbol{v}_{\boldsymbol{2}\parallel}\left(\lambda + \overline{Y_{22}^A}\right),$$

where the dimensionless parameters $\bar{X}$and $\bar{Y}$ are defined as $\bar{X} = X/3\pi\sigma_1$ and likewise $\bar{Y} = Y/3\pi\sigma_1$. This system of four equations with four unknowns can be straightforward solved as

$$\boldsymbol{v}_{\boldsymbol{1}\perp} = \frac{\lambda\overline{\boldsymbol{F}_{\boldsymbol{12}}^{\boldsymbol{h}\perp}}}{\lambda + \overline{X_{11}^A}(\lambda+1)}\,, \qquad \boldsymbol{v}_{\boldsymbol{2}\perp} = -\frac{\overline{\boldsymbol{F}_{\boldsymbol{12}}^{\boldsymbol{h}\perp}}}{\lambda + \overline{X_{11}^A}(\lambda+1)}\,,$$
$$\boldsymbol{v}_{\boldsymbol{1}\parallel} = \frac{\lambda\overline{\boldsymbol{F}_{\boldsymbol{12}}^{\boldsymbol{h}\parallel}}}{\lambda + \overline{Y_{11}^A}(\lambda+1)}\,, \qquad \boldsymbol{v}_{\boldsymbol{2}\parallel} = \frac{\overline{\boldsymbol{F}_{\boldsymbol{12}}^{\boldsymbol{h}\parallel}}}{\lambda + \overline{Y_{11}^A}(\lambda+1)}\,. \tag{3.33}$$

Similarly, the particle velocities can be solved for systems with more than two particles. In this case the particle velocity is the sum of the velocity of the

medium and the contribution from the rest of particles of the systems, i.e., $\boldsymbol{u_i} - \boldsymbol{u}_\infty = \boldsymbol{v_i} = \sum_{i\neq j} \boldsymbol{v_{ij}} = \boldsymbol{v_{ij}} + \sum_{k\neq i,j} \boldsymbol{v_{ik}}$. As an approximation to calculate $\boldsymbol{v_{ij}}$, the $\boldsymbol{v_{ik}}$ contributions will be considered of the previous instant of time$\boldsymbol{v_{ik}^0}$. The equation of motion takes the form:

$$\sum_{j\neq i} \boldsymbol{F_{ij}^{int}} = 3\pi\eta\sigma_i \sum_{i\neq j} \boldsymbol{v_{ij}} + \eta X_{ii}^A \left(\boldsymbol{v_{i\perp}} - \boldsymbol{v_{j\perp}}\right) + \eta Y_{ii}^A \left(\boldsymbol{v_{i\parallel}} - \boldsymbol{v_{j\parallel}}\right). \tag{3.34}$$

The superposition principle permits the obtaining of a system of equations equivalently to the case of two particles, and the solution of the particle velocities are given by:

$$\begin{aligned}
\boldsymbol{v_{ij\perp}} &= \frac{\lambda\left(\overline{\boldsymbol{F_{ij}^{int\perp}}} - \overline{X_{ii}^A} \sum(\boldsymbol{v_{ik\perp}^0} - \boldsymbol{v_{jk\perp}^0})\right)}{\lambda + \overline{X_{ii}^A}(\lambda+1)}, \\
\boldsymbol{v_{ji\perp}} &= \frac{-\overline{\boldsymbol{F_{ij}^{int\perp}}} - \overline{X_{ii}^A} \sum(\boldsymbol{v_{jk\perp}^0} - \boldsymbol{v_{ik\perp}^0})}{\lambda + \overline{X_{ii}^A}(\lambda+1)}, \\
\boldsymbol{v_{ij\parallel}} &= \frac{\lambda\left(\overline{\boldsymbol{F_{ij}^{int\parallel}}} - \overline{X_{ii}^A} \sum(\boldsymbol{v_{ik\parallel}^0} - \boldsymbol{v_{jk\parallel}^0})\right)}{\lambda + \overline{X_{ii}^A}(\lambda+1)}, \\
\boldsymbol{v_{ji\parallel}} &= \frac{-\overline{\boldsymbol{F_{ij}^{int\parallel}}} - \overline{X_{ii}^A} \sum(\boldsymbol{v_{jk\parallel}^0} - \boldsymbol{v_{ik\parallel}^0})}{\lambda + \overline{X_{ii}^A}(\lambda+1)}.
\end{aligned} \tag{3.35}$$

- **Magnetic interactions**

In the case of having an isolate magnetizable particle, dipolar approximation is valid and the magnetic moment of a given particle is $\boldsymbol{m_i} = \frac{\pi}{2}\beta \boldsymbol{H_0} \sigma_i^3$, where $\beta = \left(\mu_{pr} - \mu_{cr}\right)/(\mu_{pr} + 2\mu_{cr})$ is called contrast factor and is related to the relative magnetic permeabilities of particles μ_{pr} and the continuous medium μ_{cr}. However, the local field $\boldsymbol{H_{loc_i}}$ [52,56,57] at the centre of a magnetic particle i is the sum of the external magnetic field $\boldsymbol{H_0}$ and the dipolar field contribution from the rest of magnetic particles $\boldsymbol{H_{m_j}}$. In this work local magnetic field is considered, so that magnetic moment can be expressed as follows:

$$\boldsymbol{m_i} = \frac{\pi}{2}\beta \boldsymbol{H_{loc_i}} \sigma_i^3, \tag{3.36}$$

$$\boldsymbol{H_{loc,i}} = \boldsymbol{H_0} + \sum_{j\neq i}^{N_{pc}} \boldsymbol{H_{m_j}}, \tag{3.37}$$

$$\boldsymbol{H}_{\boldsymbol{m_j}} = \frac{3(\boldsymbol{m_j} \cdot \hat{\boldsymbol{r}})\hat{\boldsymbol{r}} - \boldsymbol{m_j}}{r_{ij}^3} \,, \tag{3.38}$$

where $\hat{\boldsymbol{r}}$ is the radial unit vector from particle j to particle i, with modulus $r_{ij} = |\boldsymbol{r_{ij}}|$. Figure 3.19 schematically shows the simulation box used in particle-level simulations for the case of mixtures of particles. The magnetic cut-off distance of particle i is shown in the sketch. As expected, non-magnetic particles (with null magnetic moment) do not contribute to the magnetic force acting on the magnetic particle i, even being positioned within the magnetic cut-off radius.

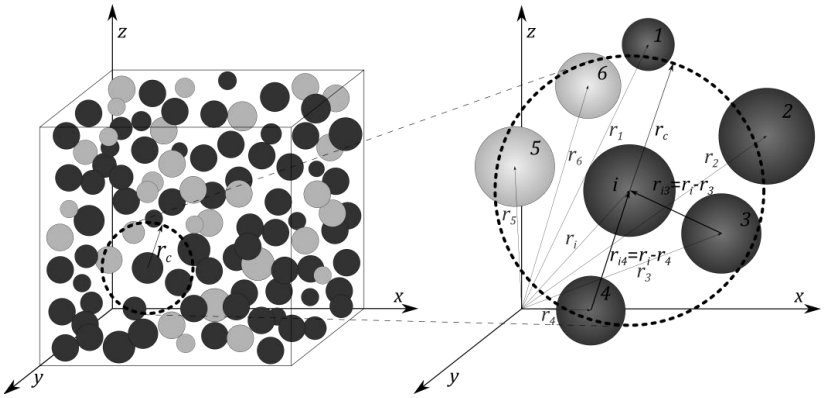

Figure 3.19: Schematic simulation box for mixtures of particles. Note that not all particles contribute to a given force acting on particle i; instead only particles with their centre located at a distance smaller than the cut-off radius (3, 4, 5, and 6) take part in the calculation of the force. In this particular case dark and light grey colours represent magnetic and non-magnetic particles, respectively, so that only particles 3 and 4 will have influence in the calculation of magnetic force acting on particle i.

From point-dipole approximation the long-range magnetostatic interaction between two magnetic particles i and j at a distance r_{ij} is:

$$\boldsymbol{F}_{\boldsymbol{ij}}^{\boldsymbol{mag}} = \frac{3}{4}\frac{\mu_0\mu_{cr}}{\pi}\left[\frac{(\boldsymbol{m_i}\cdot\boldsymbol{m_j})\boldsymbol{r_{ij}} + (\boldsymbol{m_i}\cdot\boldsymbol{r_{ij}})\boldsymbol{m_j} + (\boldsymbol{m_j}\cdot\boldsymbol{r_{ij}})\boldsymbol{m_i}}{r_{ij}^5} - 5\frac{(\boldsymbol{m_i}\cdot\boldsymbol{r_{ij}})(\boldsymbol{m_j}\cdot\boldsymbol{r_{ij}})\boldsymbol{r_{ij}}}{r_{ij}^7}\right]. \tag{3.39}$$

If Equations from 3.35 to 3.37 are substituted in Equation 3.38, the normalized magnetic force $\boldsymbol{F}_{\boldsymbol{ij}}^{\boldsymbol{m}^*}$ can be expressed as a function of other dimensionless parameters, as the magnetic local field that each particle feels, particle diameters and distance between them:

$$\boldsymbol{F_{ij}^{m}}^{*} = \sigma_i^{*3}\sigma_j^{*3}\left[\frac{\left(\boldsymbol{H_{loc_i}^{*}}\cdot\boldsymbol{H_{loc_j}^{*}}\right)\boldsymbol{r_{ij}^{*}} + \left(\boldsymbol{H_{loc_i}^{*}}\cdot\boldsymbol{r_{ij}^{*}}\right)\boldsymbol{H_{loc_j}^{*}}}{r_{ij}^{*5}} + \right.$$
$$\left. + \frac{\left(\boldsymbol{H_{loc_j}^{*}}\cdot\boldsymbol{r_{ij}^{*}}\right)\boldsymbol{H_{loc_i}^{*}}}{r_{ij}^{*5}} - 5\frac{\left(\boldsymbol{H_{loc_i}^{*}}\cdot\boldsymbol{r_{ij}^{*}}\right)\left(\boldsymbol{H_{loc_j}^{*}}\cdot\boldsymbol{r_{ij}^{*}}\right)\boldsymbol{r_{ij}^{*}}}{r_{ij}^{*7}}\right]. \tag{3.40}$$

- **Repulsive interactions**

In order to prevent particle overlap a repulsive Hertzian contact force is used [57]. It considers mechanical properties of particles that take part in the contact (Young's modulus E and Poisson's ratio ν) and it is calculated when there exists particle overlap, i.e., when the distance between two particles $h_{ij} = R_i + R_j - \left|\boldsymbol{r_{ij}}\right| < 0$. The radius of i and j particle are R_i and R_j, respectively. The Hertzian interaction is given by this expression:

$$\boldsymbol{F_{ij}^{r}} = \left(\frac{4}{3}E_{eff}\sqrt{R_{eff}}h_{ij}^{\frac{3}{2}}\right)\hat{\boldsymbol{r}}_{\boldsymbol{ij}}\,, \tag{3.41}$$

where $E_{eff} = \left(\frac{\left(1-\nu_i^2\right)}{E_i} + \frac{\left(1-\nu_j^2\right)}{E_j}\right)^{-1}$, $R_{eff} = \frac{R_i R_j}{R_i+R_j}$ and $\hat{\boldsymbol{r}}_{\boldsymbol{ij}} = \frac{\boldsymbol{r_{ij}}}{r_{ij}}$ is the unitary vector in direction of $\boldsymbol{r_{ij}}$. In its dimensionless form, Equation 3.40 changes to:

$$\boldsymbol{F_{ij}^{r}}^{*} = \frac{1}{3}E_{eff}^{*}\sqrt{R_{eff}^{*}}\,h_{ij}^{*\frac{3}{2}}\frac{\boldsymbol{r_{ij}^{*}}}{r_{ij}^{*}}. \tag{3.42}$$

- **Wall interaction**

The short-range wall force avoid particles to leave the simulation box in z-direction as it simulates the upper and bottom plates that confine the sample in experiments in parallel-plate configuration. This repulsive force has an exponential decay with particle separation as it is shown in next equation:

$$\boldsymbol{F_i^{w}}^{*} = e^{-k^{*}\left(h_i^{*}-\sigma_i^{*}/2\right)}\,\hat{\boldsymbol{z}}\,. \tag{3.43}$$

- **Brownian force**

The last contribution to the net force comes from Brownian motion, as

$$\boldsymbol{f_B^{*}} \propto \sqrt{\frac{k_B T}{\sigma_m F_0}}\sqrt{\frac{\sigma_i^{*}}{\Delta t^{*}}}, \tag{3.44}$$

where $k_B = 1.381\cdot 10^{-23}\ \mathrm{J\cdot K^{-1}}$ is the Boltzmann constant and T the absolute temperature expressed in kelvin.

3.3.2. Simulation of mixtures of particles

- **General description of the simulated system**

Magnetorheological suspensions are treated as a mixture of monodisperse (particle diameter of $\sigma = 1$ μm) magnetizable and non-magnetizable spheres in a continuous phase with Newtonian viscosity $\eta = 1\ \mathrm{mPa \cdot s}$. 3D particle-level simulations were carried out over a total number of particles of $N = 1000$. The spheres are confined in a simulation box (see Figure 3.18) of volume $V = L_x^* \times L_y^* \times L_z^*$, which has a vertex coinciding with the origin of the coordinate system. The total number of particles is related to this volume through the particle volume fraction $\phi_T = \frac{\pi\sigma^3 N}{6V}$. Periodic boundary conditions are used in x and y-direction but not in z as in the experimental case the system is bounded by solid surfaces. Sticky boundary conditions are employed to mimic these surfaces, and the height of the simulation box in all simulations was L_z^* = 20. Asterisks denote dimensionless quantities, in this case the length scale is the particle mean diameter σ_m. Parameters used to normalize each magnitude involved in this section are defined in Table 3.5. Four total particle volume fractions were studied, namely ϕ_T = 0.05, 0.10, 0.20 and 0.30, so that dimensions L_x^* and L_y^* of the simulation box change in accordance to the total volume fraction in each case, as L_z^* is fixed. The total volume fraction is the sum of the magnetic ϕ_M and non-magnetic ϕ_N particle volume fractions. Volume fractions of magnetic and nonmagnetic phases used along this work are referred to the total volume fraction, so that they are indeed relative volume fractions ϕ_i', i.e., $\phi_M' = \phi_M/\phi_T$, $\phi_N' = \phi_N/\phi_T$, and $\phi_M' + \phi_N' = 1$. The number of magnetic particle in the simulation box was varied between 50 and 1000 (i.e., $\phi_M' = 0.05 - 1$). Simulation parameters are shown in Table 3.6.

Each initial configuration of particles is generated by randomly placing the N particles in the simulation box (note that a smaller number of particles N provided statistically irrelevant results with noisy data). Forces acting on each particle are evaluated considering cut-off distances. At each simulation time net forces are evaluated for each particle and the equation of motion is solved. Then the particles are moved to their new positions and the process is repeated for the next time steps. Five initial configurations were generated for each mixture of particles (given by ϕ_T and ϕ_M') and averages of these runs were performed.

Type	Parameter	Value
General	Total number of particles	$N = 1000$
	Particle diameter	$\sigma_i = \sigma_m$
	Total volume fraction	ϕ_T = 0.05, 0.10, 0.20, 0.30
	Relative magnetic volume fraction	ϕ'_M =0.05, 0.15, 0.30, 0.50, 0.70, 1
	Height of the simulation box	$L_z = 20\ \sigma_m$
	Temperature	$T = 298$ K
Magnetic interaction	External magnetic field	$\boldsymbol{H_0} = [0, 0, H_0]$ kA/m
	Contrast factor	$\beta(H_0) = 0.706$
	Relative magnetic permeability	$\mu_{cr} = 1$
	Cut-off radius	$co_m = \frac{L_x}{2} = \frac{L_y}{2}$
Hertzian interaction	Young's modulus	$Y_M = 200$ GPa $Y_N = 3.71$ GPa
	Poisson's ratio	$\nu_M = 0.25$ $\nu_N = 0.50$
Hydrodynamic	Continuous medium viscosity	$\eta = 1$ mPa·s
	Shear rates	$\dot{\gamma} = \frac{\dot{\gamma}^*}{t_s} \in [3{\cdot}10^{-3}\text{-}100]/t_s$ s^{-1}
Wall	Exponential coefficient	$k = 100\ \sigma_m$
	Cut-off radius	$co_w = \sigma_i$
Simulation times	Structuration	$t_{ST} = t^*_{ST} t_s = 1000\ t_s$
	Shear	$t_{SH} = t^*_{SH} t_s = 4000\ t_s$

Table 3.6: Simulation parameters used in the simulation code.

- **Simulation procedure**

The simulation method used in mixtures of particles is based on a previous work [51]. The main variation consisted on the consideration of multibody contributions in magnetostatic interactions and the use of a Hertzian repulsive force. On the other hand most of simulations of mixtures of particles were carried out without taking into account lubrication forces, due to inherent higher computational costs. Hydrodynamic lubrication forces, although carefully depicted before, were only incorporated to the simulation code to compare the results with the same system where only Stokes' drag force is considered as hydrodynamic force. In Figure 5.2 the comparison of these two

cases is shown. In this sense, we considered that there was no risk in avoiding the pairwise hydrodynamic interactions as magnetic forces prevail.

The simulation procedure consisted in two stages: structuration at rest followed by a stage at constant shear, both in presence of an uniform magnetic field $\boldsymbol{H_0}$. The simulation time in the structuration step t_{ST}^* was long enough for the system to show a steady state and magnetic particles to be arranged in columnar aggregates. Once this simulation is completed the suspension is subjected to several dimensionless shear rates $\dot{\gamma}^*$ (in the range of $3 \cdot 10^{-3}$ to 100) by means of considering a no null velocity field $\boldsymbol{u_i^{\infty}}^* = \dot{\gamma}^* z_i^* \hat{\boldsymbol{x}}$, that is added to the particle velocity due to the net force. The dimensionless shear stress can be monitored with time in this stress growth test. The time evolution of stress in a start-up test provides a first region where the stress continuously increases, as a consequence of an elastic deformation of the material, up to a critical strain where a peak in the shear stress value is shown. It is the so-called static yield stress. Then the shear stress reaches an equilibrium value at high strain deformations. The main contribution to the dimensionless shear stress comes from the magnetic force, which is calculated following the next expression:

$$\tau_{xz}^{m*} = -\frac{1}{V^*} \sum_{j \neq i}^{N} z_i^* F_{x,i}^{m*} \,. \tag{3.45}$$

For simplicity, the rest of non-hydrodynamic interactions acting on the particles (repulsive, wall and Brownian forces) were not considered in the calculation of the total stress, as their relative relevance compared to magnetostatic interactions was quite low. The total stress was obtained by adding the hydrodynamic contribution from the applied shear to the static magnetic stress. This option was preferred to adding the hydrodynamic contribution to the equilibrium value of the magnetic stress as for low shear rates it takes very long times to achieve the steady state value. However, the maximum is well developed for each dimensionless shear rate in the range of selected simulation times.

Yield stress has been calculated by fitting the curves in rheogram to Casson model ($\sqrt{\tau} = \sqrt{\tau_y} + \sqrt{\eta_p \dot{\gamma}}$) and this value is compared to the yield stress obtained by averaging shear stresses at lower shear rates.

3.3.3. Squeeze simulations

Brownian dynamics simulations were carried out to simulate systems of 1000 monodisperse spherical magnetic particles. The simulation code contains three steps that are equivalent to the experimental protocol: particle structuration, squeeze and shear, while considering a constant magnetic field of $H_0 = 177\ \mathrm{kA \cdot m^{-1}}$ during the whole protocol. Both constant-volume and constant-area squeeze tests were simulated.

The volume fraction was varied among $\phi = 0.05$ and 0.30. We used periodic boundary conditions in x and y directions, and two initial gaps h_i^* were studied, namely 20 and 30 times the mean diameter σ_m, which is employed as a length scale. So that, depending on the initial gap and the volume fraction, the other two dimensions of the simulation box can be easily determined. Particles are randomly distributed in the simulation box and overlap is forbidden. The magnetic dipoles of the particles are supposed to be equal at the onset of the simulation and oriented with the magnetic field, it is, in z axis.

Local magnetic field (Equations from 3.35 to 3.39) is considered in the calculation of the magnetic force between pairs of particles. In this sense, for a given particle its magnetic force is due both to the external magnetic field and the rest of contributions from other particles that surround it at distances lower than a stablished cut-off. Apart from magnetic interactions, Stoke's drag (Equation 3.21) and Brownian forces (Equation 3.43) are taken into account, as well as an exponential repulsive force (Equation 3.45) that decays with particle separation as expressed below:

$$\boldsymbol{F_{ij}^r} = F_0 e^{-k(r_{ij}-(d_i+d_j)/2)} \hat{\boldsymbol{r}}_{\boldsymbol{ij}}\ , \tag{3.46}$$

where F_0 is the force scale (see Table 3.5), $k = 100$ and $r_{ij}$is the center-to-center distance between particles i and j. Besides, all forces are not considered in squeeze simulations.

The Langevin equation if inertia is neglected (Equation 3.17) is solved at each time step and the new particle positions are considered in the next time step. In the structuration step the main contribution to the particle movements comes from magnetic interactions. The normalized time for structuration is sufficient to obtain steady states in the magnetic energy, normal stress, normal force and number of neighbours. After that, the particle configuration is subjected to the squeeze step, in which the gap is steadily forced to diminish at a given velocity, and so the height of the simulation box. The time

during which the gap diminishes depends on the required level of deformation. In constant-volume simulations it provokes an enlargement in the other dimensions of the simulation box, so that particles have to fit in a modified simulation box that keeps the initial volume and, as a consequence, the volume fraction does not vary. On the contrary, in constant-area simulations the gap is diminished, while the other two dimensions preserve their initial lengths so that the simulation box is smaller. As it occurs in the experimental case, particles are confined in the area subjected to the magnetic field and cannot abandon the new simulation box, so that the volume fraction increases with ε in constant-area conditions. Once a given deformation is achieved, the shear flow is activated at constant shear rates. The effect of the compression of the magnetic structures in the static yield stress under shear is compared for both types of simulations.

3.3.4. EHL simulations

We followed two methods to calculate the friction coefficient using numerical simulations: i) a "simplified" solution approach and ii) a "full" solution approach. The notation of dimensional and dimensionless parameters used in EHL simulations is shown in Table 3.7 and Table 3.8, respectively.

In the simplified solution approach the lubricant was considered to be a Newtonian fluid, at a local scale, and regression formulas were used to predict the friction coefficient. In the contact, an effective shear viscosity was estimated using an iterative procedure from the lubricant's rheogram under steady shear. In the full solution approach, by a means of the finite-difference method, we solved the generalized Reynolds equation coupled with the load balance equation and the surface elastic deformation equation. From the full solution, regression equations are proposed for the prediction of the film thickness and friction coefficients for both shear-thinning and shear-thickening fluids.

Dimensional parameters	
a_H	Semi-major axis of Hertzian contact ellipse, (m)
b_H	Semi-minor axis of Hertzian contact ellipse, (m)
E_A, E_B	Elastic modulus of the materials involved in the tribological contact, (Pa)
E'	Effective elastic modulus , $2\left(\frac{1-\nu_A^2}{E_A}+\frac{1-\nu_B^2}{E_B}\right)^{-1}$, (Pa)
R_x, R_x	Equivalent radii in x-direction and y-direction, (m)
h	Film thickness, (m)
h_{cen}, h_{min}	Central and minimum film thickness, respectively, (m)
P	Pressure, (Pa)
p_H	Maximum Hertzian pressure, $3w/2\pi a_H b_H$, (Pa)
u_B, u_A	Velocity of fast and slow moving surfaces, respectively, $(\mathrm{m}\cdot\mathrm{s}^{-1})$
S	Undeformed gap, $\left(\frac{x^2}{2R_x}+\frac{y^2}{2R_y}\right)$, (m)
U	Entrainment speed, $(u_B+u_A)/2$, (m/s)
w	Normal load, (N)
$\dot{\gamma}_c$	Critical shear rate, (s^{-1})
η	Generalized viscosity, $(\mathrm{Pa}\cdot\mathrm{s})$
η_0, η_∞	Low and high shear-rate viscosity, respectively, (Pa s)
η_G	An initial guess viscosity used to make Carreau-Yasuda model dimensionless, $(\mathrm{Pa}\cdot\mathrm{s})$
η_{eff}	An average viscosity obtained from full simulation, $(\mathrm{Pa}\cdot\mathrm{s})$

Table 3.7: Notation of dimensional parameters used in EHL simulations of inelastic non-Newtonian fluids.

Dimensionless parameters	
$\bar{h}$	Dimensionless film thickness, $\bar{h} = hR_x/{b_H}^2$
$\bar{I}_n$	$\bar{I}_n = I_n\eta_G/h^{n+1}$
K	Ellipticity parameter, $K = a_H/b_H$
n	Power-law index in generalized Newtonian viscosity formula
SRR	Slide-to-roll ratio, $SRR = 2\|u_B - u_A\|/(u_\mathrm{B} + u_\mathrm{A})$
$\bar{U}$	Dimensionless speed parameter, $\bar{U} = U\eta_{eff}/E'R_x$
$\bar{U}_0, \bar{U}_\infty$	Low and high shear rate dimensionless speed parameter, $\bar{U}_0 = U\eta_0/E'R_x$, $\bar{U}_\infty = U\eta_\infty/E'R_x$
$\bar{W}$	Dimensionless load parameter, $\bar{W} = w/E'R_x^2$
$\bar{z}$	Dimensionless film coordinate, $\bar{z} = z/h$
$\bar{\dot{\gamma}}$	Dimensionless shear rate, $\bar{\dot{\gamma}} = \dot{\gamma}\eta_G/E'$
$\bar{\dot{\gamma}}_c$	Dimensionless critical shear rate parameter, $\bar{\dot{\gamma}}_c = \dot{\gamma}_c R_x/U$
$\bar{\eta}$	Dimensionless viscosity, $\bar{\eta} = \eta/\eta_G$
$\bar{\eta}_R$	$\bar{\eta}_R = \eta_\infty/\eta_0$
$\bar{\lambda}$	$\bar{\lambda} = U\eta_G R_x^2/{b_H}^3 p_H$
μ	Total friction, $\mu = \mu_P + \mu_C + \mu_D$
μ_P, μ_C	Poiseuille and Couette friction coefficient
μ_D	Elastic deformation contribution to friction
ν_A, ν_B	Poisson's ratio of the materials involved in the contact
$\bar{\phi}_x$	$\bar{\phi}_x = \bar{\rho}\phi\eta_G/\bar{\lambda}h^3$
$\bar{\phi}_y$	$\bar{\phi}_y = \bar{\phi}_x/K^2$
$\bar{\psi}$	$\bar{\psi} = SRR\left(\frac{1}{2} - \frac{\bar{\Pi}_1}{\bar{I}_0}\right)$

Table 3.8: Notation of dimensionless parameters used in EHL simulations of inelastic non-Newtonian fluids.

- **Simplified solution approach**

As a first approach, the viscosity of the lubricant was assumed to be constant in the contact, and solely dictated by the central shear rate (i.e., the sliding speed divided by the central film thickness). In order to estimate the viscosity of the lubricant in the contact, we applied the following procedure. Firstly, for a given sliding velocity, a guess value of the shear rate at the center point was assumed and the corresponding viscosity was calculated from the lubricant's rheogram. Then, the central film thickness was computed using classical regression equations for a Newtonian fluid [58].

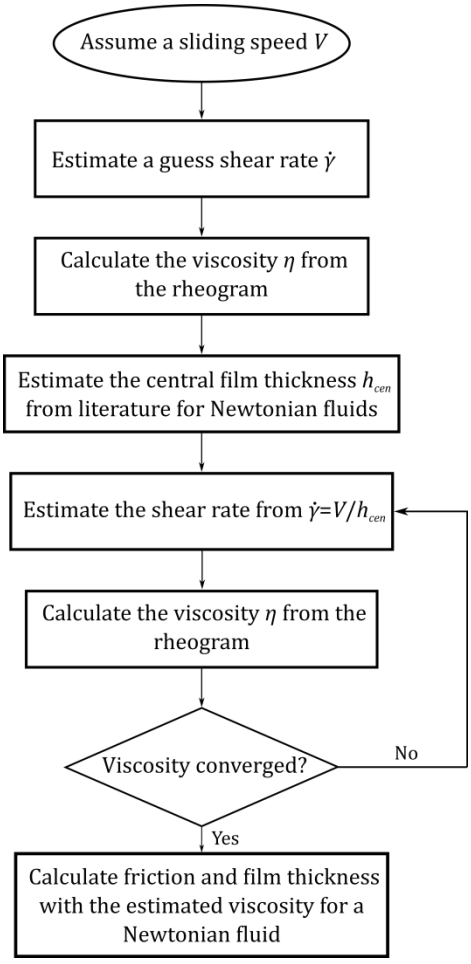

Figure 3.20: Flow chart of the simple solution approach process.

Next, the shear rate was estimated from the ratio between the sliding velocity and the calculated central film thickness. Afterwards, the viscosity was

computed for the calculated shear rate from the prescribed rheogram. In the next step, the calculated viscosity was compared to the initial guess viscosity. If the difference was small, the viscosity was accepted as the final value. Otherwise, the viscosity obtained from the rheogram was considered as a new guess value and the iteration was repeated until convergence reached. Finally, the viscosity obtained from this simple approach was used to estimate both Couette and Poiseuille friction terms using regression formulas [59] for a Newtonian fluid (see Equations from 3.52 to 3.54 below). The flow chart corresponding to this simple solution approach is shown in Figure 3.20:

- **Full solution approach**

The generalized Reynolds equation for the case of an I-EHL point contact lubricated by an inelastic incompressible non-Newtonian fluid at steady-state is given by [60,61]:

$$\frac{\partial}{\partial x}\left(\phi\frac{\partial p}{\partial x}\right)+\frac{\partial}{\partial y}\left(\phi\frac{\partial p}{\partial y}\right)=U\frac{\partial}{\partial x}\left[h(1+\psi)\right]. \tag{3.47}$$

The lubricant flow is contained in the xy plane and the film thickness points along the z-direction. $U=(u_B+u_A)/2$ is the entrainment speed in the flow direction and u_B and u_A denotes the velocity of the two shearing surfaces in the x-direction for the fast and slow moving surfaces, respectively. The entrainment speed in y-direction is zero ($v_B=v_A=0$). The integral functions in Equation 3.46 are given by $\phi=\int_0^h\frac{z}{\eta}\left(z-\frac{I_1}{I_0}\right)dz$ and $\psi=SRR\left(\frac{1}{2}-\frac{\Pi_1}{I_0}\frac{1}{h}\right)$, where $\Pi_1=\int_0^h\frac{z}{\eta}dz$ and $I_n=\int_0^h\frac{z^n}{\eta}dz$. Here, SRR is the slide-to-roll ratio. For a Newtonian fluid $\frac{\Pi_1}{I_0}=\frac{I_1}{I_0}=\frac{h}{2}$, $\psi=0$, and $\phi=\frac{h^3}{12\eta}$. Hence, for a Newtonian fluid (seeEquation 3.46) reduces to the classical Reynolds equation.

The generalized Reynolds equation has to be solved simultaneously with the elastic deformation equation

$$D(x,y)=\frac{2}{\pi E'}\int\int\frac{pdx'dy'}{\sqrt{(x'-x)^2+(y'-y)^2}}, \tag{3.48}$$

and the force balance equation over the solution domain Ω

$$\iint_\Omega pdxdy=w. \tag{3.49}$$

The film thickness is given by summation of the undeformed gap between the surfaces and the elastic deformation as follows:

$$h(x,y) = h_0 + S(x,y) + D(x,y)\,, \tag{3.50}$$

where h_0 is a constant that determines the distance between two remote points in the solids and $S(x,y)$ is the parabolic approximation of the undeformed gap. The Reynolds equation (Equation 3.46) was transformed into a dimensionless form using the parameters given in Table 3.8 as follows:

$$\frac{\partial}{\partial \bar{x}}\left(\bar{\phi}_x \frac{\partial \bar{p}}{\partial \bar{x}}\right) + \frac{\partial}{\partial \bar{y}}\left(\bar{\phi}_y \frac{\partial p}{\partial y}\right) = \frac{\partial}{\partial \bar{x}}\left(\bar{\rho}\bar{h}(1+\bar{\psi})\right) + \frac{\partial}{\partial \bar{t}}\left(\bar{\rho}\bar{h}\right). \tag{3.51}$$

- **Rheological constitutive equation of the lubricant**

In the I-EHL regime, the elastic deformation of the solids is substantial if compared to the film thickness of the lubricant separating the surfaces. However, the contact pressure is low enough to invoke any significant change in the lubricant viscosity. Therefore, the effect of pressure on the lubricant viscosity is negligible. Nevertheless, in the case of inelastic non-Newtonian fluids it is necessary to take into account the shear rate dependence of the viscosity to adequately predict the film thickness and the pressure distribution in the contact. Here, the viscosity of the lubricant was modelled using the double-Newtonian Carreau-Yasuda expression:

$$\eta = \eta_\infty + \frac{\eta_0 - \eta_\infty}{\left[1 + \left(\frac{\dot{\gamma}}{\dot{\gamma}_c}\right)^2\right]^{\frac{1-n}{2}}}, \tag{3.52}$$

where η_0 and η_∞ denote the low and high shear viscosity plateau, respectively. $\dot{\gamma} = \left\|\frac{du}{dz}\right\|$ is the magnitude of the shear rate tensor; note that $\frac{dv}{dz}$ is zero. The velocity gradient across the film thickness is $\frac{du}{dz} = \frac{1}{\eta}\left[\frac{\partial p}{\partial x}\left(z - \frac{I_1}{I_0}\right) + \frac{U \cdot SRR}{I_0}\right]$. $\dot{\gamma}_c$ is a critical shear rate that defines the departure from the low-shear viscosity region and the onset of the power-law region. n is the viscosity index and determines the slope of the viscosity in the transition region. For the special case of a zero second Newtonian viscosity, the slope of power-law is given by $n - 1$.

According to Equation 3.50, either $n = 1$ or $\eta_0 = \eta_\infty$ denote Newtonian fluids. For $n \neq 1$, the fluid is shear thinning if $\eta_\infty < \eta_0$, and shear-thickening if $\eta_0 < \eta_\infty$. A lower value of the viscosity index n, i.e., higher slope, implies a sharper change from the low shear to the high shear viscosity regions, which means a stronger shear-thickening/thinning behaviour.

- **Numerical procedure**

In order to numerically solve Equation 3.49 we used a hybrid line relaxation method [62], with a central second order discretization for the Poiseuille term and an upstream second order discretization for the wedge/squeeze term. The integration was performed across the film thickness using Simpson's rule with 18 mesh points. The simulation began with an initial guess for the pressure p_G (in particular, a Hertzian dry contact distribution with us a_H), approaching distance h_0 and viscosity guess η_G. p_G and h_0 were updated during relaxation but η_G was only used for transforming Reynolds equation into dimensionless form and was kept constant. Independently of the initial η_G, the procedure converged to a unique solution. However, a good guess value, close to the final viscosity solution at the central point, accelerated the convergence.

The numerical procedure was as follows. (i) At each mesh point in the computational domain, an average viscosity was obtained by iteration at 18 nodes across the film thickness using Simpson's rule. Then, the integral functions $\bar{I}_0$, $\bar{I}_1$, and $\overline{\Pi}_1$ were evaluated at each mesh point in the computational domain. The parameters $\bar{\phi}_x$, $\bar{\phi}_y$, $\bar{\psi}$ were computed and the pressure was updated iteratively using a hybrid line relaxation scheme until the relative error in pressure was below 10^{-4}. (ii) Next, the relative error in the normal load was calculated and the load equilibrium equation (Equation 3.47) was used to correct the approaching distance. (iii) The loops (i) and (ii) were repeated until reaching a relative error less than 10^{-4} in both pressure and load. To ensure fully-flooded conditions with a uniform mesh, the computational domain had a size of $4a_H$ in the inlet and $2a_H$ in the outlet region.

Simulations were carried out at different values of viscosity index (n), low-shear-rate viscosity (η_0), high-shear-rate viscosity (η_∞), critical shear rate ($\dot{\gamma}_c$), slide-to-roll ratio (SRR), entrainment speed (U), and normal load (w) for each lubricant.

- **Friction coefficient calculation**

Rolling and sliding are two mechanisms that are responsible for the transfer of frictional stresses between two contacting lubricated surfaces [63]. Adhesion of the contacting asperities at low velocities and the Couette flow of the lubricant film in the contact at large velocities are the two main sources of sliding friction. Furthermore, the rolling friction has two main components, one contribution arising from deformation/elastic hysteresis [64], and the

other one coming from Poiseuille flow of the lubricant in the contact at large velocities. Since interfacial adhesion is negligible when surfaces are separated by fluid film, Couette μ_C, Poiseuille μ_P, and elastic hysteresis μ_D terms are the only three contributions that are needed to determine the total friction coefficient μ in the hydrodynamic regime.

From the solution of the generalized Reynolds equations and the elastic deformation equations (Equation 3.46 and 3.47, respectively), both Couette τ_C and Poiseuille τ_P contributions to the shear stress, over the fast moving surface, can be obtained as follows:

$$\tau_C = -\frac{SRR \cdot U}{I_0}, \tag{3.53}$$

$$\tau_P = -\frac{\partial p}{\partial x}\left(h - \frac{I_1}{I_0}\right). \tag{3.54}$$

Furthermore, in the particular case of a sphere-on-flat contact, the friction coefficient contribution coming from elastic hysteresis (i.e., deformation energy losses) can be estimated as follows [63]:

$$\mu_D = \alpha \frac{3}{16}\frac{a_H}{R}, \tag{3.55}$$

where R is the sphere radius and α is the loss factor. The loss factor is given by $\alpha = k\pi\tan(\delta)$ where k is a constant in the range of 1-3 and the loss tangent $\tan(\delta)$ is reported to be 0.11 for PDMS tribopairs [64].

In the particular case of Newtonian fluids, regression equations were obtained in [59] for both Couette and Poiseuille contributions to the friction coefficient. The regression equations are:

$$\mu_{\mathrm{C}} = SRR(3.8\overline{U}^{0.71}\overline{W}^{-0.76} + 0.96\overline{U}^{0.36}\overline{W}^{-0.11}), \tag{3.56}$$

$$\mu_{\mathrm{P}} = 1.46\overline{U}^{0.65}\overline{W}^{-0.70}. \tag{3.57}$$

These two equations together with Equation 3.54 were used in the simplified solution approach to predict the friction coefficient.

3.4. References

[1] BeMiller J N and Huber K C 2011 Starch *Ullmann's Encyclopedia of Industrial Chemistry* (Wiley-VCH Verlag GmbH & Co. KGaA)

[2] Bertoft E 2017 Understanding starch structure: recent progress *Agronomy* **7** 56

[3] Vamadevan V and Bertoft E 2014 Structure-function relationships of starch components *Starch - Stärke* **67** 55–68

[4] BeMiller J N and Whistler R L 2009 *Starch: chemistry and technology* (London: Academic Press)

[5] Pratsinis S E 1998 Flame aerosol synthesis of ceramic powders *Prog. Energy Combust. Sci.* **24** 197–219

[6] Flörke O W, Graetsch H A, Brunk F, Benda L, Paschen S, Bergna H E, Roberts W O, Welsh W A, Libanati C, Ettlinger M, Kerner D, Maier M, Meon W, Schmoll R, Gies H and Schiffmann D 2008 Silica *Ullmann's Encyclopedia of Industrial Chemistry* ed Wiley-VCH Verlag GmbH & Co. KGaA (Weinheim, Germany: Wiley-VCH Verlag GmbH & Co. KGaA)

[7] Raghavan S R and Khan S A 1997 Shear-thickening response of fumed silica suspensions under steady and oscillatory shear *J. Colloid Interface Sci.* **185** 57–67

[8] Raghavan S R, Walls H J and Khan S A 2000 Rheology of silica dispersions in organic liquids: new evidence for solvation forces dictated by hydrogen bonding *Langmuir* **16** 7920–7930

[9] Warren J, Offenberger S, Toghiani H, Pittman C U, Lacy T E and Kundu S 2015 Effect of temperature on the shear-thickening behavior of fumed silica suspensions *ACS Appl. Mater. Interfaces* **7** 18650–18661

[10] Royer J R, Blair D L and Hudson S D 2016 Rheological signature of frictional interactions in shear thickening suspensions *Phys. Rev. Lett.* **116**

[11] de Vicente J, Klingenberg D J and Hidalgo-Álvarez R 2011 Magnetorheological fluids: a review *Soft Matter* **7** 3701

[12] Ashour O, Rogers C A and Kordonsky W 1996 Magnetorheological fluids: materials, characterization, and devices *J. Intell. Mater. Syst. Struct.* **7** 123–30

[13] Bombard A J F, Knobel M, Alcantara M R and Joekes I 2002 Evaluation of magnetorheological suspensions based on carbonyl iron powders *J. Intell. Mater. Syst. Struct.* **13** 471–478

[14] Ashtiani M, Hashemabadi S H and Ghaffari A 2015 A review on the magnetorheological fluid preparation and stabilization *J. Magn. Magn. Mater.* **374** 716–730

[15] Boczkowska A, Awietjan S F, Pietrzko S and Kurzydłowski K J 2012 Mechanical properties of magnetorheological elastomers under shear deformation *Compos. Part B Eng.* **43** 636–40

[16] Jolly M R, Carlson J D, Muñoz B C and Bullions T A 1996 The magnetoviscoelastic response of elastomer composites consisting of ferrous particles embedded in a polymer matrix *J. Intell. Mater. Syst. Struct.* **7** 613–622

[17] Choi H J, Park B J, Cho M S and You J L 2007 Core-shell structured poly(methyl methacrylate) coated carbonyl iron particles and their magnetorheological characteristics *J. Magn. Magn. Mater.* **310** 2835–7

[18] Fang F F and Choi H J 2007 Polymeric nanobead coated carbonyl iron particles and their magnetic property *Phys. Status Solidi A* **204** 4190–3

[19] Ulicny J C, Snavely K S, Golden M A and Klingenberg D J 2010 Enhancing magnetorheology with nonmagnetizable particles *Appl. Phys. Lett.* **96** 231903

[20] Klingenberg D J and Ulicny J C 2011 Enhancing magnetorheology *Int. J. Mod. Phys. B* **25** 911–917

[21] Powell L A, Wereley N M and Ulicny J 2012 Magnetorheological fluids employing substitution of nonmagnetic for magnetic particles to increase yield stress *IEEE Trans. Magn.* **48** 3764–3767

[22] Abdoulaye Fall 2008 *Rhéophysique des fluides complexes: Ecoulement et Blocage de suspensions concentrées* (Université Paris 7)

[23] Merkt F S, Deegan R D, Goldman D I, Rericha E C and Swinney H L 2004 Persistent holes in a fluid *Phys. Rev. Lett.* **92**

[24] de Vicente J, Stokes J R and Spikes H A 2005 Lubrication properties of non-adsorbing polymer solutions in soft elastohydrodynamic (EHD) contacts *Tribol. Int.* **38** 515–26

[25] Garrec D A and Norton I T 2012 The influence of hydrocolloid hydrodynamics on lubrication *Food Hydrocoll.* **26** 389–397

[26] Ruiz-López J A, Hidalgo-Alvarez R and de Vicente J 2016 A micromechanical model for magnetorheological fluids under slow compression *Rheol. Acta* **55** 215–21

[27] Macosko C W 1994 *Rheology: principles, measurements, and applications* (New York: VCH)

[28] Steffe J F 1992 *Rheological methods in food process engineering* (East Lansing, Mich. USA: Freeman Press)

[29] Dzuy N Q and Boger D V 1985 Direct yield stress measurement with the vane method *J. Rheol.* **29** 335–47

[30] Rabia A, Yahiaoui S, Djabourov M, Feuillebois F and Lasuye T 2014 Optimization of the vane geometry *Rheol. Acta* **53** 357–371

[31] R. J. Poole 2016 Measuring normal-stresses in torsional rheometers: a practical guide. *Rheol. Bull.* **57 (2)** 36–46

[32] López-López M T, Kuzhir P, Caballero-Hernández J, Rodríguez-Arco L, Duran J D G and Bossis G 2012 Yield stress in magnetorheological suspensions near the limit of maximum-packing fraction *J. Rheol.* **56** 1209

[33] Vagberg D and Tighe B P 2017 On the apparent yield stress in non-Brownian magnetorheological fluids *Soft Matter* **13** 7207–7221

[34] Morillas J R and de Vicente J 2019 Yielding behavior of model magnetorheological fluids *Soft Matter* **15** 3330–42

[35] Barnes H A and Walters K 1985 The yield stress myth? *Rheol. Acta* **24** 323–6

[36] Barnes H A 1999 The yield stress—a review or "παντα ρει"—everything flows? *J. Non-Newton. Fluid Mech.* **81** 133–178

[37] Bonn D and Denn M M 2009 Yield stress fluids slowly yield to analysis *Science* **324** 1401–2

[38] Dinkgreve M, Denn M M and Bonn D 2017 "Everything flows?": elastic effects on startup flows of yield-stress fluids *Rheol. Acta* **56** 189–194

[39] Moller P, Fall A, Chikkadi V, Derks D and Bonn D 2009 An attempt to categorize yield stress fluid behaviour *Philos. Trans. R. Soc. Math. Phys. Eng. Sci.* **367** 5139–55

[40] Coussot P 2014 Yield stress fluid flows: A review of experimental data *J. Non-Newton. Fluid Mech.* **211** 31–49

[41] Ovarlez G, Cohen-Addad S, Krishan K, Goyon J and Coussot P 2013 On the existence of a simple yield stress fluid behavior *J. Non-Newton. Fluid Mech.* **193** 68–79

[42] Dinkgreve M, Paredes J, Denn M M and Bonn D 2016 On different ways of measuring "the" yield stress *J. Non-Newton. Fluid Mech.* **238** 233–241

[43] Barnes H 1996 A review of the slip (wall depletion) of polymer solutions, emulsions and particle suspensions in viscometers: its cause, character, and cure *Int. J. Multiph. Flow* **22** 132

[44] Cloitre M and Bonnecaze R T 2017 A review on wall slip in high solid dispersions *Rheol. Acta* **56** 283–305

[45] Yoshimura A and Prud'homme R K 1988 Wall slip corrections for Couette and parallel disk viscometers *J. Rheol.* **32** 53–67

[46] Ahmed H. Helal 2016 *Designing devices using electro-active yield stress fluids* (Massachusetts Institute of Technology)

[47] Babick F 2016 *Suspensions of colloidal particles and aggregates* (Springer International Publishing)

[48] Malvern Instruments 2003 Zetasizer Nano Series: User Manual (MAN0317)

[49] Hunter R J 1981 The calculation of zeta potential *Zeta Potential in Colloid Science* (Elsevier) pp 59–124

[50] Hebbar R S, Isloor A M and Ismail A F 2017 Contact angle measurements *Membrane Characterization* (Elsevier) pp 219–255

[51] Fernández-Toledano J C, Ruiz-López J A, Hidalgo-Álvarez R and de Vicente J 2015 Simulations of polydisperse magnetorheological fluids: A structural and kinetic investigation *J. Rheol.* **59** 475–98

[52] Ruiz-López J A, Hidalgo-Álvarez R and Vicente J de 2016 A micromechanical model for magnetorheological fluids under slow compression *Rheol. Acta* **55** 215–221

[53] Lagger H G, Breinlinger T, Korvink J G, Moseler M, Renzo A D, Maio F D and Bierwisch C 2015 Influence of hydrodynamic drag model on shear stress in the simulation of magnetorheological fluids *J. Non-Newton. Fluid Mech.* **218** 16–26

[54] Lagger H G, Breinlinger T, Korvink J G, Moseler M, Di A, Di F and Bierwisch C 2015 Influence of hydrodynamic drag model on shear stress in the simulation of magnetorheological fluids *J. NON-Newton. FLUID Mech.* **218** 16–26

[55] Sangtae Kim S J K 1991 *Microhydrodynamics* (Elsevier)

[56] Martin J E and Anderson R A 1996 Chain model of electrorheology *J. Chem. Phys.* **104** 4814–4827

[57] Lagger H G, Bierwisch C, Korvink J G and Moseler M 2014 Discrete element study of viscous flow in magnetorheological fluids *Rheol. Acta* **53** 417–43

[58] Hamrock B, Schmid S and Jacobson B 2004 *Fundamentals of fluid film lubrication* (CRC Press)

[59] de Vicente J, Stokes J R and Spikes H A 2005 The frictional properties of Newtonian fluids in rolling–sliding soft-EHL contact *Tribol. Lett.* **20** 273–86

[60] Katyal P and Kumar P 2014 On the role of second Newtonian viscosity in EHL point contacts using double Newtonian shear-thinning model *Tribol. Int.* **71** 140–148

[61] Dowson D 1962 A generalized Reynolds equation for fluid-film lubrication *Int. J. Mech. Sci.* **4** 159–170

[62] Shahrivar K and de Vicente J 2014 Ferrofluid lubrication of compliant polymeric contacts: effect of non-homogeneous magnetic fields *Tribol. Lett.* **56** 281–92

[63] Myant C, Spikes H A and Stokes J R 2010 Influence of load and elastic properties on the rolling and sliding friction of lubricated compliant contacts *Tribol. Int.* **43** 55–63

[64] Timm K, Myant C, Spikes H A and Grunze M 2011 Particulate lubricants in cosmetic applications *Tribol. Int.* **44** 1695–1703

II

Results and discussion

4. Shear thickening in unimodal suspensions

4.1. Introduction

Suspensions of solid particles present a non-linear behaviour, which is dependent on many factors such as the chemical and physical particle features, their interactions with the fluid, the total and relative volume fraction in case of hybrid systems, or external fields. The majority of these suspensions present a shear-thinning behaviour, in which their resistance to flow decreases with the shear rate. However, in the case of highly concentrated systems the suspensions can exhibit shear thickening (ST), which is an increase in viscosity with the applied shear rate or stress [1–3], so that ST fluids are a type of non-Newtonian fluid. These counter-intuitive fluids are commonly prepared in Newtonian carriers where colloidal and nonaggregating particles are dispersed or suspended at moderate or high concentrations, such as cornstarch, silica or calcium carbonate, among others [4]. Apart from these simple formulations, some additives can be incorporated to obtain a smart fluid with a combined response [5–9]. Among them, the use of magnetic particles leads to a multi-phase system that is called magnetorheological shear-thickening fluid (MRSTF) [10,11], which may exhibit both shear-thickening and magnetorheological effects. Thus, the rheological behaviour of these bimodal smart mate-

rials can be modulated by means of the applied magnetic field and the loading conditions. However, to the authors' knowledge the formulation of shear-thickening fluids uniquely fabricated with unimodal magnetic particles has been scarcely studied [12]. Moreover, this concentrated magnetorheological fluid could, a priori, be modelled easily compared to mixtures of particles.

The phenomenon of shear thickening is an important concern in industrial processes and the applications of these complex fluids are related to energy dissipation systems, such as dampers, sandwich structures and body armour [13]. The amount of energy that can be dissipated in form of heat through the fluid is proportional to its viscosity, so that a higher viscosity (either by passive or field-active fluids) implies a better selectivity. Both the onset and intensity of this regime can be tuned with the precise knowledge in suspension rheology. This fact would help us to adapt the fluid conditions to our necessities for each practical application.

One of the earliest works on the shear-thickening behaviour correspond to Metzner and Whitlock [14], who compiled all the available quantitative data on dilatancy (volume expansion). For his part, Barnes [15] concluded in his review that in the appropriate range of shear rate a concentrated suspension of nonaggregating solid particles would always result in reversible shear-thickening behaviour. Although the terms shear thickening and dilatancy are connected and were used as synonyms, dilatancy is necessary but not sufficient for observing a strong shear thickening.

Scientists have been trying to understand the mechanisms which lead the shear-thickening phenomenon for decades. Hoffman [16] developed a micromechanical model of ST as a flow-induced order-disorder transition, which involves particles of the suspensions being in a layered orientation that is disrupted as a consequence of increasing hydrodynamic forces acting on the particles. Other researchers supported the concept of the formation of transient arrangements of particles, called hydroclusters, that develop at strong flow conditions and lead to increased lubrication drag forces between particles [17]. Other mechanism that could lead shear thickening is dilation, as it appeared in the pioneering works of Metzner and Whitlock, in which both phenomena were thought as only one. Dilation recovered attention again after the work of Brown and Jaeger [18]. They established that in conditions of confinement that may frustrate the dilation of the suspension, a restoring force is transmitted along the system by means of frictional interactions which would enable a dramatic increase in viscosity. Among these

mechanisms, the hydroclusters theory was broadly though to be the main responsible for the occurrence of this phenomenon up to the recent idea of a transition from hydrodynamically lubricated to frictional contacts. In fact, a purely hydrodynamic effect provokes a mild ST (known as continuous, CST) in less densely packed systems, but it is not sufficient to give rise to the strong or discontinuous shear thickening (DST) occurring when the volume fraction approaches the maximum packing fraction. Nowadays, new advances and improvements in computational methods are permitting very good agreements with experimental results when considering friction as an important ingredient in the appearance of shear thickening. Thanks to that, both continuous and discontinuous shear thickening are being reproduced in a satisfactory manner [19–22].

The arrangement of particles in a suspension evolves when it is subjected to shear, according to the predominant contributions to the stress at each stage. At rest, particles will move randomly as Brownian motion dominates the total force on the colloid, resulting in an isotropic microstructure. When the suspension is subjected to shear flow, hydrodynamic forces gain relevance and microstructural changes occur in the suspension, which becomes anisotropic. However, if concentration and shear rates are high enough, frictional contact networks are formed because of a predominant frictional contribution [19,23,24], compared to the hydrodynamic interactions. In terms of the first normal stress difference N_1 (see Subsection 3.2.1), moderate shear rates result in negative values of this parameter, while when the role played by friction is significant enough, this leads to a transition in the sign of N_1, from negative to positive, which means that dilation is taking place.

In this work we address the study of the rheological behaviour of concentrated suspensions subjected to shear flow. The first approach to the shear-thickening behaviour was carried out by considering model shear-thickening colloids based on starch or fumed silica particles. Due to the strong coupling with shear stress, special attention will be paid to the normal force evolution in the shear-thickening region. The evolution of the viscosity and normal force behaviour, as well as the differences found between both types of systems, is explained in terms of the type of particle involved in each suspension, its deformability and roughness. The second part is devoted to the shear-thickening response in concentrated magnetorheological suspensions. In this sense, several volume fractions, carrier fluids and magnetic field strengths were explored. These features play important roles in the onset of the shear-

thickening region and the appearance of dilation when frictional contacts overcome the hydrodynamic contribution.

4.2. Materials and methods

4.2.1. Materials

We studied two prototypical shear-thickening systems, it is, cornstarch in water and fumed silica in ethylene glycol. Later, magnetorheological suspensions were prepared in several carrier fluids and characterized on the rheometer under different applied magnetic fields.

In the case of the starch suspensions, starch from corn particles (73 % amylopectin and 27 % amylose from Sigma Aldrich, density = 1.68 $g \cdot cm^{-3}$, mean particle diameter around 10.7 μm) were suspended in distilled water. The density mismatch was not corrected as no sedimentation was observed during the measurements, and the samples were well re-dispersed and homogenized before carrying out the tests. The range of particle volume fractions studied was $\phi_{Starch} = 0.30 - 0.44$.

Hydrophilic fumed silica from Sigma Aldrich was used (size of aggregates 0.2-0.3 μm, surface area 200 ± 25 m^2/g) and suspended in ethylene glycol (Sigma Aldrich, density 1.113 g cm^{-3}). We estimated the density of this solid as 1.80 $g \cdot cm^{-3}$ in the calculations of the volume fraction of the samples. Fumed silica is obtained from the burning of silicon tetrachloride in a flame of hydrogen and oxygen. It consists of branched aggregates formed by 10 to 30 fused spherical particles of SiO_2. In presence of polar liquids, their molecules interact via hydrogen bonds with the surface hydroxyls groups in the silica aggregates. The concentration of fumed silica suspensions varied from $\phi_{FS} = 0.032$ to 0.171. Above the upper limit, corresponding to a 25 % w/w, the manual mixing become very complicated.

In the preparation of the MR suspensions we used carbonyl iron particles obtained from BASF SE Germany (EW grade). The effect of the concentration of particles was explored in a moderate-high range, i.e., $\phi_{EW} = 0.30 - 0.50$. These particles have a thin silica coating that provides them improved stability characteristics in dispersion. The coating contributes to prevent a close interparticle approach and therefore the aggregation in a primary minimum. For comparative purposes we used HS grade particles in concentrated MR suspensions that, in spite of being similar in size to EW grade particles, do not

have any coating. Four different carrier fluids were investigated, namely, two silicone oils with different viscosities (SO20 and SO100), ethylene glycol (EG), and a glycerol-water mixture (G87). The most relevant physical characteristics of these carrier fluids are summarized in Table 4.1. With these four carrier fluids we can elucidate the influence of the chemical composition for two viscosity matched carriers (silicone oil versus ethylene glycol or the glycerol-water mixture), as well as the effect of the viscosity for two carriers of the same constitution.

Fluid	Density (g/ml)	Dynamic viscosity (mPa·s)	Brand
Ethylene glycol (EG)	1.113	16.66	Sigma Aldrich
Glycerine 87 % w/w (G87)	1.23	119	Scharlau
Silicone oil 20 cSt (SO20)	0.95	18.88	Sigma Aldrich
Silicone oil 100 cSt (SO100)	0.968	90.14	Fluka

Table 4.1: Carrier fluid features. The shear viscosities were measured in a cone-plate geometry.

The preparation of these types of suspensions consisted on mixing the required amount of powders and carrier fluid with a spatula, and then exposing them to ultrasounds in order to break the particles aggregates and remove air bubbles. This step is especially important in the case of fumed silica suspensions, where several batches of mixing with spatula and ultrasounds were necessary to obtain homogeneous and transparent suspensions. Moreover, in the case of samples from MR suspensions they were introduced in the planetary mixer with an established protocol, and after that, they were put in the ultrasounds bath for several minutes before each measurement. Sedimentation of magnetic particles is prevented by this sample homogenization before each test.

All experimental data shown in this work were averages of at least three measurements. In the case of starch suspensions, fresh samples were used to carry out all the measurements, as the rheological behaviour of the samples evolved with time, mainly at high concentrations of particles. This situation is mostly thought to be due to the swelling of the starch granules that would gradually lead to a higher volume fraction. So that the range of volume fractions displayed here corresponds to those of the initial situation of the sample. On the contrary, fumed silica suspensions, once the aggregates are com-

pletely dissolved, are more stable in time. We carried out these measurements the day after the sample preparation. MR suspensions presented a much better stability, and their rheological behaviour does not change among measurements carried out in different days if a previous and a correct homogenization process is followed.

4.2.2. Rheometry

All rheological tests were carried out in a MCR501 stress-controlled rheometer from Anton Paar at 25 ºC.

For conventional ST suspensions, i.e., those with cornstarch and fumed silica particles, the geometry used was cone-plate (20 mm diameter, 2º angle, truncation 0.084 mm). The use of this geometry provides a straightforward conversion from torque and rotational speed into shear stress and shear rate. Moreover, it allows to obtain the first normal stress difference ($N_1 = \sigma_{xx} - \sigma_{yy}$) from the normal force acting on the cone ($N_1 = 2F_N/\pi R^2$). The protocol used in these measurements consisted of four steps. The sample was initially subjected to a preshear at a shear rate of $\dot{\gamma} = 1\ \mathrm{s}^{-1}$ to homogenize it. After that, rest is imposed by setting a null shear rate and so the normal force. It helps the sample not to develop normal stresses, by this manner ensuring the sample to be isotropic at the start of the last step. It consisted in applying a logarithmic increase in the torque value from 10^{-4} to 10^{2} mNm. Normal force data is also registered during this step.

In the case of the carbonyl iron based ST suspensions, the parallel-plate configuration was used (20 mm diameter, 0.3 mm gap). As a consequence, raw data from the rheometer was converted into shear rates and stresses by means of the Weissenberg-Rabinowitch correction, previously explained in Subsection 3.2.1. The sample volume employed in these tests was 110 µL. The magnetic field was generated with the aid of an external coil that is capable to apply uniform magnetic fields up to 15 mT. The protocol was as follows: first, the sample was loaded onto the geometry. Next, the magnetic field was suddenly applied and the sample was left at rest during 60 s. Then, a logarithmic ramp in shear stress was applied from 0.1 to 10 kPa.

Wall slip corrections were performed for MR samples, as described in Subsection 3.2.1, although this phenomenon mainly affected the rheological behaviour of these samples at low shear rates, and few changes appeared at high shear rates, where the shear thickening may occur.

4.3. Results and discussion

In this section the shear-thickening response of two model suspensions is analysed, as a first insight into this phenomenon. Then, we study this behaviour in concentrated MR fluids, the effect of the composition of the suspending fluid and the magnetic field strength.

4.3.1. Starch and fumed silica-based suspensions

The rheological behaviour of a suspension displaying shear thickening is displayed in Figure 1.1. In the typical case [1], an initial plateau is found when the particles are in equilibrium and can randomly collide and move at low shear rate or stress. Instead of finding this initial plateau it is possible to have high viscosity at low shear conditions if interparticle attractions are strong, what may indicate a yield stress. Then, we observe a shear-thinning region in which the viscosity of the suspension diminishes as a consequence of the alignment of particles with the flow. This zone is followed by a Newtonian plateau with a nearly constant viscosity. A critical point marks the transition from the Newtonian to the shear-thickening behaviour. It depends on volume fraction in the case of the critical shear rate but not in the related critical shear stress. The increase in viscosity at high shear rate or stress can be mild or more abrupt depending on the volume fraction. In this zone the hydrodynamic contribution leads to the formation of transient particle aggregates (hydroclusters) that prevails at moderate concentrations, while the contribution of contact friction to the shear thickening is more relevant at high volume fractions. Once the system has reached its maximum value of viscosity, a Newtonian plateau or a second shear-thinning region is found.

- **Effect of concentration, particle size and roughness**

Shear viscosity as a function of the shear stress for starch and fumed silica suspensions at several volume fractions is shown in Figure 4.1. The viscosity curves of these model suspensions slightly vary. At low shear rates, starch suspensions show an intense shear-thinning region while in the case of fumed silica the decrease in viscosity is much more moderate and a near Newtonian behaviour is observed within a great interval of shear stresses.

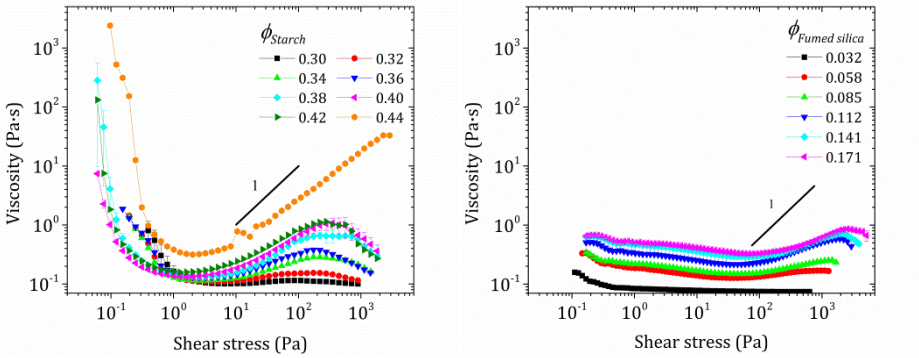

Figure 4.1: Shear viscosity as a function of the shear stress for starch and fumed silica suspensions at different particles loadings.

From the Figure 4.1, it can be observed that the minimum in viscosity appears at a constant value of shear stress around 3 Pa in the starch suspensions (although slightly dependent on the volume fraction) while for the silica case the onset of ST is found at higher critical values. On the other hand, the shear stress corresponding to the maximum viscosity increases with the loading fraction for both cases, so that the interval of shear stresses in the shear-thickening region enlarges with the concentration of particles. Moreover, according to the fumed silica system the shear-thickening behaviour is more moderate as volume fractions used are lower than the corresponding to starch. Furthermore, once the maximum viscosity is reached in starch suspensions, a second shear-thinning region is observed at high shear rates or stresses, which is also slightly envisaged in the case of fumed silica. This behaviour has been previously reported in fumed silica suspensions using polypropylene glycol as carrier fluid [25]. This region of shear thinning at high shear rates is intimately bounded to the deformability of the particles [26]. On the other hand, this region occurs in the context of frictional rheology, and the friction coefficient was found to decrease as normal load increases, so that the critical volume fraction for the divergence in viscosity increases [27]. In contrast, for colloidal systems with near hard-spheres the existence of a constant viscosity plateau after the increase in viscosity (i.e., in the shear-thickening state, STS) has been found [24,28].

Curves in Figure 4.2 show the critical shear stress and shear rate related to the minimal viscosity of the curves, as this point is the onset of the, at least, a moderate shear thickening. It can be observed that in the case of starch the critical values continuously decrease while the onset of the shear thickening

for fumed silica varies little with volume fraction [18,29]. This difference in behaviour is probably due to the effect of particle roughness on suspension rheology, which has been studied in a recent work [30]. They have found that the stress onset for ST is independent of volume fraction only in the case of smooth particles [24]. This agrees with our results because, although little, a dependence with concentration is observed in the critical stress of starch suspensions. The irregularly faceted surfaces of cornstarch granules contribute to the roughness in these particles, what would result in a not constant stress onset. Considering the case of fumed silica, both critical points (if omitting the point corresponding to the minimum volume fraction) are nearly constant for the range of volume fraction studied. Moreover, as it was expected, the critical values for starch are lower than for fumed silica, as they scale inversely with the particle size [15,29].

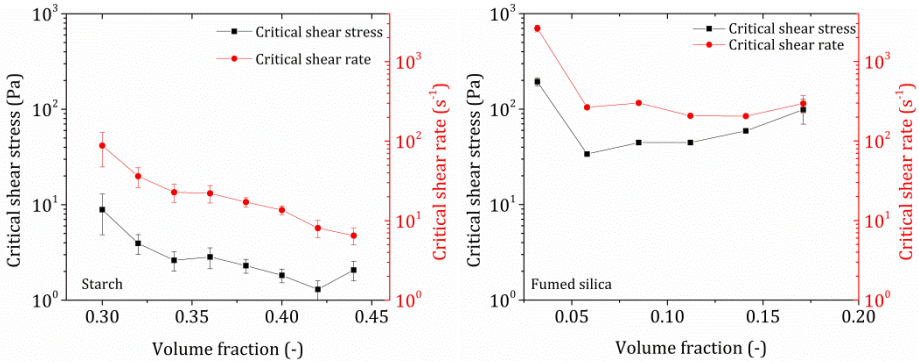

Figure 4.2: Critical shear stress and shear rate as a function of particle concentration for starch (left) and fumed silica suspensions (right).

The intensity of the thickening effect is a feature that can depends on several factors. For example, it increases with the particle volume fraction [1,15,31] and with the particle roughness [30,32,33]. This steepness can be characterized by means of the slope (β) of the curves in this zone, in a viscosity versus shear stress plot on a log-log scale ($\eta \propto \sigma^{\beta}$). In the Newtonian case, the slope is zero and progressively increases with volume fraction and the appearance of ST behaviour. The onset of the abrupt discontinuous shear thickening (DST) is reflected when this slope takes the value of unity. At intermediate situations, the increase in viscosity is mild, which corresponds to continuous shear thickening (CST). The linear fit to these slopes provides the values of β for each volume fraction, which is plotted in Figure 4.3.

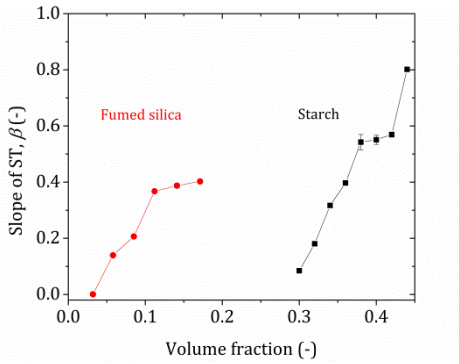

Figure 4.3: Beta parameter as a function of the volume fraction for starch and fumed silica suspensions.

In the starch suspensions the value of beta for the highest concentration measured reaches a value of 0.802 ± 0.006, which means that in all our suspensions shear thickening is still continuous. The value corresponding to the fumed silica is lower as the range of volume fraction studied is also lower. Compared to the Royer's work [24], for a given particle concentration, beta parameter is higher for both of our systems that for their micrometric silica spheres, which seems to be related to the higher roughness of the particles used in this work.

- **Normal force changes during shear-thickening**

Microstructural changes in the suspensions that occur as a consequence of the shearing affect both the shear viscosity and the normal stresses. First normal stress difference N_1 was obtained from normal force acting on the cone as previously described, and plotted in Figure 4.4-left as a function of shear stress. In this part we will focus on results from starch suspensions.

As a general trend the first normal stress difference is almost constant and negative up to a given point, and its absolute value increases with the particle concentration. Depending on the volume fraction, this inflection point gives rise to two different situations. On the one hand, at low and moderate volume fractions, the curve takes the form of a well, with N_1 reaching positive values only at very high shear stresses. In these cases, hydrodynamic interactions are predominant and become very large in accordance with the increase in shear rate. On the other hand, the inflection point can result in shear induced dilatancy for more concentrated systems, as frictional forces overcome the hydrodynamic ones. Dilatancy usually accompanies shear thickening at non-Brownian suspensions with high packing fractions as a consequence of

the stress anisotropy, which result in positive normal stress differences. Although in all studied concentrations of starch there is a crossover stress at which N_1 changes it sign, only the sample with the highest volume fraction presents real dilatancy. In the rest of concentrations this fact can be an artefact due to the second shear-thinning region. Furthermore, some authors [24,32] have reported an inverse dependence of this crossover stress with volume fraction, while in Figure 4.4-right a nearly constant value for this crossover stress in starch suspensions is observed, which is reduced at the highest concentration.

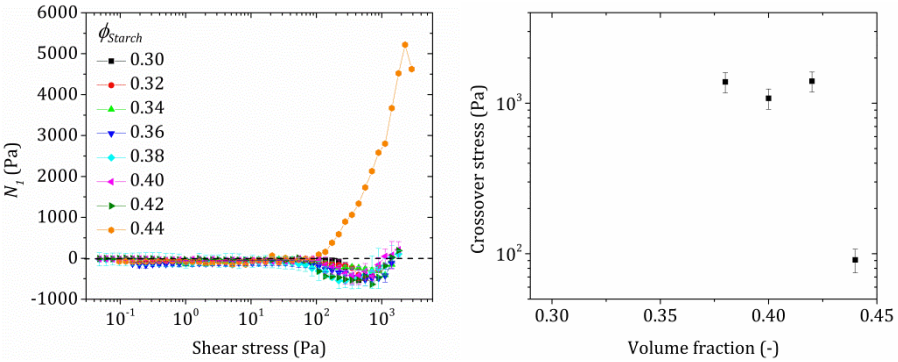

Figure 4.4: N_1 as a function of the shear stress for starch (left side) and crossover stress as a function of starch volume fraction (right side).

It is remarkable that the characteristic points that define each curve of N_1 do not correspond to the distinctive points in the shear viscosity curve of the systems that thicken. One may think, for example, that the onset of shear thickening and the crossover stress at which N_1 change its sign would coincide, but they do not. The same happens with the maximum in the shear viscosity and the minimum point in N_1 when the well appears at moderate concentrations.

As it has been previously commented, neither the starch nor fumed silica suspensions reached a shear thickened state (STS) with constant viscosity after the maximum, but a second shear-thinning region at higher shear rates. In Figure 4.5-left we performed the linear fit of N_1 without considering data beyond the maximum viscosity, that in terms of normal force nearly correspond to the monotonous reduction region before the change in tendency. From the slope values at each volume fraction, the first normal stress difference coefficient in the thickened state ($\Upsilon_{1,STS} = -N_1/\eta_f\dot{\gamma}$) is obtained, as in the work of Cwalina and Wagner [28]. The plot of Υ_1 as a function of the vol-

ume fraction, as well as its non-linear fit to the expression of Boulay and Morris model [34] is shown in Figure 4.5-right. The last provided a maximum volume fraction of 0.46.

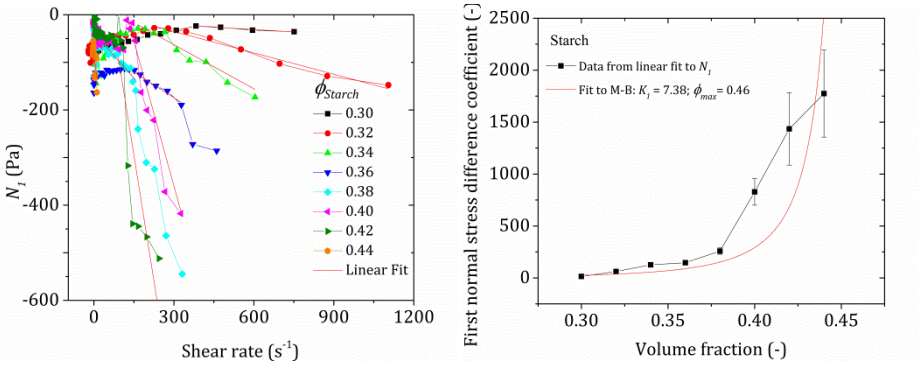

Figure 4.5: Case of not considering data beyond the maximum viscosity for starch suspensions. In the left side N_1 is plotted as a function of the shear rate and linear fits (red lines) at higher shear rates. First normal stress difference coefficient from the fit as a function of volume fraction, and non-linear fit to the B-M semiempirical model.

4.3.2. Carbonyl iron-based suspensions

- **Importance of the particle surface coating**

In this section we demonstrate the importance of the particle surface coating in the rheological performance of the magnetorheological suspensions at high particle concentration. In Figure 4.6 we compare the viscosity curves for $\phi = 0.50$, in suspensions prepared using ethylene glycol and a glycerol/water mixture as carrier fluids. As observed, the viscosity of the silica-coated iron particles at low shear rates remains at a low level if compared to the naked iron particles. Furthermore, only the silica-coated particles exhibit a shear-thickening phenomenon. The reason for this striking difference in behaviour between these two kinds of carbonyl iron particles may be the presence of stronger interparticle attractions in the case of naked iron particles in contrast to silica-coated particles. Moreover, the coating layer may incorporate certain rugosity to carbonyl iron particles that could also contribute to assist the shear thickening response.

In order to corroborate the previous assumption, Hamaker constants were determined for both types of particles interacting in EG and G87. In the Supplementary material section the process of calculation is described. According to the theory, the coating would affect van der Waals forces between

two particles in a given medium only at small separations, i.e., of the order of the coating thickness. In this sense, the calculation of Hamaker constant would depend on features of the coating medium and the suspending fluid, but not on the core properties. However, if two particles are far enough, these particles can be treated as bare particles and Hamaker constant will depend only on the core and suspending fluid properties.

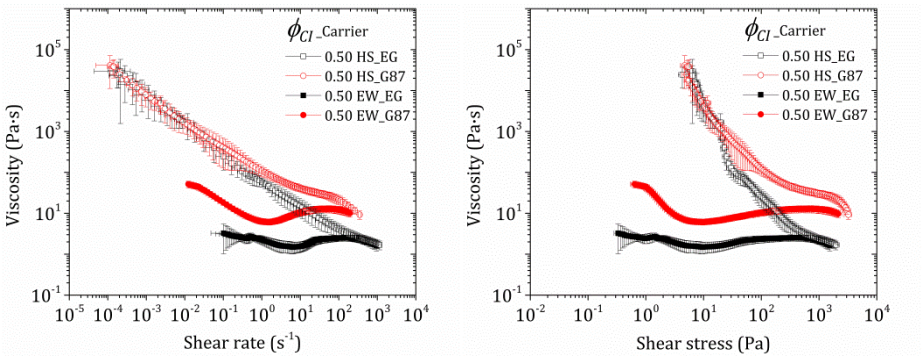

Figure 4.6: Viscosity as a function of shear rate and shear stress for concentrated suspensions of carbonyl iron particles with different grade, suspended in two carrier fluids.

From Table 4.2 it can be observed that Hamaker constant is lower for coated particles, so that the attractive van der Waals force in the case of bare particles suspended in these liquids is higher. This indicates that the coating improves the colloidal stability, by preventing magnetic particles from aggregation at low deformations, thus confirming that attraction may inhibit the shear-thickening phenomenon. In the following, we will work with silica coated iron particles in dense MR suspensions. On the other hand, the effect of the suspending medium is analysed onwards, but from the values of Hamaker constants it can be foreseen that shear thickening will be clearly displayed in G87 than in EG.

Interaction	**Approximated Hamaker constant (J)**
Small separation: silica-EG-silica	$2.122 \cdot 10^{-21}$
Large separation: iron-EG-iron	$1.084 \cdot 10^{-19}$
Small separation: silica-G87-silica	$2.189 \cdot 10^{-21}$
Large separation: iron-G87-iron	$1.057 \cdot 10^{-19}$

Table 4.2: Calculation of the Hamaker constants for silica-coated iron particles in different carrier fluids according to the separation.

- **Effect of particle concentration for a given carrier fluid**

Four carrier fluids were used as suspending phase in dense carbonyl iron-based suspensions, formulated with EW grade particles (i.e., silica coated). Figure 4.7 contains viscosity curves of these suspensions at several volume fractions in the absence of magnetic fields. This figure demonstrates that the particle concentration contribute significantly to the flow behaviour. Viscosity increases with particle concentration along the entire interval of shear rates investigated in the four suspending fluids, as expected. All systems show shear thinning at low deformations as a consequence of the progressive disruption of the static particle network, then both shear-thinning and thickening behaviours are found, depending on the fluid. Moreover, in the case of hydrophilic fluids, the onset of shear thickening and the maximum in viscosity are shifted to lower values as concentration increases. It is also interesting that EW particles suspended in EG display a shear-thickened state previous to the second shear-thinning region, in contrast to dense suspensions in G87, for which the maximum viscosity is not maintained during a range of shear rates.

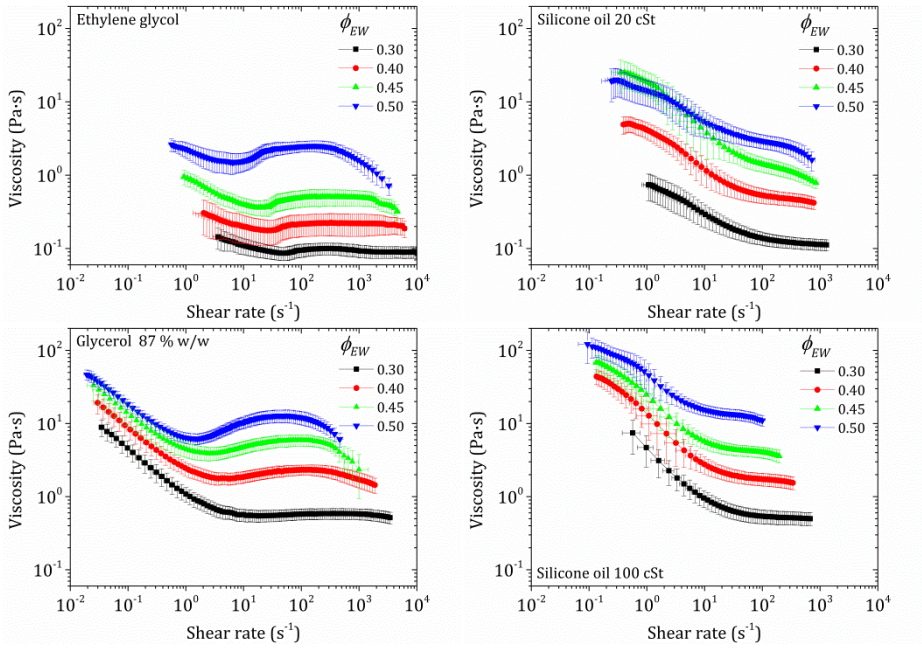

Figure 4.7: Viscosity curves as a function of shear rate for MR fluids in different carrier fluids and particle concentrations in the absence of magnetic fields.

These fluids were selected as carriers in order to evaluate the effect of the chemical composition as they can be grouped in pairs with similar viscosities,

as shown in Table 4.. Once the effect of the carrier viscosity is avoided, for a given viscosity, polarity of the fluid and their affinity with suspended particles make the difference in the rheological behaviour. We can clearly distinguish two different behaviours: suspensions in EG and G87 display shear thickening, while the viscosity in the case of silicone oils is monotonically decreases. In this sense, the composition of the carrier fluid and its interaction with suspended particles is decisive in the appearance of shear thickening.

- **Effect of carrier fluid for constant volume fraction**

Figure 4.8 contains curves of relative viscosity for the four suspensions investigated in this work, grouped in a different way to better observe the importance of the carrier fluid at constant particle volume fraction. This figure demonstrates that the carrier fluid plays a crucial role in the flow behaviour, which is more evident at higher particle concentration.

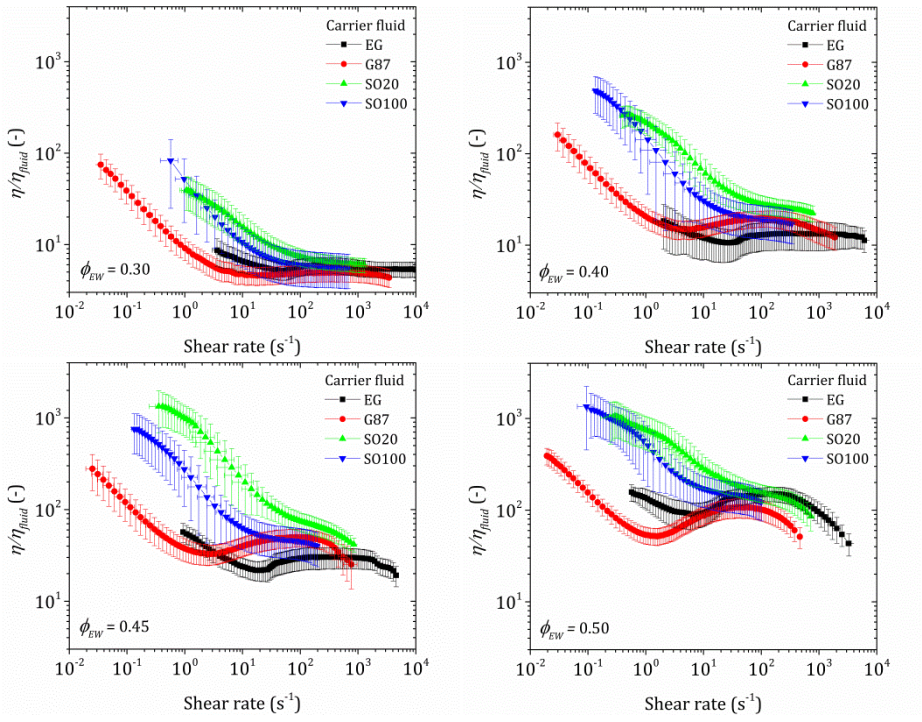

Figure 4.8: Relative viscosity curve as a function of shear rate for MR fluids at different particle volume fraction in different carrier fluids in the absence of magnetic fields.

Suspensions prepared in EG or G87 clearly exhibit a shear-thickening region in a well-defined shear rate range for the largest concentrations. As a reference, we also show results for suspensions in silicone oils with similar

viscosities to the EG and G87 carrier fluids. In contrast, in the case of silicone oils the suspensions exhibit the usual shear-thinning behaviour found in conventional MR fluids. This behaviour can be easily explained in terms of a disaggregation process upon increasing the shear rate. For very high shear rates the viscosity levels off and reaches a constant value.

The occurrence or not of shear thickening depending on the carrier fluid can be explained in terms of attraction in the system. Stronger attractive particle interactions may exist in silicone oil-based suspensions if compared to EG or G87 carriers. To support this statement, in Table 4.3 we include a simple estimation of the Hamaker constants between iron particles in the investigated carriers, considering separations among particles above the thickness of the coating. As previously explained, in the case of small separations Hamaker constant are calculated by estimating the whole particle constituted by the coating medium, and results follow the same tendency that bare particles. These parameters increase, what means more attraction, in this sense: G87<EG<SO. We can observe that as the attraction increases at a fixed volume fraction, the extent of shear thickening diminishes. In the case of silicone oils, the attraction becomes so important that shear thickening is completely obscured and for the whole range of shear rates, and only shear thinning is seen independently of the concentration.

Interaction	**Approximated Hamaker constant (J)**
Iron-EG-Iron	$1.084 \cdot 10^{-19}$
Iron-G87-Iron	$1.057 \cdot 10^{-19}$
Iron-SO20-Iron	$1.134 \cdot 10^{-19}$
Iron-SO100-Iron	$1.133 \cdot 10^{-19}$

Table 4.3: Calculation of the Hamaker constants for iron particles suspended in different carrier fluids.

Gopalakrishnan and Zukoski [35] experimentally studied the effects of increasing the strength of attraction, by means of the addition of nonadsorbing polymer to a suspension of hard sphere particles, up to and exceeding the gel transition and looked for links between gelation and shear thickening. They found that the critical shear rate (regarded to the viscosity minimum) shifted to higher values as the polymer concentration increased. The effect of the attraction in the onset of shear thickening coincides with our results when comparing viscosity curves of EG and G87 at the same particle concentration.

Our results also agree with previous simulation results. Pednekar et al. [36] analysed the effect of varying the force of attraction in concentrated colloidal suspensions. They found that attractive forces lead to increased low-shear viscosity that can obscure shear thickening at higher rates.

- **Quantification of the shear thickening**

In this part, the shear-thickening behaviour found in dense MR suspensions prepared in EG and G87 is characterized. In Figure 4.9 we show the boundaries of the shear-thickening zone. As expected, results for G87 are above those for EG because of its larger viscosity. A better way to compare the thickening characteristics is through the use of the dimensionless viscosity. In the right figure we show a very similar behaviour no matter the carrier fluid used as the curves collapse.

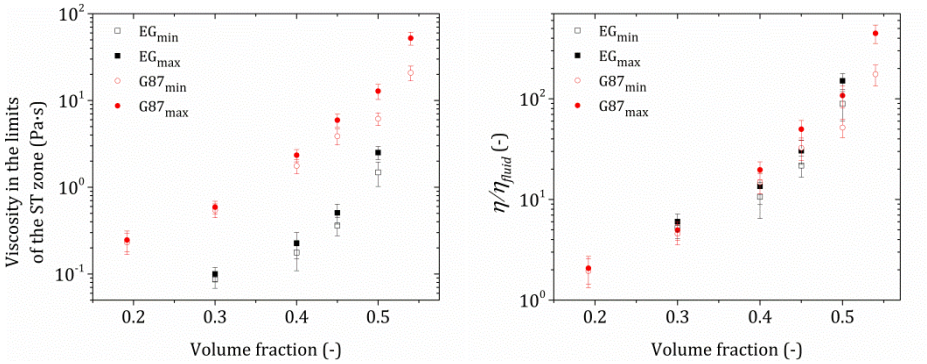

Figure 4.9: Characterization of the shear-thickening behaviour in silica-coated carbonyl iron suspensions in EG and G87.

In the left side of Figure 4.10 we show the beta exponent (i.e., the slope of the viscosity curve in the thickening region). As observed, the slope for EG is larger at each concentration, suggesting that the thickening region is localized in a narrower shear rate region compared with G87-based suspensions. Both EG and G87 suspensions display CST, according to this parameter, in the range of concentrations investigated. The beta exponent data obtained in this work for G87 is in very good agreement with other dense suspensions of silica microparticles suspended in the same carrier [24], so that it may indicate that at the studied volume fractions the particle separation is lower than the thickness of the coating, thus these particles in absence of magnetic field act as if the whole particle is composed of silica. Finally, in the right side of Figure 4.10 we show the critical shear stress and shear rate as a function of volume fraction. Again, results for glycerol-water mixtures are in good agreement

with Royer et al. [24], regarding the constant stress onset whatever the particle concentration and around 40 Pa. The critical shear rate in G87 suspensions is shifted to higher values when it refers to EG suspensions as attraction in the former is lower so shear thickening is favoured. In G87 particles and fluid are hydrophilic so that the affinity among them is high, and a solvation layer is formed around the particles, thus enhancing the stability of the particles in the system compared to slightly less hydrophilic carriers as EG.

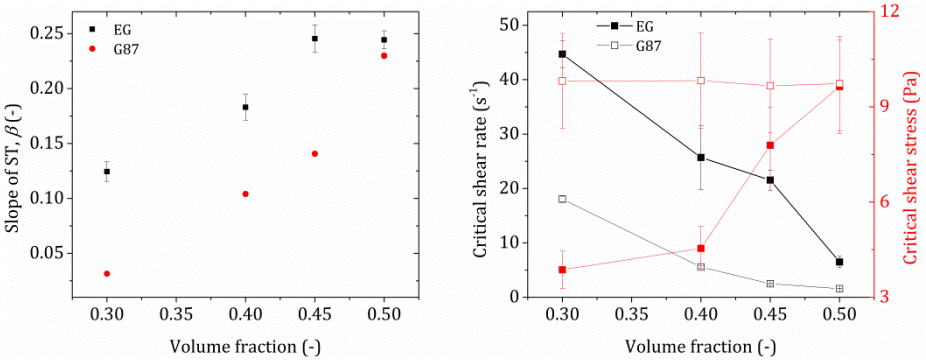

Figure 4.10: Slope of viscosity curves in the shear-thickening region (left side) and critical points characterizing the onset of shear thickening (right side) for MR suspensions in EG and G87.

- **Effect of magnetic field strength**

The influence of particle concentration, coating and carrier fluid have been previously studied in the absence of magnetic field, and it was demonstrated that attractive interactions may hide the shear-thickening behaviour in dense MR suspensions. Now, we analysed the influence of magnetic field in the rheological behaviour of the suspensions. Low field strengths were applied with an external coil, as at such magnetic concentrations higher magnetic fields would provoke very high magnetostatic interactions that would directly vanish the shear-thickening response derived from hydrodynamic and frictional interactions. Results are shown in Figure 4.11 for a fixed particle concentration of $\phi_{EW} = 0.50$ in the four carriers investigated.

The effect of the magnetic field on these dense MR fluids is mainly observable at low shear rate, as expected. It gives rise to the formation of magnetic columnar aggregates that resist the flow and the viscosity increases several orders of magnitude. These structures gradually bend and break as deformation increases, and the viscosity finally reaches the off-state value at

high shear rates. It is the consequence of a transition in the predominant forces in the system: from magnetostatic to hydrodynamic and frictional interactions.

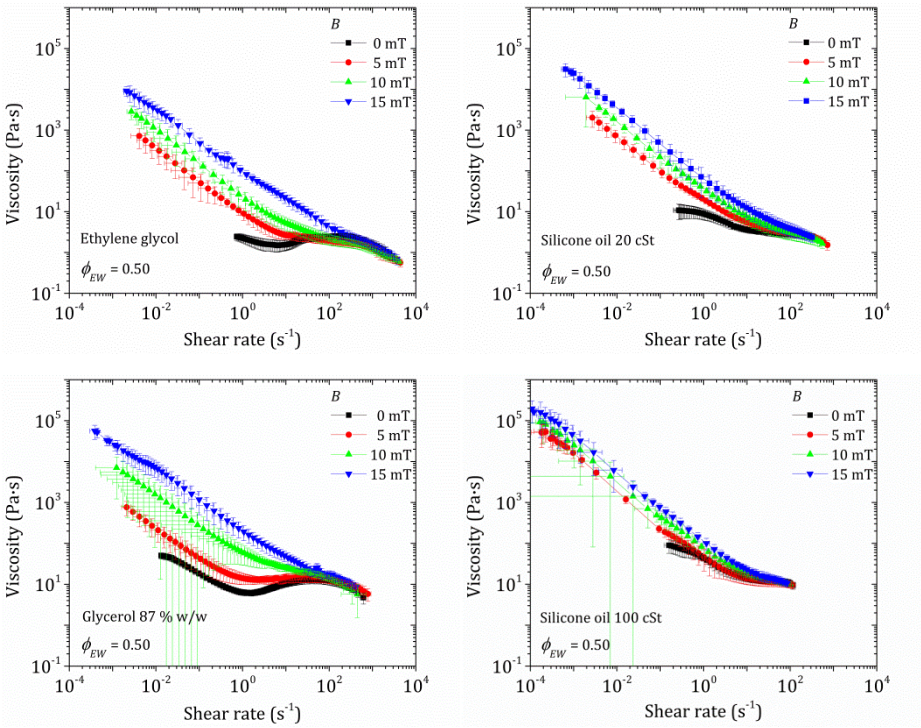

Figure 4.11: Viscosity curves as a function of stress for MR fluids under different magnetic induction values at a particle concentration of $\phi_{EW} = 0.50$.

In the case of suspensions in EG, as the shear thickening response at this concentration was weak, even the application of a very low magnetic field results in the complete disappearance of ST. However, a gradual transition is found in the rheological behaviour of G87 suspensions. Figure 4.11 demonstrates that the superposition of a low magnetic field in these dense MR fluids results in an apparent yield stress capable of masking the shear-thickening behaviour.

4.4. Conclusions

We have studied the rheological behaviour of two model suspensions exhibiting shear thickening: starch in water and fumed silica in ethylene glycol. The slope in the shear-thickening region grows with particle concentration for

both systems, as expected, but beta is always below the unity, meaning CST in all the experiments. Differences in the viscous response of starch and fumed silica suspensions can be explained in terms of particle features, as at very high concentrations friction between them is the largest contribution. In this sense, the onset of the shear thickening shifts to lower shear rates in the case of starch that may be due to a combination of higher friction of irregularly faceted surfaces of starch granules and a higher particle diameter, compared to fumed silica aggregates. On the other hand, both systems exhibit a second shear-thinning region above the shear stress of the maximum viscosity, as a consequence of the particle deformability. Regarding measurements on normal force in starch suspensions, negative values of N_1 at low shear rates correspond to a predominant contribution of hydrodynamic forces when the suspension is subjected to increasing shear rates. In this sense, N_1 scales linearly with the shear rate around the shear-thickening zone. On the contrary, at higher shear rates particles are pushed closer, which causes N_1 to become positive when frictional interactions overcome those coming from hydrodynamics. Dilation is observed at shear stresses above the onset stress of shear thickening. A characteristic well in the N_1 profile appears just before the transition in N_1 for CST situations but not at volume fractions near DST. At higher stresses, the analysis of parameters derived from normal force measurement provides a diverging volume fraction of 0.46.

On the other hand, dense MR fluids were selected for further studying shear thickening and the possibility of tuning this response. It is demonstrated that the chemical properties of particles and suspending fluids affect the appearance of shear thickening in dense suspensions. In this way, carbonyl iron particles with different grades display different rheological behaviours. Indeed, dense suspensions of carbonyl iron particles EW in silicone oil display shear thinning in the whole range of shear rates, while those formulated in EG and G87 provide shear-thickening behaviour. In this sense, a higher affinity between particles and carrier, reflected in Hamaker constant values, promotes the formation of a solvation layer that could reduce the attraction between particles, thus enhancing shear thickening. Finally, when magnetic field is applied, great magnetostatic interactions dominate the flow behaviour at low shear rates and progressively inhibit the shear-thickening response in EG and G87 suspensions.

4.5. Supplementary material

- **Van der Waals interactions**

Electrostatic repulsion together with Van der Waals interactions (attractive) are the main contributions to the colloidal stability of a suspension, according to the DLVO theory. Thus, the simplest way to minimize interactions between colloidal particles is by means of reducing the van der Waals attraction. In the common situation involving two spheres or macromolecules of radii R_1 and R_2, Van der Waals interaction energy W and force F are given by [37]:

$$W = -\frac{A}{6D}\left(\frac{R_1 R_2}{R_1 + R_2}\right), \quad F = -\frac{A}{6D^2}\left(\frac{R_1 R_2}{R_1 + R_2}\right), \tag{4.1}$$

being A the Hamaker constant, and D the separation between the surfaces of the particles.

- **Hamaker constants calculation**

In the particular case of two identical phases (1 and 2) interacting across medium 3, the Hamaker constant can be written as:

$$A = A_{131} \approx \frac{3}{4} kT \left(\frac{\varepsilon_1 - \varepsilon_3}{\varepsilon_1 + \varepsilon_3}\right)^2 + \frac{3h\nu_e}{16\sqrt{2}} \frac{(n_1^2 - n_3^2)^2}{(n_1^2 + n_3^2)^{3/2}}, \tag{4.2}$$

where $h = 6.626 \cdot 10^{-34}$ J/s is the Planck's constant, $k = 1.381 \cdot 10^{-34}$ J/K is the Boltzmann's constant, ν_e is the absorption frequency, ε the medium permittivity, n the refractive index, and T the temperature. In the absence of the real values of the absorption frequency for each component, we used $\nu_e = 10^{15}$ s^{-1} as a typical value from literature [37]. This parameter was assumed as constant for the three media involved in the calculation of the approximated Hamaker constants. The form of the equation indicates that A is always positive, so that Van der Waals force is always attractive.

In order to estimate the Hamaker constant we need to know the values of permittivity and refractive index of all the components of the suspensions. Refractive indices of carrier fluids were experimentally measured, and the rest of data were gathered from literature. In the absence of neither of these parameters for carbonyl iron particles, ε and n of iron were used instead in the calculation of the VdW interactions. They are listed in Table 4.4.

In the case of particles (medium 1) coated by an adsorbed layer (medium 2) with thickness T, the Hamaker constant used in van der Waals interaction

depends on the separation between particles [37]. At large separations (i.e., $D \gg T + T'$), it is dominated by bulk properties, while at small separations (i.e., $D \ll T + T'$), the coating gains relevance. So that in the calculation of A, particle medium is taken as the core medium and the coating medium, respectively for large ($A_{1,31}$) and small separations ($A_{2,32}$).

Medium	Refractive index, n (-)	Permittivity, ε (-)	Origin of data
Iron	2,9275 (589 nm, RT)	17.58	[39]
Silica	1,448 (RT)	3.8 (RT)	[37]
EG	1,4319 (RT)	41.4 (293.2 K)	M, [38]
G87	1,4522 (RT)	46.53	[38]
SO20	1,4043 (RT)	2.68 (25 ºC, 100 Hz)	M, [40]
SO100	1,4047 (RT)	2.73 (25 ºC, 100 Hz)	M, [40]

Table 4.4: Material properties needed for the calculation of the Hamaker constants. M refers to data obtained by own experimental measurements with a hand held refractometer (λ = 589 nm); RT: room temperature.

4.6. References

[1] Wagner N J and Brady J F 2009 Shear thickening in colloidal dispersions *Phys. Today* **62** 27–32

[2] Brown E, Forman N A, Orellana C S, Zhang H, Maynor B W, Betts D E, Desimone J M and Jaeger H M 2010 Generality of shear thickening in dense suspensions *Nat. Mater.* **9** 1–5

[3] Brown E and Jaeger H M 2014 Shear thickening in concentrated suspensions : phenomenology , mechanisms and relations to jamming *Rep. Prog. Phys.* **77** 046602

[4] Denn M M, Morris J F and Bonn D 2018 Shear thickening in concentrated suspensions of smooth spheres in Newtonian suspending fluids *Soft Matter* **14** 170–184

[5] Gürgen S, Kuşhan M C and Li W 2016 The effect of carbide particle additives on rheology of shear thickening fluids *Korea-Aust. Rheol. J.* **28** 121–8

[6] Gürgen S, Li W and Kuşhan M C 2016 The rheology of shear thickening fluids with various ceramic particle additives *Mater. Des.* **104** 312–9

[7] Gürgen S and Kuşhan M C 2017 The stab resistance of fabrics impregnated with shear thickening fluids including various particle size of additives *Compos. Part Appl. Sci. Manuf.* **94** 50–60

[8] Li D, Wang R, Liu X, Fang S and Sun Y 2018 Shear-thickening fluid using oxygen-plasma-modified multi-walled carbon nanotubes to improve the quasi-static stab resistance of Kevlar fabrics *Polymers* **10** 1356

[9] Gürgen S, Sofuoğlu M A and Kuşhan M C 2019 Rheological compatibility of multi-phase shear thickening fluid with a phenomenological model *Smart Mater. Struct.* **28** 035027

[10] Zhang X, Li W and Gong X L 2008 Study on magnetorheological shear thickening fluid *Smart Mater. Struct.* **17** 015051

[11] Peng G R, Li W, Tian T F, Ding J and Nakano M 2014 Experimental and modeling study of viscoelastic behaviors of magneto-rheological shear thickening fluids *Korea-Aust. Rheol. J.* **26** 149–158

[12] Bossis G, Grasselli Y, Meunier A and Volkova O 2016 Outstanding magnetorheological effect based on discontinuous shear thickening in the presence of a superplastifier molecule *Appl. Phys. Lett.* **109** 111902

[13] Galindo-Rosales F 2016 Complex fluids in energy dissipating systems *Appl. Sci.* **6** 206

[14] Metzner A B and Whitlock M 1958 Flow behavior of concentrated (dilatant) suspensions *Trans. Soc. Rheol.* **2** 239–54

[15] Barnes H A 1989 Shear-thickening ("Dilatancy") in suspensions of nonaggregating solid particles dispersed in Newtonian liquids *J. Rheol.* **33** 329–366

[16] Hoffman R L 1974 Discontinuous and dilatant viscosity behavior in concentrated suspensions. II. Theory and experimental tests *J. Colloid Interface Sci.* **46** 491–506

[17] Brady J F and Bossis G 1985 The rheology of concentrated suspensions of spheres in simple shear flow by numerical simulation *J. Fluid Mech.* **155** 105

[18] Brown E and Jaeger H M 2012 The role of dilation and confining stresses in shear thickening of dense suspensions *J. Rheol.* **56** 875–923

[19] Seto R, Mari R, Morris J F and Denn M M 2013 Discontinuous shear thickening of frictional hard-sphere suspensions *Phys. Rev. Lett.* **111** 1–5

[20] Fernandez N, Mani R, Rinaldi D, Kadau D, Mosquet M, Lombois-Burger H, Cayer-Barrioz J, Herrmann H J, Spencer N D and Isa L 2013 Microscopic mechanism for shear thickening of non-brownian suspensions *Phys. Rev. Lett.* **111** 1–5

[21] Mari R, Seto R, Morris J F and Denn M M 2014 Shear thickening, frictionless and frictional rheologies in non-Brownian suspensions *J. Rheol.* **58** 32

[22] Singh A, Mari R, Denn M M and Morris J F 2018 A constitutive model for simple shear of dense frictional suspensions *J. Rheol.* **62** 457–68

[23] Lin N Y C, Guy B M, Hermes M, Ness C, Sun J, Poon W C K and Cohen I 2015 Hydrodynamic and contact contributions to continuous shear thickening in colloidal suspensions *Phys. Rev. Lett.* **115**

[24] Royer J R, Blair D L and Hudson S D 2016 Rheological signature of frictional interactions in shear thickening suspensions *Phys. Rev. Lett.* **116**

[25] Raghavan S R and Khan S A 1997 Shear-thickening response of fumed silica suspensions under steady and oscillatory shear *J. Colloid Interface Sci.* **185** 57–67

[26] Kalman D P, Rosen B A, Wagner N J, Co A, Leal G L, Colby R H and Giacomin A J 2008 Effects of Particle Hardness on Shear Thickening Colloidal Suspension Rheology *AIP Conference Proceedings* (AIP)

[27] Chatté G, Comtet J, Niguès A, Bocquet L, Siria A, Ducouret G, Lequeux F, Lenoir N, Ovarlez G and Colin A 2018 Shear thinning in non-Brownian suspensions *Soft Matter* **14** 879–893

[28] Cwalina C D and Wagner N J 2014 Material properties of the shear-thickened state in concentrated near hard-sphere colloidal dispersions *J. Rheol.* **58** 949–67

[29] Maranzano B J and Wagner N J 2001 The effects of particle size on reversible shear thickening of concentrated colloidal dispersions *J. Chem. Phys.* **114** 10514

[30] Hsiao L C, Jamali S, Glynos E, Green P F, Larson R G and Solomon M J 2017 Rheological state diagrams for rough colloids in shear flow *Phys. Rev. Lett.* **119**

[31] Brown E and Jaeger H M 2009 Dynamic jamming point for shear thickening suspensions *Phys. Rev. Lett.* **103**

[32] Lootens D, Van Damme H, Hémar Y and Hebraud P 2005 Dilatant flow of concentrated suspensions of rough particles *Phys. Rev. Lett.* **95** 1–4

[33] Hsu C-P, Ramakrishna S N, Zanini M, Spencer N D and Isa L 2018 Roughness-dependent tribology effects on discontinuous shear thickening *Proc. Natl. Acad. Sci.* 1–6

[34] Morris J F and Boulay F 1999 Curvilinear flows of noncolloidal suspensions: The role of normal stresses *J. Rheol.* **43** 1213–1237

[35] Gopalakrishnan V and Zukoski C F 2004 Effect of attractions on shear thickening in dense suspensions *J. Rheol.* **48** 1321–1344

[36] Pednekar S, Chun J and Morris J F 2017 Simulation of shear thickening in attractive colloidal suspensions *Soft Matter* **13** 1773–1779

[37] Israelachvili J N 2011 *Intermolecular and surface forces* (San Diego: Academic Press)

[38] Lide D R 2012 *CRC Handbook of Chemistry and Physics* (CRC Boca Raton)

[39] M. N. Polyanskiy, "Refractive index database," https://refractiveindex.info. Accessed on 2020-02-13.

[40] Clearco Products Co., Inc., “Dielectric properties of pure silicone fluids”, http://www.clearcoproducts.com/pdf/pure-silicone/Dielectric_Properties_Pure_Silicone_Fluids.pdf. Accessed on 2020-02-13.

5. Shear thickening in bimodal suspensions

5.1. Introduction

Suspension rheology [1–3] is capturing a great interest in recent years due to the importance of complex suspensions in multitude of industrial applications. The desired performance of this kind of materials is affected by many factors that can be classified into those related to the particle properties [4–7] (e.g., size, form, size distribution, composition, concentration, electrical charge…), suspending medium (such as viscosity) and flow conditions imposed to the suspension.

Unimodal suspensions, i.e., suspensions formulated with a unique type of particle as suspended phase, are extensively investigated in literature. Among them, in this thesis special attention is paid to two remarkable types of unimodal suspensions for their ability of readily tuning their rheological behaviour, well passively by shear or actively by external fields: shear-thickening (ST) and magnetorheological (MR) fluids, both used in energy dissipating systems [8]. The formers are used as impact-resistant materials or shock absorbers in protective applications while MR fluids are very valued materials in devices for torque transfer, as clutches or dampers.

Briefly, the counter-intuitive phenomenon of shear thickening [9,10] displays a reversible increase in viscosity (continuous or discontinuous) under applied shear rates or stresses. Despite the complexity of this shear-induced response due to the substantial amount of particles involved within the system, and after several decades of debate about the physical mechanism [11–15] that originates this response, nowadays scientific community broadly agrees that ST is due to a transition from a hydrodynamically lubricated regime to a friction dominated situation [16–20]. This non-Newtonian behaviour exists above a critical volume fraction and shear rate, in systems where attraction is negligible. Indeed Barnes [21] reviewed this behaviour and stated that "given the right circumstances, all suspensions of solid particles will show the phenomenon". The possibility of controlling these critical parameters or the severity of the shear thickening poses a great challenge to scientists. In literature we can found several strategies to tune the thickening features, such as altering some properties during the formulation [15,22–24] (e.g., particle or fluid characteristics, like size, shape, polydispersity or roughness) or introducing flow disturbances [25]. In fact, shear thickening can even be completely obscured by tuning these particle features or destabilizing the system by introducing net attractive forces [26]. Dense suspensions of cornstarch in water are the typical model systems that show this dramatic change in viscosity.

On the other hand, as in the case of ST fluids, the rheological properties of MR fluids can also be varied. They are suspensions of magnetic micronsized particles suspended in a non-magnetic Newtonian fluid. When subjected to an external magnetic field these particles become polarized and aggregate in chains or columnar structures that orientate along magnetic field lines. As a result of this field-induced assembly, the suspension experiences a reversible liquid-to-solid transition as the viscosity of MR fluids rapidly increases several orders of magnitude, what is known as magnetorheological effect [27]. Under certain external fields and particle volume fractions the increase in flow resistance may develop a field-depended yield stress, thus the flow of the suspension is achieved at stresses above this value. It should be noted that some drawbacks related to the density of iron particles appear in MR fluids applications such as particle sedimentation, which is generally improved by the incorporation of additives into the carrier that decrease the density mismatch between particles and fluid. Because of the high particle density and required particle loadings to obtain large magnetic performances, devices are

quite heavy. The weight of MR devices can be reduced by partially substituting the dense carbonyl iron particles by others with lower density, but compromising the magnetic response as less as possible.

Currently, there is a great interest in understanding the rheological behaviour of hybrid suspensions. The choice of using different types of particles in bimodal suspensions has an unavoidable effect in the viscosity of concentrated suspensions.

In relation to the appearance of shear-thickening phenomenon several generalities can be asseverated: particle anisotropy [28,29] (i.e., aspect ratios above unity) causes this behaviour at lower volume fractions than isotropic or spherical particles; for a fixed concentration smaller particles, as well as a higher roughness, imply more particle-particle interactions, as they increase the total surface area, so that the viscosity increases [15,30], and the onset stress reduces with the square of particle diameter ($\sigma^* \propto d^{-2}$) [31]; polydispersity (i.e., a broader size distribution) reduces the viscosity of the suspension as the suspension flow easily, thus the critical shear rate delays [32]; the ST response may improve by changing the surface properties of the particles [33–35] or by addition of particles with other shapes and compositions. For instance, the addition of small amounts of nanofibers or nanowires produced a reinforcement in ST response [36,37], and large polymethyl methacrylate (PMMA) particles were found to facilitate the DST transition in cornstarch suspensions [38].

On the other part, magnetorheological fluids prepared by mixing magnetic and non-magnetic particles in the formulation also appeal to scientific community. In a pioneering paper [39], the authors demonstrated that the partial substitution of magnetic particles by non-magnetic ones resulted in an unexpected increase in the MR performance of the suspensions. In particular, the yield stress increased by approximately a 50 % in a concentrated and monodisperse system with a total volume fraction ϕ_T of 0.45 when a third of magnetic particles were substituted by non-magnetic ones. Besides, the partial substitution of magnetic particles by non-magnetic ones has been explored in other systems such as dimorphic MR fluids [40] or MR elastomers [41], among others. Recently, particle-level simulations of monolayer and three-dimensional magnetorheological suspensions were explored [42]. The authors observed that the addition of non-magnetisable particles provoked small changes in the microstructure, but these changes were thought not to lead to the yield stress enhancement. Later, they showed that the non-

magnetisable spheres are involved in repulsive-force clusters that are responsible for enhancing the stress.

The meeting point between ST and MR systems are magnetorheological shear-thickening (MRST) suspensions, i.e., concentrated suspensions of, at least, two particulate phases, whose rheological behaviour can be easily tuned, well passively with a given flow deformation or actively through an applied magnetic field strength. These suspensions are still scarcely studied [43–45], but these and previous examples gathered from literature highlight the easiness of these hybrid systems to be tuned and to display a combined behaviour, as a consequence of the distinct features of the involved particles.

Particularly, in this chapter we aim to provide a deeper understanding in the rheological behaviour of dense MRST suspensions formulated with mixtures of magnetic and non-magnetic particles. In this sense, through experimental and simulation approaches we will obtain actively controlled shear-thickening fluids, so that these systems will react to changes both in the type of deformation to which the fluid is subjected and to the applied field. On the experimental hand, the effect of adding magnetic particles into model shear-thickening suspensions is explored in presence and absence of external magnetic fields. Moreover, we contemplate the possibility of having a hybrid system with a unique type of particle, i.e., being formulated with iron-coated starch particles, so that they could show both the magnetic and thickening responses. A small part is devoted to the performance of these hybrid core-shell particles. Furthermore, in the last part of this manuscript particle-level simulations are carried out in systems of mixtures of magnetic and non-magnetic particles, and two scenarios are evaluated. On the one hand, simulations of mixtures of monodisperse particles are used to check the positive effect of substituting part of magnetic particles by non-magnetic ones concerning the yield stress. On the other hand, last simulations consider polydisperse systems in order to reach higher concentrations that make possible the appearance of shear thickening in simulations, when considering conditions similar to experiments.

5.2. Experimental

5.2.1. Materials

In the experimental part, we prepared two types of hybrid MRST systems: suspensions of mixtures of magnetic and non-magnetic particles, and suspensions formulated by hand-made core-shell (non-magnetic and magnetic) particles. For the sake of clarity, the terms hybrid and bimodal are used indistinctively when referring to our MRST suspensions, as two types of particles are employed, with differences in size, form, composition and magnetic response.

The non-magnetic particulate phase used in the formulation of both types of systems corresponds to starch from corn (73 % amylopectin and 27 % amylose from Sigma Aldrich, density = 1.68 $g \cdot cm^{-3}$, mean particle diameter around 10.7 μm), while the magnetic one is carbonyl iron (CC grade, density 7.874 $g \cdot cm^{-3}$, average particle diameter 3.8-5.3 μm) obtained from BASF (Germany). It is noteworthy the difference in particle size and density between starch and carbonyl iron particles. The sample preparation consisted on mixing the powders (starch and carbonyl iron) with a spatula, then adding the required amount of distilled water as suspending medium and mixing thoroughly again with the spatula.

Prior each measurement, the sample was introduced in the planetary mixer with the established protocol and, after that, it was put in the ultrasounds bath for several minutes to ensure uniform suspensions. In spite of the density mismatch among the elements of the suspensions, this redispersion and homogenization before carrying out the tests did not allow sedimentation of the samples during the measurements.

At this point it was important to determine the range of pH at which both particles (starch and carbonyl iron) are more stable in the fluid in order to discern their interactions (i.e., attractive or repulsive) and colloidal stability. It was performed in a Zetasizer Nano Z device (Malvern Instruments). The mixture of these particles, in terms of stability, is preferable when there exists electrostatic repulsion among them, i.e., when both particles share the same sign in their charges. This was found to occur at pH values above 3 (see Figure 3.14 in Subsection 3.2.5), so that we decided to prepare the MRST suspensions in distilled water (pH~7), what facilitates the process. Thus, the suspensions should have good colloidal stability and flocculation should be low.

Regarding the first type of MRST suspensions, three key concentrations of starch were selected, namely $\phi_{Starch} = 0.30$, 0.36, and 0.40. These values were selected from Figure 4.1, because they correspond to suspensions that display no ST, mild ST, and strong ST, respectively. The volume fraction of carbonyl iron was 0.05 for the lowest concentration of starch and 0.001 for the other two cases. The addition of a small amount of magnetic particles to model concentrated suspensions that exhibit shear thickening allows the tuning of their rheological response by means of an external magnetic field. The idea was, on the one hand, having a total concentration of particles for which a moderate ST to be expected (from unimodal suspensions of starch) in absence of magnetic field and, on the other hand, preserving this ST in field conditions by utilizing low enough volume fractions of carbonyl iron particles. In this sense, the magnetostatic effect due to the application of a series of magnetic field strengths to the suspension would lead to different thickening behaviours that even can be obscured if the magnetic phase or the applied field is too high.

In the second type of hybrid suspensions, the particulate phase consisted on carbonyl iron particles (OM and CC grades, from BASF) coated with starch and was again suspended in deionized water. The procedure of obtaining the hand-made core-shell particles is described in Subsection 5.2.3. We performed rheological experiments with suspensions with a magnetic particle concentration of 0.05 and 0.36.

5.2.2. Rheometry

A stress controlled rheometer from Anton Paar (MCR501) was used in the rheological measurements, both in parallel-plates (PP-20, 20 mm diameter, 1 mm gap) and in cone-plate (CP-20, 20 mm diameter, 2º angle, truncation 0.084 mm) configuration. The first geometry is preferable when magnetic fields are present, as it permits having a uniform field on the sample despite the gradient in shear rate with the plate radii. For its part, cone-plate geometry provided trustworthy normal force measurements during the tests. Plate-plate geometry was employed in both MRST systems (mixtures of particles and core-shell particles), while cone-plate geometry was only used in the case of suspensions of mixtures of particles.

The reset of normal force is carried out before setting the zero gap, and again once the sample is set in the geometry and the upper part of the geometry is in the measure position (before starting the test). The protocol consist-

ed in four steps, and a constant value of the magnetic field is used in the last two steps. First, the sample was preconditioned at 100 s^{-1} during 60 s, in order to homogenize it and remove its history effects. Then, during other minute no shear was applied, and normal force is reset. After that, a strain amplitude of 0.01% at 1Hz was applied during 60 s in presence of magnetic field. The last step corresponds to a logarithmic torque ramp from 10^{-4} to 100 mN·m for 300 s at the same magnetic field intensity than in the oscillatory shear step. So that when the magnetic field is applied, normal force is positive due to the aggregation of particles that tends to push the upper plate.

5.2.3. Coating of carbonyl iron particles

In this subsection we describe in detail the procedure carried out to recover magnetic particles of carbonyl oil with starch. The interest in this combination of ingredients resides in obtaining magnetic microparticles whose coating (if it is successful), apart from reducing the total density of the particle and so the sedimentation rate due to the mismatch between particles and medium, could influence the rheology of the suspension, as starch is well known by its shear-thickening behaviour.

There are a lot of publications and research about the coating of magnetic particles [46], mainly due to their use in biomedical applications. Materials employed in the coating can be magnetic or non-magnetic. We are focused in non-magnetic coatings, which can be inorganic or organic. The most interesting inorganic shell is silica because an inert layer can easily coat magnetic nanoparticles, so promoting them as drug-delivery vehicles in biological systems. The layer avoids electrostatic agglomeration by displaying a negative charge in the particle surface. Moreover, it improves the mechanical and thermal stability and prevents oxidation of magnetic particles. The coating can be carried out by sol-gel methods [47,48], direct silicon oxidation [49], or micelle methods [50]. Regarding to organic shells, polysaccharides can interact strongly with these magnetic particles through their multiple hydroxyl groups, carboxylic or amino acids. The nature of the mechanism of polysaccharide adsorption with iron is of acid-base type [51,52]. Moreover, solvation energy plays a significant role in these interactions [53]. These organic coatings can be achieved through in situ or post-synthesis methods.

We found in literature magnetic particles (different from carbonyl iron) coated by starch [54–56], as well as carbonyl iron particles coated with other polysaccharides different from starch [57,58]. However, to the best of our

knowledge, a method for attaining hybrid carbonyl iron-starch particles has not been found. In the absence of a stablished protocol, we considered to follow the methods employed in previous works by Dung et al. [54], Lawless et al. [57], and Sim et al. [58] (that we renamed as D, L, and S, respectively), but substituting any magnetic particle by carbonyl iron and any polysaccharide by starch, and maintaining the original proportions and reaction conditions (see Table 5.1).

We performed the coating onto two types of carbonyl iron particles, namely OM and CC grades. The former were pre-treated with HCl, as described in Vereda et al. [59], in order to increase the reactive sites (hydroxyl groups) on the surface of the magnetic particles, where hydrophilic starch would react. Measurements of zeta potential and size were carried out on the raw OM particles after a washing with water and the particles after the HCl pre-treatment. We observed a decrease in the particle size as a consequence of the reaction between iron and acid that oxidizes the particles. Moreover, particles treated with acid are more stable as they posse higher negative charge compared to raw OM particles.

Coating	Elements	Reaction conditions
D	1 g starch (*) 1 g carbonyl iron (*) 100 ml distilled water	60 ˚C 120 minutes 330 rpm
L	1 g starch 1 g carbonyl iron 100 ml 7.5 % NH_4OH	65 ˚C 15 minutes 330 rpm
DL	1 g starch 1 g carbonyl iron 100 ml 7.5 % NH_4OH	60 ˚C 120 minutes 330 rpm
S	1 g starch 20 g carbonyl iron 200 ml distilled water 1 ml ethanol added dropwise each 5 minutes	65 ˚C 30 minutes for starch dissolution at 400 rpm, and 30 minutes in contact with magnetic particles at 600 rpm

Table 5.1: Features of the methods used to fabricate core-shell particles based on carbonyl iron and starch. As clarification DL is a conflation of D and L methods. (*) Not specified.

The main differences between these coating methods lie in the magnetic to non-magnetic proportions, reaction time and pH. In general, these procedures consist on mixing the particles in excess of fluid medium at a given temperature high enough to allow the dissolution of starch particles. Once the

reaction time has finished, the suspension is let to cool, after what they are magnetically separated and washed with water several times until having a pH below 8 (very important in L and DL methods). The last washing step is carried out with ethanol, then, particles have to dry in an oven at 40 ℃.

In order to assess the success of the coverage we observed the coated particles in both scanning and transmission electron microscopy, as these techniques offers topographic images of the particles with a high degree of magnification and resolution. This will permit identifying the core-shell structure and so confirming the adsorption of starch onto the carbonyl iron particles. More information about SEM and TEM techniques can be found in Subsection 3.2.3.

5.3. Simulation method

Particle-level dynamic simulations were performed to study mixtures of magnetisable and non-magnetisable monodisperse spheres (particle diameter of $\sigma = 1$ μm) suspended in a continuous phase with Newtonian viscosity. The simulation box initially contains 1000 particles randomly distributed and periodic boundary conditions are employed in 3D. This bimodal system is first subjected to a structuration at rest, during which magnetic particles tend to join in chains along the magnetic field direction as an external magnetic field is imposed. Indeed, for each system, defined by the values of ϕ_T and ϕ'_M, the simulation code was run five times in order to have statistic reproducibility. In each run a random configuration of particles is created at the beginning of the structuration at rest, and at the end of this step an equilibrium configuration is obtained. This final configuration is taken as the initial structure for five new runs in which the code is slightly modified by imposing certain constant values of shear rate, i.e., the system is subjected to start-up tests, besides the external magnetic field. This second step of the simulation provokes the rupture of the magnetic columns formed at rest. Figure 5.1 shows the changes in the microstructure along the simulation time.

The simulation code is based on a previous work [60] that studied the effect of polydispersity in MR fluids but without considering multibody interactions in the calculation of the total magnetic force acting in a single particle. The code was customized to take into account the main pairwise interactions that contribute to the total force acting on the particles, such as magnetic interactions considering local field, Stoke's drag, repulsive and wall interac-

tions, as well as stochastic forces related to the motion of Brownian particles. The Langevin equation of motion Equation 5.1 is solved at each simulation time and particles move to their new positions. These interactions are described in detail in Subsection 3.3.1.

$$m_i \frac{d^2 \boldsymbol{r_i}}{dt^2} = \sum \boldsymbol{F_i^e} + \boldsymbol{F_i^h} + \boldsymbol{F_i^b} \,, \tag{5.1}$$

It is worth saying that in a first approximation lubrication forces were not introduced into the simulation code because of their complexity. Then, they were fully defined, as it is shown in Subsection 3.3.1, as we considered they should have a relevant role in the behaviour of concentrated systems. However, the maximum total concentration achievable in these monodisperse systems was low to observe shear thickening, so that the fact of avoiding hydrodynamic lubrication did not imply great change in the evolution of the system.

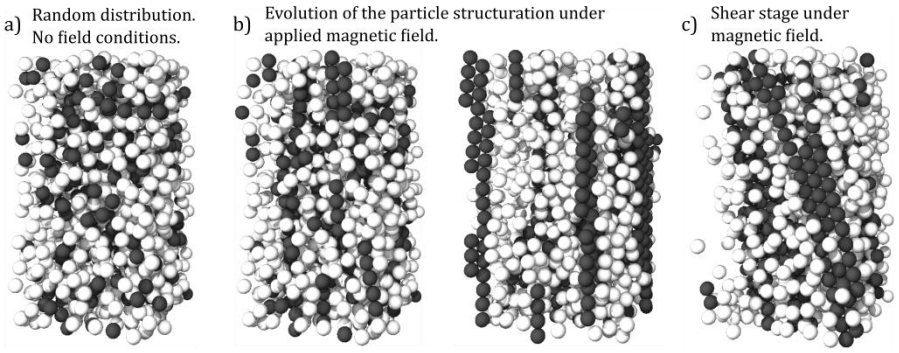

Figure 5.1: Simulation box for a system of 1000 monodisperse particles with $\phi_T = 0.20$ and $\phi'_M = 0.30$ at different simulation times. White and grey spheres represent non-magnetic and magnetic particles, respectively. a) Start of the simulation process, where particles are randomly located, b) Evolution of particle structuration at rest in the form of magnetic columnar aggregates under the presence of the magnetic field, and c) Shear stage under application of magnetic field.

In order to compare the effect of considering or not lubrication forces we ran two programs at the same time, one with the full simulation code and other taking into account only Stokes' drag. Due to the high computational cost derived from the complexity of lubrication interactions, we chose a relatively low total volume fraction. The normalized total magnetic energy during structuration is shown in Figure 5.2.

As can be observed, the incorporation of lubrication forces supposes a decrease in the absolute value of the magnetic energy at each simulation time, which indicates that magnetic structures are less stable. The delay in black

curve is thought to occur also at higher simulation times until the development of the equilibrium structure. The difference between both curves is small as the magnetic contribution prevails over other interactions in the system. This little change, together with the fact that by considering lubrication forces would require much more time to fulfil the simulation process, encouraged the decision of avoiding these interactions at the volume fractions considered in this batch of simulations.

Simulation parameters used in the simulations are presented in Table 3.6. Total volume fraction varies between 0.05 and 0.30. For its part, the number of magnetisable particles in the simulation box varied between 50 and 1000, i.e., a relative magnetic volume fraction ϕ'_M ranging from 0.05 to 1. In these simulations, the two populations of particles share the same particle diameter for simplicity, while they differ in the magnetic dipole, module of Young and Poisson's ratio, in order to the particles resemble to the magnetic and hardness features of carbonyl iron and starch granules. Moreover, dimensionless shear rates ranged from 0.003 to 100, and the external magnetic field was 177 kA/m in *z*-direction.

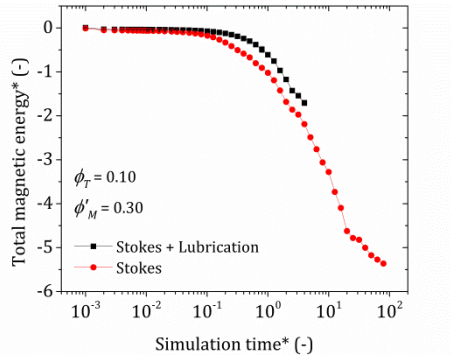

Figure 5.2: Comparison of simulations codes taking into account different hydrodynamic interactions in a system with $\phi_T = 0.10$ and $\phi'_M = 0.30$.

The range of total particle concentrations evaluated in simulations considering only monodisperse populations is delimited by the upper value of $\phi_T = 0.30$. Above this value, it is not possible to obtain an initial configuration with randomly allocated particles in the way the simulation code is presented. So that, in order to study more concentrated systems that may resemble better to the real suspensions, the incorporation of polydispersity into the simulation code becomes essential.

In this sense, a second scenario of particle-level dynamic simulations is carried out by considering polydispersity in both magnetic and non-magnetic populations, while the rest of the simulation code is maintained. Polydispersity index (PDI) is a parameter related to the standard deviation ν through the expression $PDI = 3\nu^2 + 1$. According to the size distribution analysis of cornstarch used in experiments, $PDI_{Starch,25°C} = 1.388$ (see Table 3.3), so that $= 0.36$. For the sake of simplicity, standard deviation of both particle populations will take this value. Moreover, it is imposed in the simulation code that the ratio between non-magnetic and magnetic mean particle diameters is 10, similarly to the experimental case, namely $\sigma_N = 10$ μm, and $\sigma_M = 1$ μm.

The use of this value of standard PDI allows for having more concentrated initial configurations. Comparably to the first scenario, at this point we study the rheological behaviour of hybrid systems composed of magnetisable and non-magnetisable spherical and polydisperse particles, both at rest and under shear flow, subjected to a constant magnetic field.

5.4. Results and discussion

Rheological results of bimodal suspensions are presented in this section. First, we explore the effect of the addition of magnetic particles to a model ST fluid in Subsection 5.4.1. Then, in Subsection 5.4.2the rheological behaviour of MRST fluids was investigated using core-shell particles of carbonyl iron coated with starch in the formulation of concentrated hybrid suspensions. After that, we compare rheological results of unimodal and these two types of hybrid suspensions in Subsection 5.4.3. Final subsections are devoted to the particle-level simulation results of bimodal systems, i.e., composed by magnetisable and non-magnetisable populations. The effects of magnetic field, particle concentration and volume fraction ratios are evaluated for monodisperse and polydisperse systems, in Subsection 5.4.4 and Subsection 5.4.5, respectively.

5.4.1. Bimodal MRST suspensions

In this subsection we study the rheological properties of bimodal suspensions in water. The disperse phase is constituted by two types of particles: starch and carbonyl iron (CC grade). The effect of the iron concentration and magnetic field on the rheological response of these MRST fluids is investigated.

- **Rheology of MRST suspensions**

MRST suspensions are hybrid systems whose rheological response, by means of the addition of magnetic particles to concentrated suspensions displaying shear-thickening behaviour (or inversely, the addition of a shear-thickening agent to a MR suspension), can be tuned well passively by modifying the flow conditions or actively by changing the intensity of the applied magnetic field.

As a first approach we prepared a suspension with $\phi_{Starch} = 0.36$ and $\phi_{CC} = 0.005$. This starch concentration was selected because it was previously shown to develop shear thickening by itself. Moreover, the small amount of iron, by its part, is thought to be enough to display magnetic response under field conditions without interfering excessively in the thickening behaviour. The rheological behaviour of this bimodal mixture is shown in Figure 5.3 in comparison with the unimodal MR suspension.

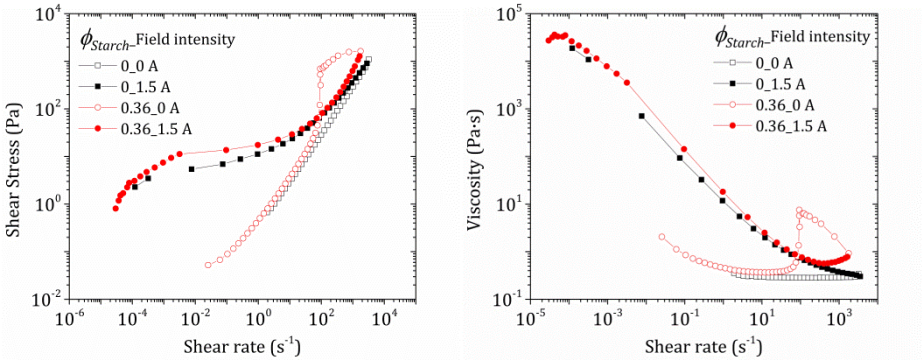

Figure 5.3: Effect of magnetic field and addition of starch to a diluted MR suspension with a fixed concentration of carbonyl iron of $\phi_{CC} = 0.005$. Plate-plate geometry.

It can be observed that the unimodal suspension, even corresponding to a very small magnetic volume fraction, shows the typical behaviour of MR fluids, i.e., in absence of field it behaves as a Newtonian fluid and in on-state conditions the viscosity increases several orders of magnitude at low shear rates, where an apparent yield stress is found (the slope in the viscosity/shear rate representation in logarithmic scales is -1), as a consequence of the orientation of magnetic particles along the magnetic lines. At higher shear rates the columnar structures begin to break and finally reach the viscosity of the suspension in no-field conditions.

In the case of the suspension formulated with mixtures of particles, the addition of non-magnetic particles implies the increase in stress (and so in

viscosity) in the whole range of shear rates, both in presence and absence of magnetic field. It is expected as the total concentration of particles has increased. In this case, the curves show the typical profile of ST fluids, i.e., the suspensions display shear-thinning, Newtonian and shear-thickening behaviours as the shear rate increases. Specifically, these particles provided a strong shear-thickening response above 100 s^{-1} in no-field conditions (as it already happened at the same concentration of starch in unimodal suspensions), which is obscured when the magnetic field is applied, and only a slight increase is found at higher shear rates compared to the off-state case.

The apparent yield stresses in the field state took the values of 5.41 Pa for carbonyl iron suspension and 11.26 Pa for the mixture of particles. However, the increase in yield stress cannot be only caused by the fact of having non-magnetic particles mixed with magnetic ones, but mainly by the high increase in total concentration.

- **Effect of carbonyl iron concentration**

A batch of hybrid MRST suspensions were prepared with different magnetic concentrations ($\phi \leq 0.05$) with a fixed $\phi_{Starch} = 0.36$. Rheological results are shown in Figure 5.4 in absence and presence of magnetic field.

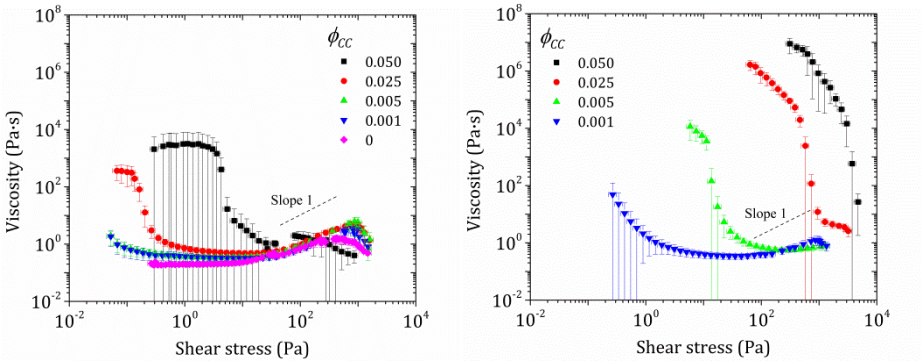

Figure 5.4: Viscosity as a function of shear stress for suspensions with $\phi_{Starch} = 0.36$ and different concentrations of carbonyl iron (CC grade), in the absence (left) and presence (right) of an external magnetic field $H_0 = 177$ kA/m. Plate-plate geometry.

The addition of a small amount of magnetic particles to shear-thickening systems results in the inclusion of others attractive interparticle interactions that affect the viscosity profile. In the absence of magnetic field it can be appreciated that the main contribution of these particles is found at low shear rates or stresses. In this sense, as the magnetic concentration increases the Newtonian plateau at low shear rates is observable and enlarges, thus causing

the delay in the appearance of the shear-thinning region. On the other hand, shear-thickening regions slightly modify their stress onset but decrease the interval of appearance, as the points of maximum viscosity are found at lower shear stresses as the magnetic concentration increases. If shear rates is considered instead, the critical parameters decreases with the increase in magnetic concentration, as expected, as the total concentration is also increasing.

When an external magnetic field of $H_0 = 177$ kA/m is applied the increase in magnetic volume fraction produces a shift of the curves to higher shear stresses, a reduction in the shear-thickening region as well as its intensity. It can be observed how shear thickening is completely obscured above $\phi_M = 0.005$, due to the predominance of magnetostatic forces over those supporting the shear-thickening response. It is noteworthy that high starch volume fractions are needed for shear thickening to take place, while a small concentration of carbonyl iron is needed to observe an increasing contribution of magnetostatic forces with the magnetic field. For a given system, the application of magnetic field provide an increase in the viscosity of several orders of magnitude compared to the off-state case, known as magnetorheological effect, and the thickening behaviour disappears only if magnetic concentration is high enough.

From Figure 5.4 it can be concluded that in MRST fluids, shear-thickening behaviour can be maintained if the magnetic concentration and field intensity are low enough. With this in mind we investigated in detail the effect of the magnetic field strength in the rheological behavior of the two lowest iron concentrations.

- **Influence of magnetic field strength**

We measured two hybrid systems with constant $\phi_{Starch} = 0.36$ and two low concentration of carbonyl iron, namely $\phi_{CC} = 0.001$ and 0.005, in a wide range of values. Viscosity curves are shown in Figure 5.5.

At the lowest carbonyl iron concentration, the change in shear-thickening behaviour is almost negligible but the viscosity at low shear stresses increases with the magnetic field, as expected. However, in the case of a $\phi_{CC} = 0.005$, both the region where magnetic forces dominate and that where shear thickening arises are influenced by the magnetic field. It is not surprising the increase in viscosity in the shear-thinning region as a consequence of stronger magnetic interactions with the magnetic field. The shear-thickening zone, by its part, is shifted to higher stresses and shear rates, and the increase in vis-

cosity is progressively been obscured. So that, in general, both higher magnetic volume fraction and field strength affect the rheological behaviour of MRST fluids in the same sense.

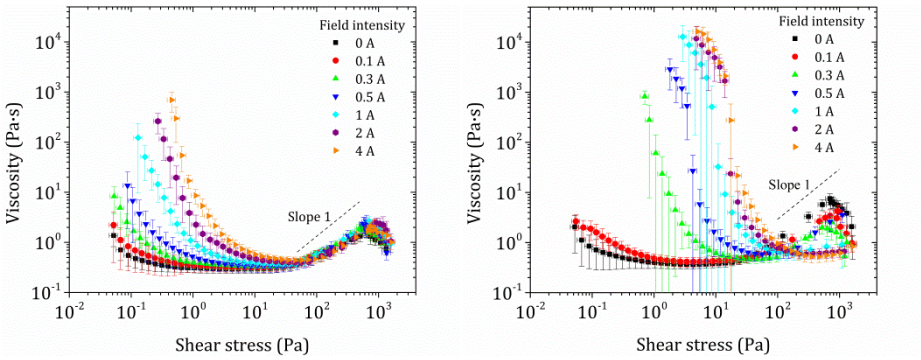

Figure 5.5: Effect of magnetic field intensity in MRST suspensions with $\phi_{Starch} = 0.36$ and $\phi_{CC} = 0.001$ and 0.005 (left and right side, respectively). Plate-plate configuration.

The influence of the magnetic volume fraction and the magnetic field strength on the shear-thickening state can be quantified with $\dot{\gamma}_c$ and β, i.e., the critical shear rate and the value of the slope of the viscosity curves plotted against the shear stress in log-log scale.

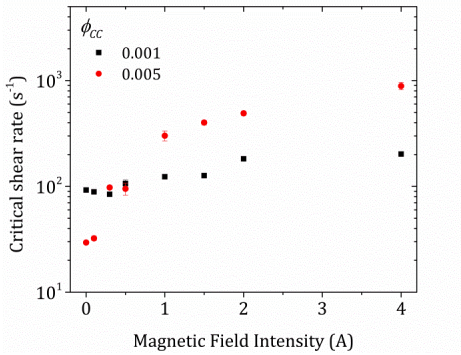

Figure 5.6: Critical shear rate as a function of the magnetic field intensity for suspensions formulated with $\phi_{Starch} = 0.36$ and two magnetic concentrations for which ST is observed. Plate-plate configuration.

The first parameter is plotted in Figure 5.6 versus several values of the magnetic field intensity for the lowest magnetic concentration. The shear-thickening region is usually preceded by a zone with Newtonian viscosity (sometimes it is reduced to a point of minimum viscosity). A transition zone is found between the Newtonian one and the consolidation of the thickening

region with a monotone increase in viscosity (in log-log scale). The critical shear rate was taken as the shear rate at the beginning of the section with constant ST slope β.

In both MRST suspensions, the critical shear rate increases with the magnetic field intensity, as we have previously seen from viscosity curves. It is worth mentioning that critical shear rates increase with the magnetic concentration from a field intensity of $I = 1\ A$ ($H_0 = 133$ kA/m) forward. However, in the absence of magnetic field, the critical shear rate decreases when the concentration of magnetic particles increases. This behaviour was also found as the total concentration increases in unimodal suspensions displaying shear thickening, as can be seen in Figure 4.7.

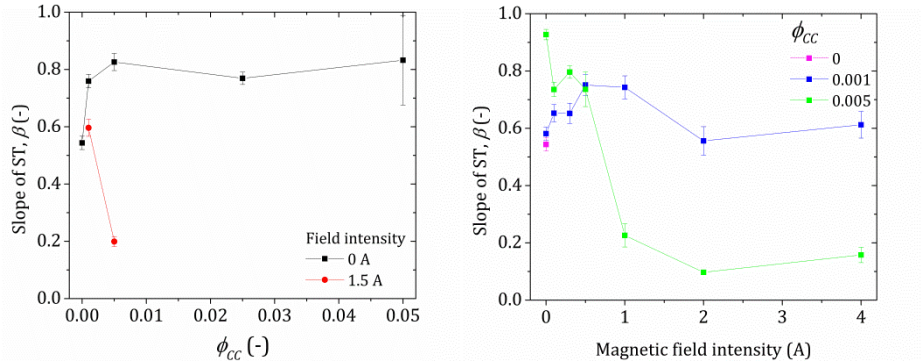

Figure 5.7: Evolution of the slope of ST in starch suspensions ($\phi_{Starch} = 0.36$) with the carbonyl iron concentration in presence and absence of magnetic field (left side) and with the applied magnetic field for several magnetic concentrations (right side). Plate-plate configuration.

Following with the analysis of the shear-thickening region, in Figure 5.7 we show the evolution of the slope in this region as a function of the magnetic concentration and the field intensity. These points are extracted from Figure 5.4 and Figure 5.5. The addition of carbonyl iron to the ST starch suspensions causes an increase in the intensity of β in no field conditions, which is maintained at least for the magnetic volume fraction investigated. However, under application of a moderate magnetic field a drastic decrease in the slope is obtained, as the ST behaviour is hindered by the increase of attractions in the system. On the other hand, the progressive increase in the magnetic field intensity for MRST suspensions with a very low $\phi_{CC} = 0.001$ does not affect considerably to the intensity of the ST response. However, a strong dependence is found for higher values of magnetic volume fraction, mainly below 1 A.

- **Normal force measurements**

Part of the rheological measurements on MRST fluids were performed in cone-plate geometry. We show in this section significant data from their respective rheograms as well as from normal force measurements during the logarithmic stress ramp, i.e., the last step in the protocol. In particular, we prepared three bimodal mixtures with $\phi_{Starch} = 0.30, 0.36$ and 0.40, and the respective magnetic concentrations being $\phi_{CC} = 0.05, 0.001$ and 0.001, but results from the intermediate system are not shown here for their similarity with the analogous experiments on plate-plate geometry.

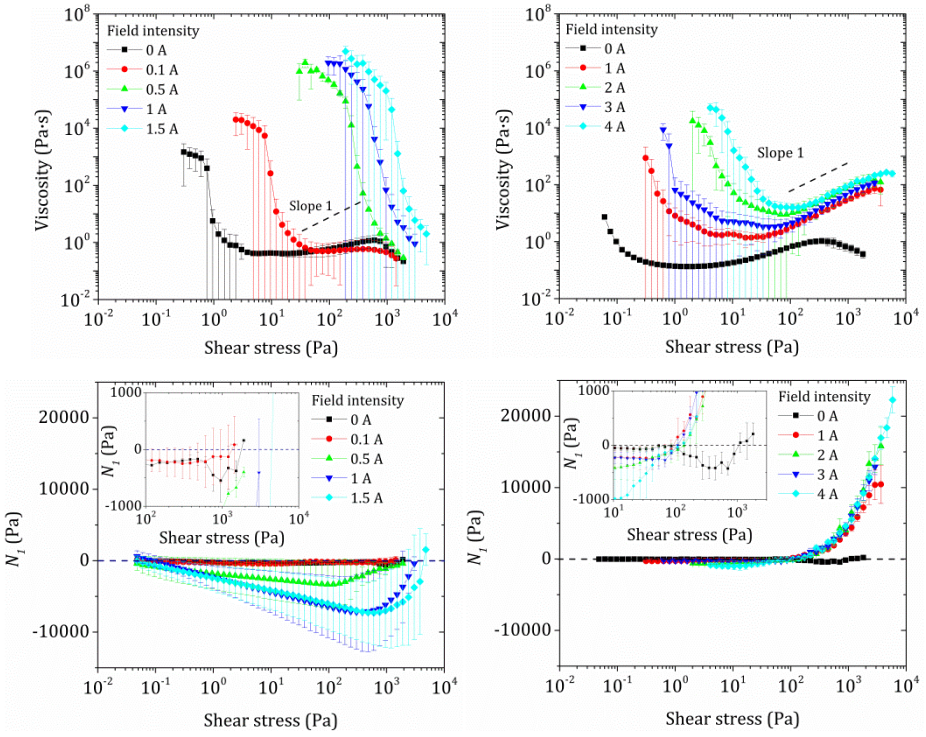

Figure 5.8: Viscosity curves and first normal stress difference (N_1) as a function of shear stress and magnetic field intensity for two MRST suspensions with ϕ_{Starch}–ϕ_{CC} being 0.30_0.05 (left side) and 0.40_0.001 (right side). Cone-plate geometry.

Viscosity curves of these systems offer the same trends previously analysed in parallel-plates experiments, i.e., the shear-thickening region is delayed and gradually vanished as both magnetic field intensity and carbonyl iron concentration increase. This is in agreement with the well-known feature needed in a system for it to display shear thickening: the absence of attraction [26]. On the other hand, at low shear rates viscosity increases with these vari-

ables due to the formation of magnetic columnar aggregates as a consequence of the induced magnetic dipolar interactions among carbonyl iron particles, which may lead to yield stress, and break as shear rate progresses.

The effect of the applied magnetic field on the normal force depends a lot on the concentration of magnetic particles in these hybrid suspensions. In the left side, where $\phi_{CC} = 0.05$, the normal force (and so N_1) continuously decreases with the applied field up to a minimum at a given shear stress. After this minimum, the response is reversed. This characteristic stress seems to coincide to the onset of the steep diminishing in viscosity in the graph above, corresponding to the yield stress. A similar behaviour was previously observed [61]. They prepared MR suspensions at a higher concentration (10 %) for which the solid phase was only composed by micronsized magnetic particles. These unimodal suspensions showed a normal force dependence with particle concentration and magnetic field, as expected. Moreover, the normal force, developed as a consequence of the application of the magnetic field, was always positive in the whole interval of shear rates. They found two plateaus at low and high shear rates, while at intermediate values the normal force reached a minimum, which was independent of the magnetic field and was related to the pre-yield regime.

In our system with starch (0.30_0.05) we also have this minimum in normal force and observe that after this minimum the suspension also start to flow, but the related shear stress varies with the field, as yield stress does. The main difference with this work in literature comes from the sign in normal force, which in the case of our bimodal suspensions is negative. This fact may be due to the great contribution of the non-magnetic particles. Although a crossover stress is not observed in the five curves (the tests have to be aborted when the sample is ejected out of the geometry), it seems to be proximately the same for a given ratio of magnetic and non-magnetic particles, regarding the tendency of the curves, as it occurs with the system with a different ratio of starch to carbonyl iron (case of 0.36_0.001).

On the other hand, in the case of highly concentrated MR suspensions, de Vicente et al. [62] found positive values of the normal force upon the application of high enough magnetic fields as a consequence of the gap spanning occurring by the formation of magnetic chains. During shearing these structures bend and, because of such a high concentration, chains join in stronger structures that also provoke the system expansion. However the curve profile of normal force against shear stress reaches a maximum (instead of a minimum)

at the onset of the flow. What is comparable among these three works is the existence of an inflection point that marks the onset of the flow after the yield stress.

Flow curves and normal force related to the system 0.40_0.001 are plotted in the right side of Figure 5.8. At this starch concentration, the shear-thickening response is very strong and the addition of such small amount of iron cannot inhibit this behaviour, even at the highest magnetic field. Due to the difficulty in having a well-mixed suspension at such a high total concentration, viscosity curves do not show a clear tendency as the previous system.

The effect of magnetic field in the normal force for the hybrid suspension with a $\phi_{CC} = 0.001$ is similar to the that found for the system with $\phi_{Starch} = 0.05$, in the sense that normal force has negative values until a given crossover stress takes place (a decade below than for the right case). Moreover, the magnitude of normal force is much lower probably due to the difference in magnetic concentration.

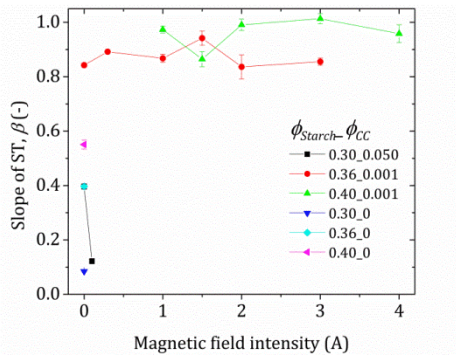

Figure 5.9: Slope of ST for unimodal and bimodal concentrated suspensions as a function of the magnetic field intensity. Cone-plate configuration.

Figure 5.9 shows the slopes of ST in MRST fluids studied in cone-plate configuration, as a function of the magnetic yield intensity. For comparison, results from unimodal starch suspensions, measured in the same geometry, are also shown. In absence of magnetic field, the studied parameter increases with the total volume fraction, as expected. When the magnetic field is applied, its effect in β depends on the magnetic concentration employed though.

It is interesting the intense reduction in β for the bimodal system with the lowest concentration in on-field state in comparison with the unimodal case of $\phi_{Starch} = 0.36$ (both systems have similar ϕ_T). The addition of such

amount of carbonyl iron greatly increases the attraction in the suspension, and so the ST behaviour is weakened in on-state field conditions. However, it is striking the noticeable increment in the ST response for MRST suspensions with a $\phi_{CC} = 0.001$, with a value of β that is nearly independent of the magnetic field and very close to unity, mainly in the most concentrated case. It is reasonable to think that these rheological measurements are slightly overestimated, as cone-plate geometry is not the most adequate configuration when the magnetic field is applied. However, both Figure 5.7 and Figure 5.9 agree on the great dependence of the slope of the ST on the magnetic concentration when the magnetic field is applied. This suggests that there is a critical volume fraction of carbonyl iron that somehow reinforces the microstructure of the system in the range of shear stresses where the shear thickening occurs. So that, besides the possibility of tuning the rheological behaviour of this system by means of the application of an external magnetic field (which mainly affects the low shear rate region and the onset of the thickening), a transition from continuous to near discontinuous shear thickening is simply achieved by the addition of a small amount of non-magnetic particles to the system.

5.4.2. Suspensions of hybrid core-shell particles

- **Environmental scanning electron microscopy (ESEM)**

We performed analysis in secondary electrons (SE) and circular backscattering (CBS) modes; the first shows the topography of the surface and the other highlights differences in concentration. The resolution in ESEM depends on the intensity of the incident primary electron beam. All images in the SE mode were taken at 5 kV. However, in the CBS mode the beam is set at 5 kV but the slide is set at 2 kV. With this trick, the beam reaches the sample decelerated, and the landing velocity of the electrons in the surface of the sample is actually 3 kV. This reduction is necessary because we expect a narrow thickness of starch coating the carbonyl iron particles (of several nanometres). A higher intensity of the incident beam involves more penetration, and micrographs would show only iron. In this sense, the micrographs obtained in SE mode have a better resolution than in the other mode, but with this last, changes in composition can be better observed with different brightness (compare images in Figure 5.10 with lower magnification).

In Figure 5.10 we show some micrographs of bimodal core-shell particles obtained following the methods of Table 5.1. Each image will be named according the type of particle and coating method employed, e.g., OM/D (a) and

b) cases). From Figure 5.10-a it can be observed that carbonyl iron particles have craters on their surfaces as a consequence of the strong action of the pre-treatment with acid. Moreover, thanks to the CBS mode we can clearly distinguish iron particles from undissolved starch granule (bigger and in darker grey). The coating of OM particles by any of the three methods did not provide good results as we found little evidence of coating and the film of starch was irregularly set onto the magnetic particles (see Figure 5.10-b). In contrast, the coating of CC particles was quite satisfactory by both DL and S methods, with similar ESEM micrographs. Following these methods a better dissolution of starch was achieved, thus leading to a better coating of the magnetic particles. As can be seen in Figure 5.10-d, particles are homogeneously covered by a film of starch.

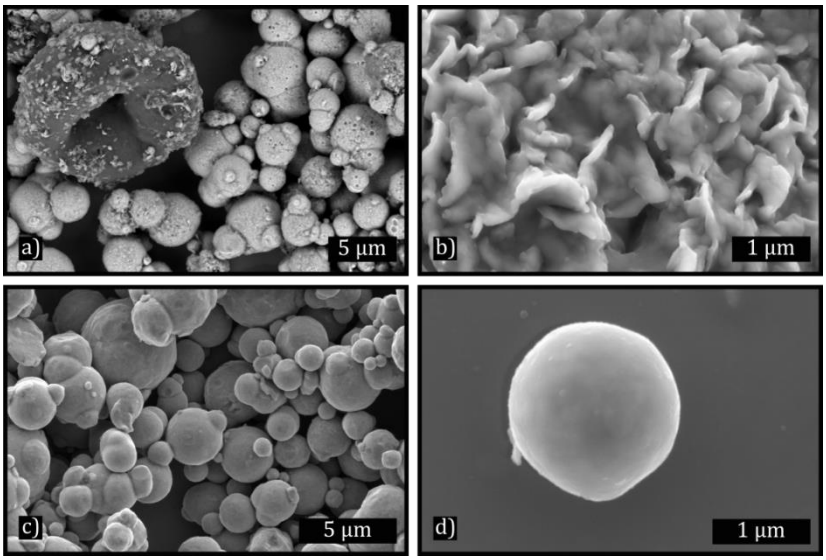

Figure 5.10: ESEM micrographs of carbonyl iron particles coated with starch. a) and b) OM/D; c) and d) CC/S. All images correspond to SE mode except a), taken in CBS mode.

- **Transmission electron microscopy (TEM)**

In this case a very diluted suspension of particles is required, as the suspension passes through a grid in which particles are retained. This technique occasionally requires a negative staining of the sample to observe organic substances, because they present some transparency. In our case this was unnecessary as the iron core presents a black colour while the layer of coating is perceived in a lighter colour.

This technique was only applied to the systems that resulted in a regular coating from ESEM images, i.e., for CC particles. Both methods of coating these magnetic particles provided similar results as it can be seen in Figure 5.11. A thin and uniform layer of starch is found on the surface of CC particles. Furthermore, this veil of starch may coat several particles at the same time, so bringing together two or more carbonyl iron particles (see Figure 5.11-a). The thickness was quantified from images; for the CC/S case it ranged between 6 and 9 nm in the particles observed (with diameters slightly above 1 μm), without considering the meniscus between the joining particles where it is clearly higher, and in the CC/DL case the thickest part reached nearly 30 nm in the particle shown below, with a diameter below 2 μm. Compared to particles pre-treated, with OM grade, CC particles were much favourably coated, with a layer of starch that gently varies its thickness but covers the whole surface of carbonyl iron.

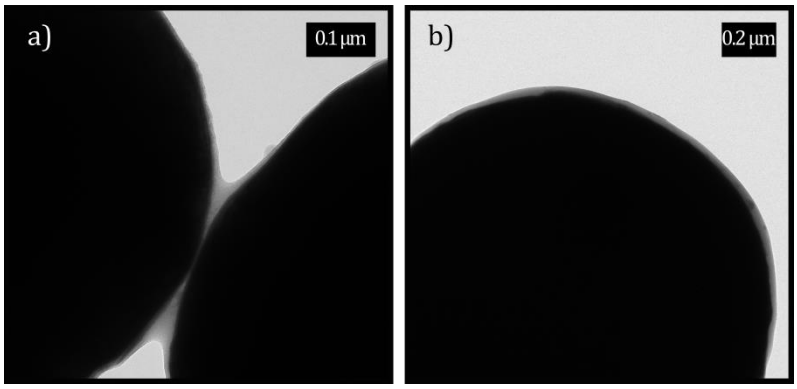

Figure 5.11: TEM micrographs of carbonyl iron particles coated with starch. a) CC/S, b) CC/DL.

- **Rheological results**

Due to the lack of precedents in the coating of carbonyl iron particles with starch, we prepared core-shell particles through small variations to previous protocols where similar reagents were involved. The amount of core-shell particles collected after the step of drying was low but enough to perform some rheological experiments, in order to compare the behaviour of the suspensions prepared with hybrid particles obtained through different coating methods. Because of this, each sample was measured just once and the rheological curves exposed within this section are not accompanied by their errors.

In Figure 5.12, the three protocols of coating carbonyl iron particles with OM-grade with starch (see Subsection 5.2.3) are compared in terms of their rheological response. MR suspensions formulated with these hybrid particles and water, at $\phi_{OM} = 0.05$, were tested in absence and presence of magnetic field ($H = 177$ kA/m). It can be observed that there is no much difference between the three coatings and the MR suspension of raw OM particles. All the suspensions display Newtonian behaviour in absence of magnetic field, and when it is present the contribution of the magnetic interactions among particles is evident, causing the increase in viscosity of several orders of magnitude and an apparent yield stress is almost found.

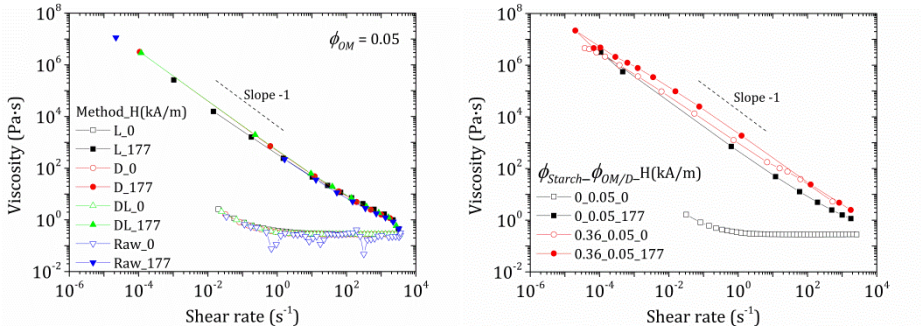

Figure 5.12: Flow curves of diluted suspensions of raw and coated carbonyl iron (grade OM) with starch according to three methods (left graph). Effect of addition of starch to a diluted suspension of OM/D hybrid particles (right graph). Open and close symbols belong to curves in the absence and presence of an external magnetic field, respectively. Plate-plate geometry.

The effect of the addition of starch to diluted MR fluids prepared with OM carbonyl iron particles coated by D-method is shown in Figure 5.12. In this sense, both systems share the same magnetic volume fraction $\phi_{OM/D} = 0.05$. In off-field state only the MR fluid is Newtonian as correspond to conventional MR fluids with low concentrations; the suspension with starch ($\phi_{Starch} = 0.36$) presents higher viscosity in the entire range of shear rates as a consequence of the high concentration. However it does not show shear thickening at high shear rates but a shear-thinning behaviour in the whole interval investigated, in spite of having a total volume fraction of 0.41. This fact coincides with results in Subsection 5.4.1, where a 5 % of magnetic particles thoroughly inhibited the appearance of ST phenomenon. However, there is a slight change in the slope of the viscosity curve of the bimodal suspension around 7 s^{-1}, which indicates that ST could happen if lower magnetic field intensities or magnetic concentrations are applied.

On the other hand, the application of the magnetic field provokes a moderate increase in viscosity as a consequence of the magnetostatic effect and shear-thinning behaviour. This relative increase when the field is applied is much lower than for the MR suspension without starch particles. This occurrence is due to the great contribution of non-magnetic particles to the viscosity in off-state conditions.

From now onwards, results of carbonyl iron with CC grade are shown, being DL-method the protocol of coating, in view of the homogeneous starch coating generated in these conditions.

In Figure 5.13 we compare three unimodal suspensions in water with the same total volume fraction, $\phi_T = 0.36$, and formulated with starch, raw carbonyl iron with CC grade or coated carbonyl iron CC by means of DL-method.

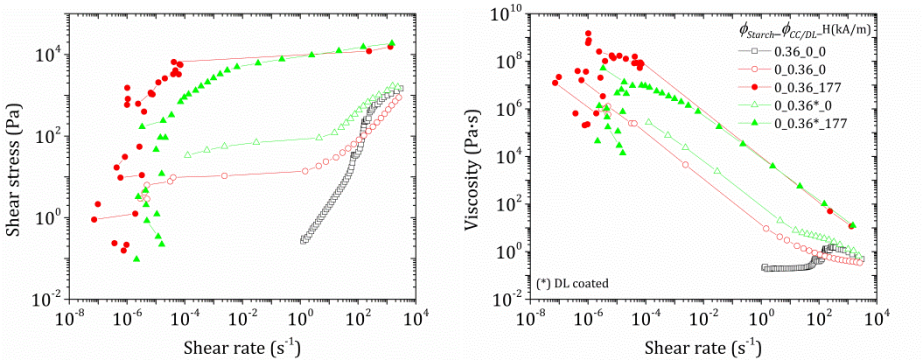

Figure 5.13: Shear stress and viscosity as a function of shear rate for concentrated suspensions formulated with an unique type of particle, and with $\phi_T = 0.36$ in all cases. Plate-plate geometry.

In the case of starch suspension, at this concentration of particles the suspension shear-thicken continuously, as expected. On the one hand, we can observe that the system totally composed by carbonyl iron particles does not present any evidence of shear thickening in this carrier. This fact indicates that a moderate concentration of particles is necessary but not sufficient to observe shear thickening. Its behaviour in absence and presence of magnetic field is typical of a MR fluid at moderate concentration, as previously explained. The interesting behaviour is that of the suspension formulated with the hybrid core-shell particles. The thin layer of starch allow for the appearance of an inflection point during the shear-thinning behaviour in the viscosity curve. The contribution of this coating is low but perceptible, what confirms that there is something more apart from the bare magnetic particles in

the system. The suspensions of magnetic particles, well starch-coated or not, are very similar in terms of particle size and sedimentation rates. The difference in viscosity curves in the absence of magnetic field can come from the fact that the layer of starch results in particles with higher roughness. Thus, in the core-shell suspension strong interactions between rough surfaces are taking place, in accordance with [63]. Apart from higher roughness, the shear-induced particle network is reinforced by hydrogen bonding between terminal hydroxyl groups from the layer of starch.

The coating in on-state field conditions mainly affects the rheogram at low shear rates. The non-coated concentrated suspension displays a clear yield stress while in the coated suspension the transition from low to intermediate shear rates is moderate in terms of shear stresses, as a consequence of a reduce magnetic particle-particle interaction.

5.4.3. Comparison between bimodal suspensions and formulated with hybrid core-shell particles

In this subsection we revisit the experimental rheological results of concentrated suspensions in water formulated by combination of two elements: starch and carbonyl iron. We consider unimodal and bimodal suspensions with a $\phi_T \geq 0.35$, well formulated with hybrid magnetic-non magnetic core-shell particles or with mixtures of these particles, respectively.

Figure 5.14 show the viscosity curves of these suspensions in absence and presence of magnetic field. From these graphs we can summarize several aspects. In the absence of magnetic field, suspensions with a $\phi_{Starch} = 0.36$ provide shear thickening whatever the magnetic concentration. The intensity of this behaviour decreases as magnetic concentration increases, although the viscosity is higher, due to a higher total concentration. The fact that magnetic particles have a smoother particle surface compared to that of starch granules, may be the reason for this reduction. The shear-induced particle network in the shear-thickening regime may flow easily when a portion of particles are smooth spheres.

However, the fact of having a $\phi_T = 0.36$ does not guarantee the exhibition of ST. The magnetic unimodal suspensions at this concentration do not display ST but a shear-thinning region in the entire range of shear rates evaluated. At low shear rates the viscosity of the magnetic suspensions is higher than for starch suspensions. It can be explained due to the difference in parti-

cle size; for a given volume fraction, the number of particles in the system will be larger when these particles are smaller, thus increasing the available area to interact with other particles, and so the viscosity.

Moreover starch-coated carbonyl iron particles enhance the viscosity of the suspension, though the thin layer of starch deposited in the magnetic core is not capable of producing ST but reduces the decrease rate in viscosity. In bimodal mixtures, a higher total volume fraction increases the viscosity, but shear thickening is observed only when the unimodal suspension with the same ϕ_{Starch} also exhibits this behaviour.

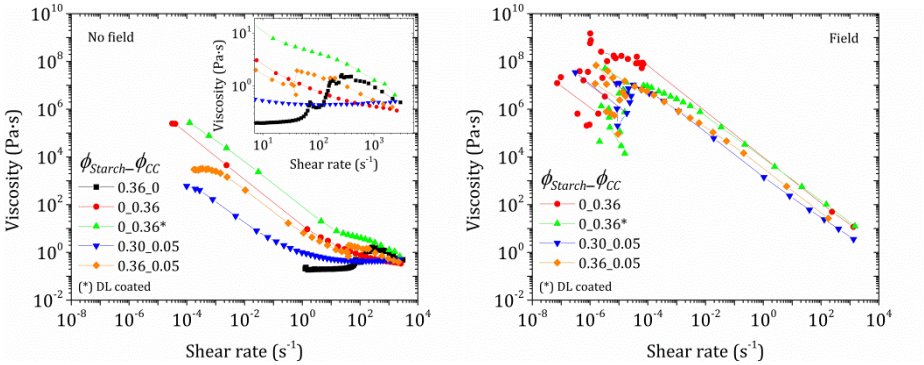

Figure 5.14: Viscosity as a function of shear rate for unimodal and bimodal concentrated suspensions, in the absence (left) and presence (right) of magnetic field $H = 177$ kA/m.

Furthermore, in presence of a sufficient magnetic field, we can assert that these systems exhibit shear-thinning behaviour preceded by an apparent yield stress (the slope of the decay in viscosity curves as a function of shear rate is -1). Shear thickening is obscured upon certain magnetic concentration and field intensity if the system displays this behaviour in off-state conditions. The magnetic volume fraction leads the increase in viscosity curves, and if magnetic concentration is fixed, the larger the total volume fraction the higher the viscosity. Finally, the layer of starch coating carbonyl iron particles soften the transition between no flow at low shear rates and the flowing state, compared to non-coated particles, as this layer reduces the magnetic interactions between particles and so the strength of the structures formed as a consequence of the magnetic field.

5.4.4. Simulation of mixtures of monodisperse particles

This subsection is the first devoted to show the simulations results for the case of having hybrid and monodisperse systems. We study the structuration

of mixtures of magnetic and non-magnetic spherical particles subjected to an external magnetic field, both at rest and under distinct values of shear rates. The final objective is to determine whether the partial substitution of magnetic particles by non-magnetic ones may enhance the yield stress in these simulations, as it is found in experimental works. Moreover, we are interested in the curves of the final rheogram, in relation to the possible appearance of shear thickening in the systems with a higher particle concentration and in the range of shear rates evaluated.

During structuration at rest, we followed the evolution of the total magnetic energy, the z-component of the magnetic moment and the average number of particles surrounding a given particle. In the start-up tests we payed attention to the evolution of the dimensionless magnetic stress during the simulation time, and the static magnetic stress was obtained from the peak of this stress growth test. The total shear stress was then calculated as the sum of this static magnetic stress and the hydrodynamic contribution from the applied shear. For simplicity, other contributions to the shear stress coming from the rest of non-hydrodynamic forces were neglected in comparison with the magnetic contribution to the stress. With this, a rheogram was constructed for each system considered, and its related yield stress was obtained.

It is noteworthy to point out that all these parameters exposed in this subsection refer to dimensionless magnitudes, and are averaged over five runs at least.

- **Structuration at rest**

In the first step of the simulation code Equation 5.1 is employed to solve the motion of particles, being the main contribution that coming from the external magnetic field, and the fluid field velocity is null. In this sense, at rest, particle aggregation and structuration takes place. Only results for $\phi'_M = 1$ and $\phi_T = 0.30$ are shown in this part, as their behaviour is representative for the rest of concentrations evaluated.

In Figure 5.15 we show the time evolution of the dimensionless total magnetic energy for some bimodal mixtures investigated. As it was expected, at the beginning of the simulation all systems share the same total magnetic energy (null) as magnetic and non-magnetic particles are randomly distributed in the simulation box. The total magnetic energy continuously decreases with time until each system reaches a plateau with small oscillations when it stabilizes. It is noteworthy that the simulation time imposed in this step is

enough to carry the systems to the steady state. The fact of having a progressive decrease in magnetic energy, it is, a more energetically favourable situation with time, comes from the magnetic particles alignment in the direction of the magnetic field. This gives rise to columnar structures in the presence of the magnetic field. The dependence of both ϕ'_M and ϕ_T for constant values of total concentration and relative magnetic volume fraction, respectively, can be observed in graphs below. The plateau at the end of the simulation time is faster reached for higher ϕ'_M and total volume fraction ϕ_T, what means that the systems become less stable as ϕ'_M and ϕ_T increase. It can be explained as the number of magnetic particles involved in the columnar aggregates is higher and so the size of these structures, compared to the ideal case of single-width particle chains in dilute systems.

Analogous results can also be interpreted in Figure 5.16 in terms of the averaged z-component of the magnetic moments m_z^* at constant particle loading and magnetic concentration, respectively. Again, in presence of a magnetic field a no null magnetic moment appears in the systems. As a consequence of the magnetic interaction among induced magnetic moments in the particles, they attract others and form chains at first and then, columnar aggregates. The approximation of magnetic particles as a consequence of the magnetic field gradually provokes the increase of m_z^* along the simulation time till a plateau is reached. Again, greater values are obtained for diluted systems, mainly dependent on the relative magnetic concentration more than on the total volume fraction, as it was expected.

Other aspect investigated during this step is the average number of particles surrounding other given particle. In Figure 5.17 the number of nearest neighbours along the simulation time is shown for some systems studied. In this sense, in the simulation code two particles as considered as neighbours when the centre-to-centre distance is $r_{ij} < 0.55\ (\sigma_i + \sigma_j)$. The particle aggregation enhances with time as the magnetic particles reallocate along the magnetic field lines, and it is higher for larger particle loading. Moreover, this parameter increases with the number of magnetic particles in the simulation box, as these particles are prone to aggregate in field conditions (in contrast to non-magnetic ones), as expected. A plateau is found at the end of the simulation time as the structure reaches its equilibrium state, when the rate of particles leaving the magnetic columnar structures equalizes that of particles that add to it. This plateau is rapidly reached at higher concentrations as the particle motion is more restricted.

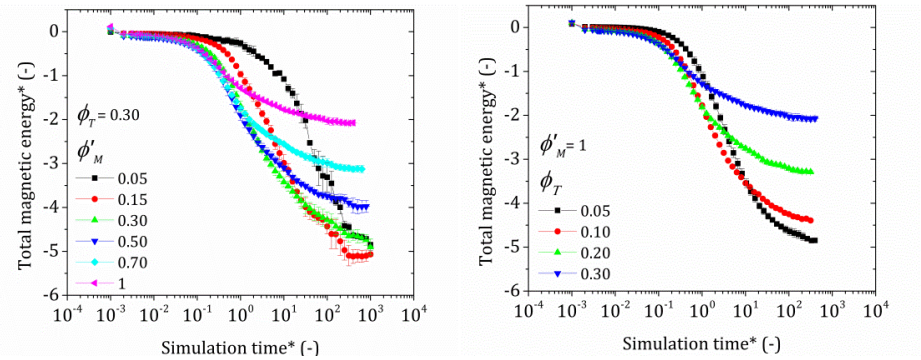

Figure 5.15: Dimensionless total magnetic energy. Influence of ϕ'_M for constant $\phi_T = 0.30$ (left side) and influence of ϕ_T for constant $\phi'_M = 1$ (right side).

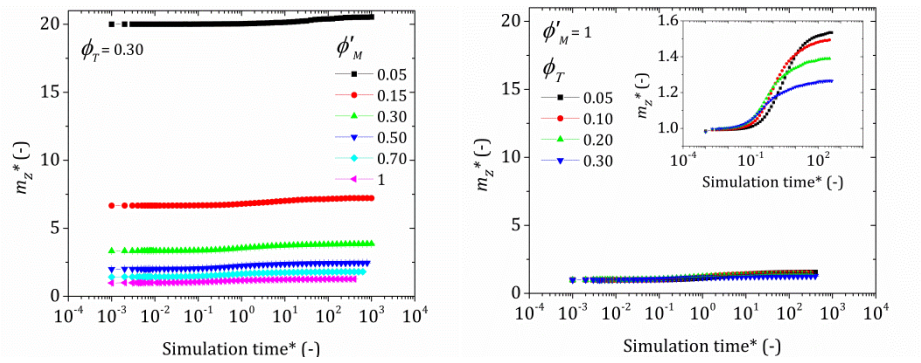

Figure 5.16: Magnetic moment in z-direction during the structuration at rest. Influence of ϕ'_M for constant $\phi_T = 0.30$ (left side) and influence of ϕ_T for constant $\phi'_M = 1$ (right side).

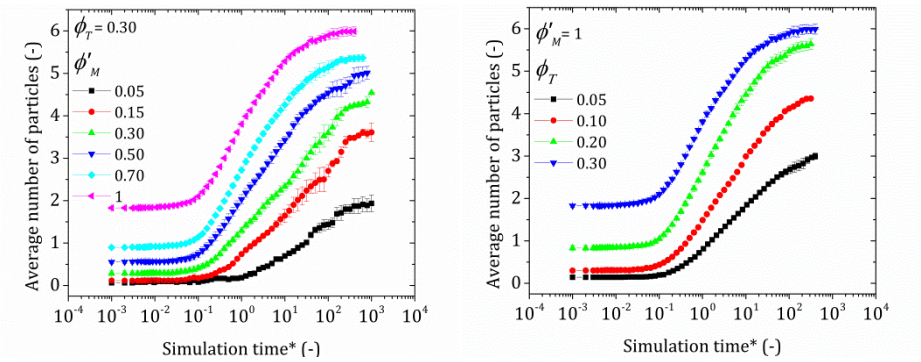

Figure 5.17: Evolution of the number of nearest neighbour particles. Influence of ϕ'_M for constant $\phi_T = 0.30$ (left side) and influence of ϕ_T for constant $\phi'_M = 1$ (right side).

- **Yielding behaviour in start-up test**

After the initial structuration at rest each steady particle configuration was subjected to several constant shear rates $\dot{\gamma}^*$. From the simulated start-up tests, the evolution of the shear stress can be tracked. In Figure 5.18 typical curves for the magnetic contribution to the stress are shown as a function of simulation time, which is proportional to the strain for constant $\dot{\gamma}^*$, for several values of shear rate. First, the stress continuously grows up to a maximum value well developed, mainly for intermediate values of $\dot{\gamma}^*$, referred to the so-called static yield stress. From this point on, the stress decreases and tends to reach the equilibrium at high strain deformation or high simulation times, i.e., dynamic yield stress.

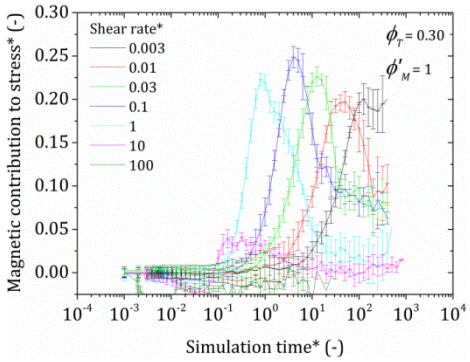

Figure 5.18: Magnetic stress growth derived from start-up tests.

It can be observed that lower shear rates require more time to develop the peak of the stress curve and, on the other hand, at $\dot{\gamma}^* = 100$ most of the curves did not show a clear static yield stress. We opted to construct the rheogram from the static yield stress because the maximum stress is easily detected in comparison with the final plateau. For example, in Figure 5.18 only the curve for $\dot{\gamma}^* = 1$ shows a clear plateau well defined, while for lower values the curves have not reached the plateau, and much more simulation time would be required. The identification of the peak stress and the steady state becomes more difficult at smaller magnetic and total volume fractions.

Static magnetic stresses (i.e., peaks of the curves in Figure 5.18) are plotted in Figure 5.19-left as a function of the applied shear rates for a constant particle loading, namely the highest investigated. The magnetic contribution to the static stress increases with the magnetic concentration of particles. Besides, a maximum generally appears at $\dot{\gamma}^* = 0.1$.

On the other hand, a typical rheogram is presented in Figure 5.19-right for the case of constant $\phi_T = 0.30$ and several relative magnetic volume fractions. The total shear stress was approximated as the addition of the hydrodynamic contribution to the static yield stress from each start-up test. The rheograms clearly exhibit two regions. At low shear rates a plateau appears and at higher values the systems can flow and curves collapse for all the studied systems. This behaviour is expected in yield-stress materials as it is the case of MR fluids. It can be observed that for systems in which half of the volume is occupied by non-magnetic particles the plateau is quite vague, whilst above a $\phi'_M = 0.50$ the plateau is well defined and the curves collapse. This behaviour is a common feature for all the rheograms constructed with a fixed total volume fraction.

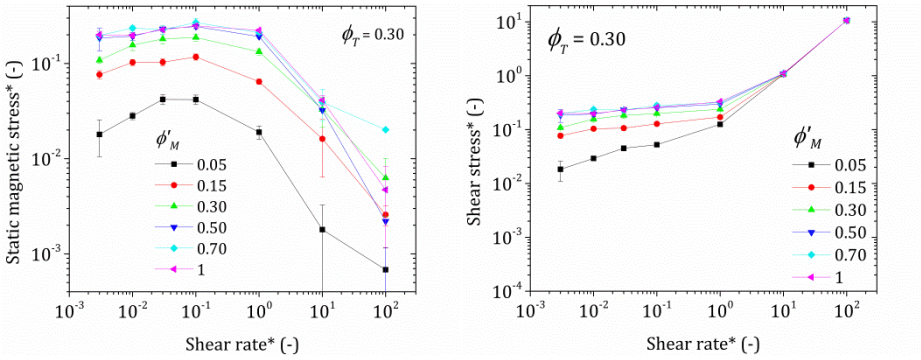

Figure 5.19: Influence of ϕ'_M to the dimensionless static magnetic stress (left side) and shear stress (right side), for $\phi_T = 0.30$.

By comparing both graphs in Figure 5.19 we can appreciate that the hydrodynamic contribution to the stress is mainly relevant at high shear rates, while at low values it is insignificant and the magnetic contribution prevails. Yield stresses for each case of bimodal system have been obtained in several ways: by averaging shear stresses at low shear rates, i.e., in the plateau zone, and by fitting the whole curves to Casson model ($\sqrt{\tau} = \sqrt{\tau_y} + \sqrt{\eta_p \dot{\gamma}}$). In Figure 5.20 we plot the dimensionless static yield stress τ_y^* as a function of the magnetic concentration for fixed values of volume fraction and vice versa. Results for yield stress obtained from Casson model offered good statistics ($R^2 \sim 1$ for most curves), however the errors associated to τ_y^* were of the same order than the value. Yield stresses from Casson model are in all the cases below the averages of stress at low shear rates. Higher yield stresses are found

as both the magnetic and total particle concentration increases, as a general trend, in accordance with experimental results.

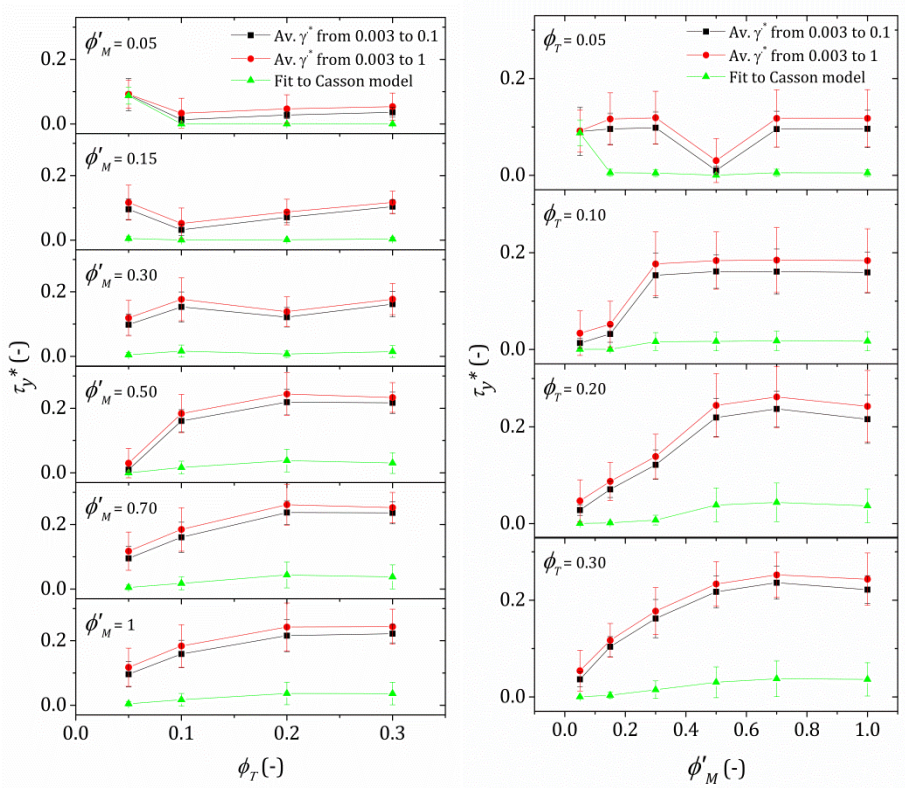

Figure 5.20: Static yield stress at constant ϕ'_M (left side) and constant ϕ_T (right side), calculated by averaging shear stresses at low shear rates and from the fit of the curves in rheograms to Casson model.

The effect of the addition of non-magnetic particles to a magnetic-based system is better observed in Figure 5.21. The yield stress of bimodal magnetic/non-magnetic mixtures (for the case of $\phi_T = 0.30$) is compared to fully magnetic systems (i.e., $\phi'_M = 1$, whatever ϕ_T), and the three ways of obtaining the yield stress are shown again. In order to make this comparison the real magnetic volume fraction ϕ_M was calculated and plotted versus the yield stress previously obtained. It can be observed that for mixtures with a higher volume fraction of non-magnetic particles, i.e., for $0 \leq \phi_M \leq 0.15$ or $0 \leq \phi'_M \leq 0.50$, and ϕ_T being 0.30, the yield stress keeps below that obtained for $\phi_M = 0.30$. However, if majority of particles are magnetic, the addition of non-magnetic particles results in a slightly higher yield stress for a fixed ϕ_M total volume fraction.

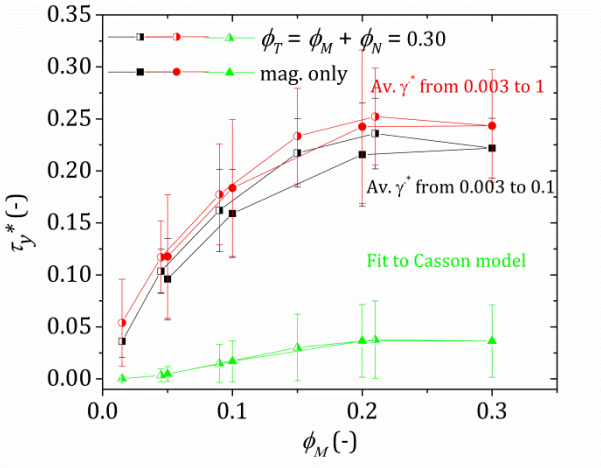

Figure 5.21: Static yield stress as a function of the real magnetic volume fraction. The total concentration is fixed at $\phi_T = 0.30$, and unimodal systems and bimodal mixtures are compared. The three ways of determining the static yield stress from rheogram in Figure 5.19 are shown.

The same behaviour was found for the case $\phi_T = 0.20$, while for lower values of ϕ_T no enhancement in yield stress has been found with the partial substitution of magnetic particles. These results are in qualitative agreement with the work of Ulicny el al. [39]. The relative increase in yield stress can be calculated in the same way that this author for the suspension with $\phi_M = 0.21$ and $\phi_N = 0.09$, compared with that with $\phi_M = \phi_T = 0.30$. The enhancement by substituting magnetic particles by non-magnetic ones is a 6.36 % for this total particle loading when the yield stress was calculated by averaging shear stresses up to a shear rate of $\dot{\gamma}^* = 0.1$ (black symbols in Figure 5.21). Ulicny et al. [39] showed a linear dependence of the enhancement with the volume fraction of non-magnetisable particles in simulation results, for a fixed concentration of magnetic spheres. In this work it is not possible to provide the analogue relationship for total loading of $\phi_T = 0.30$ or 0.20, as only one configuration (because of the lack of other intermediate ϕ'_M between 0.50 and 1) of mixtures has produced this increase in yield stress compared to the unimodal system in each case, namely those systems with $\phi'_M = 0.70$. Future work in this sense should explore in detail the range of relative magnetic concentrations of $0.50 < \phi'_M < 1$ in order to obtain a trustworthy correlation between the enhancement in yield stress and the volume fraction of one type of particle.

5.4.5. Simulation of mixtures of polydisperse particles

The rheological behaviour of MRST fluids was experimentally studied in previous subsections. From these results it was concluded that it is possible for these hybrid systems to show both magnetic and shear-thickening responses if the concentration of magnetic particles or the field intensity were kept low enough. Moreover, shear-thickening behaviour requires large concentrations of particles to occur.

Although monodisperse particles were used in Subsection 5.4.4., and these simulations agree with other authors that found a beneficial effect in the yield stress when substituting part of magnetic particles by non-magnetic ones, the second objective of observing the shear-thickening response in the constructed rheograms was not achieved. It is due to the maximum total volume fraction that could be allocated in the simulation box with monodisperse particles was $\phi_T = 0.30$. With this intention in mind higher total volume fractions are necessary, so that we performed new simulations of mixtures of particles in which both populations present polydispersity.

These simulations follow the same procedure that in the monodisperse case, i.e., structuration at rest and under constant shear flows, being the systems subjected to a constant external magnetic field in both steps. Although some results of intermediate steps are shown in this subsection, the final rheograms will be the focus of our attention. From now on, rheograms presented here are constructed by adding the hydrodynamic contribution to the total static stress, which accounts for magnetic, repulsive, wall and Brownian interactions. This is in contrast to Subsection 5.4.4., where only the magnetic contribution was taken into account in the static stress, as it was by far the main contribution to the total stress. The incorporation of polydispersity is firstly studied in bimodal systems, and then in the unimodal case, for which $\phi_N = 0$.

- **Bimodal case**

In these simulations non-magnetic volume fractions are studied in the interval $\phi_N = 0.30 - 0.50$, while magnetic volume fractions used are very low, in the range from $\phi_M = 0.0002$ to 0.0005. These values have been chosen below the experimental magnetic volume fractions in order not to obscure the appearance of shear thickening. Regarding the magnetic field intensity the mixtures are subjected to, we consider the case of the value employed in experi-

ments, i.e., $H_0 = 177$ kA/m. In this sense, experimental rheograms are compared to those obtained from particle-level simulations.

It can be observed in Figure 5.22 that the magnetic and non-magnetic dependences on the structuration at rest in these simulations are analogous to the monodisperse case (see Figure 5.15 and Figure 5.16). The progressive decrease in the total magnetic energy* (and the respective increase in m_z^*) indicates that the systems evolve towards their equilibrium state in presence of the magnetic field, while magnetic particles aggregate in columnar structures in the field direction. Once more, it is found that for a fixed non-magnetic concentration the structuration in these bimodal systems is more energetically favourable at lower values of ϕ_M. By the same token, for a fixed ϕ_M, the stability is higher as the non-magnetic concentration decreases. This fact is easy to understand when comparing the features of these structures with the single-width particle chains taken place in the ideal case of dilute systems.

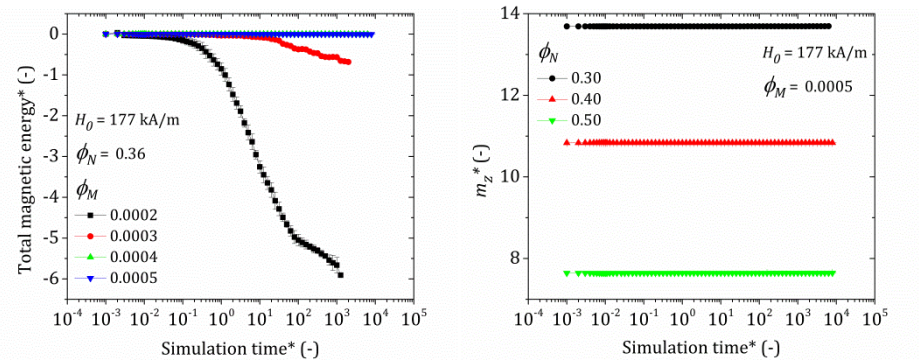

Figure 5.22: Structuration at rest of bimodal and polydisperse systems, subjected to an external magnetic $H_0 = 177$ kA/m. Effect of ϕ_M in the dimensionless total magnetic energy (left side) and effect of ϕ_N in the dimensionless magnetic moment in z-direction (right side).

After the structuration at rest step, the systems are subjected to constant dimensionless shear rates. As example, in Figure 5.23 the total static stress* is plotted for a bimodal system. Every curve shows a very well defined peak, with which the corresponding rheogram is then constructed after the addition of the hydrodynamic contribution to the stress.

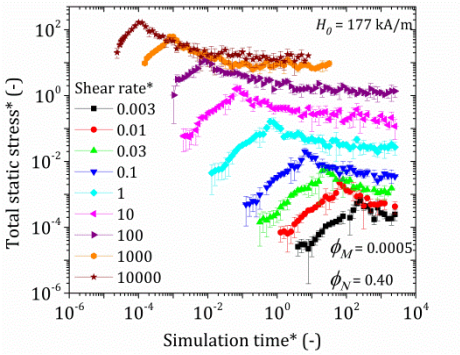

Figure 5.23: Evolution of the total static stress* during start-up tests for $\phi_M = 0.0005$, $\phi_N = 0.40$, and constant $H_0 = 177$ kA/m.

In the left side of Figure 5.24 the rheograms of bimodal systems with the same non-magnetic concentration are plotted for different and very low concentrations of the magnetisable phase. The choice of $\phi_N = 0.36$ is based on previous experimental results of starch, as the suspension with this concentration develops shear thickening in mixtures with very low iron concentration (see Figure 5.4). In the graph, however, a Newtonian behaviour is exhibited by the simulated systems along the whole range of dimensional shear rates evaluated.

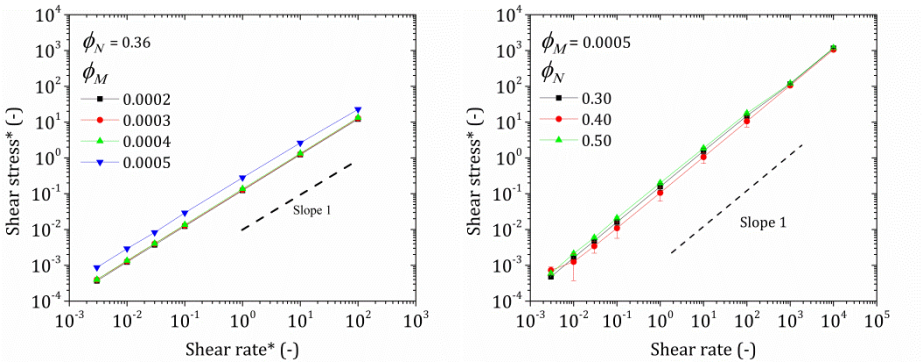

Figure 5.24: Rheograms at constant $H_0 = 177$ kA/m, for fixed $\phi_N = 0.36$ (left side) and $\phi_M = 0.0005$ (right side).

This result is in agreement with the rheogram in Figure 5.19, where the evidence of a yield stress in the mixtures becomes blurred as the magnetic concentration diminishes. So for magnetically-diluted mixtures there is no shear thinning at low shear rates and the systems present a constant viscosity, that increases with ϕ_M. It is probably due to the weakness of the magnetic

structures formed at such low magnetic concentration as a consequence of the difficulty for magnetic interactions to occur among the non-magnetic network of particles, despite the applied H_0 . However, at $\phi_N = 0.36$ shear thickening occurs in experiments at large shear rates, so that we broadened the range of dimensionless shear rates two orders of magnitude in next rheograms, i.e., $\dot{\gamma}^* = 3 \cdot 10^{-3} - 10^4$. In spite of the enlargement in shear rates, in the right rheogram of Figure 5.24 the mixtures with a fixed value of ϕ_M again show Newtonian rheology. The fact of not having found ST in these simulations despite the high concentrations used in the non-magnetisable phase suggests that magnetic particles somehow interfere in the contact between non-magnetic clusters and so the possible ST occurring at the end of the studied interval of shear rates is delayed. In this case, there is no significant difference among curves with distinct ϕ_N.

- **Unimodal case**

In the last part of this subsection we explore the case of a null value of ϕ_N, so that our system is only composed by a collection of polydisperse magnetic particles. The computational cost of these simulations is higher, as the magnetic force has to be calculated for all the particles, instead of part of the mixtures. On the contrary to the bimodal case, in this occasion we explore high magnetic volume fractions at low magnetic field, in order to, at least, qualitatively connect these results with those obtained in Subsection 4.3.2, in which the rheological behaviour of dense carbonyl iron suspensions was studied. Under these circumstances and the adequate carrier fluid, the suspensions showed shear thickening, as the low magnetostatic interactions did not impede its appearance.

Start-up tests corresponding to the second step of the simulation code are shown in Figure 5.25, namely for $H_0 = 40$ kA/m. This field strength was generated when a magnetic flux density of 5 mT was imposed in the external coil used in the measurements of dense carbonyl iron in Subsection 4.3.2. The figure for the case of $H_0 = 80$ kA/m (generated by a magnetic flux density of 10 mT in the experimental coil) is analogous. On the one hand, data in this figure have larger errors compared to data in Figure 5.23, mainly for large values of shear rates*, as well as fluctuations. The choice of the peak is thus less reliable than in Figure 5.23 where it was clearly defined.

Rheograms obtained from particle-level simulations of concentrated polidisperse magnetic systems in the presence of low magnetic fields are

shown in Figure 5.26. The most remarkable aspect in these rheograms is that three regimes are found: from the plateau at low shear rates* a yield stress can be envisaged; then a Newtonian regime (slope 1 in the rheogram); it ends in a critical shear rate* after which a sudden increase in stress is observed, belonging to the hoped-for shear-thickening regime. These three regimes are also exhibited in experiments of dense suspensions, e.g., in Figure 4.1. These results are satisfactory as it is the first time that this striking behaviour is found in our simulations, what validates the code and the interactions implemented on it concerning unimodal magnetic suspensions, at least.

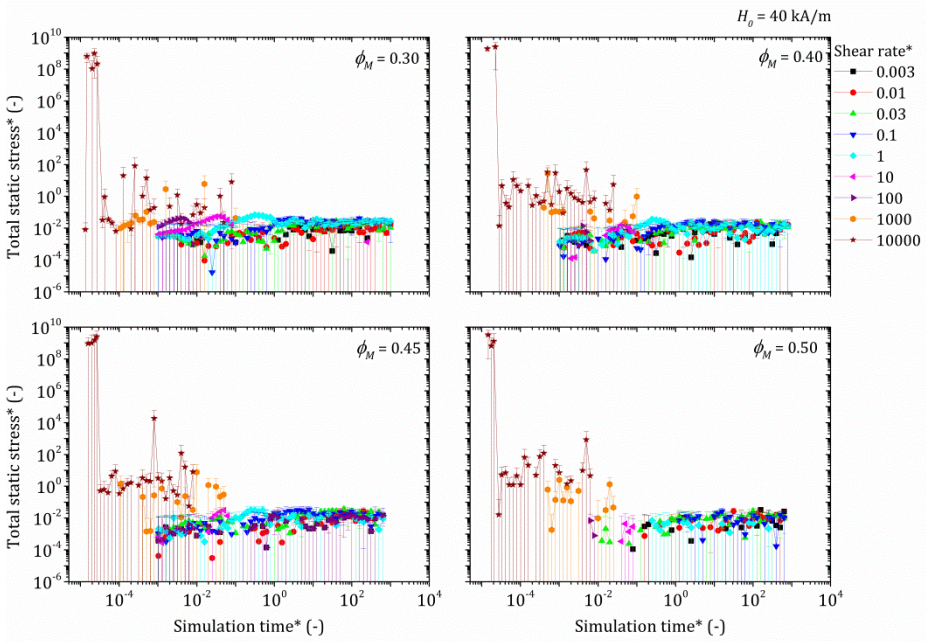

Figure 5.25: Evolution of the total static stress of four concentrated and polydisperse magnetic systems, subjected to several constant shear rates* and a low external magnetic field $H_0 = 40$ kA/m.

The effect of the total volume fraction on the stress is not as clear as in experiments, but the shear stress* related to the most concentrated systems is higher at the upper limit of shear rates*, in accordance with the effect of concentration in shear-thickening suspensions. Moreover, if both rheograms are compared, the main difference reside at $\dot{\gamma}^* = 10^3$. At $H_0 = 80$ kA/m, the onset shear stress* and the point with maximum viscosity take place at lower shear rates*. This is in qualitative agreement again with the effect of increasing the total concentration. Nevertheless, if both curves with $\phi_N = \phi_T = 0.50$

(blue triangles) are considered, this remarkable point has no sense at 80 kA/m, because for a given concentration the increase in magnetic field should delay the appearance of shear thickening and not the opposite effect, as it is shown in the experimental results.

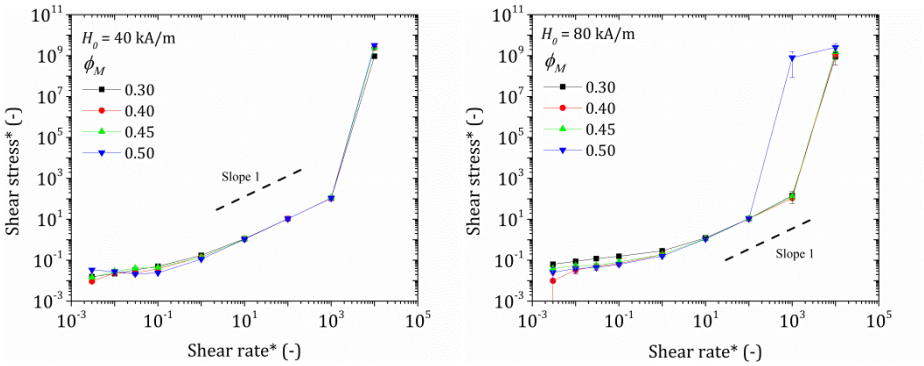

Figure 5.26: Rheograms for unimodal magnetic systems at several particle loadings, simulated at two low magnetic fields, $H_0 = 40$ kA/m (left side) and $H_0 = 80$ kA/m (right side).

This discrepancy in relation to the effects of the applied magnetic field, together with the small dependence on ϕ_T, indicate that the results have to be considered with caution in quantitative terms. However, it seems adequate to have broadened the interval of shear rates* to which the systems are subjected in the second stage of the simulation, as in the end it has been possible that shear-thickening behaviour appears. It is encouraging for searching for it also in mixtures of particles.

5.5. Conclusions

In this work we investigated the rheological behaviour of concentrated MRST suspensions. The hybrid character of these suspensions, namely, shear-thickening and magnetic responses, is provided by starch and carbonyl iron, respectively. In this sense, we prepared suspensions of mixtures of these particles and others carbonyl iron-starch core-shell particles as particulate phase. Moreover, Brownian dynamic simulations were performed to investigate the effect of the addition of non-magnetic particles to MR suspensions. In the first step, structuration of the spherical particles takes place in absence of flow and presence and magnetic field. Then, a constant shear rate is imposed, i.e., start-up test, and static yield stresses are extracted from rheograms.

The inclusion of attractive interparticle interactions, through the addition of magnetic particles, in a shear-thickening system progressively delays this phenomenon and reduces the relative increase of viscosity. In absence of magnetic field carbonyl iron particles enhance the viscosity in the entire range of shear stresses as the total concentration increases. In on-state conditions magnetostatic interactions prevails at low shear rates, so that the suspensions show shear-thinning, that may be preceded by an apparent yield stress under certain conditions. This behaviour can exist in the whole viscosity curve if the magnetic particle concentration or field intensity are high enough to completely weaken or inhibit the shear-thickening behaviour found in absence of magnetic field. In this sense, a drastic reduction in the slope of shear thickening is found for increasing magnetic fields when the magnetic volume fraction is above a critical value of 0.001. Furthermore, there is a significant effect of magnetic field in the minimum value of N_1, which is coincident to the yield stress, however this field dependence is not clear in relation to the crossover stress.

Regarding core-shell particles, several methods of coating were employed, and some of them provided a homogeneous layer of starch onto carbonyl iron particles. At moderate concentration, $\phi_T = 0.36$, coated particles increase the viscosity compared to non-coated ones, probably due to certain roughness from starch coating, that also contribute to hydrogen bonds within shear-induced particle networks. Under field conditions, the effect of the thin layer of starch is mainly appreciated at low shear rates, as the suspension gradually changes its viscosity, instead of showing a clear yield stress, which is the case of the analogue suspension with raw magnetic particles.

The simulation code adequately corroborates the formation of field-induced columnar aggregates that break during shear. As expected, a higher total and magnetic volume fraction produces thicker structures that result in a less favourable energy state if compared with the ideal diluted suspensions where single-width chains are formed. Regarding the second stage, a wide range of dimensionless shear rates was used in the growth tests to construct the rheograms. The initial plateau at low shear rates supports experimental results of magnetorheological suspensions, and the yield stress grows with both magnetic and total concentration. In agreement with other authors, an enhancement in yield stress is found when magnetic particles are partially substituted by non-magnetic ones in this type of fluids, for $\phi_T = 0.20$ and 0.30. However, there is no evidence of shear thickening when considering

these total concentrations in monodisperse mixtures (the maximum achievable is $\phi_T = 0.30$), whatever the ratio of magnetic and non-magnetic volume fractions used, in agreement with experimental results up to this value.

The incorporation of certain polydispersity and different mean diameters for each population of particles enhances the total volume fraction in the simulation box and so it allows a more realistic approach to the rheological behaviour of these dense systems. As a consequence, shear-thickening behaviour finally appeared in the simulations of dense systems formulated only with magnetisable particles. However, this viscosity enhancement has not been observed yet in our bimodal systems with similar values of volume fractions and external field compared to the experiments, probably conditioned by an insufficient limit in the upper shear rate evaluated in the second stage of the simulation code through the growth tests.

In summary, the rheological behaviour of concentrated MRST suspensions can be easily tuned by modifying the elements of the suspension. On the one hand, by minimizing particle-fluid chemical and physical interactions, the colloidal suspension stabilizes and shear thickening may be observed under adequate circumstances. On the other hand, the connection between friction at higher concentrations and particle surface features is clear. In this sense, particles can be tailored in type, size, shape, deformability and roughness to control the appearance of shear thickening and its strength.

5.6. References

[1] Stickel J J and Powell R L 2005 Fluid mechanics and rheology of dense suspensions *Annu. Rev. Fluid Mech.* **37** 129–149

[2] Mewis J and Wagner N J 2009 Current trends in suspension rheology *J. Non-Newton. Fluid Mech.* **157** 147–50

[3] Denn M M and Morris J F 2014 Rheology of non-Brownian suspensions *Annu. Rev. Chem. Biomol. Eng.* **5** 203–228

[4] Tanner R I 2018 Review Article: Aspects of non-colloidal suspension rheology *Phys. Fluids* **30** 101301

[5] Gallier S, Lemaire E, Peters F and Lobry L 2014 Rheology of sheared suspensions of rough frictional particles *J. Fluid Mech.* **757** 514–549

[6] Rastogi S R, Wagner N J and Lustig S R 1996 Microstructure and rheology of polydisperse, charged suspensions *J. Chem. Phys.* **104** 9249–9258

[7] van der Vaart K, Rahmani Y, Zargar R, Hu Z, Bonn D and Schall P 2013 Rheology of concentrated soft and hard-sphere suspensions *J. Rheol.* **57** 1195–209

[8] Galindo-Rosales F 2016 Complex fluids in energy dissipating systems *Appl. Sci.* **6** 206

[9] Wagner N J and Brady J F 2009 Shear thickening in colloidal dispersions *Phys. Today* **62** 27–32

[10] Denn M M, Morris J F and Bonn D 2018 Shear thickening in concentrated suspensions of smooth spheres in Newtonian suspending fluids *Soft Matter* **14** 170–184

[11] Metzner A B and Whitlock M 1958 Flow behavior of concentrated (dilatant) suspensions *Trans. Soc. Rheol.* **2** 239–54

[12] Hoffman R L 1972 Discontinuous and dilatant viscosity behavior in concentrated suspensions. I. Observation of a flow instability *Trans. Soc. Rheol.* **16** 155–173

[13] Hoffman R L 1974 Discontinuous and dilatant viscosity behavior in concentrated suspensions. II. Theory and experimental tests *J. Colloid Interface Sci.* **46** 491–506

[14] Brady J F and Bossis G 1985 The rheology of concentrated suspensions of spheres in simple shear flow by numerical simulation *J. Fluid Mech.* **155** 105

[15] Maranzano B J and Wagner N J 2001 The effects of particle size on reversible shear thickening of concentrated colloidal dispersions *J. Chem. Phys.* **114** 10514–27

[16] Seto R, Mari R, Morris J F and Denn M M 2013 Discontinuous shear thickening of frictional hard-sphere suspensions *Phys. Rev. Lett.* **111**

[17] Fernandez N, Mani R, Rinaldi D, Kadau D, Mosquet M, Lombois-Burger H, Cayer-Barrioz J, Herrmann H J, Spencer N D and Isa L 2013 Microscopic mechanism for shear thickening of non-Brownian suspensions *Phys. Rev. Lett.* **111**

[18] Mari R, Seto R, Morris J F and Denn M M 2014 Shear thickening, frictionless and frictional rheologies in non-Brownian suspensions *J. Rheol.* **58** 1693–1724

[19] Lin N Y C, Guy B M, Hermes M, Ness C, Sun J, Poon W C K and Cohen I 2015 Hydrodynamic and contact contributions to continuous shear thickening in colloidal suspensions *Phys. Rev. Lett.* **115**

[20] Clavaud C, Bérut A, Metzger B and Forterre Y 2017 Revealing the frictional transition in shear-thickening suspensions *Proc. Natl. Acad. Sci.* **114** 5147–5152

[21] Barnes H A 1989 Shear-thickening ("Dilatancy") in suspensions of nonaggregating solid particles dispersed in Newtonian liquids *J. Rheol.* **33** 329–366

[22] Frith W J, d'Haene P, Buscall R and Mewis J 1996 Shear thickening in model suspensions of sterically stabilized particles *J. Rheol.* **40** 531–548

[23] Egres R G and Wagner N J 2005 The rheology and microstructure of acicular precipitated calcium carbonate colloidal suspensions through the shear thickening transition *J. Rheol.* **49** 719–746

[24] Lootens D, Damme H van, Hémar Y and Hébraud P 2005 Dilatant flow of concentrated suspensions of rough particles *Phys. Rev. Lett.* **95**

[25] Lin N Y C, Ness C, Cates M E, Sun J and Cohen I 2016 Tunable shear thickening in suspensions *Proc. Natl. Acad. Sci.* **113** 10774–10778

[26] Brown E, Forman N A, Orellana C S, Zhang H, Maynor B W, Betts D E, Desimone J M and Jaeger H M 2010 Generality of shear thickening in dense suspensions *Nat. Mater.* **9** 1–5

[27] de Vicente J, Klingenberg D J and Hidalgo-Álvarez R 2011 Magnetorheological fluids: a review *Soft Matter* **7** 3701

[28] James N M, Xue H, Goyal M and Jaeger H M 2019 Controlling shear jamming in dense suspensions *via* the particle aspect ratio *Soft Matter* **15** 3649–54

[29] Brown E, Zhang H, Forman N A, Maynor B W, Betts D E, DeSimone J M and Jaeger H M 2011 Shear thickening and jamming in densely packed suspensions of different particle shapes *Phys. Rev. E* **84**

[30] Hsiao L C and Pradeep S 2019 Experimental synthesis and characterization of rough particles for colloidal and granular rheology *Curr. Opin. Colloid Interface Sci.* **43** 94–112

[31] Guy B M, Hermes M and Poon W C K 2015 Towards a unified description of the rheology of hard-particle suspensions *Phys. Rev. Lett.* **115**

[32] Pednekar S, Chun J and Morris J F 2018 Bidisperse and polydisperse suspension rheology at large solid fraction *J. Rheol.* **62** 513–526

[33] Krishnamurthy L-N, Wagner N J and Mewis J 2005 Shear thickening in polymer stabilized colloidal dispersions *J. Rheol.* **49** 1347–1360

[34] James N M, Han E, de la Cruz R A L, Jureller J and Jaeger H M 2018 Interparticle hydrogen bonding can elicit shear jamming in dense suspensions *Nat. Mater.* **17** 965–70

[35] Chen Y, Zhou Y, Pi H and Zeng G 2019 Controlling the shear thickening behavior of suspensions by changing the surface properties of dispersed microspheres *RSC Adv.* **9** 3469–78

[36] Ghosh A, Chauhan I, Majumdar A and Butola B S 2017 Influence of cellulose nanofibers on the rheological behavior of silica-based shear-thickening fluid *Cellulose* **24** 4163–71

[37] Tan Z, Ge J, Zhang H, Zhai P and Li W 2017 Dynamic response of shear thickening fluid reinforced with SiC nanowires under high strain rates *Appl. Phys. Lett.* **111** 031902

[38] Madraki Y, Hormozi S, Ovarlez G, Guazzelli É and Pouliquen O 2017 Enhancing shear thickening *Phys. Rev. Fluids* **2**

[39] Ulicny J C, Snavely K S, Golden M A and Klingenberg D J 2010 Enhancing magnetorheology with nonmagnetizable particles *Appl. Phys. Lett.* **96** 1–4

[40] Bombard A J F, Gonçalves F R, Morillas J R and Vicente J de 2014 Magnetorheology of dimorphic magnetorheological fluids based on nanofibers *Smart Mater. Struct.* **23** 125013

[41] Boczkowska A and Awietj S 2012 Microstructure and Properties of Magnetorheological Elastomers *Advanced Elastomers - Technology, Properties and Applications* ed A Boczkowska (InTech)

[42] Wilson B T and Klingenberg D J 2016 Effects of nonmagnetizable particles on the structure of magnetorheological fluids *Curr. Smart Mater.* **1** 35–48

[43] Li W H and Zhang X Z 2008 Rheology of magnetorheological shear thickening fluids *Adv. Mater. Res.* **32** 161–4

[44] Zhang X, Li W and Gong X L 2008 Study on magnetorheological shear thickening fluid *Smart Mater. Struct.* **17** 015051

[45] Tian Y, Jiang J, Meng Y and Wen S 2010 A shear thickening phenomenon in magnetic field controlled-dipolar suspensions *Appl. Phys. Lett.* **97** 151904

[46] Lu A-H, Salabas E L and Schüth F 2007 Magnetic nanoparticles: synthesis, protection, functionalization, and application *Angew. Chem. Int. Ed.* **46** 1222–44

[47] Bruncková H, Kabátová M and Dudrová E 2009 The effect of iron phosphate, alumina and silica coatings on the morphology of carbonyl iron particles *Surf. Interface Anal.*

[48] Malecki P, Kolman K, Piglowski J, Kaleta J and Krzak J 2015 Sol-gel method as a way of carbonyl iron powder surface modification for interaction improvement *J. Solid State Chem.* **226** 224–30

[49] Wang S, Tang J, Zhao H, Wan J and Chen K 2014 Synthesis of magnetite–silica core–shell nanoparticles via direct silicon oxidation *J. Colloid Interface Sci.* **432** 43–46

[50] Narita A, Naka K and Chujo Y 2009 Facile control of silica shell layer thickness on hydrophilic iron oxide nanoparticles via reverse micelle method *Colloids Surf. Physicochem. Eng. Asp.* **336** 46–56

[51] Liu Q, Zhang Y and Laskowski J S 2000 The adsorption of polysaccharides onto mineral surfaces: an acid/base interaction *Int. J. Miner. Process.* **60** 229–45

[52] Laskowski J S, Liu Q and O\textquotesingleConnor C T 2007 Current understanding of the mechanism of polysaccharide adsorption at the mineral/aqueous solution interface *Int. J. Miner. Process.* **84** 59–68

[53] Ma X 2008 Role of solvation energy in starch adsorption on oxide surfaces *Colloids Surf. Physicochem. Eng. Asp.* **320** 36–42

[54] Dung T T, Danh T M, Hoa L T M, Chien D M and Duc N H 2009 Structural and magnetic properties of starch-coated magnetite nanoparticles *J. Exp. Nanosci.* **4** 259–267

[55] Subramanian S and Natarajan K A 1989 Adsorption behaviour of an oxidised starch onto haematite in the presence of calcium *Miner. Eng.* **2** 55–64

[56] Jiang J-S, Gan Z-F, Yang Y, Du B, Qian M and Zhang P 2008 A novel magnetic fluid based on starch-coated magnetite nanoparticles functionalized with homing peptide *J. Nanoparticle Res.* **11** 1321–1330

[57] Lawless B D and Williams J 1993 Carbonyl iron particles in magnetic cell sorting *Sep. Sci. Technol.* **28** 1939–45

[58] Sim H H, Kwon S H and Choi H J 2012 Xanthan gum-coated soft magnetic carbonyl iron composite particles and their magnetorheology *Colloid Polym. Sci.* **291** 963–969

[59] Vereda F, Segovia-Gutiérrez J P, Vicente J de and Hidalgo-Álvarez R 2014 Particle roughness in magnetorheology: effect on the strength of the field-induced structures *J. Phys. Appl. Phys.* **48** 015309

[60] Fernández-Toledano J C, Ruiz-López J A, Hidalgo-Álvarez R and de Vicente J 2015 Simulations of polydisperse magnetorheological fluids: A structural and kinetic investigation *J. Rheol.* **59** 475–98

[61] López-López M T, Kuzhir P, Durán J D G and Bossis G 2010 Normal stresses in a shear flow of magnetorheological suspensions: Viscoelastic versus Maxwell stresses *J. Rheol.* **54** 1119–36

[62] de Vicente J, González-Caballero F, Bossis G and Volkova O 2002 Normal force study in concentrated carbonyl iron magnetorheological suspensions *J. Rheol.* **46** 1295–303

[63] Hsu C-P, Ramakrishna S N, Zanini M, Spencer N D and Isa L 2018 Roughness-dependent tribology effects on discontinuous shear thickening *Proc. Natl. Acad. Sci.* 1–6

6. Isoviscous elastohydrodynamic lubrication of inelastic non-Newtonian fluids

K. Shahrivar, E.M. Ortigosa-Moya, R. Hidalgo-Álvarez, J. de Vicente

The content of this chapter is published in: *Tribology International,* **2019**, *140*, 105707.

https://doi.org/10.1016/j.triboint.2019.03.065

Abstract

We simulate the thin-film and frictional properties of shear-thinning and shear-thickening fluids in the isoviscous elastohydrodynamic (I-EHL) regime in point contacts. A double-Newtonian Carreau-Yasuda viscosity model is employed to incorporate the shear rate dependence of the viscosity. Regression formulas for the film thickness and friction coefficient are proposed for both non-Newtonian fluids. A master curve is proposed by using the product between the entrainment speed and the effective viscosity in the contact. Numerical results are satisfactorily compared with experimental data in xantham gum solutions and fumed silica suspensions in the form of Stribeck curves.

6.1. Introduction

The understanding of the tribological properties of inelastic non-Newtonian fluids in compliant isoviscous elastohydrodynamic lubrication (I-EHL) is a hot topic today [1–4]. On the one hand, inelastic non-Newtonian fluids are purely dissipative fluids with a shear rate dependent viscosity. On the other hand, the I-EHL occurs when either the tribopair has a small-reduced elastic modulus or the lubricant has a very low pressure-viscosity index [5]. In the I-EHL regime the pressure is high enough to cause elastic deformation but not sufficient to produce a substantial change in viscosity.

Many biotribological contacts operate in the I-EHL. Some examples concern the microcirculation of red blood cells in capillaries, blinking of eyes, contact lenses, respiratory motion between pleural surfaces, synovial joints and food products in mouth [4,6]. On the one hand, biological lubricants exhibit non-Newtonian characteristics. Blood is an example that shows a strong shear-thinning behaviour at the physiological concentration of 50 % red blood cells. On the other hand, biological bearing surfaces often involve complex structures and large deformations. These characteristics in compliant biological tissues are responsible for the major contribution of fluid film action to the lubrication at both tissue and cellular levels [7].

Reynolds presented the differential equation that governs the pressure distribution in the full-film lubrication regime in his classical paper in 1886 [8]. Reynolds neglected inertia and gravitational effects in relation to viscous action, and the analysis was restricted to an isoviscous and incompressible fluid. Since then, many researchers tried to explain the full-film lubrication in gears and mechanical components based on Reynolds theory, however, with little success. In 1949, Grubin [9] incorporated the pressure-viscosity coefficient of the lubricant and the elastic deformation of the surfaces in the analysis. This work resulted in the emergence of the EHL theory. Using numerical calculations, Dowson and Higginson [10,11] developed a regression formula for the prediction of the film thickness in line contacts. The most widely used film thickness formula that is currently employed in EHL was introduced by Hamrock and Dowson [12,13] for oil lubrication in circular contacts. Later researchers further improved the method and extended the operating conditions range, in particular, to achieve higher loads [14]. In 1987, Lubrecht [15] introduced multilevel techniques. With this methodology it was possible to numerically solve the partial differential equations at a lower computational

cost with very dense meshes. Nijenbanning *et al.* [16] developed new film thickness equations using this technique. More recently, Venner and Lubrecht wrote a comprehensive book on this topic [17].

With regards to the friction characteristics, major efforts in developing EHL theory were devoted in the past to study the full-film lubrication behaviour of Newtonian fluids despite the fact that there are many applications where the lubricant is non-Newtonian. Hooke [18] and Ehret *et al.* [19] proposed approximate methods to describe the flow of non-Newtonian lubricants. Later, Greenwood [20,21] compared those two methods with non-Newtonian fluid models where an exact solution existed. Following Greenwood's approach [20] for coupling Carreau model to Reynolds equation, Liu *et al.* [22] simulated the two-dimensional generalized Reynolds equation. The dependence of the lubricant's viscosity with pressure and shear was obtained from experimental data. Their results showed a good agreement for the friction coefficient and the film thickness. Jang *et al.* [23] investigated the use of sinh-law and Carreau model for treating shear-thinning fluids. They found the sinh-law model failed to capture the behaviour of EHL line contacts while the Carreau model showed a good agreement with the experiments. Bair and Qureshi [24] also reported similar conclusions on the suitability of the Carreau viscosity model for the prediction of the friction coefficient and the film thickness. The modified Reynolds-Carreau equation was also used to develop thermal-EHL prediction formulas for fluid film formation [25,26].

With regards to the film thickness, Jang *et al.* [23] and Bair [27] performed numerical calculations on shear-thinning lubricants in line contacts and proposed a film thickness correction factor that included the slide-to-roll ratio. Kumar and Khonsari [28] introduced correction factors to account for the shear-thinning behaviour on the central and the minimum film thickness in pure rolling, circular contacts. Katyal and Kumar [29] developed a central film thickness formula under pure rolling. They used a Doolittle's free volume based pressure-viscosity model and a Carreau-type constitutive equation for treating the shear-thinning effect. Later, similar prediction formulas were proposed under sliding/rolling conditions [30]. Habchi *et al.* [31] fitted numerical results for different ultra-low viscosity fluids and presented a central film thickness formula for I-EHL contacts. It is worth mentioning that most of the experimental and numerical investigations addressed cases with zero value of the second Newtonian viscosity plateau [23–32]. More recently, some researchers [33–35] have studied the importance of the second-Newtonian

viscosity plateau in the Carreau-Yasuda model. Interestingly, Katyal and Kumar [34] concluded that with a non-zero second Newtonian viscosity plateau, the film thickness approaches to the Newtonian values. The effect of shear-thinning parameters, i.e., power-law index and Newtonian limit on the EHL film thickness became less noticeable with increasing the second Newtonian viscosity plateau level.

In most of the previous works the emphasis was given to the calculation of the film thickness in non-Newtonian fluids, mostly shear-thinning fluids, at very high pressures by incorporating a pressure-viscosity model. Significantly, less attention was paid to predict the friction coefficient. An example is that of de Vicente et. al. [36] who employed numerical simulations in the I-EHL regime to derive predictive formulas for Couette and Poiseuille friction in a point contact. In this chapter we simulate the frictional properties of both shear-thinning and shear-thickening fluids in the I-EHL regime. We employ a double-Newtonian Carreau-Yasuda viscosity model to incorporate the shear rate dependence of the viscosity. Finally, the numerical results are compared with experiments.

6.2. Experimental and simulations

Inelastic non-Newtonian fluids were prepared by dissolving biopolymers and dispersing nanoparticles in a Newtonian carrier liquid. The Newtonian liquid employed in this work was a glycerol/water mixture with a shear viscosity of 119 mPa · s (87 wt%, purchased from Sigma-Aldrich).

As a model shear-thinning fluid, we employed biopolymer solutions based on xanthan gum (XG, Sigma-Aldrich). These biopolymer solutions exhibit a very strong shear-thinning character that can be easily tuned through the polymer concentration. They were prepared by slow addition of XG to the carrier fluid at 25 °C under continuous stirring to facilitate the dissolution of the polymer [37]. On the other hand, as a model shear-thickening fluid we used fumed silica (FS, Sigma-Aldrich) dispersions. These suspensions are well known to exhibit a strong shear thickening response [38]. They were carefully prepared, removing the air bubbles, with alternating steps that involve mixing with a spatula and using ultrasounds to completely disintegrate FS agglomerates.

Rheological tests were carried out using a cone-plate geometry (radius 25 mm, angle 1°) in a torsional MCR501 rheometer from Anton Paar. Rheological

tests were performed by applying a shear torque which logarithmically increased from 10^{-4} to 10^{2} mN · m. Tribological tests were carried out under pure sliding conditions in a ball-on-three-plates geometry with polydimethyl siloxane PDMS-PDMS tribopairs (Young modulus of 1.84 MPa and Poisson ratio of approximately 0.5) [39,40]. PDMS tribopairs were prepared in situ using conventional techniques from a two-component silicone elastomer kit (SylgardTM 184, Dow Corning). A schematic representation of the experimental set-up is shown in Figure 6.1. The ball radius was $R = 6.35$ mm and the plates were parallelepipeds with dimensions 3 mm × 6 mm × 16 mm. The tribological experiments consisted of two intervals. In the first interval, the normal force was adjusted to 1 N. In the second interval, the ball was rotated and the rotational speed was logarithmically increased from 0.1 to 2000 rpm still at a normal force of 1 N. The friction coefficient was monitored during the second interval. Both rheological and tribological tests were carried out at 25 °C on fresh new samples in order to avoid water evaporation and undesirable changes in the particle volume fractions. In particular, the tribopairs were newly assembled for each test. Experimental data shown here are the result of sample averaging over at least three repetitions.

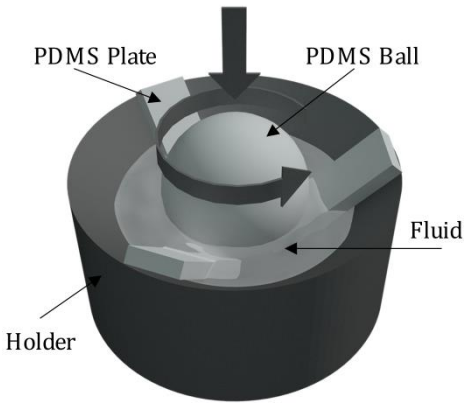

Figure 6.1: Schematic representation of the experimental set-up employed to measure friction. The rheometer exerts a torque (T) and a normal force (T) to the ball. To maintain a commanded sliding speed, the rheometer applies the necessary torque to the ball. The normal load is fixed constant during the experiment in order to keep the ball and three plates in contact. The normal load supported at the contact point by each plate is: $w = \sqrt{2}F/3$.

In this work we followed two methods to calculate the friction coefficient using numerical simulations: i) a “simplified” solution approach and ii) a “full” solution approach. In the simplified solution approach the lubricant was con-

sidered to be a Newtonian fluid, at a local scale, and regression formulas were used to predict the friction coefficient. In the contact, an effective shear viscosity was estimated using an iterative procedure from the lubricant's rheogram under steady shear. In the full solution approach, by means of the finite-difference method, we solved the generalized Reynolds equation coupled with the load balance equation and the surface elastic deformation equation. From the full solution, regression equations are proposed for the prediction of the film thickness and friction coefficients for both shear-thinning and shear-thickening fluids. A detailed description of both approaches is included in Subsection 3.3.4.

The range of parameters investigated in this work is given in Table 6.1.

Simulation parameters	**Shear thinning**	**Shear thickening**
η_0 (Pa · s)	0.5-1.0	0.05-0.40
η_∞ (Pa · s)	0.05-0.40	0.5-1.0
n $(-)$	0.5-1.0	
$\dot{\gamma}_c$ (s^{-1})	10.0-50.0	
Slide-to-roll ratio, SRR $(-)$	0-2.0	
Normal load, w (N)	0.47-4.77	
Maximum Hertzian pressure, p_H (MPa)	0.150-0.324	

Table 6.1: Simulation parameters used in this work.

Table 6.2 shows the mesh dependency of the numerical procedure employed. In view of Table 6.2, finer meshes than 201×201 caused negligible changes in the film thickness and friction coefficient (less than 1 %).

$n_x \times n_y$	h_{min}/R_x	h_{cen}/R_x	$\mu_C(R_x/a_H)^2$	$\mu_P(R_x/a_H)^2$
65×65	3.351879×10^{-2}	4.499650×10^{-2}	1.615028	2.704045×10^{-1}
129×129	3.363395×10^{-2}	4.844874×10^{-2}	1.586407	2.817525×10^{-1}
201×201	3.386840×10^{-2}	4.903752×10^{-2}	1.576763	2.827550×10^{-1}
301×301	3.394526×10^{-2}	4.921764×10^{-2}	1.576360	2.838316×10^{-1}
401×401	3.401441×10^{-2}	4.932213×10^{-2}	1.571989	2.838246×10^{-1}

Table 6.2: Convergence of film thickness (h_{min} and h_{cen}) and friction coefficient terms (μ_C and μ_P) as a function of the mesh size. $n = 0.7$, $\eta_0 = 1.0$ Pa · s, $\eta_\infty = 0.05$ Pa · s, $\dot{\gamma}_c = 10\ \mathrm{s}^{-1}$, $w = 0.47$ N, $U = 0.0125\ \mathrm{m \cdot s}^{-1}$ and $SRR = 2.0$.

6.3. Results and discussion

6.3.1. Simplified solution approach

Figure 6.2 shows the viscosity and Stribeck curves for the model Newtonian fluid (the glycerol/water mixture), a shear-thinning fluid (a XG solution), and a shear-thickening fluid (a FS suspension). The rheogram corresponding to the XG solution shows a clear shear-thinning behaviour in a wide range of shear rates ($10^{-1} - 10^{3}$ s^{-1}). The viscosity decreases from 13.84 at low shear rates to 0.266 Pa·s at high shear rates. On the other hand, the FS suspension is slightly shear-thinning at low and moderate shear rates ($\dot{\gamma} < 29$ s^{-1}, stage I) and exhibits a shear-thickening behaviour for $\dot{\gamma} > 29$ s^{-1} up to $\dot{\gamma}$~1000 s^{-1} (stage II). Table 6.3 contains the best fitting parameters to the Carreau-Yasuda equation (Equation 3.51).

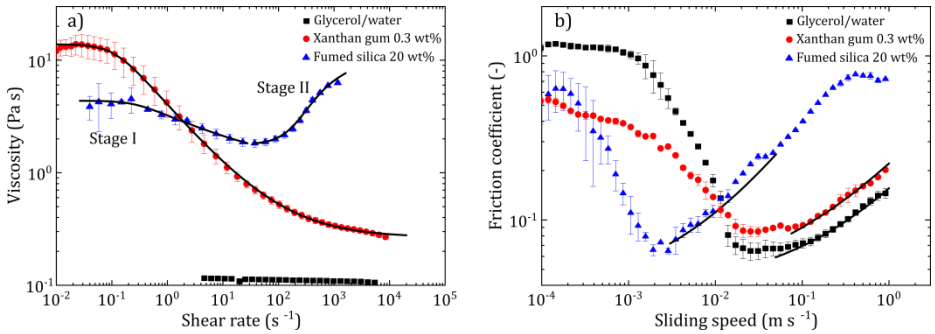

Figure 6.2: Experimental viscosity and Stribeck curves for xanthan gum (XG) and fumed silica (FS) suspensions. a) Shear viscosity as a function of shear rate for the glycerol/water mixture, XG solution and FS suspension. Lines are fitting curves to the Carreau-Yasuda model (see Table 6.2). b) Friction coefficient as a function of sliding speed for PDMS/PDMS tribopairs lubricated by the glycerol/water mixture, XG solution and FS suspension. Solid lines correspond to the simplified solution approach prediction.

As shown in Figure 6.2-b, the friction coefficient data follow a typical Stribeck curve with three differentiated regimes. At low velocities the contact operates in the boundary-lubrication regime. At intermediate velocities the contact enters in the mixed-lubrication regime as the friction coefficient decreases monotonically and reaches a minimum value. Finally, at very high velocities the hydrodynamic regime is obtained. The fact that the full film lubrication regime is achieved earlier for the FS suspension, followed by the XG solution and finally the glycerol/water mixture is expected because the tri-

bopair operates at high shear rates (definitely above 10 s^{-1}, see Figure 6.2-a). This point will be addressed in detail below.

Suspension	n	η_0 (Pa · s)	η_∞ (Pa · s)	$\dot{\gamma}_c$ (s^{-1})
Fumed silica FS 20 wt% (Stage I)	0.701	4.364	0.991	0.262
Fumed silica FS 20 wt% (Stage II)	0.500	1.782	11.920	288.600
Xanthan gum XG 0.2 wt%	0.556	1.899	0.212	0.253
Xanthan gum XG 0.3 wt%	0.420	13.840	0.266	0.111

Table 6.3: Experimental best fitting parameters to the double-Newtonian Carreau-Yasuda model Equation 3.51 (from experimental data in Figure 6.2).

Despite the fact that the microscopic mechanism behind the experimental observation is very different [41,42]; XG polymers are expected to disentangle and align with the flow while FS particles are expected to roll and form hydroclusters or frictional contacts under shear, the tribological behaviour of the two colloidal systems is surprisingly well explained under a continuum approach perspective where microstructural details are not relevant. The validity of a macroscopic description is clearly demonstrated in Figure 6.2-b. Together with the experimental data, in Figure 6.2-b we also show the Newtonian prediction for the glycerol/water mixture -as obtained from the summation of the three contributions to the friction coefficient (Equations from 3.54 to 3.56) and the predictions for the XG solution and FS suspension. As expected, the regression prediction for the glycerol/water mixture collapses very well with the experimental data. A reasonable agreement is also found for the XG solution and the FS suspension using the simple solution approach. However, a close look to the data reveals that the simple solution approach slightly overestimates the friction coefficient for the XG solution and underestimates it for the FS suspension. A full solution approach is needed to ascertain this issue.

6.3.2. Full solution approach

- **Effect of the power-law index**

Figure 6.3-a and Figure 6.3-b show typical Carreau-Yasuda viscosity curves used in the simulations. It is worth noting that for higher values of the viscosity index n, i.e., smaller slope in the viscosity transition region, the viscosity shows a smoother transition from the low-shear to the high-shear viscosity plateau. In addition, for intermediate shear rates, the shear-thinning fluid

with larger n exhibits a larger viscosity level (see Figure 6.3-a); on the contrary, for the shear-thickening fluid a larger n results in lower viscosity values (see Figure 6.3-b). In any case, at exceedingly small or high shear rates the curves collapse on the first or second-Newtonian plateau.

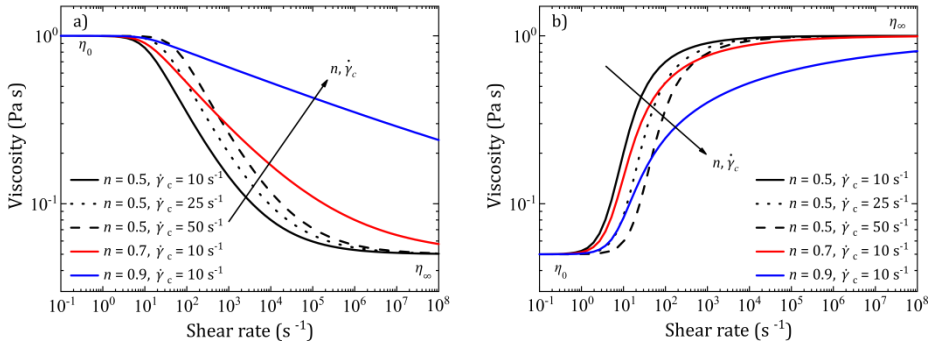

Figure 6.3: Viscosity curves (viscosity as a function of shear rate) for some inelastic non-Newtonian fluids simulated in this work as a function of the viscosity index parameter n and critical shear rate $\dot{\gamma}_c$. a) Shear-thinning fluid, b) shear-thickening fluid.

In Figures from 6.4 to 6.8 we demonstrate the effect of power-law index and critical shear rate on various parameters under pure-sliding condition ($SRR = 2$). The effect of SRR is afterwards discussed and shown in Figure 6.9. Figure 6.4-a and Figure 6.4-b compare the central and minimum film thickness (h_{cen} and h_{min}) for a shear-thinning (Figure 6.4-a) and a shear-thickening (Figure 6.4-b) fluid for three different power-law indexes n. For completeness, the predicted minimum film thickness for a Newtonian fluid is shown with black lines. In view of Figure 6.4-a both h_{cen} and h_{min} follow a power law behaviour with the entrainment speed U. Also, the film thickness increases as the viscosity index increases hence approaching the low shear viscosity plateau. Similarly, the film thickness decreases as the viscosity index decreases hence approaching the high shear viscosity plateau. Katyal and Kumar [30] showed that for shear-thinning fluids $h_{cen} \propto \bar{R}^{-1.3(1-n)^{1.3}} \bar{S}^{-1.2(1-n)^{1.92}}$ being $\bar{R}$ and $\bar{S}$ the rolling and sliding correction factors, respectively. These two parameters captured the effect of entrainment speed, load, sliding-roll-ratio, and critical shear rate on the film thickness. Our results are in qualitative agreement with their work as we observe a substantial decrease in the film thickness when n decreases. Moreover, Figure 5a shows that the slope of the film thickness slightly changes with n. It is well established in the literature that the film thickness dependence with the sliding velocity can be represented by a power-law function

$h_{cen} \propto U^{\beta}$ with $\beta \sim 0.6$ ($\beta = 0.64$ in Ref. [12] and $\beta = 0.60$ in Ref. [36]) for Newtonian fluids in the I-EHL regime. In the current simulations we observe that β slightly decreases from 0.60 ± 0.01 to 0.58 ± 0.01 when the viscosity index decreases from 0.9 to 0.5, respectively.

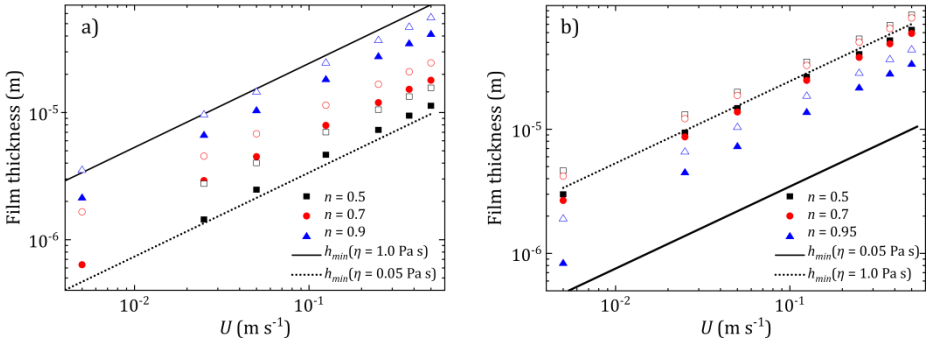

Figure 6.4: Simulated film thickness versus entrainment speed data for a) shear-thinning and b) shear-thickening fluids. Solid and dashed lines correspond to the predictions for a Newtonian fluids with the first and second plateau viscosities, respectively. The normal load is 0.47 N and $\dot{\gamma}_c = 10\ \mathrm{s}^{-1}$. Closed symbols h_{min}. Open symbols h_{cen}.

Figure 6.5-a and Figure 6.5-b show contour plots for the shear rate $\dot{\gamma}$ at the contact zone. The main feature to be noticed is that shear rate reaches its maximum at the side lobes where the film thickness reaches its minimum. In Figure 6.5-c the central shear rate is plotted as a function of the entrainment speed U. It is observed that for the shear-thinning case, as the viscosity index increases the central shear rate decreases at a constant velocity. This was expected, because in Figure 6.4-a it was observed that a larger viscosity index resulted in a larger film thickness and subsequently the shear rate would decrease. This is, also, in agreement with the results reported in Ref. [30] taking into consideration that central shear rate is inversely proportional to the film thickness.

In Figure 6.4-b we demonstrate that a power-law behaviour also occurs for the central and minimum film thickness (h_{cen} and h_{min}) versus entrainment speed U curves in shear-thickening fluids. The film thickness data are essentially constrained between Newtonian references (see lines in Figure 6.4-b). As observed, the slope of $\log h_{cen}$ vs. $\log U$ curves is very close to the Newtonian fluids prediction $\beta \sim 0.6$ [12,36]. In contrast to shear-thinning fluids, for shear-thickening fluids the film thickness increases as the viscosity index decreases hence approaching the high shear viscosity plateau. Similarly, the film thickness decreases as the viscosity index increases hence approach-

ing the low shear viscosity plateau. Film thickness data shown in Figure 6.4-b are in good correspondence with central shear rates reported in Figure 6.5-d.

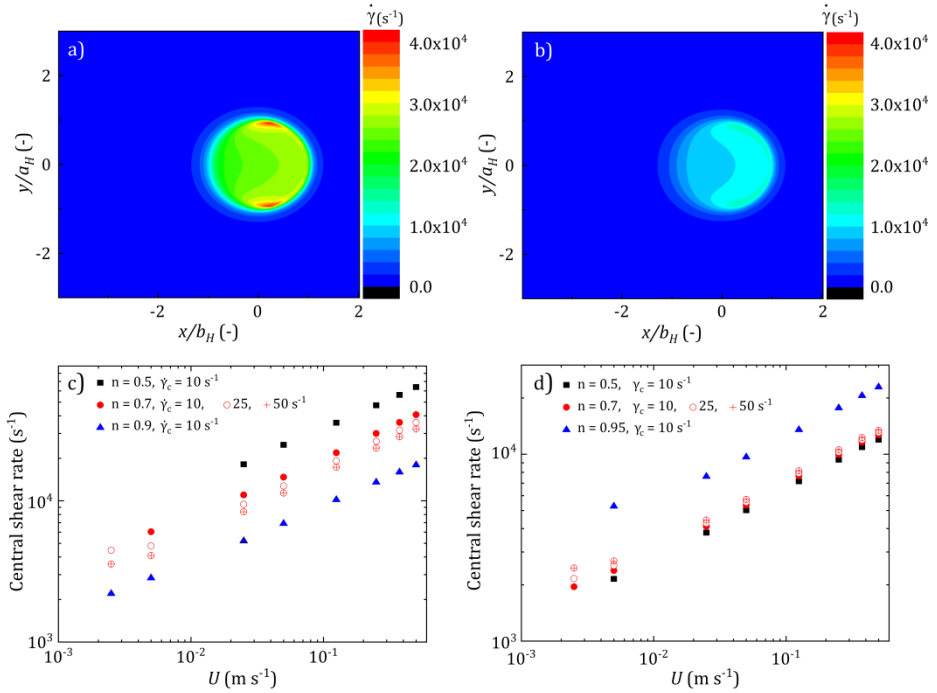

Figure 6.5: a) and b) Simulated shear rate contour plot in the lubricated contacts. c) and d) Central shear rate as a function of the entrainment speed for different viscosity indexes n and critical shear rates $\dot{\gamma}_c$. Left column: shear-thinning fluid. Right column: shear-thickening fluid.

Figure 6.6 shows the partial (Couette and Poiseuille) contributions to the friction coefficient. Generally speaking, the Couette term was found to be one order of magnitude larger than the Poiseuille term. Again the friction coefficient results are bounded between the predictions for Newtonian fluids (see lines in Figure 6.6). Figure 6.6-a and Figure 6.6-c show that for shear-thinning fluids both the Couette and Poiseuille contributions to the friction coefficient increase as the viscosity index increases. This behaviour was expected since a higher index results in higher viscosity (friction $\propto \eta$). In contrast, friction decreases when increasing the viscosity index for shear-thickening fluids. Figure 6.7 compares the total friction coefficient (Couette plus Poiseuille terms) for both model fluids. As expected, the results are very similar to Figure 6.6-a and Figure 6.6-b.

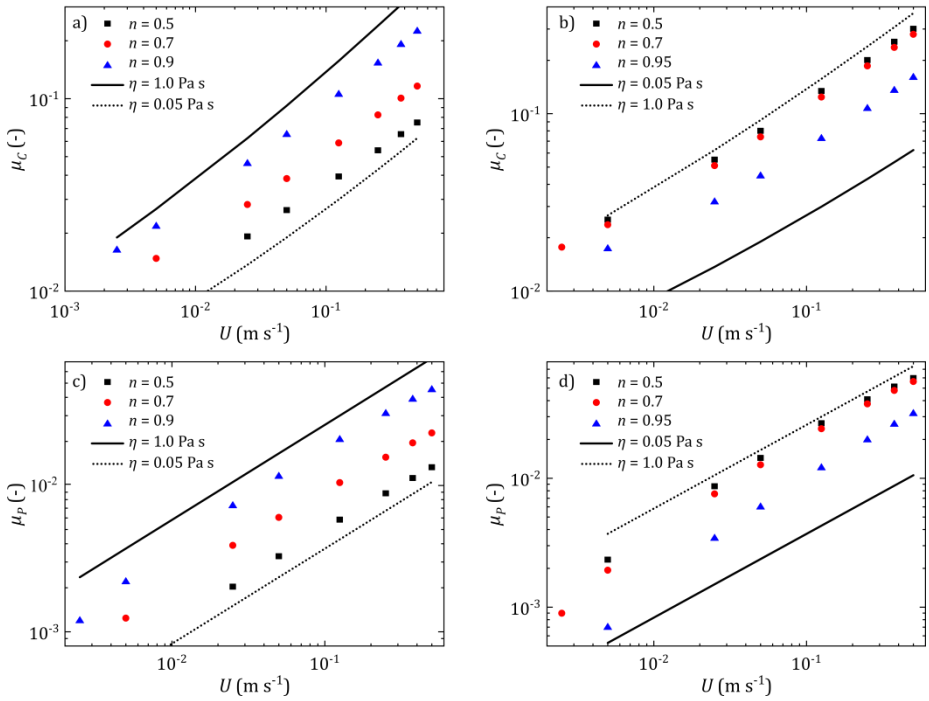

Figure 6.6: Partial contributions to the friction coefficient in shear thinning (left column) and shear thickening (right column) fluids. Top: Couette contribution μ_P. Bottom: Poiseuille contribution μ_C.

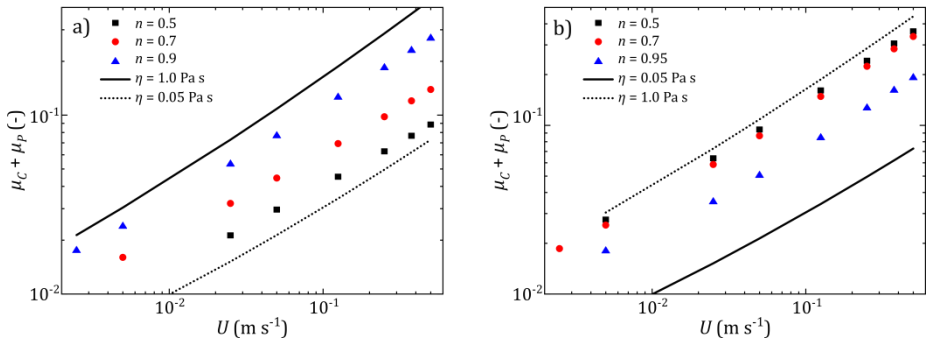

Figure 6.7: Total friction coefficient ($\mu = \mu_C + \mu_P$) as a function of entrainment speed U in a) shear-thinning and b) shear-thickening fluids.

- **Effect of the critical shear rate**

Previous papers in this field are focused on shear-thinning fluids [27,28,32]. They report a direct relationship between the film thickness and the critical shear rate (typically expressed as a critical shear stress). Of particular inter-

est is the paper by Katyal and Kumar [30] that offers regression formulas for predicting the film thickness at a range of critical shear stresses. As previously shown in Figure 6.3, the effect of the critical shear rate $\dot{\gamma}_c$ is to delay the transition, from the low shear viscosity plateau to the power-law region, to higher shear rates (i.e., higher velocities). Therefore, at constant shear rate (i.e., constant velocity), higher values of the critical shear rate result in higher viscosity levels for a shear-thinning fluid and lower viscosity levels for a shear-thickening fluid.

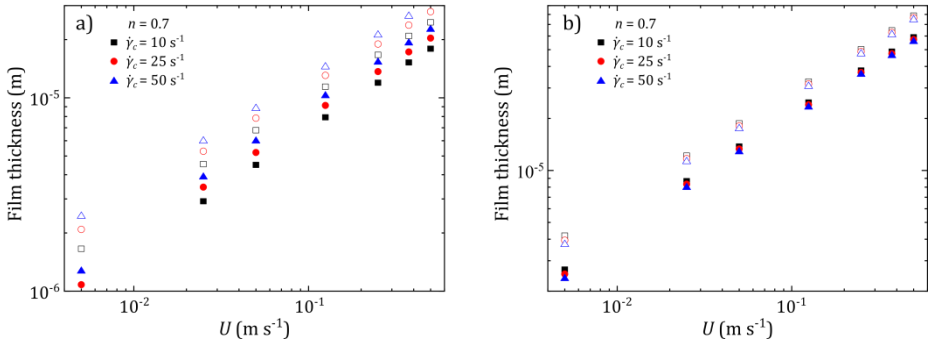

Figure 6.8: Film thickness as a function of entrainment speed U in a) shear-thinning and b) shear-thickening fluids. Closed symbols: h_{min}. Open symbols: h_{cen}.

Figure 6.8 shows the influence of the critical shear rate $\dot{\gamma}_c$ on the film thickness versus entrainment speed curves. Figure 6.8-a shows the results for shear-thinning fluids. As expected, the film thickness increases with the increase in the critical shear rate for a given entrainment speed. This is expected because the viscosity increases with the critical shear rate at a given shear rate (see Figure 6.3). This observation is in agreement with central shear rate curves depicted in Figure 6.5-c. In Figure 6.5-c result showed a decrease in the central shear rate at the higher $\dot{\gamma}_c$ that is compatible with achieving a larger film thickness. These results are in qualitative good agreement with previous works that predict a thicker film at larger critical shear rates [30,32].

Figure 6.8-b shows the influence of the critical shear rate $\dot{\gamma}_c$ in the case of shear-thickening fluids. To the best of our knowledge, there are no previous publications on the effect of the critical shear rate on the film thickness in shear-thickening fluids. In contrast to shear-thinning fluids, our results demonstrate that the film thickness decreases when increasing $\dot{\gamma}_c$ due to the viscosity enhancement (see Figure 6.3-b). This observation is also in good

agreement with the increase in the central shear rate the higher $\dot{\gamma}_c$ reported in Figure 6.5-d.

- **Effect of the slide-to-roll ratio**

Figure 6.9 shows the effect of the slide-to-roll ratio (SRR) on the film thickness and friction coefficient for three different entrainment speeds U (from 0.05 to 0.5 $\mathrm{m} \cdot \mathrm{s}^{-1}$). For shear-thinning fluids, both the film thickness and the Poiseuille contribution to friction slightly decrease as SRR increases up to pure sliding conditions; i.e., $SRR = 2$. It is a well-known fact that sliding along with rolling yield higher shear stresses; hence, a more substantial shear-thinning diminishes the effective viscosity in the contact zone. Due to this effect, a moderate decrease of the film thickness with the increase of SRR is observed. The maximum reduction in the film thickness at pure sliding was around 15%. This film thickness reduction is in agreement with results by Bair [27] and Katyal and Kumar [30]. They proposed a power-law form to describe effect of SRR on film thickness. They reported a gradual film thinning with increasing SRR. The film thinning was reported to be more substantial at higher speeds and lower viscosity indexes. In contrast, in the case of shear-thickening fluids the film thickness and Poiseuille friction term increased with increase in SRR. The film thickness showed a 5% increase as the SRR increased to 2. As the SRR increased, inducing higher shear stresses, the viscosity increased and resulted in a subtle film thickening. This increase in film thickness was found to be a feature of non-Newtonian lubricants exhibiting a viscosity increase when sheared. It is worth noting that for Newtonian fluids, contrary to non-Newtonian fluids studied in this work, both the film thickness and Poiseuille friction term are independent of the SRR [36].

Independently on whether the fluid is shear-thinning or shear-thickening, the Couette contribution to the friction coefficient shows a power-law relationship with the SRR ($\mu_C \propto SRR^{\alpha}$). In view of Figure 6.9, the power law exponent for shear-thinning fluids is 0.87 ± 0.01 while for shear thickening fluids the exponent is 1.05 ± 0.01. Our finding is in contrast to the isothermal isoviscous Newtonian fluids that predict the Poiseuille term and film thickness to be independent of SRR and the Couette friction term to be proportional to SRR [32]. Interestingly, for non-Newtonian fluids the friction coefficient contributions (Couette and Poiseuille) and film thickness are nonlinear functions of SRR (see next section).

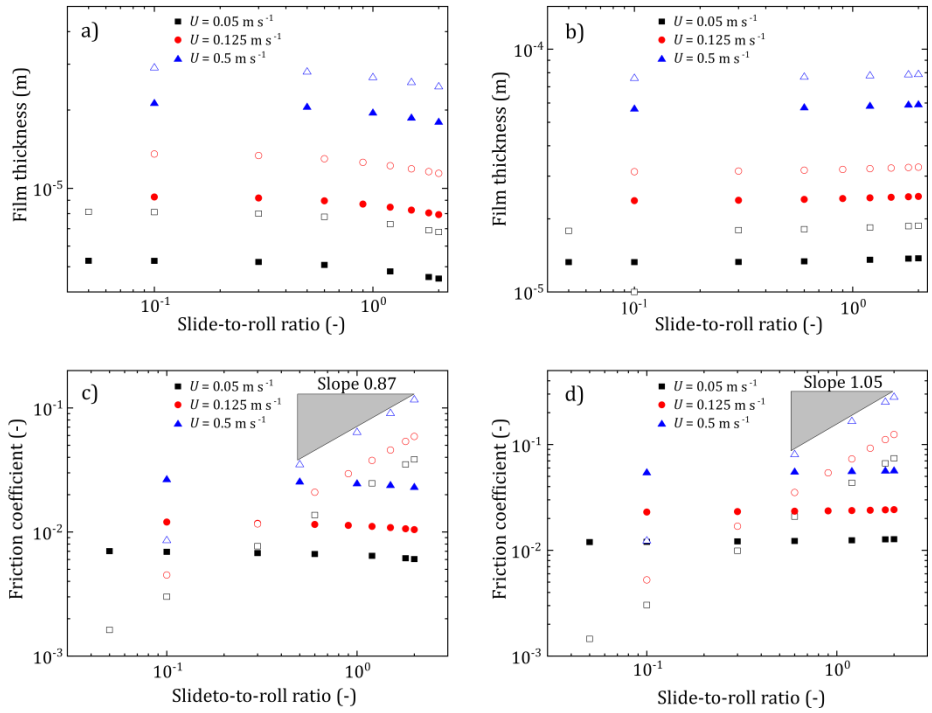

Figure 6.9: Film thickness and friction coefficient as a function of slide-to-roll ratio (SRR) for $n = 0.7$ and $\dot{\gamma}_c = 10\ \mathrm{s}^{-1}$. a) and b) closed symbols: h_{min}; open symbols: h_{cen}. c) and d) closed symbols: μ_P; open symbols: μ_C. Left column: shear-thinning. Right column: shear-thickening.

To sum up, the viscosity index n, the critical shear rate $\dot{\gamma}_c$, and the SRR have opposite effects on shear-thinning and thickening fluids. For shear-thinning fluids, a higher viscosity index results in a larger film thickness, a lower central shear rate and a larger friction coefficient. The effect of increasing the critical shear rate is analogous to increasing the viscosity index. Finally, a larger slide-to-roll ratio generates higher shear stresses therefore resulting in a smaller film thickness.

- **Effective viscosity prediction**

An effective viscosity η_{eff} in the Hertzian contact zone was calculated to represent the rheological properties of the lubricant. For this aim, we employed Buckingham's pi theorem as a powerful dimensional analysis technique for developing the scaling law relating the physical parameters (rheological model and operating conditions) and the effective viscosity in the contact region. The functional relationship is as follows:

$$f\left(\eta_{eff}, U, E', R_x, \eta_0, \eta_\infty, w, \dot{\gamma}_c, SRR, n\right) = 0. \quad (6.1)$$

The dimensional matrix created by listing the powers of ten parameters involved in the problem, physical quantities and variables, has a rank of three. Therefore, seven independent dimensionless groups could be constructed. We chose $U, \dot{\gamma}_c, R_x$ as the repeating parameters to obtain the dimensionless parameters. By further combining the established groups we found the following groups to be the best parameters for developing the scaling law: $\overline{U} = U\eta_{eff}/E'R_x$, $\overline{U}_0 = U\eta_0/E'R_x$, $\bar{\eta}_R = \eta_\infty/\eta_0$, $\bar{\dot{\gamma}}_c = \dot{\gamma}_c R_x/U$, $\overline{W} = w/E'R_x^2$, SRR, and $m \equiv 1 - n$. The parameter m represents the severity of shear-thinning/thickening effect. Figure 6.10 shows the dependence of the effective viscosity for a shear-thinning fluid η_{eff} as a function of four dimensionless groups $\overline{U}_0$, $\bar{\eta}_R$, $\bar{\dot{\gamma}}_c$ and $\overline{W}$. As observed, the dimensionless parameters exhibit a power-law behaviour. The slope of the scaling parameters $\overline{U}_0$, $\bar{\eta}_R$ and $\bar{\dot{\gamma}}_c$ was higher with increasing m. In contrast, for $\overline{W}$ the exponent was negative and decreased as m increased. The choice of the appropriate form for the viscosity (Equation 6.1) comes from Equation 3.51 and Figure 6.10 that suggests that the scaling parameters exhibit a power law. Therefore, the following form was proposed:

$$\frac{\eta_{eff} - \eta_\infty}{\eta_0 - \eta_\infty} = \bar{S}\overline{U}_0^b \bar{\eta}_R^c \bar{\dot{\gamma}}_c^d \overline{W}^e \quad (6.2)$$

The slope of each graph in Figure 6.10 is the exponent of the corresponding parameter (b, c, d and e) in Equation 6.2. These exponents were found to be simply a function of m and could be accurately expressed as αm^β. In the case of a Newtonian fluid ($m = 0$) $\eta_{eff} = \eta_0$, which requires exponents b, c, d, and e to be zero [c.f. Figure 6.10]. Also, $\lim_{n\to 1} \bar{S} = 1$. Additionally, in the case of pure rolling (SRR = 0) $\bar{S}$ should have a finite value. We found that $\bar{S} = e^{\alpha m^\beta}$ with $\alpha \propto SRR$ and $\beta = const.$ could capture the tendency of the data.

The regression analysis was carried out in three stages so that the accuracy of the fitting is preserved: (I) b, c, and d were determined for different power-law indexes at a constant normal load and pure sliding conditions. (II) Keeping exponents b, c, and d from the previous stage, by varying the load parameter $\overline{W}$, we obtained the exponent e for different power-law exponents. (III) Finally, SRR was changed in the interval [0-2] and hence, α and β were obtained. The regression parameters obtained from the fitting are given in Table 6.4.

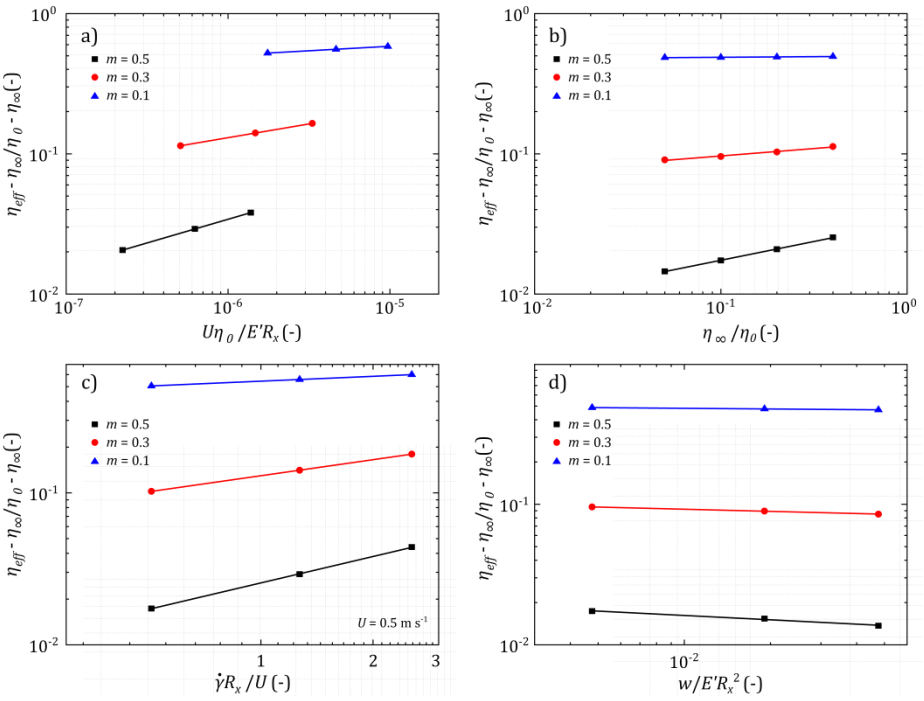

Figure 6.10: Effective viscosity prediction as a function of the dimensionless groups: $\bar{U}_0 = U\eta_0/E'R_x$, $\bar{\eta}_R = \eta_\infty/\eta_0$, $\bar{\dot{\gamma}}_c = \dot{\gamma}_c R_x/U$ and $\bar{W} = w/E'R_x^2$,. The slope of each curve in this plot is the exponent of the corresponding dimensionless group in (6.2).

$(\eta_{eff} - \eta_\infty)/(\eta_0 - \eta_\infty) = \bar{S}\bar{U}_0^b \bar{\eta}_R^c \bar{\dot{\gamma}}_c^d \bar{W}^e$										
$\bar{S} = e^{(a_1 + a_2 SRR)m^{a_3}}$			$b = b_1 m^{b_2}$		$c = c_1 m^{c_2}$		$d = d_1 m^{d_2}$		$e = e_1 m^{e_2}$	
a_1	a_2	a_3	b_1	b_2	c_1	c_2	d_1	d_2	e_1	e_2
Shear thinning										
4.244	-0.940	1.325	0.782	1.052	1.423	2.393	1.143	1.023	-0.217	1.056
Shear thickening										
1.608	-0.650	1.010	0.640	1.024	0.685	1.138	1.000	1.037	-0.190	0.984

Table 6.4: Effective viscosity parameters obtained from full numerical calculations.

- **Master curve**

It is well-known that in the case of Newtonian fluids it is possible to collapse all the -film thickness and friction coefficient- curves on a master curve using the product between the entrainment speed and the Newtonian fluid viscosity, $U\eta$ [36].

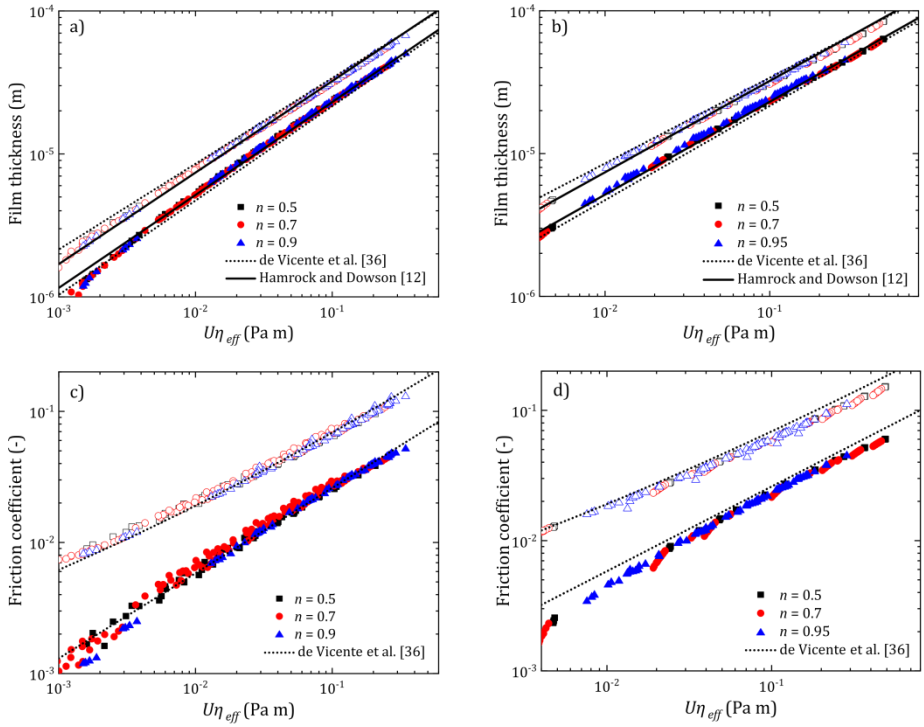

Figure 6.11: Simulated master curves. Left column shear-thinning and right column shear thickening. a) and b) closed symbols: h_{min}; open symbols: h_{cen}. Dot line represents the film thickness prediction for Newtonian fluids from de Vicente *et al.* [36] and solid line represents the film thickness prediction for Newtonian fluids from Hamrock and Dowson [12]. c) and d) closed symbols: μ_P; open symbols: μ_C/SRR. Dashed line represents the friction coefficient prediction for Newtonian fluids from de Vicente *et al.* [36].

However, a complication arises in the case of non-Newtonian fluids where the viscosity changes in the contact plane and also across the film thickness. Nevertheless, in this section we demonstrate that a similar master curve can be constructed from the simulation data by calculating an effective viscosity η_{eff} in the Hertzian contact region as presented in the previous section. Interestingly, $U\eta_{eff}$ is capable to collapse all the data on a master curve following a power-law function. Figure 6.11 shows the collapse of the simulation results for combinations of the operating parameters and lubricant properties (see Table 6.1). The power law could be represented as $\alpha\overline{U}^{\beta}\overline{W}^{\theta}$, where α, β, and θ are constants and $\overline{U}$ and $\overline{W}$ are dimensionless velocity and load parameters, respectively. The dimensionless speeds explored in this work were in the range $1.6 \times 10^{-7} < \overline{U} < 3.21 \times 10^{-5}$ and the dimensionless load is in the range $4.75 \times 10^{-3} < \overline{W} < 4.75 \times 10^{-2}$.

Table 6.5 gives the regression fitting parameters to the simulation results for both shear-thinning and shear-thickening fluids. The exponent β and θ were obtained to be very similar for both non-Newtonian fluids. Also, a good agreement was observed between simulation results and predictive formulas from the literature [13,32]. This observation indicates that existing predictive formulas for Newtonian fluids can be used for non-Newtonian fluids when the effective viscosity as proposed in (6.2) is considered.

$\alpha\overline{U}^{\beta}\overline{W}^{\theta}$	Fluid	h_{min}/R_x	h_{cen}/R_x	μ_P	μ_C/SRR
α	Thinning	2.323	3.579	1.619	5.038
	Thickening	2.461	3.651	2.692	5.863
	Newtonian	2.8	3.3	1.46	3.8
β	Thinning	0.624	0.616	0.588	0.534
	Thickening	0.623	0.619	0.64	0.556
	Newtonian	0.66	0.60	0.65	0.71
θ	Thinning	-0.189	-0.146	-0.544	-0.387
	Thickening	-0.177	-0.147	-0.536	-0.387
	Newtonian	-0.22	-0.14	-0.7	-0.76

Table 6.5: Fitting parameters for shear-thinning and shear-thickening fluids. The dimensionless speed and load explored in this work are in the ranges $1.6 \times 10^{-7} < \overline{U} < 3.21 \times 10^{-5}$ and $4.75 \times 10^{-3} < \overline{W} < 4.75 \times 10^{-2}$, respectively. Together with inelastic non-Newtonian fluid predictions we also include the exponents for Newtonian fluids [36].

- **Comparison with experiments**

In order to check the simulation results, in this section we compare the friction coefficient predictions with the two model fluids. Figure 6.12 shows the Stribeck curves for two model non-Newtonian fluids: shear thinning (Figure 6.12-a) and shear thickening (Figure 6.12-b fluids).

In Figure 6.12-a we show the friction coefficient versus sliding speed curves for XG solutions at two different biopolymer concentrations. For the experimentally accessible sliding speeds, the simulation results reveal that the shear rate is in the interval from $9.2 \cdot 10^3$ to $3 \cdot 10^4\ s^{-1}$. These shear rates are beyond the sensitivity of the rheometer. For the 0.20 wt% solution, the viscosity was nearly 0.22 Pa · s in this shear rate range (uncertainty below 5 %). This is very close to the high shear viscosity $\eta_\infty = 0.212$ Pa · s. Similarly, for the 0.30 wt% solution, the viscosity was approximately 0.28 Pa · s being

$\eta_\infty = 0.266$ Pa · s. In summary, for the XG solutions the simulation results are in reasonably good agreement with the experiments.

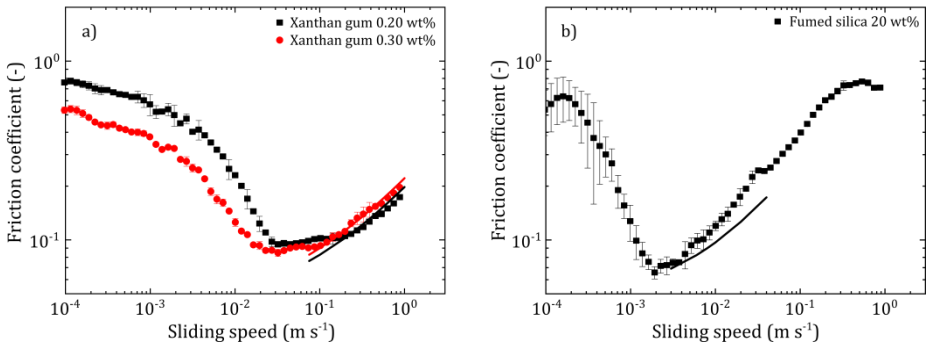

Figure 6.12: Experimental friction coefficient data as a function of sliding speed: a) shear-thinning fluids, b) shear-thickening fluids. Solid and dashed lines correspond to the simulation predictions.

In Figure 6.12-b we show the friction coefficient versus sliding speed curves for FS suspensions. Simulations for FS suspensions predicted an effective viscosity of 5.35 Pa · s and a film thickness of 6.87 μm at the "mixed-full film" transition point in the hydrodynamic region. At the maximum simulated sliding speed, 0.04 m · s^{-1}, the effective viscosity was 6.74 Pa · s and the film thickness was 27.78 μm. Because of the limitation in measuring the viscosity at very high shear rates in FS suspensions (see Figure 6.2-a), the simulations were restricted to a maximum shear rate of 1000 s^{-1}. As observed in Figure 6.12-b, the simulation data underestimate experimental ones. This is surprising, especially because a better agreement was found between experiments and simulation data from the simplified solution approach (compare Figure 6.2-b with Figure 6.12-b). Even though we do not have a clear explanation for this, a possible explanation could be the existence of a rolling friction contribution coming from FS aggregates. FS suspensions truly consist of ~0.1-0.2 μm size clusters made of ~10 nm size spherical particles [42]. Under a sliding motion, the FS clusters are expected to roll causing an extra contribution to the total friction that is not taken into account in our simulation.

6.4. Conclusions

The tribological properties of inelastic non-Newtonian fluids in isoviscous elastohydrodynamic contacts are investigated by numerically solving the generalized Reynolds equation and performing experiments in a ball-on-three

plates tribometer. Two particular lubricants are investigated: shear-thinning and shear-thickening fluids.

A double-Newtonian Carreau-Yasuda model is used to describe the viscosity thinning and thickening under increasing shear rates. First, a simplified solution approach is proposed to estimate the film thickness and the friction coefficient. In this approach, the fluid viscosity is estimated, using an iterative procedure, from the experimental viscosity curve as a function of the shear rate. Second, a full solution approach is described where the generalized Reynolds equation is numerically solved. Regression formulas are presented to define an effective lubricant viscosity. Interestingly, this effective viscosity is capable to collapse all the simulation data on a master curve where the friction coefficient is plotted as function of the entrainment speed multiplied by the effective viscosity. Regression formulas are also proposed for the film thickness.

A reasonably good agreement is obtained when comparing the simulation predictions and experimental data on model inelastic non-Newtonian fluids: xanthan gum solutions and fumed silica suspensions.

6.5. References

[1] Timm K, Myant C, Spikes H A and Grunze M 2011 Particulate lubricants in cosmetic applications *Tribol. Int.* **44** 1695–1703

[2] Yakubov G E, Branfield T E, Bongaerts J H H and Stokes J R 2015 Tribology of particle suspensions in rolling-sliding soft contacts *Biotribology* **3** 1–10

[3] Zhang B, Selway N, Shelat K J, Dhital S, Stokes J R and Gidley M J 2017 Tribology of swollen starch granule suspensions from maize and potato *Carbohydr. Polym.* **155** 128–135

[4] Olivares M L, Shahrivar K and Vicente J de 2019 Soft lubrication characteristics of microparticulated whey proteins used as fat replacers in dairy systems *J. Food Eng.* **245** 157–165

[5] Esfahanian M and Hamrock B J 1991 Fluid-film lubrication regimes revisited *Tribol. Trans.* **34** 628–632

[6] Pradal C and Stokes J R 2016 Oral tribology: bridging the gap between physical measurements and sensory experience *Curr. Opin. Food Sci.* **9** 34–41

[7] Jin Z and Dowson D 2005 Elastohydrodynamic lubrication in biological systems *Proc. Inst. Mech. Eng. Part J J. Eng. Tribol.* **219** 367–380

[8] Reynolds O 1886 On the theory of lubrication and its application to Mr. Beauchamp Tower's experiments, including an experimental determination of the viscosity of olive oil *Philos. Trans. R. Soc. Lond.* **177** 157–234

[9] Grubin A N 1949 Investigation of the contact of machine components *Cent. Sci. Res. Inst Tech Mech Eng*

[10] Dowson D and Higginson G R 1959 A numerical solution to the elasto-hydrodynamic problem *J. Mech. Eng. Sci.* **1** 6–15

[11] Dowson D 1966 Elastohydrodynamic lubrication *Fundam. Roll. Gear Lubr.*

[12] Hamrock B J and Dowson D 1976 Isothermal elastohydrodynamic lubrication of point contacts: Part 1—Theoretical formulation *J. Lubr. Technol.* **98** 223

[13] Hamrock B, Schmid S and Jacobson B 2004 *Fundamentals of Fluid Film Lubrication* (CRC Press)

[14] Lugt P M and Morales-Espejel G E 2011 A Review of Elasto-Hydrodynamic Lubrication Theory *Tribol. Trans.* **54** 470–496

[15] Lubrecht A A, Napel W E ten and Bosma R 1987 Multigrid, an alternative method of solution for two-dimensional elastohydrodynamically lubricated point contact calculations *J. Tribol.* **109** 437

[16] Nijenbanning G, Venner C H and Moes H 1994 Film thickness in elastohydrodynamically lubricated elliptic contacts *Wear* **176** 217–229

[17] Venner C H and Lubrecht A A 2000 *Multilevel methods in lubrication* (Amsterdam ; New York: Elsevier)

[18] Hooke C J 2000 The behaviour of low-amplitude surface roughness under line contacts: Non-Newtonian fluids *Proc. Inst. Mech. Eng. Part J J. Eng. Tribol.* **214** 253–265

[19] Ehret P, Dowson D and Taylor C M 1998 On lubricant transport conditions in elastohydrodynamic conjuctions *Proc. R. Soc. Lond. Ser. Math. Phys. Eng. Sci.* **454** 763–787

[20] Greenwood J A and Kauzlarich J J 1998 Elastohydrodynamic film thickness for shear-thinning lubricants *Proc. Inst. Mech. Eng. Part J J. Eng. Tribol.* **212** 179–191

[21] Greenwood J A 2000 Two-dimensional flow of a non-Newtonian lubricant *Proc. Inst. Mech. Eng. Part J J. Eng. Tribol.* **214** 29–41

[22] Liu Y, Wang Q J, Bair S and Vergne P 2007 A quantitative solution for the full shear-thinning EHL point contact problem including traction *Tribol. Lett.* **28** 171–181

[23] Jang J Y, Khonsari M M and Bair S 2007 On the elastohydrodynamic analysis of shear-thinning fluids *Proc. R. Soc. Math. Phys. Eng. Sci.* **463** 3271–3290

[24] Bair S and Qureshi F 2003 The generalized Newtonian fluid model and elastohydrodynamic film thickness *J. Tribol.* **125** 70

[25] de la Guerra Ochoa E, Echávarri Otero J, Chacón Tanarro E and del Río López B 2018 A thermal resistances-based approach for thermal-elastohydrodynamic calculations in point contacts *Proc. Inst. Mech. Eng. Part C J. Mech. Eng. Sci.* **232** 2088–102

[26] de la Guerra Ochoa E, Echávarri Otero J, Sánchez López A, Chacón Tanarro E and del Río López B 2018 Film thickness formula for thermal EHL line contact considering a new Reynolds–Carreau equation *Tribol. Lett.* **66**

[27] Bair S 2005 Shear thinning correction for rolling/sliding elastohydrodynamic film thickness *Proc. Inst. Mech. Eng. Part J J. Eng. Tribol.* **219** 69–74

[28] Kumar P and Khonsari M M 2008 EHL circular contact film thickness correction factor for shear-thinning fluids *J. Tribol.* **130** 041506

[29] Katyal P and Kumar P 2012 Central film thickness formula for shear thinning lubricants in EHL point contacts under pure rolling *Tribol. Int.* **48** 113–121

[30] Katyal P and Kumar P 2014 New central film thickness equation for shear thinning lubricants in elastohydrodynamic lubricated rolling/sliding point contact conditions *J. Tribol.* **136** 041504

[31] Habchi W, Vergne P, Eyheramendy D and Morales-Espejel G E 2011 Numerical investigation of the use of machinery low-viscosity working fluids as lubricants in elastohydrodynamic lubricated point contacts *Proc. Inst. Mech. Eng. Part J J. Eng. Tribol.* **225** 465–477

[32] Jang J Y, Khonsari M M and Bair S 2008 Correction factor formula to predict the central and minimum film thickness for shear-thinning fluids in EHL *J. Tribol.* **130** 024501

[33] Habchi W, Bair S, Qureshi F and Covitch M 2013 A film thickness correction formula for double-Newtonian shear-thinning in rolling EHL circular contacts *Tribol. Lett.* **50** 59–66

[34] Katyal P and Kumar P 2014 On the role of second Newtonian viscosity in EHL point contacts using double Newtonian shear-thinning model *Tribol. Int.* **71** 140–148

[35] Bair S 2018 Generalized Newtonian viscosity functions for hydrodynamic lubrication *Tribol. Int.* **117** 15–23

[36] de Vicente J, Stokes J R and Spikes H A 2005 The frictional properties of Newtonian fluids in rolling–sliding soft-EHL contact *Tribol. Lett.* **20** 273–86

[37] de Vicente J, Stokes J R and Spikes H A 2006 Soft lubrication of model hydrocolloids *Food Hydrocoll.* **20** 483–91

[38] Raghavan S R and Khan S A 1997 Shear-thickening response of fumed silica suspensions under steady and oscillatory shear *J. Colloid Interface Sci.* **185** 57–67

[39] Shahrivar K and de Vicente J 2014 Ferrofluid lubrication of compliant polymeric contacts: effect of non-homogeneous magnetic fields *Tribol. Lett.* **56** 281–92

[40] Bombard A J F and de Vicente J 2012 Boundary lubrication of magnetorheological fluids in PTFE/steel point contacts *Wear* **296** 484–90

[41] de Vicente J, Stokes J R and Spikes H A 2005 Lubrication properties of non-adsorbing polymer solutions in soft elastohydrodynamic (EHD) contacts *Tribol. Int.* **38** 515–26

[42] Raghavan S R, Walls H J and Khan S A 2000 Rheology of silica dispersions in organic liquids: new evidence for solvation forces dictated by hydrogen bonding *Langmuir* **16** 7920–7930

7. Soft lubrication of cornstarch-based shear-thickening fluids

E.M. Ortigosa-Moya, K. Shahrivar, R. Hidalgo-Álvarez, J. de Vicente

The content of this chapter is published in: *Smart Materials and Structures*, **2019**, *28*, 085044 (12 pp).

https://doi.org/10.1088/1361-665X/ab22e5

Abstract

The behaviour of complex fluids in thin films under the isoviscous elastohydrodynamic lubrication regime is a topic of current interest. A vast majority of the materials used to lubricate compliant contacts are shear-thinning fluids and, in comparison, very little is known about the lubrication properties of shear-thickening (ST) fluids. In this work we carried out both rheological and tribological experiments on ST fluids based on cornstarch suspensions. We investigated the influence of the polarity and viscosity of the carrier fluid and the cornstarch particles' concentration. From a rheological perspective, the ST response is diminished (as the shear-thinning region enlarges) when non-polar carriers are used (e.g., silicone oil) while a marked thickening is observed for polar carriers (e.g., glycerol-water mixtures). From a tribological perspective, the friction coefficient at slow sliding speeds is strongly affected

by the nature of the carrier fluid, and in particular its wettability in contact with hydrophobic PDMS tribopairs. We demonstrate that experimental data, plotted in terms of Stribeck curves, provide useful information on the entrainment of particles/fluid through the contact. Finally, experimental results are also compared with numerical solutions of the Reynolds equation for inelastic non-Newtonian fluids in the isoviscous elastohydrodynamic regime. A Carreau–Yasuda constitutive equation for the viscosity-shear rate relationship is used.

7.1. Introduction

Shear-thickening (ST) fluids are inelastic materials whose viscosity (or stress) increases when sheared [1,2]. Such materials are of practical interest in dampers and shock absorbers [3,4], as well as in mechanical polishing applications [5]. Shear-thickening characteristics rely on several factors, namely: particle volume fraction [6], interparticle attraction [7–9], polydispersity [10], size [11,12], shape [13], roughness [14–17], and particle interactions with the carrier fluid [18,19].

Several mechanisms and theories have been proposed to be at the origin of the shear-thickening behaviour [20]. Early in the seventies, an order-disorder transition mechanism was proposed by Hoffman [21] to explain the continuous shear-thickening transition (CST) exhibited by monodisperse suspensions of polymeric resins (i.e., a slight increase in viscosity when increasing the shear rate). Another mechanism is dilatancy [22]. Here, the suspension volume increases under shear, resulting in additional stresses from solid-solid friction. Other researchers [23] support a mechanism based on the formation of transient particle aggregates (i.e., hydroclusters). The hydroclusters develop at strong flow conditions and lead to increased lubrication drag forces between particles. Nowadays, it is well known that the appearance of one mechanism does not exclude or require the presence of another, and this complicates the analysis of the CST.

Apart from the CST, a reversible and dramatic shear stress jump (of several orders of magnitude) when increasing the shear rate has been documented in the literature. This is referred to as discontinuous shear thickening (DST). For the DST to occur, the particle loading fraction has to be extraordinarily large (close to the maximum packing fraction) and it is well-known today that hydrodynamic forces are not sufficient to explain and/or predict the DST reported in experiments [24]. Instead, the rheological behaviour of these

suspensions is intimately related to frictional mechanisms [25] occurring at the microscale rather than viscous dissipation. This is so because at high loadings the thickness of the fluid layer surrounding the particles is very small compared to the characteristic particle length and tribological phenomena come into play. Nowadays, the DST behaviour is thought to be based on frictional interactions [26] occurring among the particle asperities at high volume fractions and high shear rates. It is worth noting here that the occurrence of shear thickening at low shear rates has also been reported for field-responsive dipolar suspensions, when particles interact under the application of high electric or magnetic field strengths [27,28]. In DST conditions, the suspension develops a contact network and positive normal stresses appear, which result in suspension dilation. Among the many suspensions exhibiting DST, water-based concentrated starch suspensions are probably the most frequently investigated despite the fact that they are not the simplest ones [24,29,30]. In this chapter we investigate concentrated cornstarch suspensions as model ST fluids.

The field of tribology deals with friction, wear and lubrication phenomena between surfaces in relative motion. It may be considered as the borderline between bulk and interfacial rheology, since the friction coefficient already contains information on the rheological properties of the fluid and the physico-chemical characteristics of the bounding surfaces. In this context, a particular subcategory of tribology -Biotribology- is attracting a lot of interest today. For instance, biotribological contacts are present during the oral processing of food and in-use of personal care products [31,32]. In particular, studies mimicking oral tribological performance have attracted interest in Food Science researchers that aim to find a link between frictional and texture performances. In this context, starch is a significant contributor to the commercial food industry; starch is typically isolated or processed commercially from maize, wheat, rice potato, and cassava [33]. As stated in the paragraph above, cornstarch has been a well characterized ST material from a rheological point of view. However, very little is known about the tribological behaviour of these suspensions.

Traditionally, the tribological behaviour of a lubricated tribopair is well described by the so-called Stribeck curve. In this representation, the friction coefficient μ is plotted as a function of the Gumbel ratio $U\eta_f/w$ being U the entrainment speed, η_f the viscosity of the lubricant, and w the applied load per unit of length. Three regimes are identified: boundary, mixed, and hydro-

dynamic lubrication. The boundary lubrication regime is found at low ratios, where the separation between the surfaces is so small that there is no lubricant separating the surfaces. When the ratio increases the fluid is capable to enter the gap, hence separating the surfaces and reducing the number of asperity contact points; this is the so-called mixed lubrication regime. For very large ratios a thin film of lubricant forms and the contacting surfaces separate, entering in the hydrodynamic lubrication regime. The isoviscous elastohydrodynamic lubrication (IEHL) regime is a particular case within the hydrodynamic regime where where significant elastic deformation occurs in the surfaces and the contact pressure is not sufficient to cause any substantial increase in the lubricant viscosity (i.e., compliant contacts). The IEHL regime applies in many biotribological contacts (e.g., human body joints and oral food processing) as well as in other engineering applications (e.g., wet tires and elastomeric joints) [34].

Generally speaking, the behaviour of complex fluids in thin films under the IEHL regime is a topic of current interest. Most frequently, the lubricants are assumed to behave as Newtonian fluids in the contact with a constant shear viscosity. However, a vast majority of the materials used to lubricate compliant contacts are shear-thinning fluids [35,36]; in the case of polymer solutions a very good agreement was found between experiments and simulations if the lubricant was assumed to be Newtonian with a high shear viscosity [35]. Surprisingly, very little is known about the lubrication properties of shear-thickening fluids in compliant contacts [37–39]. In this context, in this manuscript we investigate the tribological properties of concentrated cornstarch suspensions in compliant polydimethylsiloxane (PDMS) contacts that are widely used to mimic oral lubrication [40].

7.2. Experimental and simulations

Shear-thickening fluids were prepared by dispersing cornstarch particles in water, glycerol 87 %w/w (Scharlau, density 1.23 $g \cdot cm^{-3}$), glycerol 99 %w/w (Sigma Aldrich, density 1.25 $g \cdot cm^{-3}$), and silicone oil with a nominal viscosity of 90.14 $mPa \cdot s$ (Sigma Aldrich, density 0.968 $g \cdot cm^{-3}$). The nomenclature from now on will be the one in Table 7.1. Starch from corn particles was purchased from Sigma Aldrich (73 % amylopectin and 27 % amylose) with density of 1.68 $g \cdot cm^{-3}$ and mean particle diameter ca. 10.7 μm (see Figure S1 in the Supplementary material section). Rheological tests were carried out at 25 ºC using an Anton Paar MCR 501 rheometer in cone-plate configuration. The

protocol consisted in two steps. In the first one the normal force was reset to zero and the sample was allowed to rest for 1 min. In the second step, the mechanical torque was increased logarithmically from 10^{-4} to 10^{2} mN · m.

Code	**Carrier fluid**	**Shear viscosity**, η (mPa·s)	**Contact angle**, θ (°)
W	Deionized water	0.89 ± 0.01	106.2 ± 0.8
G87	Glycerol 87 % w/w	119 ± 5	97.3 ± 0.8
G99	Glycerol 99 % w/w	834 ± 16	97 ± 1
SO100	Silicone oil 100 cSt	90 ± 19	15 ± 1

Table 7.1: Shear viscosity η of the carrier fluids used in the preparation of ST fluids and contact angle θ against PDMS surfaces. Measurements were carried out at $T = 25$ °C.

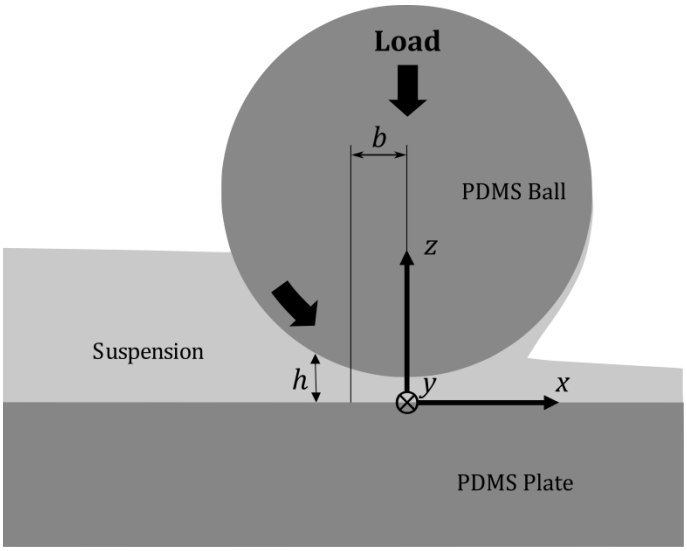

Figure 7.1: Schematic representation of the ball-on-plate simulated contact.

Sliding friction measurements were also carried out at 25 ºC, in a non-conforming ball-on-three-plates geometry (T-PTD 200 tribology cell) using an Anton Paar MCR 302 rheometer. Polydimethylsiloxane (PDMS) tribopairs were used to generate a compliant contact and to operate in the IEHL regime. In this experimental set-up, a ball of radius $R = 6.35$ mm is loaded at a given normal force $F_N = 1$ N against three plates mounted on a movable holder with their surface normal in tetrahedral coordination relative to the ball rotation axis (see Figure 7.1). This ensures an equal distribution of the applied load on the three frictional pairs (see Figure 1a in [41]). The load experienced by each plate was $w = \sqrt{2}F_N/3$, and the maximum Hertzian pressure p_H (i.e.,

at the contact center) was 0.15 MPa [41]. It is obtained as $p_H = \frac{3w}{2\pi ab}$, where a and b are the major and minor axis in the Hertzian elliptical contact [42]. The balls and plates were prepared in situ using conventional techniques from a two-component silicone elastomer kit (SylgardTM 184, Dow Corning). PDMS components have a Young's modulus of 1.84 MPa, Poisson's ratio of 0.5 [41,43] and hardness (Shore A) of 46.68 [44]. Once the sample was added into the geometry, the ball was lowered to the measurement position. Then, the normal force was adjusted to the commanded value during 1 min. In a second step, the normal force was kept at the desired value and the ball was rotated at a logarithmically increasing sliding speed (V) from $5 \cdot 10^{-4}$ to $1\,\mathrm{m} \cdot \mathrm{s}^{-1}$ during 5 minutes.

In order to get reproducible results a thorough cleaning procedure was implemented. After every test, the sample was removed with paper and deionized water, and all the pieces (ball, plates and holder) were dismounted and carefully cleaned with ethanol. The PDMS ball and three plates were replaced when a different batch of samples had to be measured, i.e., when a different carrier fluid was employed. Also, after every test, the plates were carefully inspected for worn spots. The plates were also replaced when a worn spot appeared on the surfaces. Both rheological and tribological tests were carried out with fresh new samples in order to avoid water evaporation and changes in the particle volume fraction. As it will be shown later this was especially important in the case of the G87-based suspensions (see Figure S2). Experimental data reported here were obtained from sample averaging over at least two repetitions.

Simulations were also performed to calculate the friction coefficient in the IEHL regime. A detailed explanation of the simulation approach is given in Subsection 3.3.4. The generalized Reynolds equation (Equation 3.46) governs the flow behaviour in thin lubricated films [45–47]. Its numerical solution involves the determination of the pressure distribution $p(x, y)$ and the film thickness $h(x, y)$ in the contact. In shear thickening fluids the viscosity increases with the shear rate, and this dependency is well captured by the Carreau-Yasuda model (Equation 3.51) as constitutive equation. In a typical simulation the gap profile and pressure distribution are not uniform. As a result, at a given sliding velocity, the shear rate at each point within the contact region changes, and so does the viscosity. Hence, at each node within the solution domain, the viscosity was obtained iteratively across the fluid film using

Equation 3.51. The calculation of the friction coefficient considers the summation of three contributions: Couette, Poiseuille and elastic hysteresis [41,42].

7.3. Results and discussion

7.3.1. Rheological characterization

The carrier fluids employed in this work were all Newtonian. They consisted of glycerol G (at different dilutions in water W) and silicone oil SO100. Their shear viscosities are shown in Table 7.1. Of course, the larger the concentration of G in the G/W mixture, the larger the viscosity. Note that the SO100 used in this work deliberately has a very similar viscosity as G87 but very different polar character and wettability (see the contact angles in Table 7.2). Figure 7.2 shows the relative shear viscosity η_r (i.e., $\eta_r = \eta_s/\eta_f$, the suspension viscosity divided by the carrier fluid viscosity) as a function of the shear rate $\dot{\gamma}$ for two starch suspensions with volume fractions being $\phi = 0.30$ and 0.36. Together with experimental data, in Figure 7.2 we also include the predictions from the semi-empirical Quemada expression:

$$\eta_r = \frac{\eta_s}{\eta_f} = \left(1 - \frac{\phi}{\phi_m}\right)^{-2} \tag{7.1}$$

Interacting media	Refractive index, n	Dielectric permittivity, ε	A_{22} (J)	A_{121} (J)
W	1.3330	80.20	$3.726 \cdot 10^{-20}$	$2.946 \cdot 10^{-22}$
G87	1.4522	50.91	$6.192 \cdot 10^{-20}$	$5.324 \cdot 10^{-21}$
G99	1.4690	46.53	$6.575 \cdot 10^{-20}$	$6.488 \cdot 10^{-21}$
SO100	1.5020	2.73	$7.142 \cdot 10^{-20}$	$8.349 \cdot 10^{-21}$

Table 7.2: Refractive index n, dielectric permittivity ε, Hamaker constant of the carriers A_{22} and estimated non-retarded Hamaker constant A_{121} for starch particles (phase 1) interacting across the carrier fluid (phase 2). A_{121} values are estimated from the Hamaker constants in vacuum for particles ($A_{11} = 3.093 \cdot 10^{-20}$J) and fluids A_{22} using $A_{121} = \left(\sqrt{A_{11}} - \sqrt{A_{22}}\right)^2$.

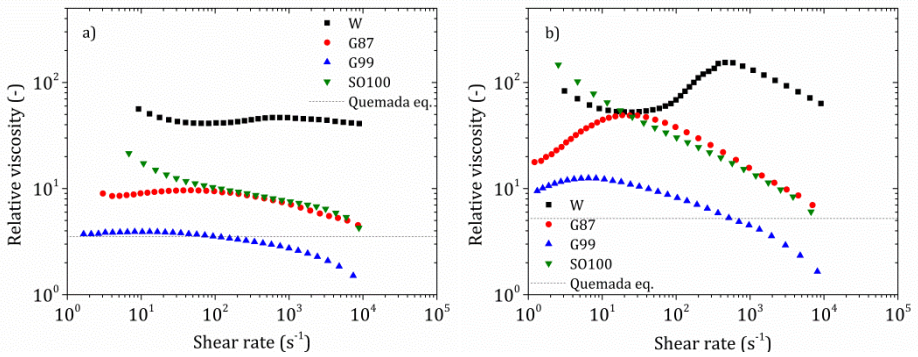

Figure 7.2: Relative viscosity $\eta_r = \eta_s/\eta_f$ as a function of the shear rate $\dot{\gamma}$ for cornstarch suspensions with a) $\phi = 0.30$ and b) $\phi = 0.36$. Horizontal lines correspond to the Quemada expression for Hard Spheres $\eta_r = \left(1 - \frac{\phi}{\phi_m}\right)^{-2}$ with $\phi_m = 0.64$, which corresponds to a random close packing.

The maximum packing fraction ϕ_m value for hard spheres is often taken as 0.64, which is the value associated with a random close packing. For the case of the lowest starch concentration ($\phi = 0.30$) the suspensions behave as shear-thinning materials (see Figure 7.2-a); the viscosity continuously decreases with the shear rate. On the contrary, at a concentration of $\phi = 0.36$, W, G87, and G99-based suspensions show a shear-thickening behaviour in a window of shear rates above a critical value (see Figure 7.2-b). A maximum value in the viscosity is also found in these shear-thickening suspensions, which is followed by a continuous decrease in viscosity. The onset of the ST region occurs at a lower critical shear rate the higher the viscosity of the carrier fluid (i.e., the smaller the amount of W in the G/W mixture). Interestingly, SO100-based suspensions were shear thinning in the whole range of shear rates applied.

The fact that suspensions with $\phi = 0.36$ suspensions exhibit a shear-thickening regime in G/W mixtures was expected in view of previous data in the literature [19,48,49]. Brown and Jaeger [48] reported the appearance of CST for a starch concentration of 40 wt% ($\phi = 0.32$) in similar systems consisting in a mixture of G, W and CsCl. It is well-known that for the ST to be observed, particles must behave as Hard Spheres (with negligible interparticle attractions) [29]. Otherwise, the existence of interparticle attractions result in a shear-thinning behaviour at low shear rates (coming from the shear-induced erosion of the aggregates) and eventually, if the attraction is suffi-

ciently large, to the appearance of a yield stress that may hide the shear thickening phenomenon [6,7,9,29].

In the systems investigated in this work, interparticle attractions are necessarily present as a result of van der Waals forces that, in their turn, depend on the non-retarded Hamaker constant. Estimations of the non-retarded Hamaker constant A_{121} for two cornstarch particles (phase 1) separated by a carrier fluid (phase 2) are shown in Table 7.2. The value of the Hamaker constant for cornstarch in vacuum $A_{11} = 3.093 \cdot 10^{-20}$ J was obtained from measurements of adhesive forces [50], while the values for the carrier fluids A_{22} were calculated from the refractive indexes and dielectric permittivities of the carriers found in the literature [51]. The non-retarded Hamaker constant is then obtained from $A_{121} = \left(\sqrt{A_{11}} - \sqrt{A_{22}}\right)^2$. Differences observed in the shear-thickening response between the carrier fluids employed in this work can be explained in terms of interparticle interactions. In brief, pure water based suspensions exhibit the smaller A_{121} values and concomitantly the stronger shear thickening effect. This is in agreement with the hydrocluster mechanism proposed by Brady and coworkers. Upon the addition of glycerol, interparticle attractions are promoted (i.e., A_{121} increases) and the critical rate for shear thickening is shifted to lower values (see Figure 7.2-b). Finally, SO100-based suspensions exhibit the stronger interparticle attractions (larger A_{121} values). In these particular suspensions the viscosity diverges at low shear rates (i.e., a slope of -1 is envisaged in Figure 7.2-b at low shear rates) in agreement with the appearance of a yield stress that overcomes the critical stress for shear thickening. As a result the shear thickening is masked. Apart from this qualitative explanation in terms of the hydrocluster mechanism, it is important to remark that a more efficient electrostatic stabilization in G/W mixtures is also expected since hydroxyl groups available onto the starch particles could form hydrogen bonds with polar molecules in G/W carriers [52,53].

7.3.2. Tribological characterization

Figure 7.3-a shows the friction coefficient μ as a function of the sliding speed V for the four different carrier fluids investigated (without particles). Regardless the nature of each particular liquid, three regions are identified. At low speed, the friction is essentially constant and originates from the interaction between the two surfaces (boundary friction). With increasing speed the fluid partially fills the space between both surfaces so that they are pushed apart

and only large asperities are in contact (mixed regime). As a consequence of this separation, the friction coefficient decreases in this zone. At high sliding speeds, the lubricating film thickness is large enough to prevent any contact between the surfaces, and the bulk properties of the fluid become the major contribution to friction (hydrodynamic regime).

In Figure 7.3-b we show the Stribeck curve in terms of the friction coefficient μ as a function of the entrainment speed multiplied by the carrier fluid viscosity $U\eta_f$. A very good collapse was found in the full film lubrication regime, $U\eta_f > 10^{-2}$ Pa · m, that was expected because the frictional behaviour in this region is governed by the viscosity of the carrier fluids. In contrast, large differences were found in the boundary and mixed regimes. This is attributed to the different wettability characteristics of the liquids onto the PDMS substrates (see Table 7.1). The PDMS surfaces are strongly hydrophobic, so that they will be more easily wetted by low polarity carriers. The different wetting characteristics of the studied carriers explain the increased friction coefficient for polar fluids (i.e., glycerol-water mixtures) and reduced friction coefficient for non-polar fluids (i.e., silicone oil) [35].

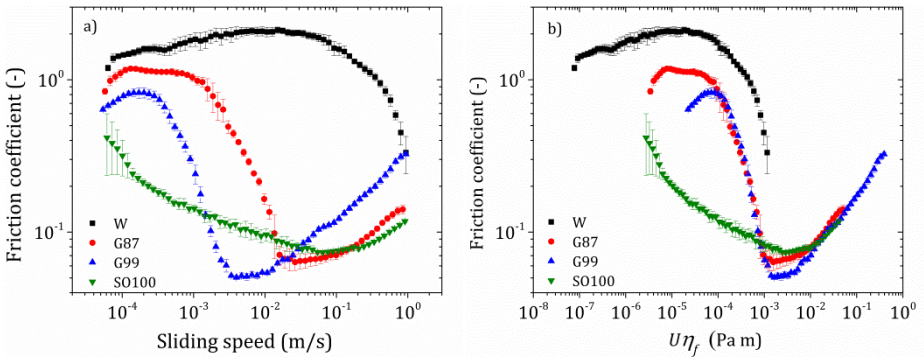

Figure 7.3: a) Friction coefficient μ curve as a function of the sliding velocity V for the carrier fluids. b) Friction coefficient μ as a function of the entrainment speed times the carrier fluid viscosity $U\eta_f$. All tribological measurements were carried out in a non-conforming PDMS ball-on-three-plates geometry.

As stated in the Experimental section, sample evaporation was a challenge in these concentrated suspensions especially when using G87. As a way of example, in Figure S2 in the Supplementary material section we show the friction curves for different aging times. As observed, the full film formed earlier when the waiting time increased. It was expected from the fact that water evaporation and granule swelling may result in an increasing effective volume

fraction and hence a larger viscosity. Therefore, in this manuscript the samples prepared in G87 were measured immediately after preparation.

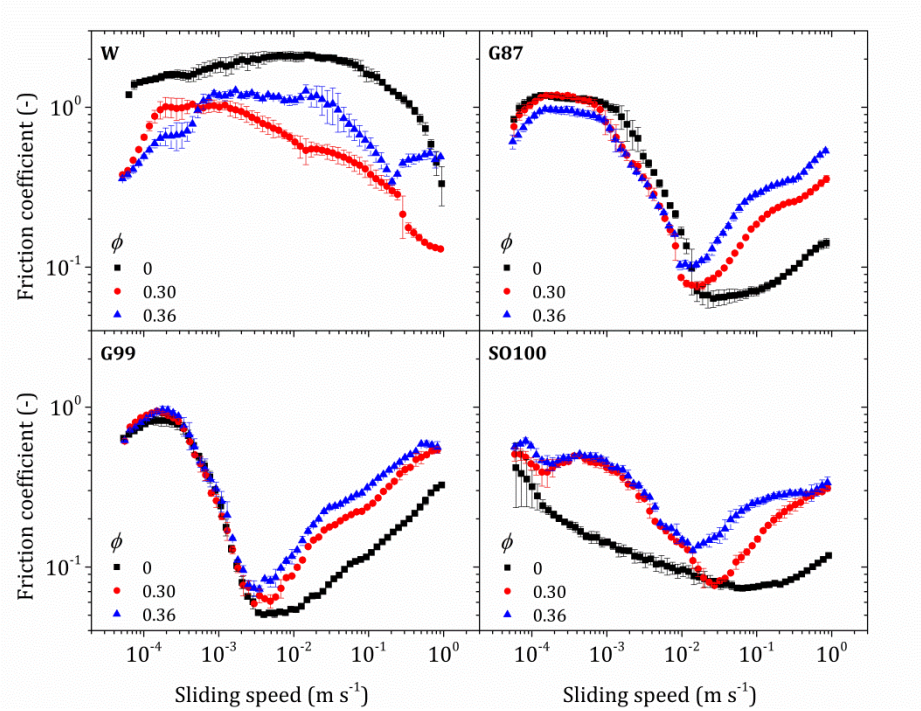

Figure 7.4: Friction coefficient μ as a function of sliding speed V for the starch suspensions ($\phi = 0.30$ and $\phi = 0.36$). Together with data on cornstarch suspensions we also include results for the carrier fluids.

Figure 7.4 shows the friction curves of the starch suspensions ($\phi = 0.30$ and $\phi = 0.36$) together with the friction curve of the corresponding carrier fluid. For water, only the boundary regime is observed due to its low viscosity. In this case, the addition of starch particles reduces the friction level. Starch particles in water have a higher colloidal stability than in other carrier fluids due to reduced interparticle attractions. When dispersed in water, starch granules do not aggregate, and therefore, they are amenable to roll along the contact thus reducing the friction coefficient. On the contrary, for silicone oil the friction coefficient increases upon the addition of particles. When dispersed in oil, the particles might aggregate due to higher Van der Waals interaction forming clusters of particles that are not easy to roll, hence resulting in a friction increase. In this sense, the trend in the friction coefficient in the boundary lubrication regime, as compared to the carrier without particles, depends on the size of particle aggregates and their ability to roll,

which is related to the existing van der Waals interactions. As expected, in the full film regime the friction increases with the particle concentration. Along with this increase in the friction coefficient, the sliding speed related to the minimum in the friction curve is also shifted. In this sense, a large surface roughness has been shown to shift the minimum in the Stribeck curve to larger values of $U\eta_f$ and raise the corresponding friction coefficient [54].

In Figure 7.5 we show the friction coefficient for starch suspensions as a function of the sliding speed. Results are the same previously shown in Figure 7.4 but now the curves have been grouped in a different way. In particular, with this representation we can easily compare the effect of the carrier fluid for a fixed starch concentration. The behaviour is similar for both volume fractions investigated. In both cases, the minimum in the friction coefficient is achieved at a different sliding speed depending on the carrier fluid. Specifically, the more viscous the carrier liquid is, the earlier the onset of the full film regime.

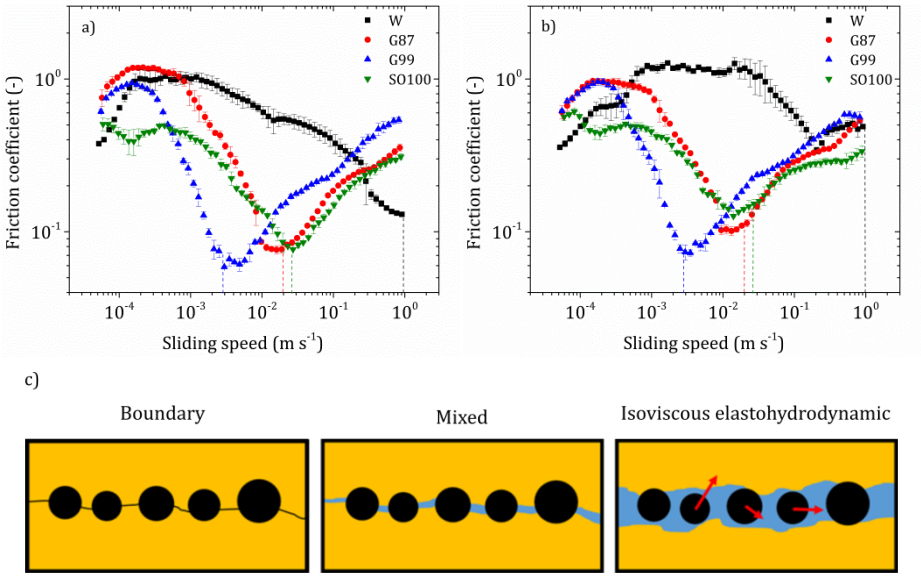

Figure 7.5: Friction coefficient μ as a function of sliding speed V curves for different starch concentrations with a) $\phi = 0.30$ and b) $\phi = 0.36$. Vertical dashed lines correspond to a representative minimum particle size of 2 μm (see Figure S3). c) Schematic of the boundary, mixed and IEHL lubrication regimes.

Next we estimated the central film thickness h_c generated by the carried liquid (without particles). For this aim we used the IEHL lubrication theory [55]. For each carrier fluid, the calculated central film thickness is plotted in

Figure S3 in the Supplementary material section as a function of the sliding speed. Horizontal/vertical lines in Figure S3 correspond to representative film thicknesses (2, 5 and 8 μm)/sliding speeds. The vertical lines in Figure 7.5 correspond to the critical speeds identified in Figure S3 for a central film thickness of 2 μm. It can be observed that the speeds corresponding to a central film thickness of 2 μm are very close to the critical sliding speeds corresponding to the minimum in the friction curves. This suggests that, as a first approximation, the minimum in the friction coefficient is correlated with the viscosity of the carrier fluid. Later, in subsection 7.3.3 we will see that a more appropriate description is given by the suspension viscosity instead of the carrier fluid viscosity.

In an attempt to rationalize the central film thickness associated to the minimum in the Stribeck curve, we performed a thorough particle size analysis. Starch particles used in this work are highly polydisperse as shown in Figure S1 in the Supplementary material section. If a normal distribution is considered, the minimum particle diameter is approximately given by $\mu_m - 3\sigma_m$, being $\mu_m = 10.7$ μm the average diameter and $\sigma_m = 3.3$ μm the standard deviation. With this, the minimum particle diameter is approximately 1-2 μm, which is very close to that obtained from IEHL lubrication calculations. As a result, the minimum in Figure 7.5 can be interpreted as follows: below the critical speed, associated to the minimum in the friction coefficient, particles are not allowed to pass through the contact. However, above the critical speed the gap is sufficiently large for most of the particles to pass through (see Subsection 7.2.4). This suggests that the corresponding sliding speed to the minimum in the friction coefficient is associated to the (minimum) particle size. This explanation is summarized in the schematic in Figure 7.5.

Next, we constructed the Stribeck curves by multiplying the entrainment speed by the shear viscosity of the carrier fluid (without particles) -and not by that of the particular suspension that changes with the shear rate-. These results are shown in Figure 7.6. The fact that the curves collapse in the mixed lubrication regime demonstrates that the transition from the boundary to the mixed regime is dictated by the viscosity of the carrier liquid, hence suggesting that in the boundary regime the particles simply roll when the ball slides above the plates, and that in the transition to the mixed regime the carrier liquid is capable to be entrained in the contact (see schematics in Figure 7.5).

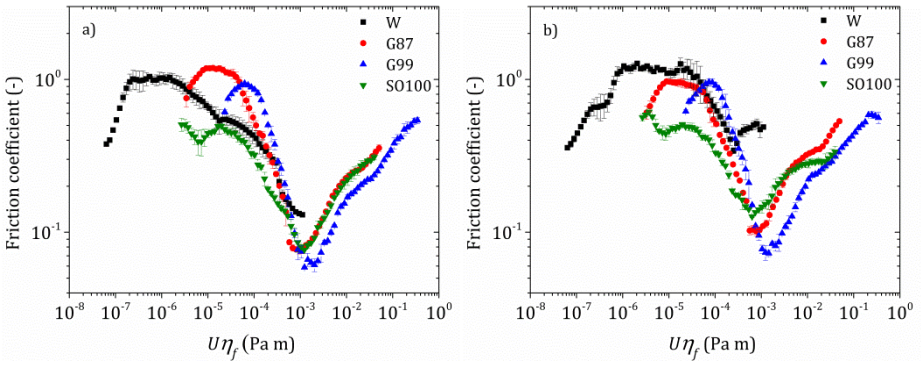

Figure 7.6: Stribeck curve (friction coefficient μ as a function of the entrainment speed times the carrier fluid viscosity $U\eta_f$) for starch suspensions in several carrier fluids. a) $\phi = 0.30$ and b) $\phi = 0.36$.

7.3.3. Effect of starch concentration

After exploring the effect of the carrier fluid at a fixed particle concentration, in this section we interrogate the influence of starch concentration in suspensions prepared in G99. The results are shown in Figure 7.7.

In Figure 7.7-a we show the viscosity curves as a function of the shear rate. As expected, a Newtonian behaviour is found at very low concentrations. As the volume fraction increases (up to $\phi = 0.25$) the suspensions exhibit a shear-thinning behaviour -for all shear rates-. For higher concentrations ($\phi > 0.25$) the suspensions progressively thicken at low shear rates. The increase in viscosity is then followed by a pronounced shear-thinning region at a critical shear rate that is thought to be related to the particle deformability [55,56]. This shear thinning region (so-called limiting elastohydrodynamic behaviour) has been reported in polymeric colloidal dispersions [57] but not in concentrated systems of harder particles [58]. Kalman [56] proposed that the mechanical properties of the particles strongly determine the limiting elastohydrodynamic behaviour, and according to this, the suspension viscosity scales with the shear rate with a slope of -0.5. This scaling agrees reasonably well with the results shown in Figure 7.2-b and Figure 7.7-a. In view of Figure 7.7-a both the onset of the shear-thickening regime and the critical shear rate associated to the maximum in viscosity shift towards lower shear rates for higher particle concentrations in good agreement with the literature [16,26,59,60].

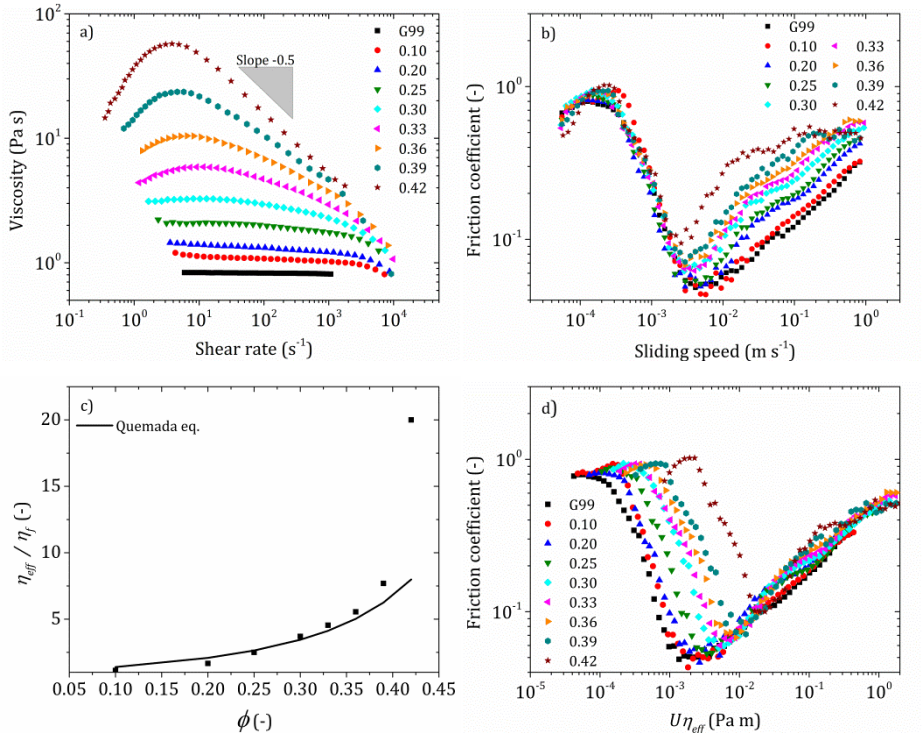

Figure 7.7: a) Viscosity curves and b) friction curves of starch suspensions ($\phi = 0 - 0.42$) in G99. c) Stribeck curves for starch suspensions ($\phi = 0 - 0.42$). d) Relative effective viscosity as a function of starch concentration and comparison with Quemada equation (black solid line).

In Figure 7.7-b we show the friction curves as a function of the sliding speed. Interestingly, all the curves collapse in the boundary and mixed lubrication regime ($V \lesssim 10^{-3}\ \mathrm{m \cdot s^{-1}}$). This is in agreement with the schematics shown in Figure 7.5: for low speeds the particles are not allowed to flow along the contact. In contrast, for higher sliding speeds ($V \lesssim 10^{-2}\ \mathrm{m \cdot s^{-1}}$) the friction coefficient increases as a result of the formation of a thin film where starch particles are now free to move. The fact that the curves do not collapse at high sliding speeds suggests that: i) the "effective" surface roughness changes with the particle concentration and ii) it is truly the suspension viscosity that governs and not the carrier fluid (cf. Figure 7.7-c below).

Even though PDMS substrates used in this work are reasonably smooth (surface roughness $R_q < 0.2$ µm), the presence of deposits of particles in the contact -in the boundary and mixed lubrication regimes- is expected to play a role on the onset of the IEHL regime that may resemble an effective surface

roughness. The influence of surface roughness in soft tribology has been described in the literature [54]. In the case of rough surfaces, the transition from the mixed to the IEHL regime occurs for lower values of the film thickness parameter at smaller sliding speeds. A rougher contact is generated in this work by simply increasing the particle concentration. As a result, it is not surprising that the onset of the IEHL regime occurs at smaller sliding speeds in good agreement with Figure 7.7-b.

The literature demonstrates that the entrainment of particles in suspension play a crucial role in the IEHL regime. Dwyer-Joyce and Heymcr [61] and Yakubov et al. [37] showed how particles of different size behaved in and around EHL contacts. In rolling motion, the friction forces on the particles in the inlet zone provokes its drag through the contact, whereas in sliding motion the particles tends to rotate as a consequence of a friction couple [62]. For pure sliding, most particles tend to accumulate in the inlet to cause starvation. Timm et al. [63] found that in fully flooded contacts, the addition of particles to a carrier liquid had no significant effect on the friction level because very few particles could pass through the contact (only particles close to central streamline would enter the contact). However, for partially lubricated contacts particles appeared to concentrate around the contact region. In summary, the dependence of the hydrodynamic transition speed with concentration suggests that a layer of deformed starch particles is likely to form at the contact hence modifying the effective surface roughness.

To obtain an estimate of the effective viscosity of the suspension being entrained in the contact, values have been calculated by forcing the Stribeck curves to collapse within the hydrodynamic regime on a master curve. The master curve is shown in Figure 7.7-c. These effective viscosity values, denoted as η_{eff}, were compared to Quemada equation in Figure 7.7-d. The calculated viscosity and theoretical predictions are in a good agreement up to $\phi = 0.39$. Only for $\phi = 0.42$ a large deviation was observed from the theoretical prediction. This suggests that the rheological response of the thin film formed between the PDMS surfaces could be assimilated as a suspension of hard spheres.

7.3.4. Comparison between experiments and numerical simulations

In Figure 7.8-a we show experiments together with numerical simulations. For the sake of comparison we also include experiments and simulations for G99 (without particles). The black solid line corresponds to the calculations for G99 as obtained from regression formulas reported in de Vicente et al. [55].

Three starch concentrations with pronounced shear-thickening characteristics were chosen to be simulated ($\phi = 0.36$, 0.39 and 0.42). The fitting parameters obtained from the Carreau-Yasuda equation to the viscosity curves are given in Table 7.3. As observed in Figure 7.8-a, the agreement is qualitatively good bearing in mind that the simulation results predict a film thickness in the range from 2 to 50 μm and a shear rate in the range from 10^3 to 10^5 s^{-1}. Clearly, the separation between contacting surfaces is much smaller than the gap in rheological measurements (i.e., 300 μm) and shear rates are significantly larger than the ones achieved in the rheometer (i.e., 10^3 s^{-1}). Overall, we have substantially extended the applicability range of the Carreau-Yasuda model. Moreover, in the most favourable conditions, at the maximum sliding speed, the film thickness is of only 5 times the mean particle diameter. As a result, the continuum approach used in the numerical calculations is also questioned.

$\boldsymbol{\phi}$	$\boldsymbol{n}$	$\boldsymbol{\eta_0}$(Pa · s)	$\boldsymbol{\eta_\infty}$(Pa · s)	$\boldsymbol{\dot{\gamma}_c}$($s^{-1}$)
0.36	0.70	10.51	0.85	20.01
0.39	0.59	24.62	1.00	10.63
0.42	0.45	62.26	1.11	7.62

Table 7.3: Best fitting experimental parameters to the Carreau-Yasuda model in experiments on model starch suspensions in G99.

Figure 7.8-b, shows the collapse of the simulation and experimental data as a function of the entrainment speed multiplied by the effective viscosity. Friction curves show a good collapse for starch suspensions. In this figure, the effective viscosities used for the experimental data are those from Figure 7.7-d, while the effective viscosities for simulation data were obtained from the numerical calculations. An effective viscosity was estimated by calculating an average viscosity over the Hertzian region. Note that for a Newtonian fluid, in the IEHL regime the friction coefficient increases as $\mu \propto \left(U\eta_f\right)^{\beta}$ and the ex-

ponent usually takes a value in the range of $\beta \in [0.40 - 0.55]$. This exponent is characteristic of the IEHL regime and does not depend on the viscosity of the lubricant. However, we observed that the slope of $U\eta_{eff}$ is higher for starch suspensions in comparison to the carrier fluid. A slope of 0.52 and 0.40 was obtained for the suspension and the carrier fluid, respectively.

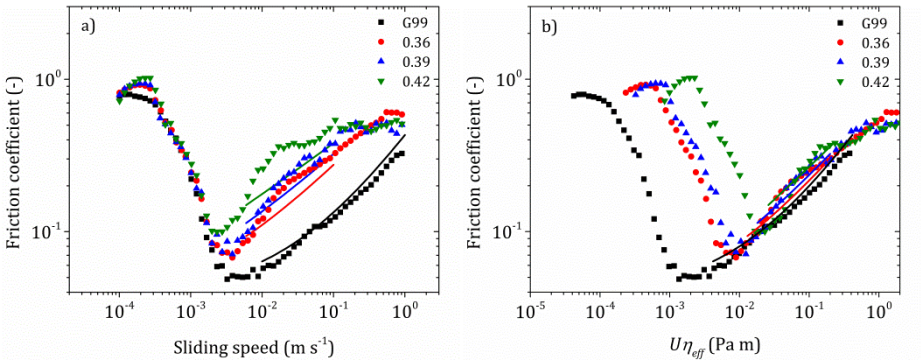

Figure 7.8: Comparison between experiments (symbols) and simulations in the IEHL regime (lines). Simulation parameters are listed in Table 7.3.

7.4. Conclusions

A rheological and tribological investigation is described on concentrated starch suspensions at different particle concentrations. Experiments are also compared with numerical simulations. Cornstarch suspensions exhibited shear thickening for three of the carriers investigated, namely water and two G/W mixtures (G87 and G99), being the onset of this phenomenon inversely related to the viscosity of the carrier. Suspensions containing a range of starch concentrations were prepared in G99 and SO100. Suspensions in G99 exhibited a more pronounced shear thickening as the concentration increased, and a second shear-thinning region related to the particles deformability at high shear rates. On the contrary, suspensions in SO100 did not exhibit any shear-thickening effect in the range of shear rates evaluated but displayed a shear-thinning behaviour whatever the volume fraction. The difference between these fluids is probably related to their polarity and electrostatic stabilization mechanism; the use of SO100 would promote interparticle attraction, inhibiting the appearance of shear thickening even at large particle concentrations.

Friction curves corresponding to the carrier fluids showed the signatures of a characteristic Stribeck curve. The main differences were found in the

boundary region, where friction increased with the carrier polarity, as it provides a different wettability on the hydrophobic PDMS plates. The critical sliding speed at the minimum friction coefficient evolved as expected; it shifted to lower values with increasing the fluid viscosity. The addition of cornstarch particles showed an increase in friction in the hydrodynamic region for all the carriers. However, the effect of the addition of particles in the boundary friction coefficient differs for each carrier, due to different van der Waals interactions. In the case of water (a highly polar carrier), the addition of particles reduced friction as compared to the friction curve of the carrier, while for SO100 (a non-polar carrier) their tribological behaviour was opposed and friction coefficient increased. This suggests that the particle-fluid interactions greatly affect the response; in water, starch particles would simply roll, while in SO100, the interparticle attraction would lead to the formation of aggregates. These aggregates would act as asperities in such small contact, leading to a friction increase with particle concentration in this region. For G99-based suspensions, friction curves collapse in the boundary lubrication and mixed regimes whatever the concentration, what suggests that only the carrier fluid goes through the contact at slow sliding speeds. On the other hand, if Stribeck curves are constructed and forced to collapse in the IEHL regime, the critical friction increases and shifts to higher values of $U\eta_{eff}$ with the suspension concentration. This shift was also observed to happen when the surface roughness is modified. In the present work it is attributed to a layer of deformed starch particles at the contact, hence effectively roughening the PDMS surfaces. Numerical simulations in the IEHL regime were compared with tribological experiments of G99-based starch suspensions. The agreement was not as good for suspensions as for the Newtonian carrier fluids without particles. This discrepancy is thought to be due to the formation of a different microstructure in rheological and tribological tests.

7.5. Supplementary material

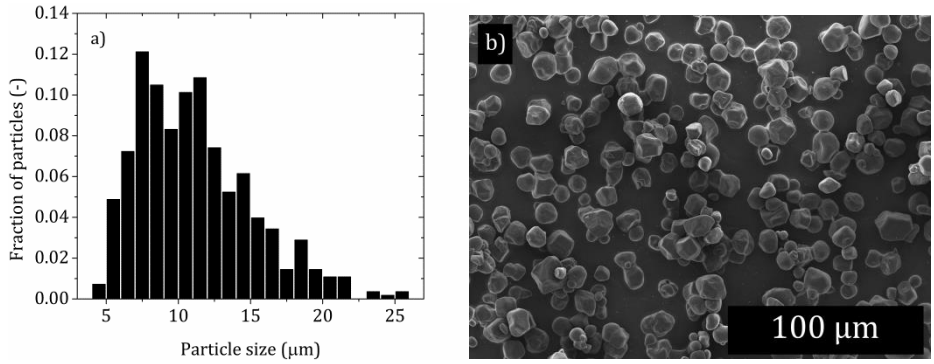

Figure S1: a) Cornstarch particle size distribution. The mean particle diameter is $\mu_m = 10.7$ μm and the standard deviation is $\sigma_m = 3.3$ μm. b) ESEM micrograph of cornstarch particles.

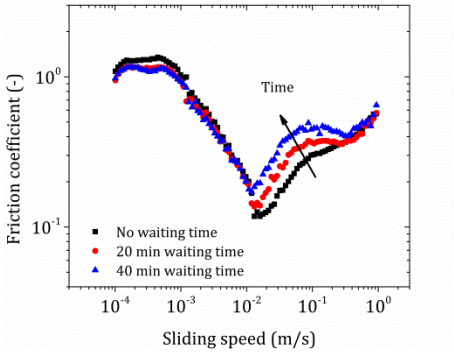

Figure S2: Friction coefficient μ as a function of sliding speed V curves for different aging times in G87 starch suspensions at $\phi = 0.36$.

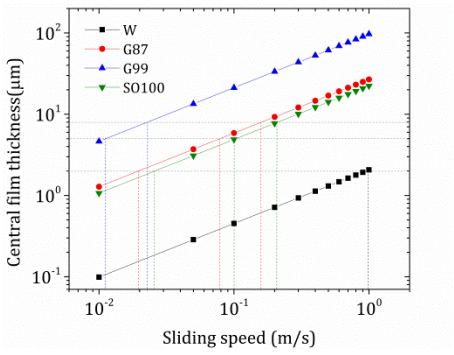

Figure S3: Calculated central film thickness h_c for several Newtonian fluids using regression equations from de Vicente et al. [55]. Horizontal lines correspond from bottom to top to central film thicknesses of h_c= 2, 5 and 8 μm.

7.6. References

[1] Macosko C W 1994 *Rheology: principles, measurements, and applications* (New York: VCH)

[2] Denn M M, Morris J F and Bonn D 2018 Shear thickening in concentrated suspensions of smooth spheres in Newtonian suspending fluids *Soft Matter* **14** 170–184

[3] Shenoy S S, Wagner N J and Bender J W 2003 E-FiRST: Electric field responsive shear thickening fluids *Rheol. Acta* **42** 287–294

[4] Lee Y S, Wetzel E D and Wagner N J 2003 The ballistic impact characteristics of Kevlar® woven fabrics impregnated with a colloidal shear thickening fluid *J. Mater. Sci.* **38** 2825–2833

[5] Crawford N C, Williams S K R, Boldridge D and Liberatore M W 2012 Shear thickening of chemical mechanical polishing slurries under high shear *Rheol. Acta* **51** 637–647

[6] Barnes H A 1989 Shear-thickening ("Dilatancy") in suspensions of nonaggregating solid particles dispersed in Newtonian liquids *J. Rheol.* **33** 329–366

[7] Gopalakrishnan V and Zukoski C F 2004 Effect of attractions on shear thickening in dense suspensions *J. Rheol.* **48** 1321–1344

[8] Melrose J R and Ball R C 2004 Continuous shear thickening transitions in model concentrated colloids—The role of interparticle forces *J. Rheol.* **48** 937–960

[9] Pednekar S, Chun J and Morris J F 2017 Simulation of shear thickening in attractive colloidal suspensions *Soft Matter* **13** 1773–1779

[10] Gamonpilas C, Morris J F and Denn M M 2016 Shear and normal stress measurements in non-Brownian monodisperse and bidisperse suspensions *J. Rheol.* **60** 289–296

[11] Maranzano B J and Wagner N J 2001 The effects of particle size on reversible shear thickening of concentrated colloidal dispersions *J. Chem. Phys.* **114** 10514–10527

[12] Guy B M, Hermes M and Poon W C K 2015 Towards a unified description of the rheology of hard-particle suspensions *Phys. Rev. Lett.* **115**

[13] Brown E, Zhang H, Forman N A, Maynor B W, Betts D E, DeSimone J M and Jaeger H M 2011 Shear thickening and jamming in densely packed suspensions of different particle shapes *Phys. Rev. E* **84**

[14] Lootens D, Damme H van, Hémar Y and Hébraud P 2005 Dilatant flow of concentrated suspensions of rough particles *Phys. Rev. Lett.* **95**

[15] Jamali S, Boromand A, Wagner N and Maia J 2015 Microstructure and rheology of soft to rigid shear-thickening colloidal suspensions *J. Rheol.* **59** 1377–1395

[16] Hsiao L C, Jamali S, Glynos E, Green P F, Larson R G and Solomon M J 2017 Rheological state diagrams for rough colloids in shear flow *Phys. Rev. Lett.* **119**

[17] Hsu C-P, Ramakrishna S N, Zanini M, Spencer N D and Isa L 2018 Roughness-dependent tribology effects on discontinuous shear thickening *Proc. Natl. Acad. Sci.* **115** 5117–5122

[18] Antosik A, Gluszek M, Zurowski R and Szafran M 2017 Influence of carrier fluid on the electrokinetic and rheological properties of shear thickening fluids *Ceram. Int.* **43** 12293–12301

[19] Swarna, Pattanayek S K and Ghosh A K 2017 Role of hydrogen bond interactions in water–polyol medium in the thickening behavior of cornstarch suspensions *Colloid Polym. Sci.* **295** 1117–1129

[20] Brown E and Jaeger H M 2014 Shear thickening in concentrated suspensions: phenomenology, mechanisms and relations to jamming *Rep. Prog. Phys.* **77** 046602

[21] Hoffman R L 1974 Discontinuous and dilatant viscosity behavior in concentrated suspensions. II. Theory and experimental tests *J. Colloid Interface Sci.* **46** 491–506

[22] Fall A, Huang N, Bertrand F, Ovarlez G and Bonn D 2008 Shear thickening of cornstarch suspensions as a reentrant jamming transition *Phys. Rev. Lett.* **100**

[23] Brady J F and Bossis G 1985 The rheology of concentrated suspensions of spheres in simple shear flow by numerical simulation *J. Fluid Mech.* **155** 105

[24] Fall A, Bertrand F, Hautemayou D, Mezière C, Moucheront P, Lemaître A and Ovarlez G 2015 Macroscopic discontinuous shear thickening versus local shear jamming in cornstarch *Phys. Rev. Lett.* **114**

[25] Fernandez N, Mani R, Rinaldi D, Kadau D, Mosquet M, Lombois-Burger H, Cayer-Barrioz J, Herrmann H J, Spencer N D and Isa L 2013 Microscopic mechanism for shear thickening of non-Brownian suspensions *Phys. Rev. Lett.* **111**

[26] Mari R, Seto R, Morris J F and Denn M M 2014 Shear thickening, frictionless and frictional rheologies in non-Brownian suspensions *J. Rheol.* **58** 1693–1724

[27] Tian Y, Jiang J, Meng Y and Wen S 2010 A shear thickening phenomenon in magnetic field controlled-dipolar suspensions *Appl. Phys. Lett.* **97** 151904

[28] Tian Y, Zhang M, Jiang J, Pesika N, Zeng H, Israelachvili J, Meng Y and Wen S 2011 Reversible shear thickening at low shear rates of electrorheological fluids under electric fields *Phys. Rev. E* **83**

[29] Brown E, Forman N A, Orellana C S, Zhang H, Maynor B W, Betts D E, DeSimone J M and Jaeger H M 2010 Generality of shear thickening in dense suspensions *Nat. Mater.* **9** 220–224

[30] Fall A, Bertrand F, Ovarlez G and Bonn D 2012 Shear thickening of cornstarch suspensions *J. Rheol.* **56** 575–591

[31] Stokes J R, Boehm M W and Baier S K 2013 Oral processing, texture and mouthfeel: From rheology to tribology and beyond *Curr. Opin. Colloid Interface Sci.* **18** 349–359

[32] Chen J 2009 Food oral processing—A review *Food Hydrocoll.* **23** 1–25

[33] Eliasson A-C 2004 *Starch in food structure, function and applications* (Cambridge: Woodhead Pub.)

[34] Myant C, Spikes H A and Stokes J R 2010 Influence of load and elastic properties on the rolling and sliding friction of lubricated compliant contacts *Tribol. Int.* **43** 55–63

[35] de Vicente J, Stokes J R and Spikes H A 2006 Soft lubrication of model hydrocolloids *Food Hydrocoll.* **20** 483–91

[36] Stokes J R, Macakova L, Chojnicka-Paszun A, Kruif C G de and Jongh H H J de 2011 Lubrication, adsorption, and rheology of aqueous polysaccharide solutions *Langmuir* **27** 3474–3484

[37] Yakubov G E, Branfield T E, Bongaerts J H H and Stokes J R 2015 Tribology of particle suspensions in rolling-sliding soft contacts *Biotribology* **3** 1–10

[38] Yakubov G E, Zhong L, Li M, Boehm M W, Xie F, Beattie D A, Halley P J and Stokes J R 2015 Lubrication of starch in ionic liquid–water mixtures: Soluble carbohydrate polymers form a boundary film on hydrophobic surfaces *Carbohydr. Polym.* **133** 507–516

[39] Morell P, Chen J and Fiszman S 2017 The role of starch and saliva in tribology studies and the sensory perception of protein-added yogurts *Food Funct.* **8** 545–553

[40] Olivares M L, Shahrivar K and Vicente J de 2019 Soft lubrication characteristics of microparticulated whey proteins used as fat replacers in dairy systems *J. Food Eng.* **245** 157–165

[41] Shahrivar K and de Vicente J 2014 Ferrofluid lubrication of compliant polymeric contacts: effect of non-homogeneous magnetic fields *Tribol. Lett.* **56** 281–92

[42] Hamrock B, Schmid S and Jacobson B 2004 *Fundamentals of fluid film lubrication* (CRC Press)

[43] Bombard A J F, Gonçalves F R, Shahrivar K, Ortiz A L and Vicente J de 2015 Tribological behavior of ionic liquid-based magnetorheological fluids in steel and polymeric point contacts *Tribol. Int.* **81** 309–320

[44] Johnston I D, McCluskey D K, Tan C K L and Tracey M C 2014 Mechanical characterization of bulk Sylgard 184 for microfluidics and microengineering *J. Micromechanics Microengineering* **24** 035017

[45] Dowson D 1962 A generalized Reynolds equation for fluid-film lubrication *Int. J. Mech. Sci.* **4** 159–170

[46] Katyal P and Kumar P 2012 Central film thickness formula for shear thinning lubricants in EHL point contacts under pure rolling *Tribol. Int.* **48** 113–121

[47] Katyal P and Kumar P 2014 New central film thickness equation for shear thinning lubricants in elastohydrodynamic lubricated rolling/sliding point contact conditions *J. Tribol.* **136** 041504

[48] Brown E and Jaeger H M 2012 The role of dilation and confining stresses in shear thickening of dense suspensions *J. Rheol.* **56** 875–923

[49] Hermes M, Guy B M, Poon W C K, Poy G, Cates M E and Wyart M 2016 Unsteady flow and particle migration in dense, non-Brownian suspensions *J. Rheol.* **60** 905–916

[50] Shimada Y, Yonezawa Y, Sunada H, Nonaka R, Katou K and Morishita H 2000 The development of an apparatus for measuring the adhesive force between fine particles. *J. Soc. Powder Technol. Jpn.* **37** 658–664

[51] Haynes W M 2014 *Handbook of Chemistry and Physics* (CRC Boca Raton)

[52] Raghavan S R, Walls H J and Khan S A 2000 Rheology of silica dispersions in organic liquids: new evidence for solvation forces dictated by hydrogen bonding *Langmuir* **16** 7920–7930

[53] Taylor S E 2013 Rheology and structure of cornstarch suspensions in water-poly(propylene glycol) mixtures *J. Dispers. Sci. Technol.* **34** 887–897

[54] Bongaerts J H H, Fourtouni K and Stokes J R 2007 Soft-tribology: Lubrication in a compliant PDMS–PDMS contact *Tribol. Int.* **40** 1531–1542

[55] de Vicente J, Stokes J R and Spikes H A 2005 The frictional properties of Newtonian fluids in rolling–sliding soft-EHL contact *Tribol. Lett.* **20** 273–86

[56] Dennis P. Kalman 2010 *Microstructure and rheology of concentrated suspensions of near hard-sphere colloids* (University of Delaware)

[57] Chatté G, Comtet J, Niguès A, Bocquet L, Siria A, Ducouret G, Lequeux F, Lenoir N, Ovarlez G and Colin A 2018 Shear thinning in non-Brownian suspensions *Soft Matter* **14** 879–893

[58] Hoffman R L 1972 Discontinuous and dilatant viscosity behavior in concentrated suspensions. I. Observation of a flow instability *Trans. Soc. Rheol.* **16** 155–173

[59] Egres R G and Wagner N J 2005 The rheology and microstructure of acicular precipitated calcium carbonate colloidal suspensions through the shear thickening transition *J. Rheol.* **49** 719–746

[60] Cwalina C D and Wagner N J 2014 Material properties of the shear-thickened state in concentrated near hard-sphere colloidal dispersions *J. Rheol.* **58** 949–967

[61] Dwyer-Joyce R S and Heymcr J 1996 The entrainment of solid particles into rolling elastohydrodynamic contacts *Tribology Series* (Elsevier) pp 135–140

[62] Wan G T Y and Spikes H A 1988 The behavior of suspended solid particles in rolling and sliding elastohydrodynamic contacts *Tribol. Trans.* **31** 12–21

[63] Timm K, Myant C, Spikes H A and Grunze M 2011 Particulate lubricants in cosmetic applications *Tribol. Int.* **44** 1695–1703

8. On the squeeze-strengthening effect in magnetorheology

8.1. Introduction

Magnetorheological (MR) fluids are field-responsive materials composed of magnetizable particles suspended in a non-magnetic carrier fluid. Soft magnetic materials with a high saturation magnetization and low coercivity (i.e., easily magnetized and demagnetized) are commonly used in the formulation of MR fluids, as carbonyl iron particles [1–4]. Particles in MR suspensions have micrometric size so that they present magnetic multi-domains. In the absence of an applied external magnetic field the fluid displays a Newtonian behaviour, while under the application of a magnetic field these domains align, and dipolar interactions give rise to particle aggregation in the field direction. The chains or columns of magnetic particles restrict the flow, resulting in a drastic increase in the viscosity of the suspension. Under these conditions rheological properties of MR fluids are generally assumed to obey a Bingham law. This process produces a reversible and quick transition from liquid to solid state which can be accompanied by an apparent yield stress τ_y, which is a field-dependent parameter.

MR suspensions have one of their main applications [2,3] in stress transfer devices, such as automotive brakes and clutches, thereby the yield stress obtained from these suspensions under a magnetic field is a key factor for

these purposes. In this sense, large values of yield stress are preferred, and it is desirable a great change in viscosity with a reduced particle concentration and magnetic field strength. In comparison with electro-rheological (ER) fluids, MR suspensions have improved functionality and require a lower electrical power input to attain yield stresses (typical value being $\tau_{y,MRF}$~100 kPa) about tenfold higher than in ER fluids [1,5]. This fact made MR fluids preferable to ER fluids in many applications.

These fluids can be employed in several operational modes [6,7], namely valve or flow mode [8,9], shear or torsional mode [10,11], squeeze mode [12,13], and combinations of these modes [14–16]. Among them, squeeze mode is the less understood but it has been proved to provide higher yield stresses compared to shear and valve modes. In squeeze flow the sample is usually set between parallel plates, one stationary and other movable, that approach at a constant speed, or at a given frequency and axial displacement in oscillatory squeeze [17], narrowing the gap. In any case, this compression provokes the appearance of a normal force that can be measured. The squeeze mode undoubtedly affects the final microstructure of the magnetic aggregates and so the MR performance of the material.

The squeeze flow can be applied in constant-area and constant-volume modes [18,19]. In the former, part of the sample is forced to abandon the plate area as the compression progresses. The compression of ER fluids was first and broadly investigated than in the case of their analogous MR fluids [20–22]. Moreover, the main consequences of this type of flow acting on ER fluids can be also applicable to MR fluids. In the case of ER fluids, if the electric field is applied during compression, particles remain in the gap while the carrier fluid is squeezed out of the gap [23,24]. This is called sealing or condensation effect and gives rise to higher concentrations within the plates, what could interfere in the apparent squeeze-strengthening effect. Moreover, some particles might leave the gap together with the fluid even if the field is applied, so that the volume fraction is unfortunately undetermined. This problem is avoided in the constant-volume mode as the sample is always below the limits of the plates. During compression the contact area between the sample and the plates increases, but the sample volume is constant, so that the volume fraction does not change in this stage [25–27].

The study of rheological properties of MR fluids under compression is a topic of current interest in the field. In view of the squeeze-strengthening effect, the material becomes stronger when it is compressed under field. Tang

et al. [28] first ascribed the super-strong behaviour of MR fluids after a compression-assisted-aggregation (in the field direction) to the restructuring of particles into shorter, thicker and stronger magnetic columns. The yield stress obtained in squeeze mode was one order of magnitude higher than the analogous without compression (i.e., in direct-shear or valve modes). Other experimental works also confirm the increase in yield stress [12,17,27,29,30], while some authors have found no change in the magnetorheological response upon compression [7,14]. While the compressive flow of these fluids has been broadly studied in experimental works, squeeze flow theoretical modelling and simulations are instead limited. Ghaffari et al. [31] reviewed the simulation models used to study the behaviour of MR fluids under different flow modes, and classified them into continuum or discrete approaches. While the former approach considers the fluid as homogeneous, discrete models are more realistic as they differentiate between particles and fluids. In this sense, particle-level simulations require a higher computational cost compared to continuum approaches, but offer more reliable results to apply to the design of devices using MR fluids. Continuum approaches make use of appropriate rheological models [32] (being the Bingham plastic and Herschel-Bulkley models the most commonly used) or structural ones [33,34], for which the characteristics of the suspension (e.g., volume fraction, particle size or magnetic field) affect the yield stress and viscosity. Ruiz-López et al. [35] proposed a micromechanical model to predict the response of magnetorheological suspensions under slow compression, and validated it with experiments at small deformations and low particle concentrations. Later, they performed particle-level simulations of model MR fluids subjected to squeeze mode [36], and found discrepancies at high concentrations with the yield compressive stress/concentration dependence obtained from experiments.

In this work we studied MR fluids subjected to squeeze tests followed by shear stress ramps. The yield stress was obtained for several compressive strains and both constant-volume and constant-area conditions were explored. Differences in the squeeze strengthening effect between both operation modes are ascribed to the densification occurring in the constant-area mode. Moreover, we explored the effect of the carrier fluid and the significance of the field gradient during compression of MR fluids in constant-volume tests. Experimental results were complemented with particle-level simulations, where the compression (and later shear) of randomly distributed magnetic particles under constant volume and area was conducted.

8.2. Materials and Methods

8.2.1. Materials

MR fluids investigated in this work were prepared by dispersion of carbonyl iron microparticles in silicone oil at a particle volume fraction of $\phi = 0.05$. The carbonyl iron particles were a gift from BASF SE (Germany). In particular, we used HQ grade particles with mean particle size of 1.5 μm and density $7.874\ \mathrm{g \cdot cm^{-3}}$. The silicone oil was purchased from Sigma-Aldrich. It has a viscosity of $20\ \mathrm{mPa \cdot s}$, and a density of $0.95\ \mathrm{g \cdot cm^{-3}}$.

In the preparation of the MR fluids, the particles were first dispersed in the silicone oil using a spatula. Then, the suspension was subjected to ultrasounds for several minutes. Next, a centrifugal mixer was used to completely homogenize the MR suspension, and finally ultrasounds were again employed. This preparation protocol was repeated before each experiment with fresh new samples, because this system destabilizes as a consequence of particle sedimentation.

In a second part of this work we used glycerol, instead of silicone oil, to study the effect of surface tension in the compression behaviour of MR fluids. Glycerol was purchased from Sigma-Aldrich (99 % w/w; viscosity $0.58\ \mathrm{Pa \cdot s}$; density $1.261\ \mathrm{g \cdot cm^{-3}}$) and used without further purification. The sample preparation is the same than that used in the preparation of MR fluids in silicone oil.

8.2.2. Rheological tests

An Anton Paar magnetorheometer (MCR 501, MRD70-SN81112937) was used in plate-plate configuration (radius $R = 10\ \mathrm{mm}$) using sandblasted plates to prevent wall slip. Plates used in this study were non-magnetic and this is the reason why we worked with the external magnetic field instead of the internal one. The testing temperature was set at 25 °C. First, the sample was loaded onto the lower plate. Next, the upper plate was displaced downwards to reach the measurement position at an "initial" gap separation h_i.

Once the sample was loaded onto the rheometer base, the magnetic field was suddenly applied ($H_0 = 133\ \mathrm{kA \cdot m^{-1}}$ for most measurements except in Subsection 8.5.5., where $H_0 = 11.9\ \mathrm{kA \cdot m^{-1}}$) and the test started. The protocol involved three steps during which the magnetic field is maintained at the

value previously established. i) First, the sample was left to rest between the plates in the absence of shear during 60 s. During this step the particles became magnetized and interacted to form elongated structures in the field direction. ii) Second, in the compression step, the upper plate was displaced at a commanded speed of 1 μm · s^{-1} up to the desired "final" gap h_f, thus reaching a total compression strain that can be calculated as $\varepsilon_T = (h_i - h_f)/h_i$. During this step the field-induced structures were squeezed. iii) Finally, a steady shear flow test was performed in the last step by steeply increasing the stress from 1 to 10000 Pa in order to break the field-induced structures and determine the yield stress τ_y of the MR fluid. The error bar of the measured τ_y was significantly reduced by increasing the density of stress points. Preliminary tests demonstrated that the yielding region was approximately in the stress range of 250-800 Pa whatever the level of compression. The experimental data reported in this chapter are the average of three repetitions with fresh new samples.

In the slow-compression tests, the deformation at a given gap h was determined by the compression strain $\varepsilon(h) = (h_i - h)/h_i$, where h_i is the "initial" gap separation. Therefore, the total deformation was quantified as follows $\varepsilon_T = (h_i - h_f)/h_i$, where h_f is the final gap separation. In this work, the compression step was carried out in both constant-area and constant-volume modes described below (see Figure 3.3).

Experiments under constant volume ($V = 110$ μL) were performed by squeezing the MR fluid at a constant approaching speed of 1 μm · s^{-1} from a given initial gap h_i to a final gap of $h_f = 300$ μm. Note that in the final position the sample volume completely fulfils the space between both plates. By changing the initial gap h_i, different total strains ε_T were achieved (see Table 8.1). The maximum h_i value investigated in this work was $h_i = 1000$ μm, that corresponds to a total strain of $\varepsilon_T = 0.7$.

Experiments under constant area ($S = \pi \cdot 10^{-4}$ m^2, i.e., the plate area) were performed by squeezing the MR fluid from an initial gap of $h_i = 300$ μm up to a given final gap h_f. During compression the plate area in contact with the sample does not vary, and part of the sample volume is forced to abandon the gap between the plates. Note that measurements with smaller sample volumes were not reproducible. By changing the final gap h_f, different total strains ε_T were achieved. The minimum h_f value investigated in this work was $h_f = 60$ μm, which corresponds to $\varepsilon_T = 0.8$.

Table 8.1 summarizes the total strains ε_T applied to the sample before starting the shearing test under constant-volume and constant-area tests, respectively.

	Constant volume		**Constant area**	
$\boldsymbol{\varepsilon_T}$	**Initial gap**, h_i (μm)	**Final gap**, h_f (μm)	**Initial gap**, h_i (μm)	**Final gap**, h_f (μm)
0	300	300	300	300
0.1	333	300	300	270
0.2	375	300	300	240
0.3	429	300	300	210
0.4	500	300	300	180
0.5	600	300	300	150
0.6	750	300	300	120
0.7	1000	300	300	90
0.8	-	-	300	60

Table 8.1: Experimental conditions as a function of the required total strain ε_T for constant-volume and area tests.

The yield stress determination may result greatly affected by the wall slip phenomenon so that corrections were performed when needed to obtain the true rheograms. Furthermore, similarly to the shear yield stress in the flow tests, in squeeze experiments a compressive yield stress is defined as the normal force in the low-strain region divided by the area of sample subjected to squeeze. A deeper explanation of the compressive yield stress appears in Section 8.3.

8.3. Theory

The slow-compression of MR fluids has been extensively studied in the literature [13,28,37]. Generally speaking, the behaviour of concentrated MR fluids is well described by a Continuous media Theory (CT) [33], while the behaviour of dilute MR fluids is described by Micromechanical Models (MM) [35].

For concentrated MR fluids in the filtration dominated regime (slow enough velocities) the Continuous media Theory (CT) predicts that the normal force F_{CT} is a power-law function of the compressive strain ε. In the case of constant-volume tests, according to Ruiz-López et al. [33] this normal force is given by:

$$F_{CT} = \frac{2\pi\tau_y R^3}{3h} = \frac{2\tau_y V^{3/2}}{3\sqrt{\pi}h_i^{5/2}(1-\varepsilon)^{5/2}}. \tag{8.1}$$

However, for constant-area tests this equation takes the form:

$$F_{CT} = \frac{2\pi\tau_y R^3}{3h} = \frac{2\tau_y S^{3/2}}{3\sqrt{\pi}h_i(1-\varepsilon)}. \tag{8.2}$$

In the case of dilute MR fluids, a Micromechanical Model applies. The particles are assumed to be monodisperse spheres that under the presence of an external magnetic field form single-particle width straight chains in the field direction. Under a micromechanical perspective, the normal force F_{MM} scales with ε as

$$F_{MM} = \frac{27}{32}\phi\mu_0\mu_{cr}\beta_a^2 H_{loc}^2 \frac{V_0}{h_i}\frac{1}{(1-\varepsilon)^2}, \tag{8.3}$$

where ϕ is the particle volume fraction, $\mu_0 = 4\pi 10^{-7}$ and $\mu_{cr} = 1$ are the magnetic permeability of the vacuum and the relative permeability of the continuous medium, β_a is the contrast factor referred to the aggregates and H_{loc} is the local field. In contrast to the equation of normal force in CT, Equation 8.3 is valid for both constant-volume and constant-area tests. It is important to note that the general expression can be slightly modified if the initial volume fraction ϕ_0 has to be used instead. For constant volume $V_0 = V$ and $\phi = \phi_0$, while for constant area $V_0/h_i = S_0 = S$, and $\phi = \phi_0/(1-\varepsilon)$.

In the calculation of β_a it is necessary to know the magnetic permeability of the aggregates μ_a. In this chapter we use a Mean Field Approach (i.e., Böttcher's formula) to relate the particle volume fraction within the aggregates ϕ_a, the effective magnetic permeability of the aggregates μ_a and the relative magnetic permeability of the particles μ_{pr}:

$$\beta_a = \frac{\mu_a - \mu_{cr}}{\mu_a + 2\mu_{cr}}, \qquad \frac{\mu_a - \mu_{cr}}{3\mu_a} = \phi_a \frac{\mu_{pr} - \mu_{cr}}{\mu_{pr} + 2\mu_{cr}}. \tag{8.4}$$

In the particular case in which the aggregate is assumed to have cylindrical shape, the particle volume fraction within the aggregates ϕ_a is simply given by:

$$\phi_a = \frac{\frac{4}{3}\pi R^3}{\pi R^2 h} = \frac{\frac{4}{3}\pi R^3}{\pi R^2 2R} = \frac{2}{3}. \tag{8.5}$$

The relative magnetic permeability of the particles μ_{pr} is calculated here using the Fröhlich-Kennelly equation [38]:

$$\mu_{pr}(H_0) = 1 + \frac{(\mu^0 - 1)\frac{M_s}{H_0}}{(\mu^0 - 1) + \frac{M_s}{H_0}}. \tag{8.6}$$

The relative initial magnetic permeability and the saturation magnetization were taken as $\mu^0 = 40$ and $M_s = 1550\ \mathrm{kA \cdot m^{-1}}$, respectively [39]. The relative magnetic permeability of the particles at the external magnetic field used in the experiments was $\mu_{pr} = 9.97$. By solving the Böttcher's equation, $\mu_a = 5.84$, and $\beta_a = 0.617$.

At this stage it is very important to note that Equation 8.3 is valid for both constant-volume and constant-area operation modes. In both CT and MM models, the normal force can be normalized by a pre-factor A, that corresponds to the low-strain normal force plateau: $F = A/(1-\varepsilon)^B$. In summary, while for CT the normal force scales with $(1-\varepsilon)^{-5/2}$, in MM it scales according to $(1-\varepsilon)^{-2}$. In the following section we will compare experimental data with MM predictions.

8.4. Squeeze simulations

Similarly to the experimental case, squeeze simulations were performed in constant-area and constant-volume modes. Particle-level simulations were employed and Langevin equation (Equation 3.16) was solved at each time step. It is the equation of motion that better describes the interactions between Brownian particles, as it contains terms accounting for the deterministic motion of the particles but also additional stochastic forces. The simulation code contains three steps that are equivalent to the experimental protocol: particle structuration, squeeze and shear, while considering a constant magnetic field of $H_0 = 177\ \mathrm{kA \cdot m^{-1}}$ during the whole protocol.

Brownian dynamics simulations were carried out to simulate systems of 1000 monodisperse spherical magnetic particles. The volume fraction was varied among $\phi = 0.05$ and 0.30. We used periodic boundary conditions in x and y directions, and two initial gaps h_i were studied, namely 20 and 30 times the mean diameter σ_m (i.e., $h_i = 20\ \sigma_m, 30\ \sigma_m$), which is employed as a length scale. So that, depending on the initial gap and the volume fraction, the other two dimensions of the simulation box can be easily determined. Particles are

randomly distributed in the simulation box and overlap is forbidden. The magnetic dipoles of the particles are supposed to be equal at the onset of the simulation and oriented with the magnetic field, it is, in *z* axis.

Local magnetic field $\boldsymbol{H}_{\boldsymbol{loc}_i}$ is considered in the calculation of the magnetic force between pairs of particles (see Equations from 8.7 to 8.10). In this sense, for a given particle its magnetic force is due both to the external magnetic field $\boldsymbol{H_0}$ and the rest of dipolar contributions from other particles $\boldsymbol{H}_{\boldsymbol{m_j}}$ that surround it at distances lower than a stablished cut-off.

$$\boldsymbol{m_i} = \frac{\pi}{2}\beta \boldsymbol{H}_{\boldsymbol{loc}_i}\sigma_i^3 \,, \tag{8.7}$$

$$\boldsymbol{H}_{\boldsymbol{loc,i}} = \boldsymbol{H_0} + \sum_{j\neq i}^{N_{pc}} \boldsymbol{H}_{\boldsymbol{m_j}} \,, \tag{8.8}$$

$$\boldsymbol{H}_{\boldsymbol{m_j}} = \frac{3(\boldsymbol{m_j}\cdot\hat{\boldsymbol{r}})\hat{\boldsymbol{r}} - \boldsymbol{m_j}}{r_{ij}^3} \,, \tag{8.9}$$

$$\boldsymbol{F}_{\boldsymbol{ij}}^{\boldsymbol{m}} = \frac{3}{4}\frac{\mu_0\mu_{cr}}{\pi}\left[\frac{(\boldsymbol{m_i}\cdot\boldsymbol{m_j})\boldsymbol{r_{ij}} + (\boldsymbol{m_i}\cdot\boldsymbol{r_{ij}})\boldsymbol{m_j} + (\boldsymbol{m_j}\cdot\boldsymbol{r_{ij}})\boldsymbol{m_i}}{r_{ij}^5} - 5\frac{(\boldsymbol{m_i}\cdot\boldsymbol{r_{ij}})(\boldsymbol{m_j}\cdot\boldsymbol{r_{ij}})\boldsymbol{r_{ij}}}{r_{ij}^7}\right] \tag{8.10}$$

Apart from magnetic interactions, Stoke's drag (Equation 8.11) and Brownian forces (Equation 8.12) are taken into account, as well as an exponential repulsive force that decays with particle separation (Equation 8.13) as expressed below:

$$\boldsymbol{F_i^S} = -\xi_i\left(\frac{d\boldsymbol{r_i}}{dt} - \boldsymbol{u_i^\infty}\right) = -3\pi\eta\sigma_i\boldsymbol{v_i} \,, \tag{8.11}$$

$$\boldsymbol{f_B^*} \propto \sqrt{\frac{k_BT}{\sigma_m F_0}}\sqrt{\frac{\sigma_i^*}{\Delta t^*}} \,, \tag{8.12}$$

$$\boldsymbol{F_{ij}^r} = F_0 e^{-k(r_{ij}-(\sigma_i+\sigma_j)/2)}\hat{\boldsymbol{r}}_{\boldsymbol{ij}} \,, \tag{8.13}$$

where $\xi_i = 3\pi\eta\sigma_i$ is the friction coefficient of particle i, η is the fluid viscosity and σ_i is the particle diameter; $k_B = 1.381\cdot10^{-23}\,\mathrm{J\cdot K^{-1}}$ is the Boltzmann constant and T the absolute temperature expressed in kelvin; F_0 is the force

scale, $k = 100$ and $r_{ij}$is the center-to-center distance between particles i and j.

Langevin equation used within the simulation code neglects inertia so that it takes the form of

$$\xi_i \frac{d\boldsymbol{r_i}}{dt} = \xi_i \boldsymbol{u_i^{\infty}} + \boldsymbol{F_i^m} + \boldsymbol{F_i^r} + \boldsymbol{F^b} \,. \tag{8.14}$$

In order to solve Equation 8.14 it is convenient to make it dimensionless by means of scaling parameters showed in Table 3.5.

The inertialess Langevin equation (Equation 8.14) is solved at each time step and the new particle positions are considered in the next time step. In the structuration step the main contribution to the particle movements comes from magnetic interactions. The normalized time for structuration is sufficient to obtain steady states in the magnetic energy, normal stress, normal force and number of neighbours. After that, the particle configuration is subjected to the squeeze step, in which the gap is steadily forced to diminish at a given velocity, and so the height of the simulation box. The time during which the gap diminishes depends on the required level of deformation. In constant-volume simulations it provokes an enlargement in the other dimensions of the simulation box, so that particles have to fit in a modified simulation box that keeps the initial volume and, as a consequence, the volume fraction does not vary. On the contrary, in constant-area simulations the gap is diminished, while the other two dimensions preserve their initial lengths so that the simulation box is smaller. As it occurs in the experimental case, particles are confined in the area subjected to the magnetic field and cannot abandon the new simulation box, so that the volume fraction increases with ε in constant-area conditions. Once a given deformation is achieved, the shear flow is activated at constant shear rates. The effect of the compression of the magnetic structures in the static yield stress under shear is compared for both types of simulations.

8.5. Results and Discussion

8.5.1. Squeeze flow behaviour of MR fluids

The compression curves for constant-volume tests ($V = 110$ μL) are shown in Figure 8.9-a. Accordingly with the equation of normal force in micromechanical models (Equation 8.3), for a given ε_T, the experimental normal force F_N

increases with the compressive strain ε. Moreover, the increase of the initial gap h_i at a given deformation provokes a decrease in F_N, again in agreement with Equation 8.3.

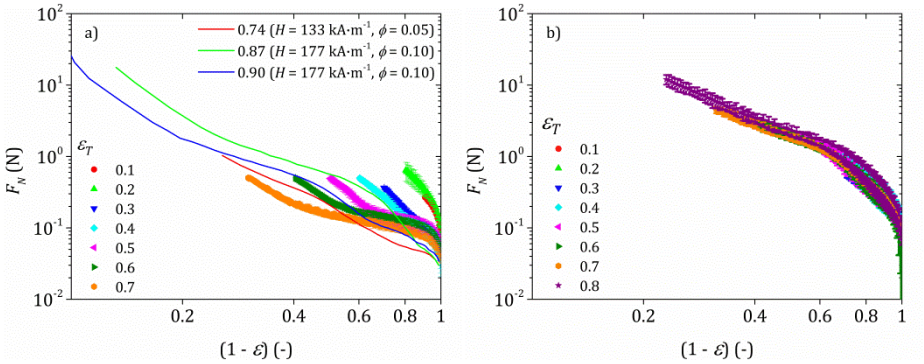

Figure 8.9: Compression curves for $\phi = 0.05$ suspensions in silicone oil at $H_0 = 133$ kA · m^{-1}. a) Constant-volume tests. $V = 110$ µL. Lines correspond to constant-volume experiments from Ruiz-López et al. [35] ($V = 20$ µL, other experimental conditions are specified within the legend). b) Constant-area tests.

In Figure 8.9-a we also plot the experimental results by Ruiz-López et al. [35] for a range of concentrations and magnetic field strengths. As observed, in our experiments we do not reach such a large total strain, essentially because we imposed a limitation over the final gap of $h_f = 300$ µm in order to perform reproducible steady shear flow tests after the compression step. Note that to apply a larger ε_T we would need to increase h_i above one millimetre. However, it is not possible due to the surface tension of the silicone oil. Despite the fact that it is not possible to quantitatively compare our results with those in the literature, there still exists a reasonably good qualitative agreement.

The compression curves for constant-area tests are shown in Figure 8.9-b. In this case the normal force F_N again increases with ε, but in contrast to what happened in the case of constant-volume tests, the curves collapse. This was expected because the initial gap did not change in the constant-area tests. This result was expected in accordance to the micromechanical model (note that normal force is independent of the initial gap in Equation 8.3for the constant-area case).

As stated before, the Micromechanical Model (Equation 8.3) is applicable in both constant-volume and constant-area modes. Therefore, the next step was to compare our experimental data with the theoretical MM predictions.

For this aim, the curves must be scaled by the low-strain normal force plateau, A. Theoretically, a straight line with slope of -2 is expected in a double logarithmic representation.

The theoretical expression of this parameter is $A = \frac{27}{32}\phi\mu_0\mu_{cr}\beta_a^2 H_{loc}^2 \frac{V_0}{h_i}$. It can be also called yield normal force F_Y as it is the value of the force in the limit of no deformation. Accordingly, by dividing the yield normal force by the surface area of the sample, the yield compressive stress can be obtained as $\tau_{YC} = \frac{27}{32}\phi\mu_0\mu_{cr}\beta_a^2 H_{loc}^2$, that again is the normal stress in the limit of no deformation. This definition is analogous to that of the yield stress τ_y in shear mode, it is, the shear stress τ in the limit of no shear rate $\dot{\gamma}$.

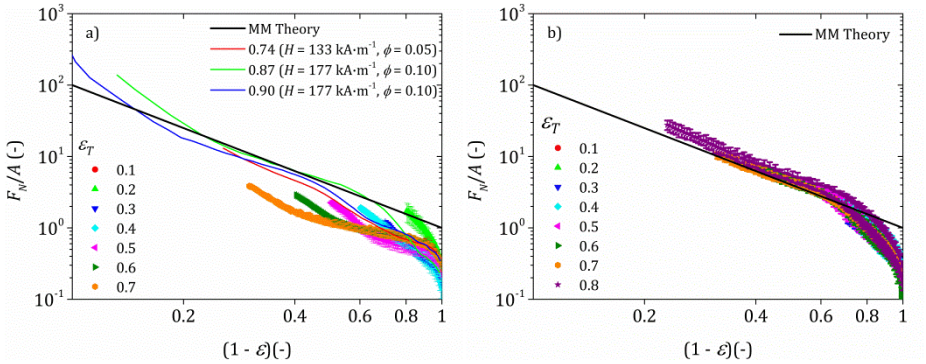

Figure 8.10: Dimensionless compression curves for $\phi = 0.05$ suspensions in silicone oil at $H_0 = 133$ kA · m^{-1}. a) Constant-volume tests. $V = 110$ µL. Lines correspond to constant-volume experiments from Ruiz-López et al. [35] ($V = 20$ µL, other experimental conditions are specified). b) Constant-area tests. Straight black line corresponds to the MM prediction.

For constant-volume experiments A takes a different value for each initial gap. However, for constant-area measurements all the curves are made dimensionless by dividing the normal force by the same value of A. This is because V_0/h_i is constant whatever the total strain ε_T in constant-area tests.

In Figure 8.10-a we show results for the constant-volume tests together with experimental data from Ruiz-López et al. [35] and theoretical MM predictions. Qualitatively speaking the experimental data obtained in this work are in good agreement with previous experiments, especially taking into account that experimental conditions are different (e.g., sample volume, magnetic field strength, particle volume fraction and total compressive strain). Because of the limited strain range explored, a fitting of our experimental da-

ta to $F = A/(1-\varepsilon)^B$ is not feasible. Nevertheless, experiments in this work tend to asymptotically approach the theoretical line.

In Figure 8.10-b we show analogous curves for constant-area tests. Experimental curves collapse reasonably well and there is a good agreement with the theoretical prediction for $\varepsilon > 0.2$. Deviations for small ε values are expected to be due to inertia [35].

8.5.2. Steady shear flow of compressed MR fluids

The steady shear rheological response of the previously compressed MR fluids are shown in Figure 8.11 in the form of shear stress τ as a function of shear rate $\dot{\gamma}$. Curves included in Figure 8.11 correspond to different ε_T values both for constant-volume (Figure 8.11-a) and constant-area (Figure 8.11-b) experiments. In this representation, the yield stress τ_y can be easily identified by the sudden jump in shear rate when gradually increasing the shear stress. A common feature of both test modes is the increasing dependence of the flow curves with the compressive strain reached in the previous squeeze step. This is more evident in the constant-area case, as a consequence of the increase in particle volume fraction with ε_T.

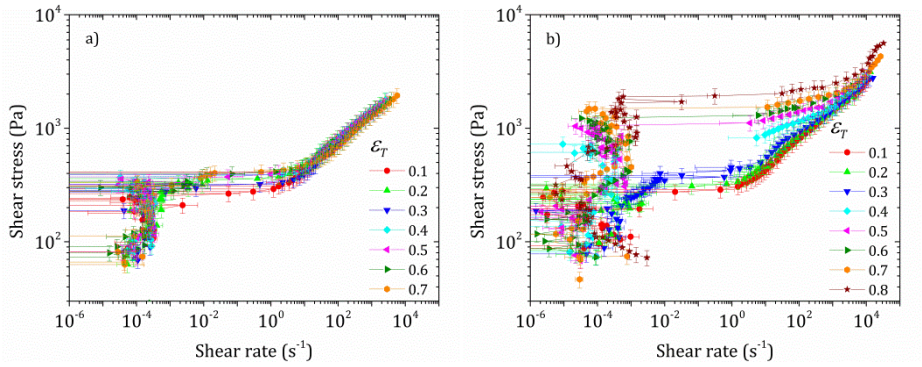

Figure 8.11: Flow curves at several final compressive strains for a) constant-volume, and b) constant-area experiments. Samples were silicone oil-based suspensions with $\phi = 0.05$, $H_0 = 133$ kA $\cdot$ m^{-1}.

In Figure 8.12 we show the yield stress τ_y -as obtained from Figure 8.11- as a function of the total strain ε_T reached in the compression step. In the case of constant-volume tests, τ_y experiences a minor increase with ε_T if compared to the case of constant-area tests for which the increase is clearly more pronounced. This observation can be explained in terms of a densification process under constant area as follows (see Figure 8.13). It is worth highlight-

ing that in the particular case of constant-volume tests the volume fraction of the MR fluid subjected to the shearing process is always the same. However, in the case of constant-area tests, this volume fraction changes during compression. Specifically, the particle concentration is expected to increase during compression because the particles remain within the polar regions of the magnetocell while the carrier is filtrated in the radial direction. Such increase in the volume fraction with ε_T is coherent with the increase of τ_y with ε_T observed and reported for constant-area experiments in Figure 8.12.

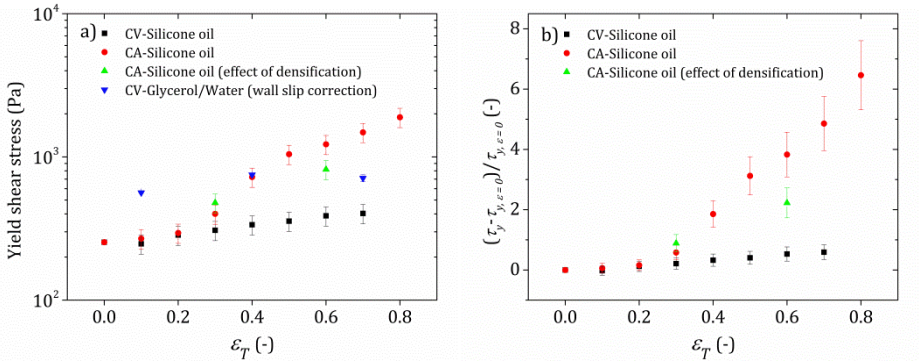

Figure 8.12: a) Yield shear stress and b) relative yield stress for constant-volume (CV) and constant-area (CA) experiments as a function of the final compressive strain. Black squares and red circles refer to experiments carried out with an initial volume fraction of $\phi_i = 0.05$, and the magnetic field was applied during the whole tests. On the contrary, green upward triangles account for experiments with initial (and final) volume fractions of $\phi_i =$ 0.071 and 0.125, for $\varepsilon_T = 0.3$ and 0.6, respectively. In this case magnetic field was not applied during the compression process (i.e., $\phi_f = \phi_i$) and the surplus of sample after this step was removed and substituted by silicone oil, in order to mimic red circles experiments at the corresponding values of ε_T. Blue downward triangles belong to experiments with $\phi_i = 0.05$ in a glycerol and water mixture (prepared with the same viscosity that silicone oil), after applying the wall slip correction.

8.5.3. Effect of the densification process in constant-area experiments

As described in the section above, the difference between constant-volume and constant-area experiments may come from the densification in the gap during compression that may occur in constant-area tests. In order to elucidate the importance of this process, we designed another test. MR fluids were prepared at concentrations of $\phi = 0.071$ and $\phi = 0.125$. It is worth noting that these concentrations correspond to the compression-induced volume fractions between the plates in constant-area tests for an initial sample vol-

ume fraction of $\phi_i = 0.05$ at $\varepsilon_T = 0.3$ and 0.6, respectively, when the magnetic field is applied (see central column in schematic of Figure 8.13). Then, the prepared MR fluids were loaded onto the rheometer base to fully fill an initial gap of $h_i = 300$ µm. In the absence of a magnetic field, the MR fluid was then compressed up to a final gap of $h_f = 210$ and $h_f = 120$ µm, respectively. After that, the surplus of sample was removed and replaced by silicone oil. Finally, the steady shear test was conducted. In that manner, it is assured that the sample concentration during the shear step is the same that the one obtained when the starting volume fraction was 0.05 and the magnetic field is applied also during squeeze, i.e., experiments showed in the previous subsections.

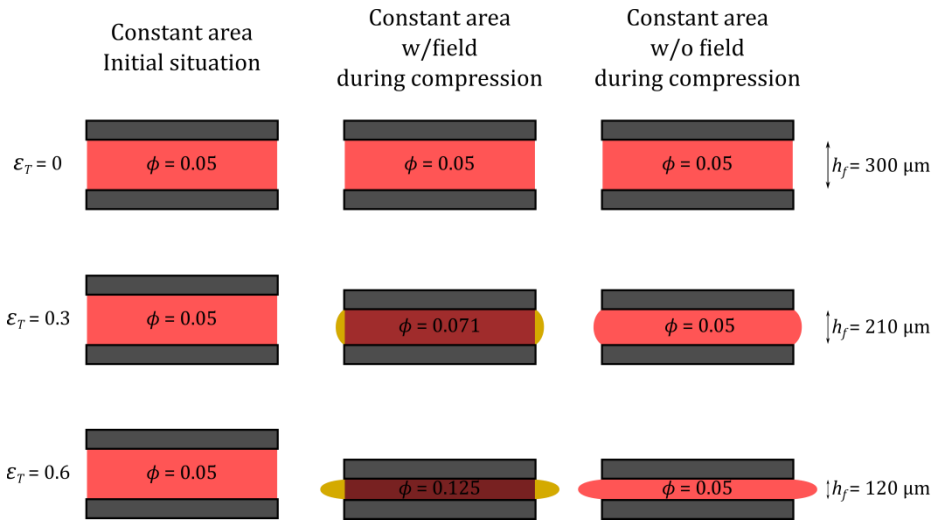

Figure 8.13: Schematic of the change in volume fraction as a function of compressive strain in constant-area experiments. In the second column magnetic field is on during the whole process, so that magnetic particles remain between the plates with the subsequent increase in volume fraction, depicted with a darker colour. In contrast, the last column shows the case of not applying magnetic field during compression, hence both the carrier and the particles are expelled from the plate area.

From these steady shear flow tests the yield stress was obtained and plotted in Figure 8.12. Note that the difference between the two constant-area tests was simply the presence or not of a field during the compression process, so this truly addresses the squeeze-strengthening effect. The results demonstrate that the local increase in concentration after the compression step in constant-area tests is the main contribution to the total yield stress as the values are again above the yield stress obtained in constant-volume experiments. Discrepancies with the red point at $\varepsilon_T = 0.6$ may be due to an ex-

cessive removal of sample at the end of the squeeze step, that would mean a lower magnetic particle concentration and would explain the lower τ_y.

8.5.4. Influence of the carrier fluid in the compression behaviour of MR fluids in constant-volume tests

As observed in Figure 8.10-a, corresponding to constant-volume experiments with silicone oil, there is a shoulder in most of the curves at small deformations, which could be associated to surface tension effects, wall slip, wettability or sedimentation. In order to evaluate the importance of the carrier fluid employed in the compression process we decided to prepare a new set of MR fluids based on glycerol.

In Figure 8.14-a we show the normalized normal force as a function of the compressive strain in constant-volume essays. All the curves are above the theoretical MM prediction. This is in contrast to the case of silicone oil suspensions and can be related to higher surface tension in glycerol. The curve corresponding to the highest compressive strains (i.e., the largest initial gap) is closer to the theoretical line, maybe because edge effects are reduced in comparison with lower gaps. In Figure 8.14-b we show the rheograms of the compressed glycerol-based MR fluids. As observed, there is a clear shoulder evidencing wall slip. In this case the breaking process is smoother if compared to silicone oil-based MR fluids.

In order to give a better insight we decided to prepare MR fluids in glycerol (87 % w/w, Scharlau)-water mixtures (80.59:19.41 % w:w) with exactly the same viscosity as the silicone oil employed before (19 mPa). By doing this, the influence of viscosity can be discarded. In Figure 8.15-a we present the normal force curves for three different total compressive strains ($\varepsilon_T =$ 0.1, 0.4 and 0.7) at four different final gaps ($h_f =$ 0.1, 0.2, 0.3 and 0.4 mm). In this sense, the volume of sample was varied proportionally to the final gap in order to the sample completely fill the volume between plates at the beginning of the shear step. Four different gaps where tested in order to correct the wall slip in the steady shear process [40]. As expected, there is not a difference for the h_f studied. It can be explained from Equation 8.3 as the volume of sample is proportional to the final gap, so that at a given ε_T the ratio V_0/h_f is the same for each measurement condition and the normal force does not change. For the same reason, higher final compressive strains result in lower

normal forces as it appears in the figure, and they increase with the compressive strains:

$$F_{MM} \propto \frac{V_0}{h_i}\frac{1}{(1-\varepsilon)^2} = \frac{V_0(1-\varepsilon_T)}{h_f}\frac{1}{(1-\varepsilon)^2} = \frac{C(1-\varepsilon_T)}{(1-\varepsilon)^2}. \qquad (8.15)$$

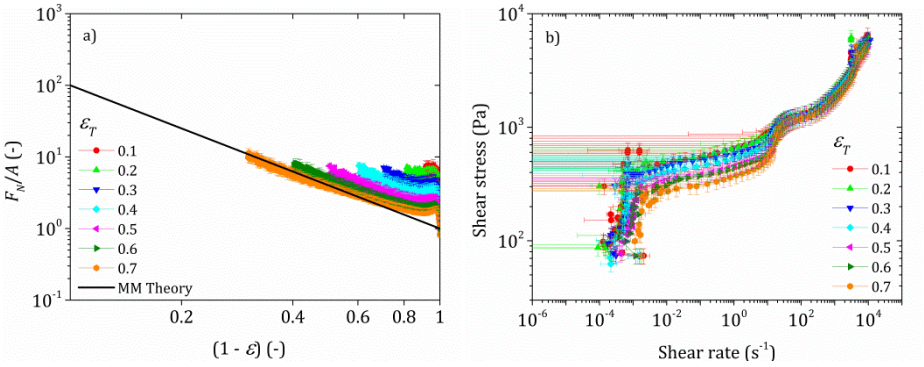

Figure 8.14: a) Normalized normal force and b) rheogram for several final compressive strains carried out in constant-volume conditions for glycerol (99 % w/w)-based suspensions ($\phi = 0.05$) at $H_0 = 133$ kA · m^{-1}.

Also, as shown in Figure 8.15-b the dimensionless normal force (normalized by the low-strain normal force plateau) is in good qualitative agreement with the MM prediction.

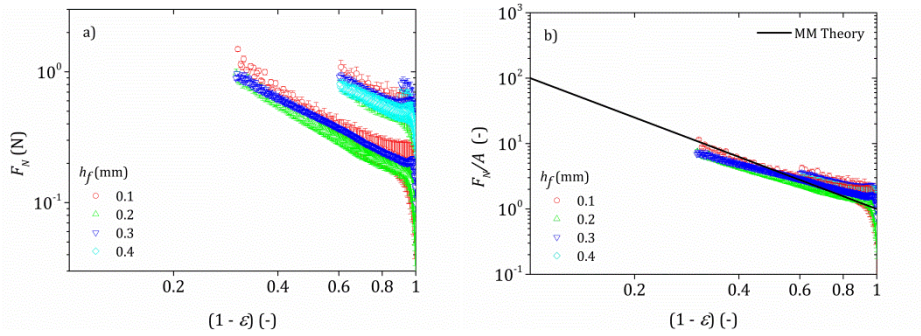

Figure 8.15: a) Normal force and b) normalized normal force as a function of compression in constant-volume experiments. A mixture (80.59:19.41 % w/w) of glycerol (87 % w/w) and water was used as carrier fluid ($\phi = 0.05$) at $H_0 = 133$ kA · m^{-1}. Three final compressive strains were achieved and four final gaps were employed to perform the wall slip correction.

Yield stresses as obtained from the wall-slip corrected rheograms are shown in Figure 8.12. The results demonstrate that the normal force dependence with the final strain compression is again moderate and slightly higher

for higher ε_T as in the case of using silicone oil as carrier fluid. However, higher yield stresses are found compared to constant-volume experiments in silicone oil. It is likely to be due to the difference in surface tension as the viscosity was mimicked. Moreover, wall slip effects were corrected and sedimentation cannot play any role in presence of magnetic field.

8.5.5. Importance of the field gradient in the compression behaviour of MR fluids in constant-volume tests

In order to elucidate the importance of the existence of a field gradient in the sheared volume during the steady shear test we carried out an additional experiment with an open coil instead of the electromagnetic circuit (see Subsection 3.2.7). In these new experiments the magnetic field strength was fixed at 11.9 kA · m^{-1}. Constant-volume experiments were carried out with a final gap $h_f = 300$ μm and several compressive strains in MR fluids prepared in the glycerol-water mixture. The surfaces confining the samples were exactly the same as in the experiments carried out in the electromagnetic assembly.

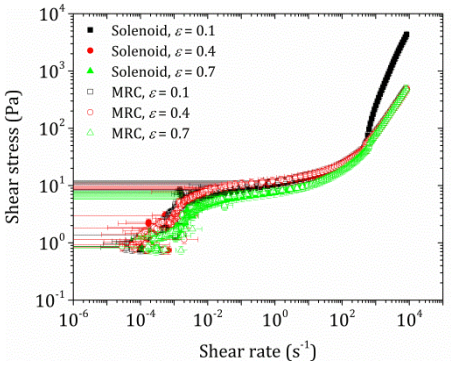

Figure 8.16: Comparison among two ways of applying the magnetic field ($H_0 = 11.9$ kA · m^{-1}) to determine the effect of field gradient. A mixture of glycerol (87 % w/w) and water (80.59:19.41 % w/w) was used as carrier fluid ($\phi = 0.05$).

In Figure 8.16 we show the stress versus shear rate curves for the solenoid (w/o gradient) and electromagnetic assembly (w/ gradient). Since the curves are very similar, it can be concluded that the field gradient is irrelevant when using the MRC.

8.5.6. Simulations for constant-volume and constant-area conditions

Particle-level simulations were performed over 1000 magnetizable particles randomly placed in a simulation box that is periodically repeated in two dimensions (x and y). The volume fractions used were $\phi = 0.05$, 0.10 and 0.20, and data shown here are the result of averaging five simulations in the same conditions. As it occurs in the experimental case their structuration, squeeze and shear was carried out while a constant and external magnetic field is considered. The length of the simulation box in z direction, i.e., the analogue to initial gap separation in experiments, in both constant-volume and area conditions was taken as 20 and 30 times the particle mean diameter at the beginning of each simulation. Due to this, the structuration process in presence of magnetic field produced the same final steady state in constant-volume and area conditions for a given combination of volume fraction and initial gap.

Results regarding the squeeze step are shown in Figure 8.17 for constant-volume and in Figure 8.18 for constant-area conditions. As a general trend, magnetic normal force is higher for higher particle concentrations, whatever the compressive strain, as expected from Equation 8.3. Curves also display an initial increase in the magnetic normal force at low values of ε followed by the appearance of a maximum and a fluctuating final decrease at higher compressions. This feature is not found in the experimental case, where normal force steadily increases, and may be due to difficulties in the reallocation of particles as higher compression develops. The fact that the maximum in the curves occurs at lower ε for higher particle concentration and lower initial gap h_i^* supports this explanation. Besides, it is more pronounced in constant-area simulations, where volume fraction increases because the particles are forced to remain in smaller simulation volumes as the compressive strain increases.

In the shear step, particle configurations in a range of compressive strains ($\varepsilon = 0 - 0.5$) were sheared at different rates of deformation, from $\dot{\gamma}^* = 10^{-5}$ to 10^{1}. The corresponding dimensionless shear stress τ^* was obtained from the addition of the hydrodynamic stress to the maximum magnetic shear stress (static). The last is difficult to be found for the two lowest shear rates as the peak in the curve of magnetic stress versus simulation time is barely developed. So that the yield stress has been calculated from the fit of the rheograms to a Casson model, $\tau^{0.5} = \tau_y^{0.5} + (\eta_\infty \dot{\gamma})^{0.5}$, without considering $\dot{\gamma}^* = 10^{-5}$ and 10^{-4}.

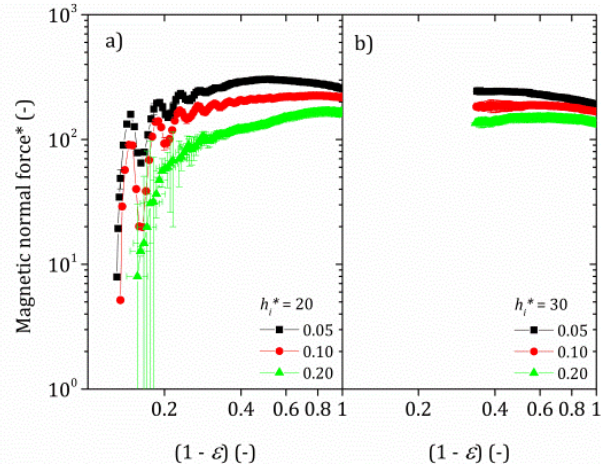

Figure 8.17: Compression curves for several volume fractions $\phi = 0.05$, 0.10 and 0.20 in constant-volume simulations of 1000 particles. Results for two initial gaps h_i^* are shown, namely 20 and 30 times the mean particle diameter in a) and b), respectively. Magnetic field was 177 kA · m^{-1}.

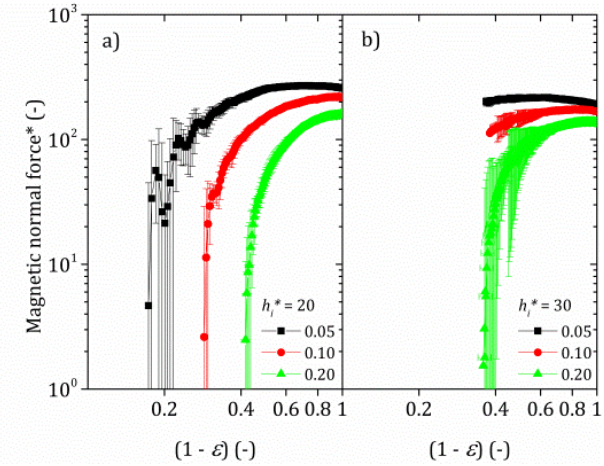

Figure 8.18: Compression curves for several volume fractions, $\phi = 0.05$, 0.10 and 0.20 in constant-area simulations of 1000 particles. Results for two initial gaps h_i^* of a) 20 and b) 30 (i.e., h_i being $20\sigma_m$ and $30\sigma_m$, respectively) are shown. Magnetic field was 177 kA · m^{-1}.

In Figure 8.19 the dimensionless yield stress is plotted as a function of the compressive strain for each studied situation. It is observed the clear dependence of this parameter with the volume fraction involved in the simulation and that it is always higher for constant-area simulations, as expected from the increase in volume fraction. However, the dependence with the

compressive strain agrees with experiments only in constant-area results and at low volume fractions, where the yield stress* increases with the level of compression in the squeeze step as a consequence of the densification process. In contrast, for constant-volume simulations the yield stress* slightly decreases with the compressive strain.

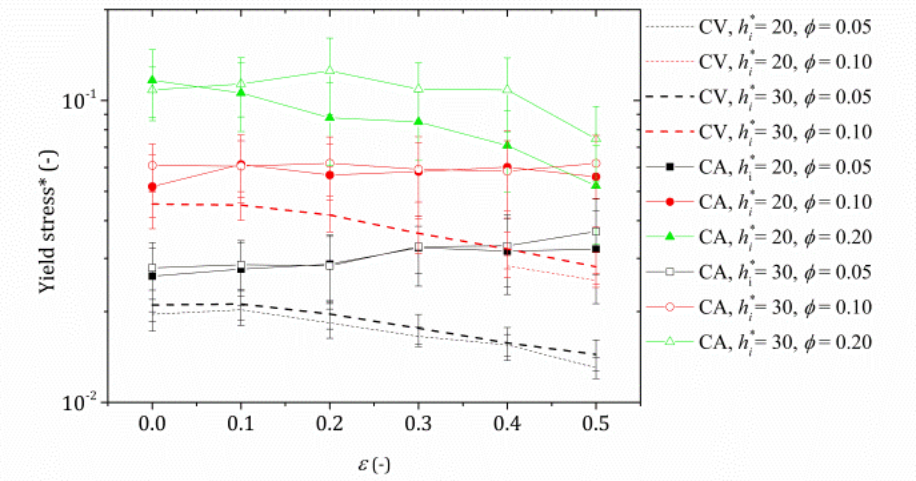

Figure 8.19: Normalized yield stress for constant-volume and constant-area simulations. The Casson model was used in rheograms, in the range of normalized shear rates of $\dot{\gamma}^* = 10^{-3}$ and 10^{1}.

8.6. Conclusions

In this work we carried out a detailed study on the squeeze-strengthening effect in diluted magnetorheological fluids, by means of experiments and particle-level simulations and under both constant-volume and constant-area conditions. The behaviour of MR fluids under slow compression is theoretically described by Micromechanical Models, valid for both conditions. This theory relates the compressive normal force with parameters such as the compressive strain, particle volume or the initial gap. Both type of tests provided good agreement with the predictions for compressive strains up to 0.8, although it was better in the case of constant-area.

Regarding the shear step, flow curves of the suspensions previously compressed showed an increasing dependence of the yield stress with the level of compression in the preceding stage, i.e., squeeze-strengthening effect, which was moderate for constant-volume experiments. We demonstrated that the densification of the suspension occurring during the constant-area compres-

sion is responsible to a large extent of the higher values of yield stress compared to constant-volume tests. Moreover constant-volume squeeze experiments were carried out in silicone oil and glycerol/water mixtures with the same particle loading. In this sense, we observed for each compressive strain an increasing effect in the yield stress that may be uniquely due to the surface tension in the yield stress, as the viscosities were matched. Additionally, we compared experiments carried out using a coil and a magnetorheological cell and evidenced an insignificant effect of the field gradient.

Particle-level simulations mimicked the experimental stages, i.e., structuration at rest, compression and shear, and the effect of volume fraction, total compressive strains up to 0.5, and initial gap under constant-volume and constant-area conditions were studied. In these simulations we found a dependence of yield stress with the compressive strain, and although both positive and negative tendencies are shown, yield stress values from constant-area simulations are always above those from the constant-volume case as a consequence of the densification process, in agreement with experiments.

8.7. References

[1] Rankin P J, Ginder J M and Klingenberg D J 1998 Electro- and magneto-rheology *Curr. Opin. Colloid Interface Sci.* **3** 373–381

[2] Klingenberg D J 2001 Magnetorheology: Applications and challenges *AIChE J.* **47** 246–249

[3] Ginder J M 2003 Rheology Controlled by Magnetic Fields *Digital Encyclopedia of Applied Physics* ed Wiley-VCH Verlag GmbH & Co. KGaA (Weinheim, Germany: Wiley-VCH Verlag GmbH & Co. KGaA)

[4] de Vicente J, Klingenberg D J and Hidalgo-Álvarez R 2011 Magnetorheological fluids: a review *Soft Matter* **7** 3701

[5] Carlson J D and Jolly M R 2000 MR fluid, foam and elastomer devices *Mechatronics* **10** 555–569

[6] Olabi A G and Grunwald A 2007 Design and application of magneto-rheological fluid *Mater. Des.* **28** 2658–2664

[7] Kulkarni P, Ciocanel C, Vieira S L and Naganathan N 2003 Study of the Behavior of MR Fluids in Squeeze, Torsional and Valve Modes *J. Intell. Mater. Syst. Struct.* **14** 99–104

[8] Wang X and Gordaninejad F 2006 Study of magnetorheological fluids at high shear rates *Rheol. Acta* **45** 899–908

[9] Rodríguez-Arco L, Kuzhir P, López-López M T, Bossis G and Durán J D G 2013 Instabilities of a pressure-driven flow of magnetorheological fluids *J. Rheol.* **57** 1121–46

[10] de Vicente J, López-López M T, Durán J D G and González-Caballero F 2004 Shear flow behavior of confined magnetorheological fluids at low magnetic field strengths *Rheol. Acta* **44** 94–103

[11] Ramos J, Klingenberg D J, Hidalgo-Alvarez R and Vicente J de 2011 Steady shear magnetorheology of inverse ferrofluids *J. Rheol.* **55** 127–152

[12] Zhang X Z, Gong X L, Zhang P Q and Wang Q M 2004 Study on the mechanism of the squeeze-strengthen effect in magnetorheological fluids *J. Appl. Phys.* **96** 2359–2364

[13] de Vicente J, Ruiz-lópez J A, Andablo-reyes E, Segovia-gutiérrez J P and Hidalgo-alvarez R 2011 Squeeze flow magnetorheology *J. Rheol.* **55** 753–79

[14] See H, Mackenzie S and Chua B T 2006 Effect of compression on the response of a magneto-rheological suspension *Korea-Aust. Rheol. J.* **18** 121–126

[15] Bigué J-P L, Charron F and Plante J-S 2015 Understanding the superstrong behavior of magnetorheological fluid in simultaneous squeeze-shear with the Péclet number *J. Intell. Mater. Syst. Struct.* **26** 1844–1855

[16] Becnel A C, Sherman S G, Hu W and Wereley N M 2015 Squeeze strengthening of magnetorheological fluids using mixed mode operation *J. Appl. Phys.* **117** 17C708

[17] Vieira S L, Ciocanel C, Kulkarni P, Agrawal A and Naganathan N 2003 Behaviour of MR fluids in squeeze mode *Int. J. Veh. Des.* **33** 36

[18] Dienes G J and Klemm H F 1946 Theory and Application of the Parallel Plate Plastometer *J. Appl. Phys.* **17** 458–71

[19] Covey G H and Stanmore B R 1981 Use of the parallel-plate plastometer for the characterisation of viscous fluids with a yield stress *J. Non-Newton. Fluid Mech.* **8** 249–260

[20] Williams E W, Rigby S G, Sproston J L and Stanway R 1993 Electrorheological fluids applied to an automotive engine mount *J. Non-Newton. Fluid Mech.* **47** 221–38

[21] Monkman G J 1995 The electrorheological effect under compressive stress *J. Phys. Appl. Phys.* **28** 588–93

[22] Vieira S L and de Arruda A C F 1998 Electrorheological Fluids Response under Mechanical Testing *J. Intell. Mater. Syst. Struct.* **9** 44–52

[23] Chu S-H, Lee S J and Ahn K H 2000 An experimental study on the squeezing flow of electrorheological suspensions *J. Rheol.* **44** 105–120

[24] Meng Y and Filisko F E 2005 Unidirectional compression of electrorheological fluids in electric fields *J. Appl. Phys.* **98** 074901

[25] McIntyre E C and Filisko F E 2007 Squeeze Flow of Electrorheological Fluids Under Constant Volume *J. Intell. Mater. Syst. Struct.* **18** 1217–1220

[26] Guo C, Gong X, Xuan S, Yan Q and Ruan X 2013 Squeeze behavior of magnetorheological fluids under constant volume and uniform magnetic field *Smart Mater. Struct.* **22** 045020

[27] Yangguang Xu, Xinglong Gong, Taixiang Liu and Shouhu Xuan 2014 Squeeze flow behaviors of magnetorheological plastomers under constant volume *J. Rheol.* **58** 659–79

[28] Tang X, Zhang X, Tao R and Rong Y 2000 Structure-enhanced Yield Stress of Magnetorheological Fluids *J. Appl. Phys.* **87** 2634

[29] Tang X, Zhang X and Tao R 2001 Enhance the Yield Shear Stress of Magnetorheological Fluids *Int. J. Mod. Phys. B* **15** 549–56

[30] Hegger C and Maas J 2016 Investigation of the squeeze strengthening effect in shear mode *J. Intell. Mater. Syst. Struct.* **27** 1895–1907

[31] Ghaffari A, Hashemabadi S H and Ashtiani M 2014 A review on the simulation and modeling of magnetorheological fluids *J. Intell. Mater. Syst. Struct.* **26** 881–904

[32] Farjoud A, Ahmadian M, Mahmoodi N, Zhang X and Craft M 2011 Nonlinear modeling and testing of magneto-rheological fluids in low shear rate squeezing flows *Smart Mater. Struct.* **20** 085013

[33] Ruiz-López J A, Hidalgo-Alvarez R and de Vicente J 2012 On the validity of continuous media theory for plastic materials in magnetorheological fluids under slow compression *Rheol. Acta* **51** 595–602

[34] Guo C, Gong X, Xuan S, Qin L and Yan Q 2013 Compression behaviors of magnetorheological fluids under nonuniform magnetic field *Rheol. Acta* **52** 165–76

[35] Ruiz-López J A, Hidalgo-Alvarez R and de Vicente J 2016 A micromechanical model for magnetorheological fluids under slow compression *Rheol. Acta* **55** 215–21

[36] Ruiz-López J A, Wang Z W, Hidalgo-Alvarez R and de Vicente J 2017 Simulations of model magnetorheological fluids in squeeze flow mode *J. Rheol.* **61** 871–81

[37] See H 2003 Field dependence of the response of a magnetorheological suspension under steady shear flow and squeezing flow *Rheol. Acta* **42** 86–92

[38] Jiles D 1991 *Introduction to Magnetism and Magnetic Materials* (Springer-Science+Business Media, B.V.)

[39] de Vicente J, Vereda F, Segovia-Gutiérrez J P, del Puerto Morales M and Hidalgo-Álvarez R 2010 Effect of particle shape in magnetorheology *J. Rheol.* **54** 1337–62

[40] Mooney M 1931 Explicit Formulas for Slip and Fluidity *J. Rheol.* **2** 210–22

III

Conclusions

9. Conclusions

In this dissertation we delved into several aspects entailing the appearance of shear thickening in unimodal and bimodal concentrated suspensions, and their relation to the frictional properties of these systems. Moreover we studied diluted MR fluids under slow compression. The aim of this chapter is to summarize the main conclusions found along the research work. According to the classification made in the outline of the thesis, conclusions can be gathered in three topics, as follows:

Rheology in dense suspensions

- As introduction to shear-thickening behaviour, concentrated model systems based on starch and fumed silica were studied, and displayed the typical features of this phenomenon:
  - At low shear, the flow produces a decrease in the viscosity of the suspension because it induces the break of the initial static particle network. At intermediate values, the suspension shows a Newtonian behaviour. Lastly, at high shear rates the system exhibit shear thickening.
  - The intensity of this growth in viscosity increases with the concentration of particles. It was quantified in both unimodal systems and their behaviour is identified as continuous shear thickening in the range of concentrations considered. Moreover, the

onset of the fluid-like to solid-like transition occurs at lower shear rates when the concentration increases.

- Both types of suspensions show a second shear-thinning region after the maximum viscosity, related to the particle deformability, in contrast to a shear-thickened state found in near hard-sphere particles.

- Along with changes in viscosity, shear flow generates stress anisotropy at high concentrations. In this sense, at high enough volume fractions, a transition from negative to positive first normal stress difference is obtained from normal force measurements. Dilation is found to occur at crossover stresses above the onset stress of shear thickening, when hydrodynamic interactions are surmounted by frictional ones.

- Regarding dense unimodal suspensions formulated with magnetic particles, it is remarkable the influence of the type of suspending fluid in the appearance of the shear-thickening regime. While ethylene glycol and diluted glycerol assist this behaviour, silicone oil completely inhibited it. This situation is explained in terms of attraction in the systems: the Hamaker constant for two iron particles suspended in silicone oil is higher than in the rests of fluids. So that attraction can entirely obscures shear-thickening. This is also the reason of the vanishing of shear thickening when an externally applied magnetic field increases. Furthermore, rheological measurements with silica-coated and bare carbonyl iron particles pointed a promoting effect of the silica layer in the appearance of shear-thickening when they are suspended in adequate liquids.

- Considering dense bimodal suspensions formulated with mixtures of both magnetic and non-magnetic particles, the inclusion of attractive interparticle interactions, through the addition of magnetic particles or the increase in magnetic field in a shear-thickening system, progressively delays this behaviour. Especifically, at $\phi_{CC} = 0.005$, shear thickening is completely inhibited for a $\phi_{Starch} = 0.36$ above a field intensity of 1 A, and shear thinning is observed instead.

- Hybrid core-shell particles were prepared by coating carbonyl iron particles with starch. The coating was successful for two methods (S and DL) with starch surrounding magnetic particles in a uniform layer. This thin coating increased the viscosity of the suspension and was

capable of destroying the yield stress when compared with a concentrated suspension of raw magnetic particles in presence of magnetic field, probably associated with a higher particle roughness.

- Particle-level simulations of monodisperse mixtures of magnetisable and non-magnetisable particles show an increasing yield stress with volume fraction as a consequence of thicker magnetic columnar aggregates, and up to $\phi_T = 0.30$ only shear thinning and Newtonian regimes are found. However, from the calculation of yield stresses it is demonstrated that above $\phi_T = 0.20$ it enhances when a magnetic system is partially substituted by non-magnetic particles is observed.
- Higher total concentrations were obtained by introducing polydispersity in the simulation box, and shear-thickening behaviour was finally observed in the case of concentrated unimodal suspensions of magnetic particles at very low magnetic fields.
- The rheological behaviour of concentrated MRST suspensions depends on multiple factors, such as volume fraction, particle-particle interactions within the carrier fluid, shape and roughness of particles, and shear flow conditions, but under the correct combination of factors it is possible to observe shear-thickening behaviour.

Tribology in inelastic non-Newtonian fluids

- Numerical simulations on the tribological properties of shear-thinning and shear-thickening fluids have provided regression formulas for the film thickness and friction coefficient within the isoviscous elastohydrodynamic lubrication (IEHL) regime.
- From the full solution approach an effective lubricant viscosity is expressed in a regression formula that is able to collapse all the simulation data on a master curve. Predictions from numerical simulations show a good agreement with experimental data.
- Concentrated suspensions of starch in several carrier fluids showed very distinct rheological behaviour, from shear thickening in polar carriers to shear thinning in non-polar ones that would promote interparticle attraction.
- In relation to friction curves, friction coefficient is strongly affected in the boundary region by the nature of the carrier fluid, in particular its wettability in contact with the hydrophobic PDMS. Besides, the parti-

cle-fluid interactions greatly affect the particle loading tendencies in this region. In this sense, relevant information on the entrainment of particles/fluid through the contact can be extracted from the Stribeck curves.

- Carreau-Yasuda constitutive equation was used for the calculation of the viscosity-shear rate relationship of G99-based starch suspensions, and numerical simulations in the IEHL regime showed certain discrepancies between simulations and experiments with suspensions, however a better agreement was found for the Newtonian carrier fluid.

Rheology of diluted MR fluids under squeeze flow

- Experiments under constant-volume and constant-area conditions provided good agreement with the predictions of micromechanical models for diluted MR fluids under slow compression.
- The comparison of yield stresses obtained for two suspensions with different carrier fluids evinced the effect of surface tension in the yield stress. Moreover the effect of the field gradient within squeeze experiments because of the magnetorheological cell was insignificant.
- Compression under constant-area conditions apparently gives rise to an enhanced squeeze-strengthening effect in comparison with constant-volume conditions. However, it was demonstrated that these higher yield stresses found in the first case were due to a densification effect, both in experiments and in particle-level simulations.